THRUST AREA REPORT • UCRL 53868-97

FY 97

Engineering Research, Development and Technology

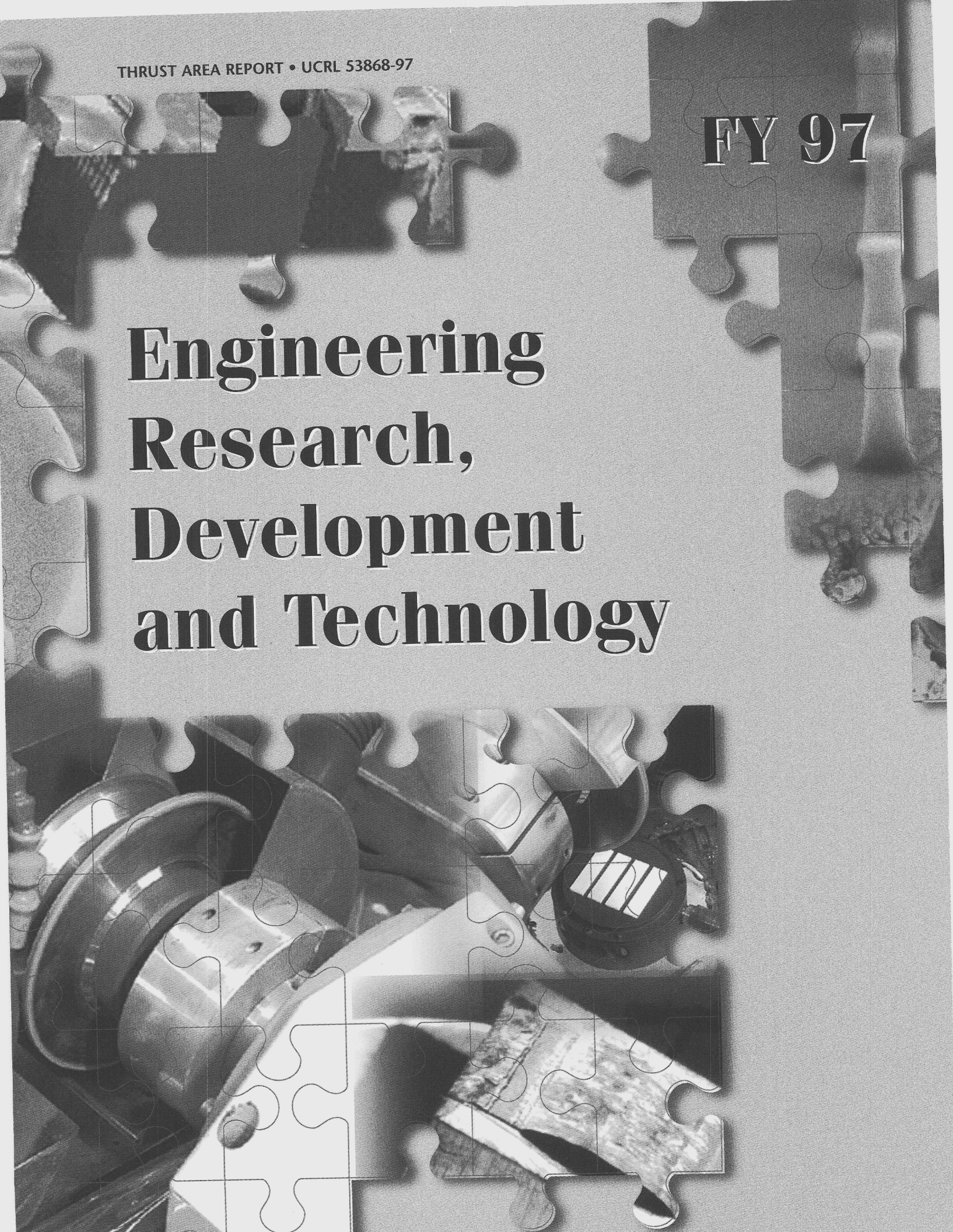

Acknowledgments

Scientific Editing
Robert T. Langland
Camille Minichino

Composition
Sharlene R. Markow

Graphic Design
Pamela A. Allen

Art Production/Layout
Kenneth M. Ball
Dennis Chan
Irene J. Chan
Kirk T. Hadley
Galen B. Hazelhofer
Penny L. Keenan
Robert J. Smith
Melissa A. Villarante

Publication Services
Jody A. Johnson

Available to the public from the
National Technical Information Service
U.S. Department of Commerce
5285 Port Royal Rd.,
Springfield, VA 22161

DISCLAIMER

This document was prepared as an account of work sponsored by an agency of the United States Government. Neither the United States Government nor the University of California nor any of their employees makes any warranty, express or implied, or assumes any legal liability or responsibility for the accuracy, completeness, or usefulness of any information, apparatus, product, or process disclosed, or represents that its use would not infringe privately owned rights. Reference herein to any specific commercial products, process, or service by trade name, trademark, manufacturer, or otherwise, does not necessarily constitute or imply its endorsement, recommendation, or favoring by the United States Government or the University of California. The views and opinions of authors expressed herein do not necessarily state or reflect those of the United States Government or the University of California and shall not be used for advertising or product endorsement purposes.

Work performed under the auspices of the U.S. Department of Energy by Lawrence Livermore National Laboratory under Contract W–7405–Eng–48.

THRUST AREA REPORT • UCRL 53868-97

FY 97

Engineering Research, Development and Technology

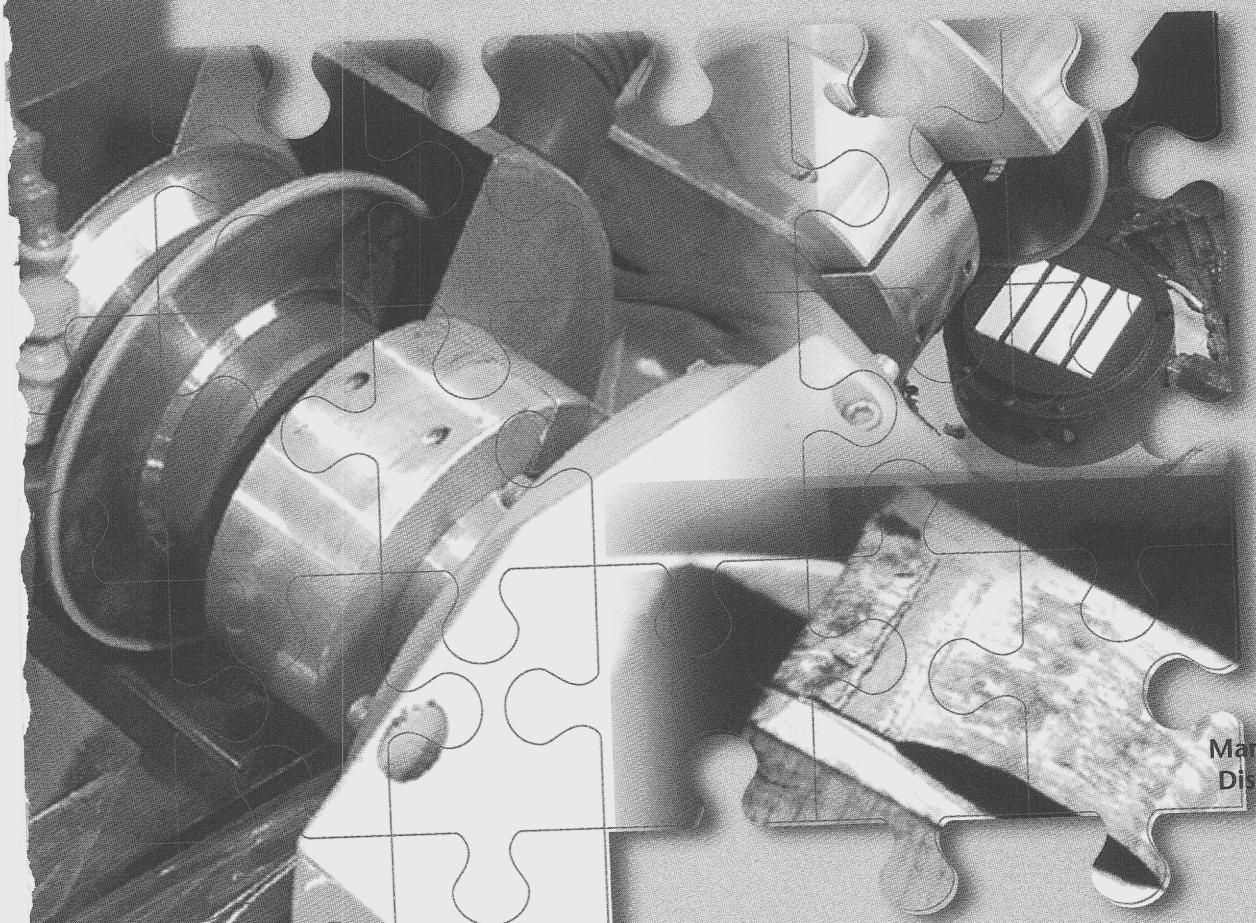

Manuscript Date January 1998
Distribution Category UC-706

Introduction

Spiros Dimolitsas, Associate Director for Engineering

1. Computational Electronics and Electromagnetics

Overview
Clifford C. Shang, Thrust Area Leader

Technologies for Advanced Induction Accelerators
Maurice A. Hernandez *1-1*

TIGER: An Object-Oriented Time-Domain Electromagnetics Simulation Code
David J. Steich, Jeffrey S. Kallman, and Gerald J. Burke *1-5*

Multi-Scale Electrodynamics (MELD): A CAD Tool for Photonics Analysis and Design
Richard P. Ratowsky, Jeffrey S. Kallman, Robert J. Deri, and Michael D. Pocha *1-11*

2. Computational Mechanics

Overview
Peter J. Raboin, Thrust Area Leader

Energy- and Momentum-Conserving Rigid-Body Contact for NIKE3D and DYNA3D
Michael A. Puso and Edward Zywicz *2-1*

Computational Modeling of Prosthetics: A New Approach to Implant Design
Karin Hollerbach, Scott A. Perfect, and Harry E. Martz *2-5*

Characterization of Laser-Induced Mechanical Damage of Optical Components
Douglas R. Faux *2-11*

Parallel Algorithm Research for Solid Mechanics Applications Using Finite Element Analysis
Carol G. Hoover, Daniel C. Badders, Anthony J. De Groot, and Robert J. Sherwood *2-17*

An Accurate One-Step Elasto-Plasticity Algorithm for Shell Elements in DYNA3D
Jerry I. Lin *2-25*

3. Microtechnology

Overview
Raymond P. Mariella, Jr., Thrust Area Leader

Gas and Vapor Preconcentrator
Conrad N. Yu, Jackson C. Koo, and Norman F. Raley 3-1

Compliant Silicon Nitride Cantilever Beams for Atomic Force Microscope Applications
Dino R. Ciarlo 3-3

Sub-Micron Lithography
Dino R. Ciarlo 3-5

Complementary Metal-Oxide Semiconductor Electronics and Micro-Electro-Mechanical Systems
Charles F. McConaghy and Abraham P. Lee 3-7

Monolithic High-Performance Three-Dimensional Coil Inductors for Wireless Communication Applications
Vincent Malba, Darrin J. Young, Jia-Jiunn Ou, Anthony F. Bernhardt, and Bernhard E. Boser 3-11

Vertical-Lasing Semiconductor Optical Amplifiers
Jeffrey D. Walker and Sol P. Dijaili 3-17

Field-Emission Cathode Micro-Electro-Mechanical System Technology for Sensors, Diagnostics, and Microelectronics
Jeffrey D. Morse, Jackson C. Koo, Robert T. Graff, Alan F. Jankowski, and Jeffrey P. Hayes 3-21

Blue Laser Diode Process Development
Glenn A. Meyer, Gregory A. Cooper, Stacy L. Lehew, and Steven DenBaars 3-25

Laser Transceiver for Safeing Applications
Charles F. McConaghy and Karla G. Hagans 3-31

4. Manufacturing Technology

Overview
Kenneth L. Blaedel, Thrust Area Leader

A Spatial-Frequency-Domain Approach to Designing Precision Machine Tools
Debra A. Krulewich *4-1*

Micro-Drilling of ICF Capsules
Steven A. Jensen *4-13*

5. Materials Science and Engineering

Overview
Donald R. Lesuer, Thrust Area Leader

Evolution of Anisotropic Yield Behavior
Daniel J. Nikkel, Jr., Arthur A. Brown, and James Casey *5-1*

Modeling of Shear Localization in Materials
Donald R. Lesuer, Mary M. LeBlanc, Robert A. Riddle, and Bert R. Jorgensen *5-7*

Modeling of Casting Microstructures and Defects
Arthur B. Shapiro and J. Del Eckels *5-13*

6. Power Conversion Technologies

Overview
Ronald E. Haigh, Thrust Area Leader

High-Density Photovoltaics
Ronald E. Haigh, Gerard F. Jacobson, and Steve Wojtczuk *6-1*

7. Nondestructive Evaluation

Overview
Harry E. Martz, Thrust Area Leader

Image Recovery Techniques for X-Ray Computed Tomography in Limited-Data Environments
Dennis M. Goodman, Jessie A. Jackson, and Maurice B. Aufderheide, and Erik M. Johansson *7-1*

Techniques for Enhancing Laser Ultrasonic Nondestructive Evaluation
Graham H. Thomas, Diane J. Chinn, Robert D. Huber, James V. Candy, and James Spicer *7-7*

Optical Inspection of Glass-Epoxy Bonds
Diane J. Chinn, Dwight E. Perkins, and Raymond M. Brusasco *7-11*

Miniature X-Ray Source Development
Jeffrey D. Morse, Robert T. Graff, Alan F. Jankowski, and Jeffrey P. Hayes *7-15*

Improving Computed Tomography Design and Operation Using Simulation Tools
G. Patrick Roberson, Daniel J. Schneberk, Jerry J. Haskins, Clint M. Logan, Harry E. Martz, Dwight E. Perkins, and Derrill R. Rikard *7-19*

8. Optical Engineering

Overview
Theodore T. Saito, Thrust Area Leader

Precision Machining of Micro-Features in Structural Ceramics
Mark A. Piscotty, Pete J. Davis, Barry L. Freitas, Jay A. Skidmore, and Theodore T. Saito *8-1*

Selected Engineering Publications

Selected Engineering Publications *PB-1*

Author Index

Author Index *AI-1*

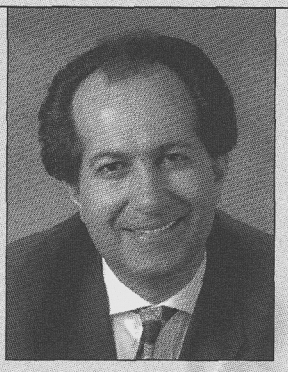

Spiros Dimolitsas, Associate Director for Engineering

The mission of the Engineering Research, Development, and Technology Program at Lawrence Livermore National Laboratory (LLNL) is to develop the knowledge base, process technologies, specialized equipment, tools and facilities to support current and future LLNL programs. Engineering's efforts are guided by a strategy that results in dual benefit: first, in support of Department of Energy missions, such as national security through nuclear deterrence; and second, in enhancing our collaboration with U.S. industry and universities in pursuit of the most cost-effective engineering solutions to LLNL programs.

To accomplish this mission, the Engineering Research, Development, and Technology Program has two important goals: (1) identify key technologies relevant to LLNL programs where we can establish unique competencies, and (2) conduct high-quality research and development to enhance our capabilities and establish ourselves as the world leaders in these technologies. To focus Engineering's efforts, technology thrust areas are identified and technical leaders are selected for each area. The thrust areas are comprised of integrated engineering activities, staffed by personnel from the nine electronics and mechanical engineering divisions, and from other LLNL organizations.

The thrust area leaders are accountable to me for the quality, programmatic relevance and progress of their activities, but have sufficient latitude to manage resources allocated to them. Thrust area leaders are also expected to establish strong links with LLNL programs and industry; be knowledgeable in the state of the art outside of LLNL; use university contacts to supplement and complement their efforts; and use outside and inside experts to critically review the quality and direction of their work.

For the past several years, the Engineering Research, Development, and Technology Program has played a significant role in leveraging LLNL technology to enhance U.S. competitiveness, and in allowing us to access the best of industrial technologies for the benefit of LLNL programmatic missions.

This annual report, organized by thrust area, describes Engineering's activities for fiscal year 1997. The report provides timely summaries of objectives, methods, and key results from eight thrust areas: Computational Electronics and Electromagnetics; Computational Mechanics; Microtechnology; Manufacturing Technology; Materials Science and Engineering; Power Conversion Technologies; Nondestructive Evaluation; and Optical Engineering.

Readers desiring more information are encouraged to contact the individual thrust area leaders or authors, or to consult the selected list of publications by engineering authors given at the end of this report.

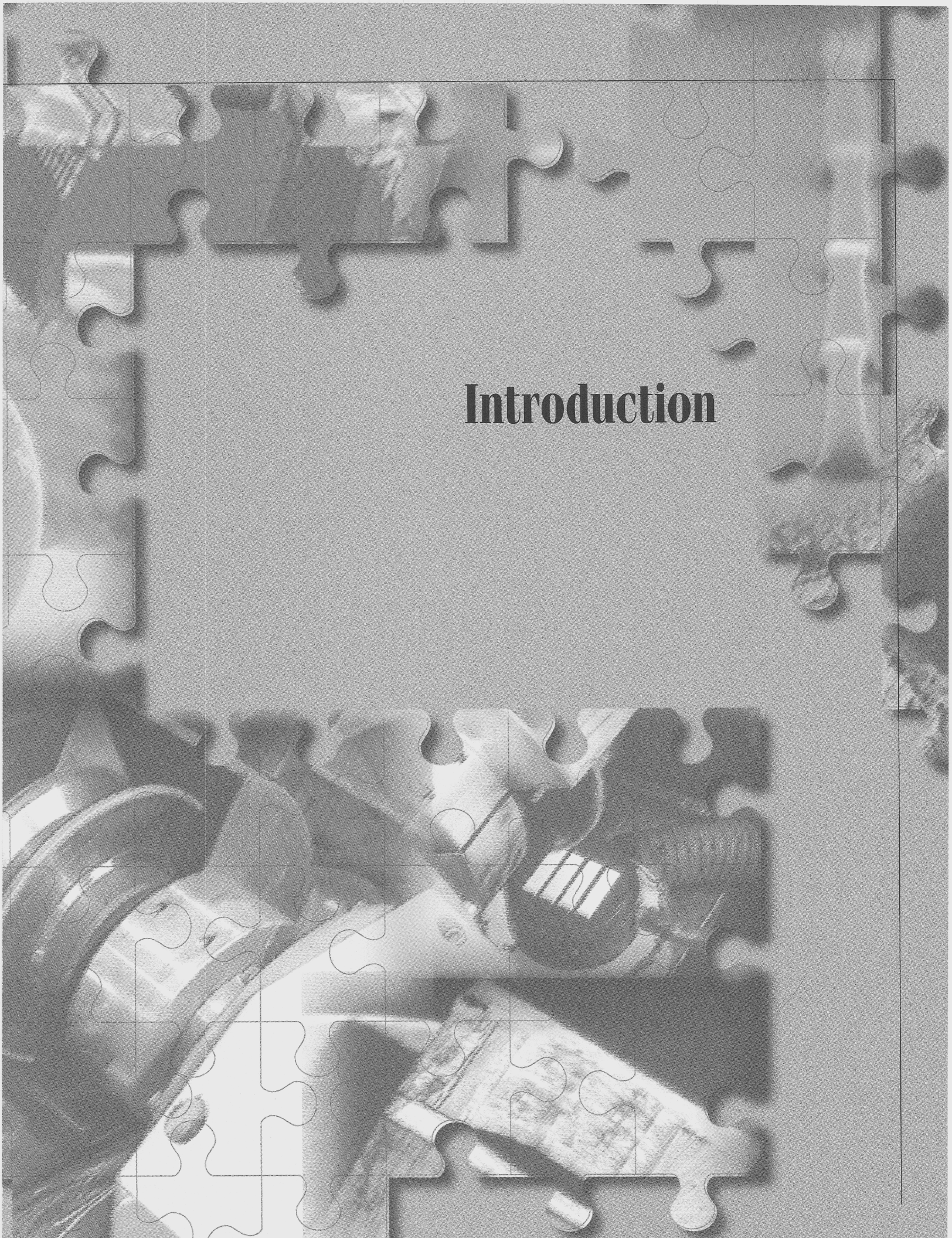

Introduction

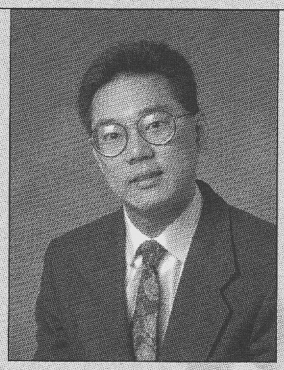

Clifford C. Shang, Thrust Area Leader

The Computational Electronics and Electromagnetics thrust area serves as the focal point for Engineering R&D activities for developing computer-based design and analysis tools. Representative applications include design of particle accelerator cells and beamline components; design of transmission line components; engineering analysis and design of high-power (optical and microwave) components; photonics and optoeletronics circuit design; electromagnetic susceptibility analysis; and antenna synthesis.

The FY-97 effort focuses on development and validation of 1) accelerator design codes; 2) 3-D massively parallel, time-dependent EM codes; 3) material models; 4) coupling and application of engineering tools for analysis and design of high-power components; and 5) development of beam control algorithms coupled to beam transport physics codes.

These efforts are in association with techology development in the power conversion, nondestructive evaluation, and microtechnology areas. The efforts complement technology development in Lawrence Livermore National programs.

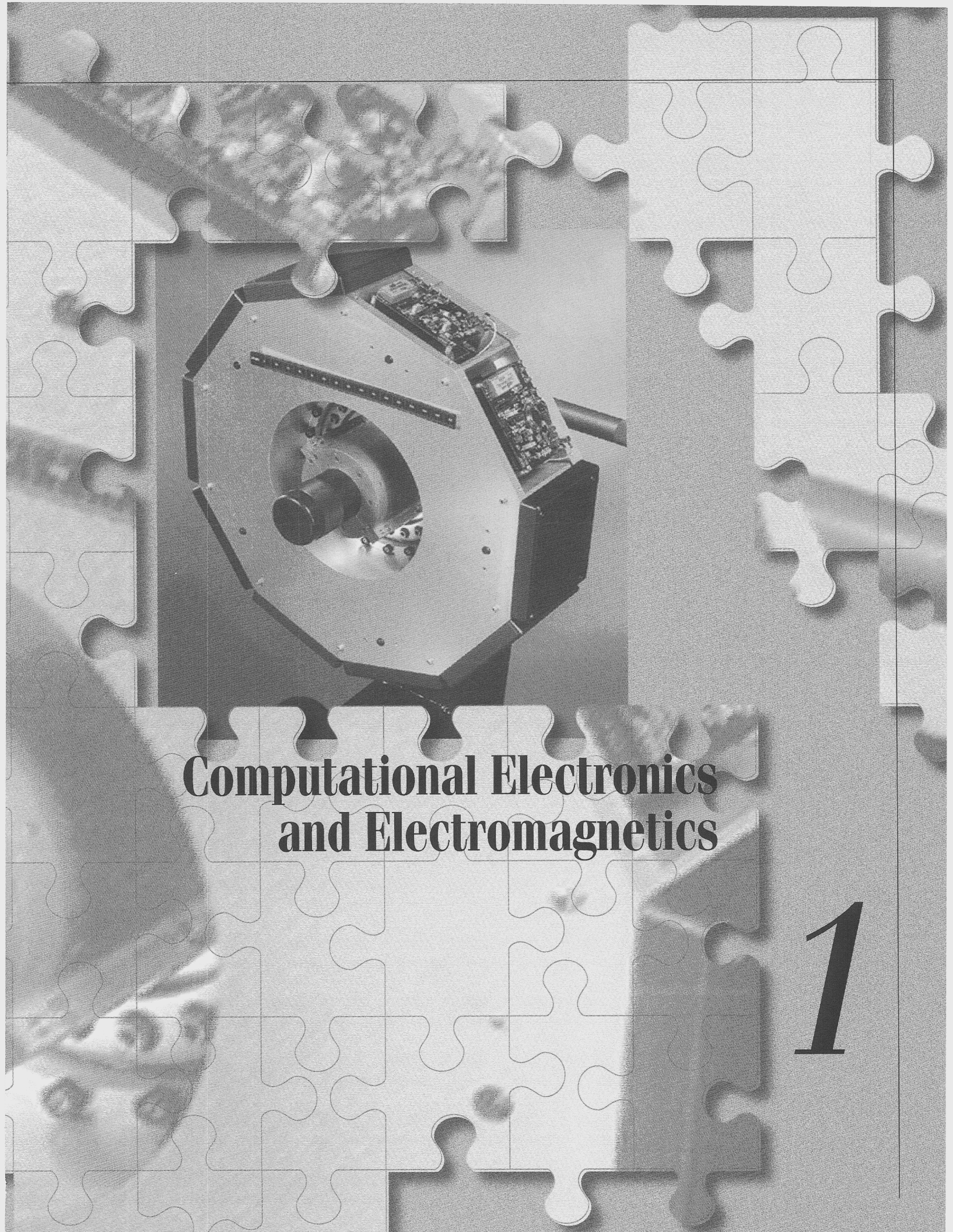

Computational Electronics and Electromagnetics

1

1. Computational Electronics and Electromagnetics

Overview
Clifford C. Shang, Thrust Area Leader

Technologies for Advanced Induction Accelerators
Maurice A. Hernandez *1-1*

TIGER: An Object-Oriented Time-Domain Electromagnetics Simulation Code
David J. Steich, Jeffrey S. Kallman, and Gerald J. Burke *1-5*

Multi-Scale Electrodynamics (MELD): A CAD Tool for Photonics Analysis and Design
Richard P. Ratowsky, Jeffrey S. Kallman, Robert J. Deri, and Michael D. Pocha *1-11*

Technologies for Advanced Induction Accelerators

Maurice A. Hernandez
Defense Sciences Engineering Division
Electronics Engineering

In FY-97 we laid the groundwork for the development of a sophisticated system, capable of real-time control of the Heavy Ion Fusion (HIF) recirculating accelerator at Lawrence Livermore National Laboratory (LLNL). Our efforts included modeling the ion beam dynamics; designing and deploying a new injector pulser; and work to model, design, and test induction core modulators, as well as pulsers for the steering dipoles and insertion/extraction kickers.

Introduction

A 1991 study[1] showed that a recirculating ion beam accelerator (recirculator) is a promising candidate for a cost-effective driver for inertial fusion energy. Its promise is derived from the fact that the beam passes many times through each accelerating component; thus, fewer and more effective accelerating elements, as well as fewer focusing magnets, are required. This leads to a cost savings relative to a linear accelerator, which uses each accelerating core and focusing quadrupole only once per pulse (**Fig. 1**).

With the recirculator concept, we can also avoid beam resonance effects by using an active control system to rapidly ramp the bending field, and rapidly accelerate the beam (since the oscillating frequency of the particles in the confining field is rapidly changing, and hence is not resonant). Thus, much larger currents can be transported than are possible in a conventional synchrotron. However, these advantages are achieved at the expense of entering a regime in which the total path length traversed by the beam is greater, the repetition rate of the induction modules is higher, and the dynamics of transporting beams around the bends are unexplored.

These new and unexplored regimes make the development path leading to a small, scaled recirculator ground-breaking and rich in potential scientific discovery and technological innovation. The results of this project are expected to prove useful for a range of applications in defense and pure science.

As of the end of FY-97, several technology elements in this program are well along the development path to a complete recirculator. We have carried out a large complement of beam-transport modeling simulations, used to develop control algorithms and to help derive performance specifications on some accelerator components. A new injector pulser was developed that greatly enhanced the initial beam

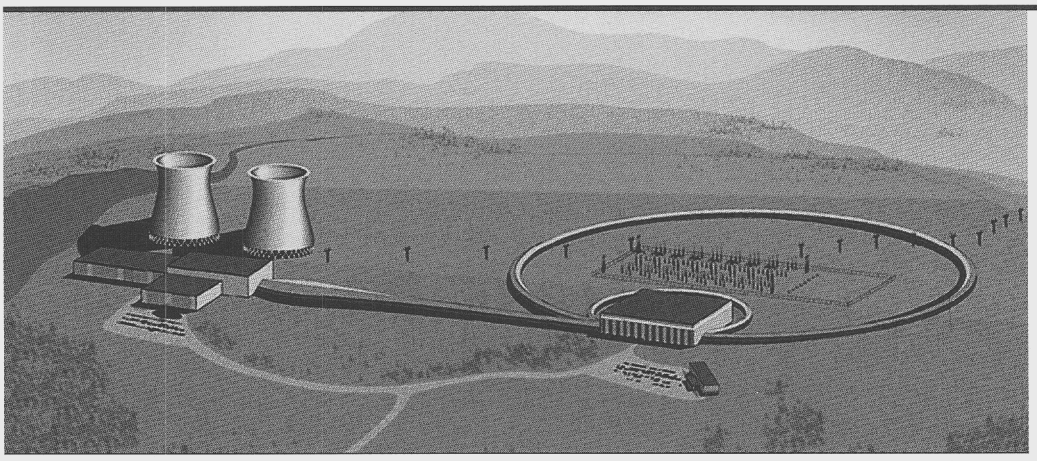

Figure 1. Conceptual drawing of a future Heavy Ion Fusion Power Plant.

quality. Matching and magnetic transport experiments have been carried out on a completed injector, matching section, and insertion section.

We have co-developed, with Lawrence Berkeley National Laboratory (LBNL), a pulser capable of dynamically driving the bending dipoles at the proper rate for beam steering. A similar pulser has been designed to drive the ion beam insertion/extraction kickers. The prototype induction modulator package has been built and tested extensively.

Significant further development, which will carry over into FY-98, will be necessary before the prototype can be replicated in quantity. We have completed construction of 10 half-lattice periods (modulator and dipole assemblies), enough to complete 90° of the recirculator. Tailored acceleration (adaptive control of modulator pulse characteristics) coupled with ramping of the dipole (bending) fields, to be addressed as part of our FY-98 work, is the next essential element for concept validation. We propose to build a full 360°-ring by some time around the end of FY-99. Our initial goal in the completed ring will be to transport the beam for fifteen laps.

Progress

Beam-Transport Modeling

We set out to answer a number of questions through the modeling of the beam-transport dynamics. The level of precision required for successfully transporting the beam around the recirculator factors into the specifications for many system components. Through modeling, we can determine the relative effects on beam quality of different errors in the injector, acceleration, steering, and sensor sub-systems. We can then focus our development efforts on those sub-systems that are most critical to successful beam transport. We were also able to evaluate the effectiveness of proposed control algorithms, and refine the algorithms to optimize the beam quality (**Fig. 2**).

Early modeling results pin-pointed the importance of initial (injected) beam quality, and identified the injector sub-system as a problem area. The voltage pulse produced by the original injector pulser created an ion beam with small, inherent errors. Subsequent beam acceleration magnified the errors, creating instabilities that make beam control more difficult. Because of these findings, an effort was initiated to redesign the injector pulser. The results are covered later in this report.

Our simulation strategy called for sensing the position of a pulse, then applying corrections to subsequent pulses as opposed to attempting to apply corrections to the same pulse on successive laps around the recirculator (a much more difficult implementation prospect). Matched centroid positions were calculated, with position and velocity corrections applied at succeeding bending dipoles. We then verified the corrections at subsequent sensors. Simulations were carried out assuming error-free sensors. In practice, we anticipate that sensor errors will be small compared to cumulative errors in the steering components.

Random errors were introduced in bend strength (simulating dipole pulser errors), bend and quadrupole alignment, and beam characteristics, (such as stability, oscillations, energy, and uniformity). Error magnitudes on the order of 1% to 2% were found to be sufficient to cause the beam to impact the accel-

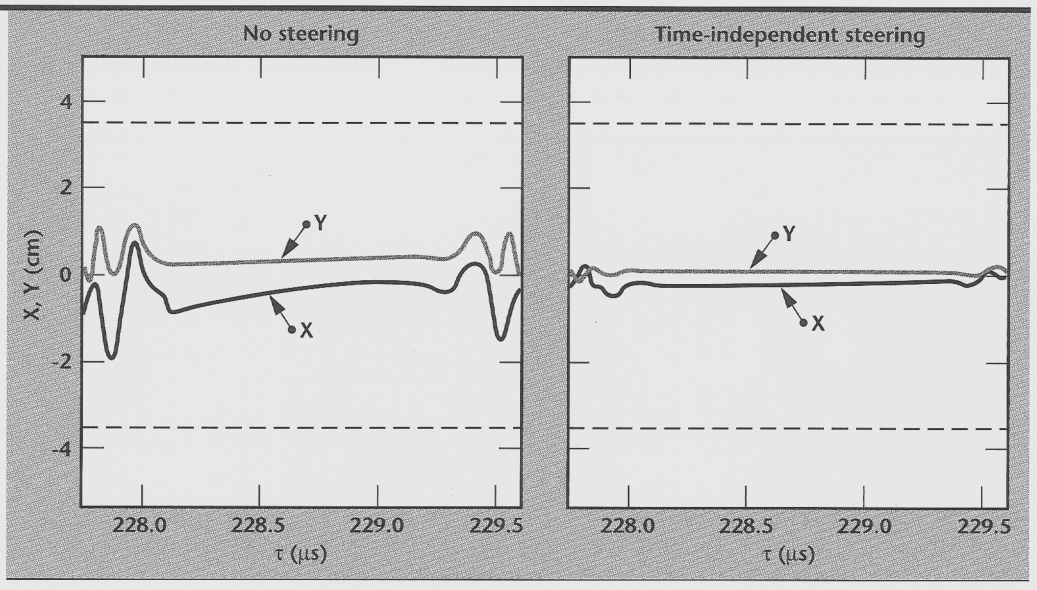

Figure 2. Simulated beam centroid position, showing the results of applied steering. The dashed lines represent the accelerator tube wall. Beam diameter is approximately 2.5 cm.

erator tube wall. Applying corrections as described in the previous paragraph demonstrated the ability to control the beam centroid within ±6 mm.

Design and Deployment of New Injector Pulser

As previously described, our modeling results revealed the need for redesigning our high potential ion source. The recirculator injector pulse modulators must be capable of producing very precise, repeatable voltage pulses to reduce the current modulation and achieve the required beam reproducibility. Initial beam control efforts will be focused on making corrections to the steering and acceleration waveforms on a pulse-to-pulse basis. Therefore, it is essential that the beam energy and timing from one pulse to the next are as nearly identical as possible. Modeling simulations have determined that errors greater than 0.1% in the flatness of the injector pulse can create intolerable beam energy deviations. Achieving these specifications pushes the limits of present pulse-power technology, including the methods used to measure the error in the modulator voltage pulse (**Fig. 3**).

To date, a new, higher voltage (120 kV), higher reliability pulse generator, which surpasses the previous generator in several key parameters, has been constructed, tested, and incorporated into the recirculator. The new generator produces a 5-μs pulse which is flat to less than ~0.1%. The rise and fall times of the pulse have an RC-type shape which is now adjustable by simply modifying resistor values. We have given a more detailed description of the new pulser in another report.[2]

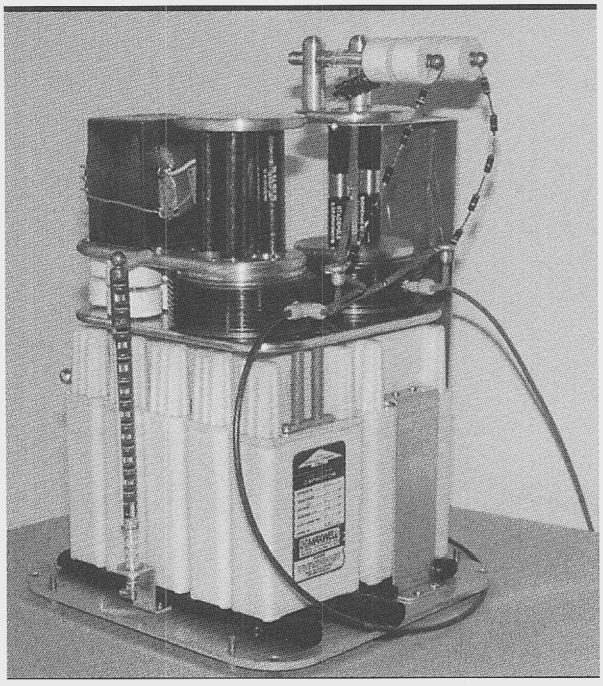

Figure 3. Photograph of the new injector pulser.

During FY-98, we propose to conduct a complete assessment and characterization of the injector performance, including beam measurements.

Dipole and Kicker Pulser Development

The dipole and kicker pulsers make use of modeling and design efforts carried out at LBNL. As the recirculator ion beam is accelerated around the ring, it is gaining both kinetic and electrical energy. Thus, a larger electric field must be developed across each succeeding dipole pair to keep the beam centered in the beam tube. The pulser uses stacked transformers to achieve the required voltage levels and response.

Our recirculator design calls for driving the steering dipoles with a quadratic waveform ramping from 7 kV to 27 kV over a time span of 228 μs (the time required to complete 15 laps). Modeling results indicate that driving the dipoles with a fixed ramp will be sufficient to steer the beam within the required tolerances. This will require precise control of the induction core modulator (acceleration) waveforms. Part of our future work will involve investigating the option of varying the dipole driver waveform to adapt to acceleration errors. The present pulser design is adaptable to this option.

Induction Core Modulator Development

The recirculator requires state-of-the-art high-repetition rate and highly variable pulse modulators for the induction cores. Modulator specifications call for high bandwidth and dynamic power control, with the ability to produce a programmable wave with a high degree of flatness and reproducibility (<1% error) over the entire pulse length, and repetition rates on the order of 100 kHz (**Fig. 4**).

The initial modulator work has been conducted by researchers in LLNL's Power Conversion Technologies Thrust Area, resulting in a prototype which has been used for performance testing. The baseline modulator design contains two feedback paths: fast local feedback, with a single pole at 1.0 MHz, and a slower main feedback returned from the ferrite or Metglass cores. The ratio of feedback from these sources will be adjusted to maintain overall stability, while still maintaining a specified degree of waveform fidelity between the input and output signals. To date, one test-bed modulator has been constructed. Experimental results have

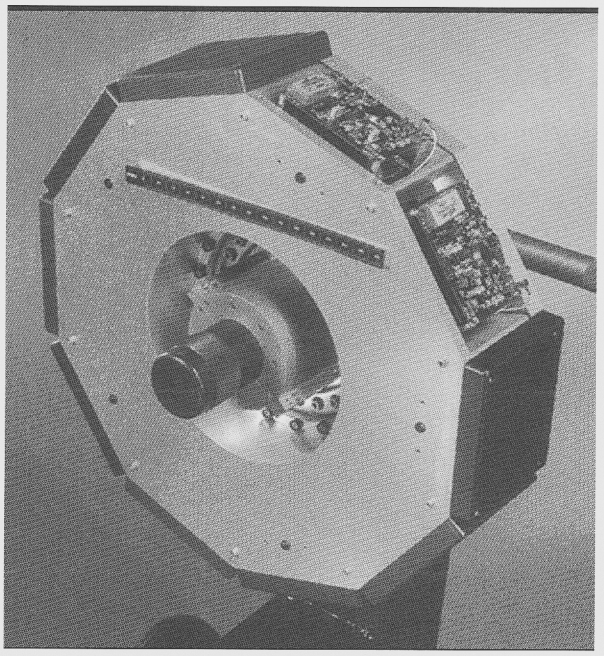

Figure 4. Prototype induction modulator with the drive electronics covers removed.

demonstrated a very good correlation between the measured modulator output voltage and the modeling data. However, our modeling results have also shown that the level of overshoot exhibited by the prototype may be beyond the required error tolerance. We will address this issue as part of our future work.

Future Work

A large portion of the development and testing, as well as the integration of the modulators with the induction cores will be carried out as part of the proposed work for FY-98. Through funding provided by other sources, we will complete construction of 180° of the recirculator by October, 1998.

We also plan to incorporate the dipole pulser, modulator waveform shaping, and additional beam diagnostics into the recirculator. We will design and conduct experiments to study the beam-transport dynamics in the presence of these new components, and to verify our modeling results. This will include our initial attempts to apply shot-to-shot beam-control adjustments, the first step toward real-time control. These experiments will provide a better understanding of the control elements, and help us to refine our component and algorithm designs. We will also be able to assess the performance of our diagnostics in providing enough feedback to effectively control the beam.

Results of these experiments will be used to extend the technologies to the full recirculator (expected to be completed around October, 1999), and to other future accelerators which will require dynamic control. Further small-scale modeling efforts may be carried out to support the experimental work.

Acknowledgments

The authors would like to acknowledge L. Reginato of LBNL for his work on the dipole pulser design. We would also like to acknowledge D. Goerz, who contributed much to the work on the new injector pulser.

References

1. Barnard, J. J. (1991), *Study of Recirculating Induction Accelerators as Drivers for Heavy Ion Fusion,* Lawrence Livermore National Laboratory, Livermore, CA, (UCRL-LR-108095).

2. Wilson, M. J., D. A. Goerz, R. Speer, and R. Moal (1997), *Heavy Ion Fusion (HIF) Impulse Injector Design, Construction, and Checkout,* Lawrence Livermore National Laboratory, Livermore, CA, (in press).

TIGER: An Object-Oriented Time-Domain Electromagnetics Simulation Code

David J. Steich, Jeffrey S. Kallman, and Gerald J. Burke
Defense Sciences Engineering Division
Electronics Engineering

This report discusses our progress to date and our future plans for the Time Domain Generalized Excitation and Response (TIGER) code. TIGER is an object-oriented computational electromagnetics (CEM) field solver. A prototype version of the TIGER code was completed this year. Preliminary results modeling a simplified 3-D kicker structure are shown. More than a 100-fold reduction in required cell count has been achieved, compared to previous modeling efforts. Our FY-98 plans include the parallelization of the TIGER code and the continued generalization and hybridization of the object-oriented framework.

Introduction

There is a significant need for more advanced time-domain CEM modeling capabilities related to the design of the Advanced Hydro Facility (AHF) at Lawrence Livermore National Laboratory (LLNL). Current CEM capabilities are represented by LLNL codes such as AMOS and TSAR, and by commercial codes such as MAFIA and XFDTD. These codes all have severe limitations, which include grid specific physics kernels; restricted material modeling capabilities; single-threaded physics methodologies; poor radiation boundary conditions; single-processor applicability (non MPP); simplified source inputs; and virtually non-existent interface algorithms. Many of these limitations occur because of historical scientific programming styles, largely induced by the use of FORTRAN, and preclude flexibility and extensibility. TIGER aspires to overcome these difficulties.

The development of a computational wakefield tool for the design of AHF accelerator components was the primary focus of our efforts this year. The design of a multi-pulse, multi-axis induction accelerator flash x-ray source for AHF requires development of accelerator components never designed before. Vital AHF components such as the induction cells, split beam-pipes, beam-line bends, and kicker structures require electromagnetic simulation to aid their design and ensure high beam-performance characteristics essential for the success of AHF.

The difficulty in accurately modeling these accelerator components can not be over-stated. Solving the full-wave physics of a high-space-charge-dominated electron beam being accelerated past induction cells, bent around corners, and split by kickers and septum magnets is presently an intractable problem using conventional 3-D particles-in-cell (PIC) codes. Even separating the problem into full-wave physics and beam-transport analysis regimes does not make the problem tractable. Beam-transport codes track beam dynamics such as beam envelope and centroid positions, but cannot be used where the beam experiences significant wakefields caused by perturbations in pipe cross-section. Currently, we are not directly addressing the beam-transport regime of modeling.

Our focus has been on the full-wave physics modeling required in areas where the pipe significantly changes cross-section, as is the case with the AHF components described above. These high wakefield regions can lead to beam instabilities known as beam break-up (BBU). To reduce the computational burden, linear electromagnetic full-wave physics calculations are performed to obtain wakefield impedances, under the assumptions that space charge effects can be ignored and that the wakefields do not influence the beam trajectory (that is, no coupling between wake fields and electron beam).

The first assumption is usually not of large concern, but must be kept in mind and checked whenever possible with analysis, experimentation, or with PIC simulations that include particle-particle interactions. To a large extent, the second assumption can be removed by post-processing the wakefield impedances and obtaining a better

approximation for the beam trajectory, then, in an iterative fashion, re-running the problem with the improved trajectory and obtaining improved wakefields until convergence is achieved. These assumptions allow linear electromagnetic wakefield simulations to be used, which are much more efficient than PIC simulations. However, even linear electromagnetic wakefield calculations are intractable using present codes.

Progress

During the past year we successfully built a full working prototype version of TIGER, capable of modeling 3-D wakefield structures relevant to AHF. This prototype version implements our object-oriented memory and mesh management abstractions. Our goal was to test the usability, efficiency, flexibility, and extensibility of these abstractions in a real application setting. The physics kernel abstractions were implemented in elementary form. This allowed a much quicker working version of TIGER, and also provided a platform to test our on-going object-oriented research. The implementation of the wakefield physics and modeling of a simplified kicker structure (known as a Beam Position Monitor) was the primary emphasis of this year's thrust area project.

As a first example of TIGER's prototype capabilities, we considered the wake potential calculation of a relativistic electron beam going through a pillbox. We implemented a unstructured non-orthogonal discrete surface integral (DSI) method[1] to solve for the fields, using advanced radiation boundary conditions (RBCs),[2] and the latest in object-oriented techniques.[3,4]

Figure 1 shows a picture of the pillbox and a 2-D cross-section of the 3-D mesh blow-up of the pipe region. The pillbox height is 35 cm; the pipe radius is 1.1875 cm, and the gap width is 2 cm. A Gaussian pulse electron beam current source is used, with a full-width-half-maximum of 0.49486 ns. Quasi-analytic solutions exist for this problem.[5,6] The analytic solution of Weiland and Zotter assumes the pipe radius is zero.[5]

Shown in **Fig. 2** is a comparison of the two quasi-analytic solutions and TIGER. With this geometry, the solution of Weiland and Zotter overestimates the wake potential, especially near s = 0, due to the neglect of the finite pipe radius. The Dome solution takes into account the finite pipe radius, but neglects the frequency shifts in the solution due to the pipe. However, Dome states that this error is on the order of (pipe radius)^3/(gap length × pillbox radius)^2, which is ~ 0.000683.

The TIGER code used only 12,448 cells for this calculation. A TSAR calculation of this geometry using structured grid required just over a million cells. This example demonstrates TIGER's use of complex sources, advanced RBCs, general diagnostics, and wakefield formulations for a conforming, non-orthogonal, unstructured grid.

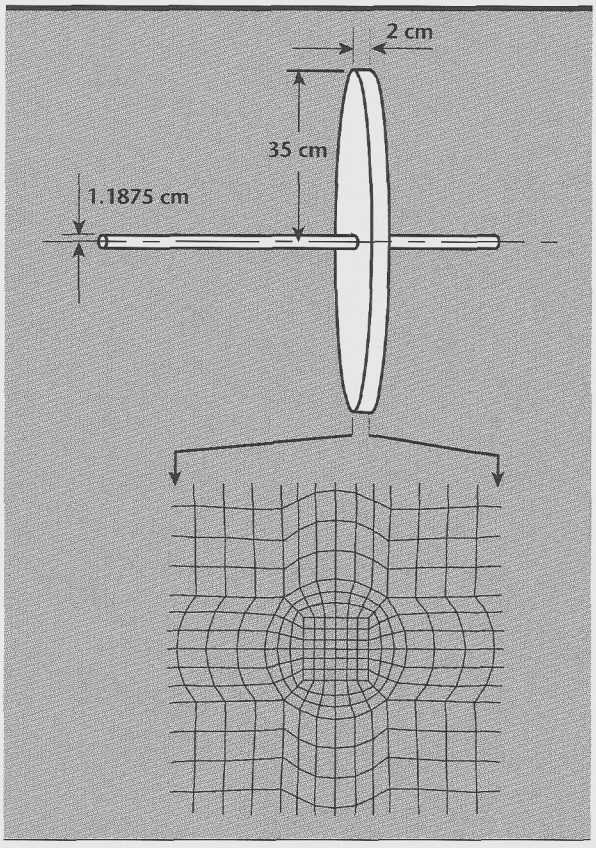

Figure 1. Two-dimensional mesh cross-section of three-dimensional pillbox.

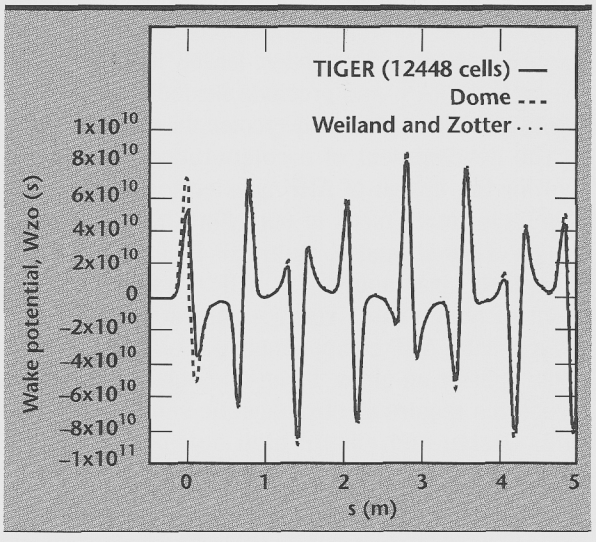

Figure 2. Wake potential comparison for pillbox geometry.

Next, we modeled a simplified kicker structure known a beam position monitor (BPM). Shown in **Fig. 3** is a picture of a BPM (the actual model did not include the beam-splitting section at the right in **Fig. 3**). For this example, each of the four kicker plates subtended 55° and was located at the unperturbed pipe radius. Modeling a BPM using TSAR required up to 30 million cells, 700+ MB RAM, weeks of CPU time, and was at the limit of what could be modeled. Thus, modeling a BPM would be a good demonstration of the new code.

We successfully modeled the BPM and compared results with existing simulation data and simplified analytic solutions. Over a 100-fold reduction in the number of cells was achieved with comparable or improved accuracy. This 100-fold reduction was accomplished by simultaneously using better boundary conditions (to truncate the problem space much closer to the kicker), conforming non-orthogonal grids (to avoid staircasing errors), extensive complex source modeling (to increase accuracy), and improved wakefield physics (to reduce both run time and required data storage).

Existing TSAR simulations required making two runs, gigabytes of data storage, at least a week of CPU time, and substantial post-processing. The new prototype code required only one run, kilobytes of data storage, two hours CPU time, and minimal post-processing. It also demonstrated new physics trends not shown in existing models.

Shown in **Figs. 4** and **5** are several preliminary TIGER results for the real and imaginary parts of the monopole wakefield impedance. The transmission line theory results are that of Ng[7] and do not take into account the cavity. The two TIGER results using 27.5K cells and 162.5K cells are in close agreement with one another, while the 8-million-cell TSAR result is further off. TSAR has only cubical cell capabilities, and so a staircased approximation was used for the BPM geometry. Due to the size of the model, running a more refined TSAR mesh was not possible using present resources.

Also shown in **Fig. 5** are 2-D results and an analytical solution of Heitfets and Kheitfets.[8] The designations, 'Heitfets and Kheitfets,' and '2-D no kicker,' correspond to results in the absence of the four kicker plates. Note the increasing trend of the analytic solution, the 2-D results, and the TIGER results. This increasing trend in imaginary longitudinal monopole impedance is due to the cavity. The transmission line theory does not take this into account. Note that the TSAR results also did not pick up the cavity part of the solution. It is unclear

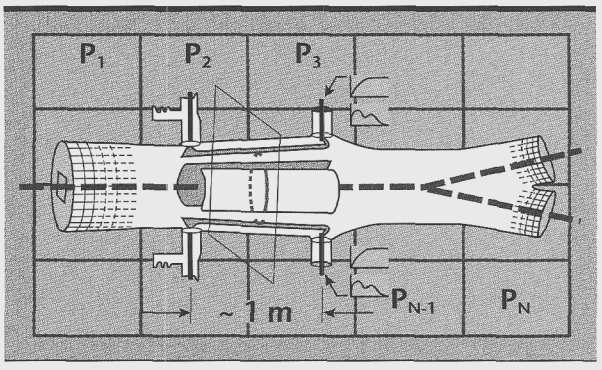

Figure 3. Kicker structure.

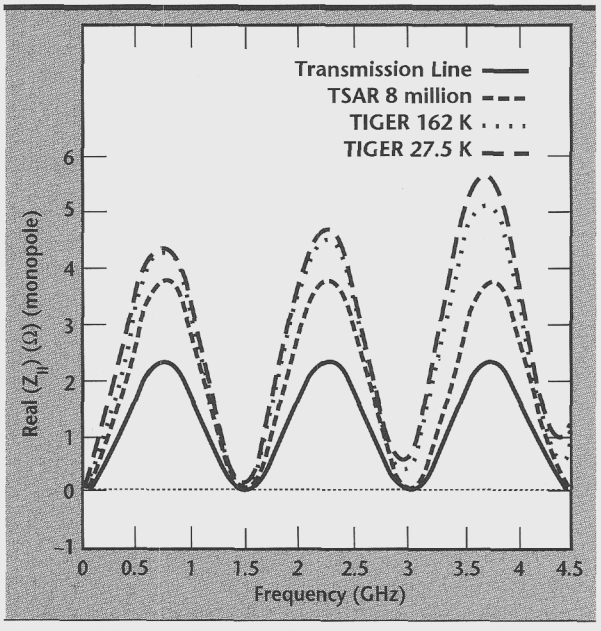

Figure 4. Real $Z_{||}$ monopole results.

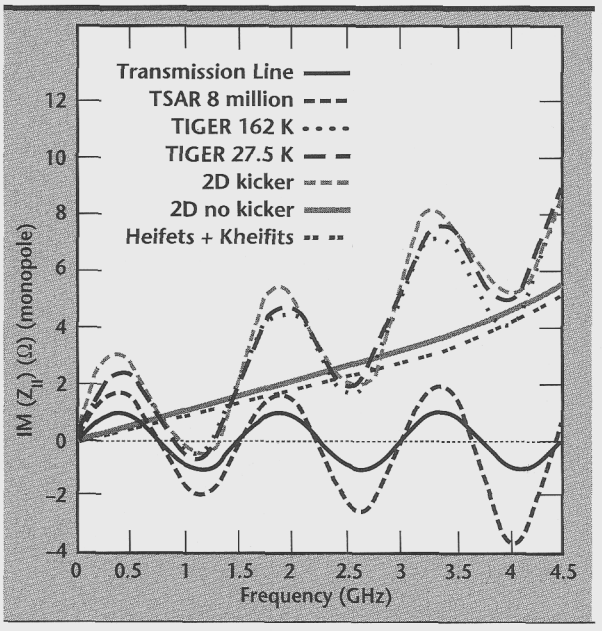

Figure 5. Imaginary $Z_{||}$ monopole results.

at this time why TSAR is not picking up this bias trend in the results. It is also possible, although unlikely, that the TIGER results shouldn't show this upward trend in impedance. There is mounting evidence to suggest that the TIGER results are correct, but further research of these preliminary results still needs to be done.

Shown in **Figs. 6** and **7** is a similar set of results for the real and imaginary parts of the dipole transverse wakefield impedance of the BPM. Notice again, in **Fig. 7**, the amplitude shift for the imaginary part of the dipole impedance not being captured in the TSAR results. This constant displacement corresponds, through a frequency domain version of the Panofsky-Wenzel Theorem,

$$Z_{\perp}(\omega,r)=\frac{V}{\omega r_0}\nabla_{\perp}Z_{\ell}(\omega,r),$$

to a constant slope trend in the longitudinal impedance for m = 1, similar to that seen for m = 0, where m is the impedance mode number.

To test TIGER further, we did a series of test and validation exercises. Shown in **Fig. 8** are grid refinement tests indicating quick convergence of the TIGER results. **Figure 9** shows that the boundary conditions are very accurate for this test case and are not influencing the results with spurious reflections at the problem space truncation boundaries. **Figure 10** shows the calculated effective resistance modeling a 25-Ω coaxial feed using a 6-cell lumped

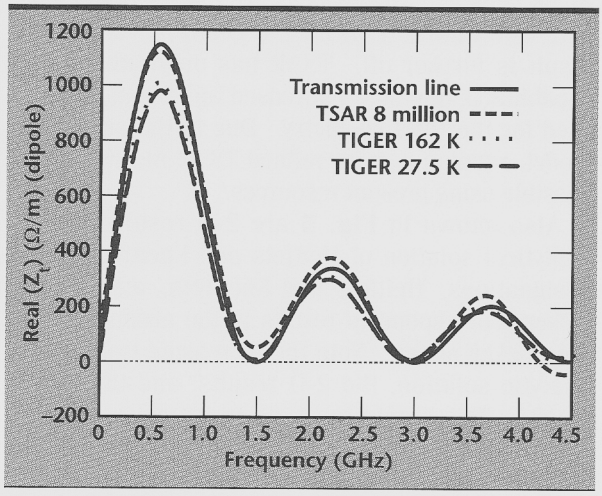

Figure 6. Real Z_t dipole results.

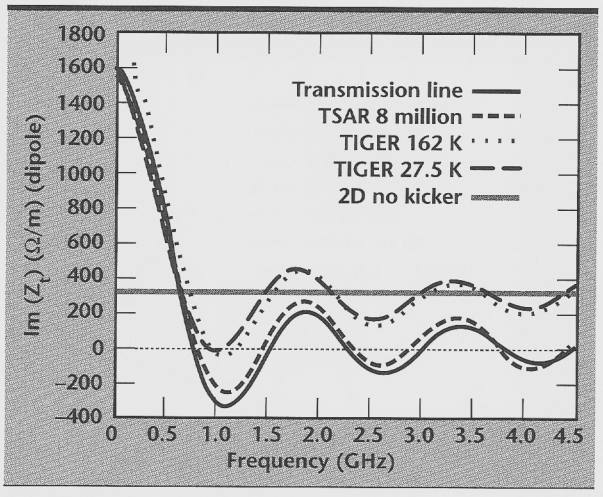

Figure 7. Imaginary Z_t dipole results.

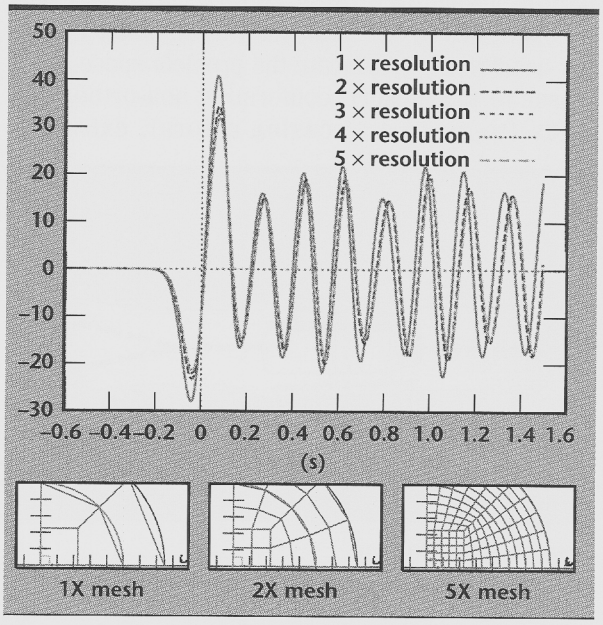

Figure 8. Results of grid refinement tests.

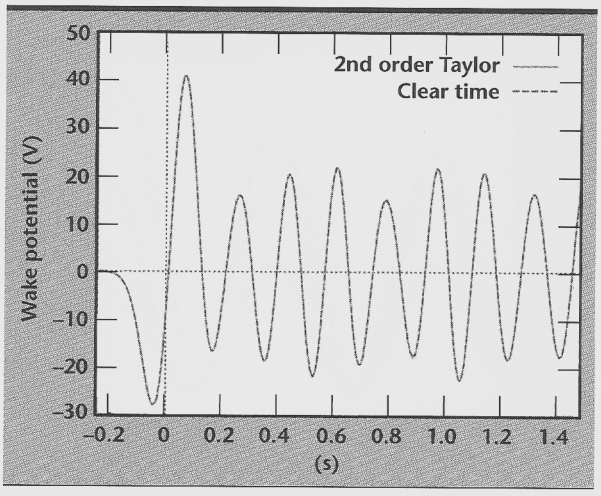

Figure 9. Results of boundary condition convergence tests.

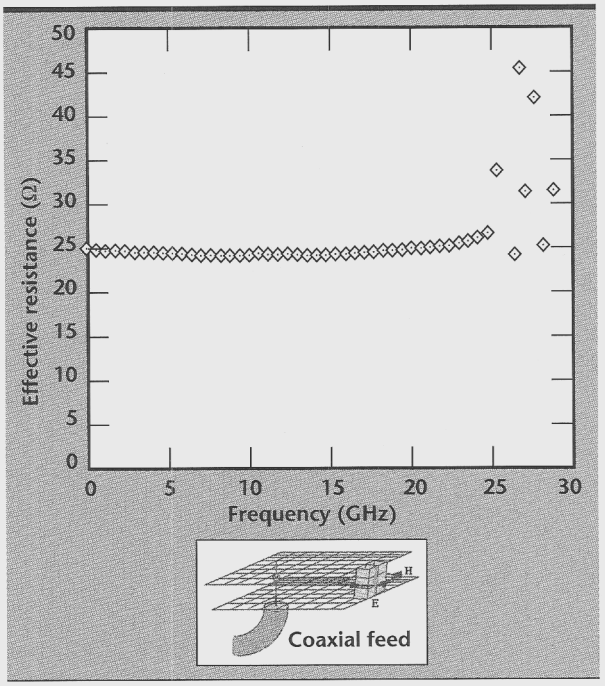

Figure 10. Results of coaxial feed modeling tests.

load resistor. The results show excellent agreement with the theoretical value of 25 Ω up to a frequency of 20 GHz, which is far above the highest frequency of interest.

Future Work

Next year, our focus will be on the enhancement of TIGER to include antenna and radar cross-section (RCS) sourcing and sensing capabilities. Specifically, we will be incorporating a near-to-far zone transform, antenna excitation capabilities, and antenna diagnostic capabilities. This will allow TIGER to excite antennas, compute radiation patterns, and provide output information such as input impedances, currents, and voltages for narrow- and wide-band situations.

Also, we will be looking into using PMESH, (a parallel platform meshing project) to help with our meshing concerns as we model more complex geometries.

Acknowledgment

The authors wish to thank B. Poole for providing TSAR modeling data for the monopole and dipole wakefield impedance comparisons.

References

1. Madsen, N. K., and R. W. Ziolkowski (1988), "Numerical Solution of Maxwell's Equations in the Time Domain Using Irregular Nonorthogonal Grids," *Wave Motion,* Vol. **10**, pp. 583–596.

2. Steich, D. J. (1995), Local Outer Radiating Boundary Conditions for the Finite-Difference Time-Domain Method Applied to Maxwell's Equations, Ph.D. thesis, Pennsylvania State University, Middletown, PA.

3. Veldhuizen, T. (1995), "Expression Templates," *C++ Report Magazine,* Vol. **7**, (5).

4. Myers, N. (1995), "A New and Useful Template Technique: 'Traits'," *C++ Report Magazine,* Vol. **7**, (5).

5. Weiland, T., and B. Zotter (1981), "Wake Potentials of a Relativistic Current in a Cavity," *Particle Accelerators,* Vol. **11**, pp. 143–151.

6. Dome, G. (1985), "Wake Potentials of a Relativistic Point Charge Crossing a Beam-Pipe Gap: An Analytical Solution," *IEEE Trans. Nuclear Science,* Vol. **NS-32**, pp. 2531–2534.

7. Ng, K.-Y. (1988), "Impedances of Stripline Beam-Position Monitors," *Particle Accelerators,* Vol. **23**, p. 93.

8. Heifets, S. A., and S. A. Kheifets (1991), "Coupling Impedance in Modern Accelerators," *Reviews of Modern Physics,* Vol. **63**, (3).

Multi-Scale Electrodynamics (MELD): A CAD Tool for Photonics Analysis and Design

Richard P. Ratowsky and Jeffrey S. Kallman
Defense Sciences Engineering Division
Electronics Engineering

Robert J. Deri and Michael D. Pocha
Electronics Engineering Technologies Division
Electronics Engineering

In FY-97 we completed work on the multi-scale electrodynamics (MELD) code, a comprehensive, multiple-length-scale, graphical user interface (GUI)-driven photonics design tool. In 1997, MELD was rated one of the one hundred most technologically significant new products of the year by *Research and Development* magazine.

Introduction

Photonics circuits using integrated and micro-optic devices are important because they will form the basis of all future high-speed and high-bandwidth communication systems, computers, and signal and image processing hardware. Computational simulation of these devices significantly reduces development and optimization time and cost. However, as photonics devices mature and increase in complexity, designers are faced with components that cannot be modeled using existing methods. A critical reason for this shortcoming is the presence of device feature sizes ranging from fractions of a wavelength to thousands of wavelengths, which are not amenable to a single numerical method.

As illustrated in **Fig. 1**, a photonics device or structure can be placed into one of three classes: optically large; optically small; or optically mixed, meaning large- and small-scale features are present in the same device.

Optically large components can be treated using beam propagation methods (BPM), which are, however, limited to unidirectional (paraxial) propagation. Optically small components can be modeled using codes that rigorously solve Maxwell's equations, such as finite-difference time-domain (FDTD) methods, to capture wavelength-scale physics. Optically mixed components are more difficult to model. If the length scales within the component can be decoupled to a good approximation, then hybrid methods using a combination of BPM methods and Maxwell solvers in succession may be effective. However, for some problems, a decoupling of length scales is very difficult, or impossible.

To address these issues, the Photonics Analysis and Design project was proposed in FY-96 to create a comprehensive, multiple-length-scale, GUI-driven photonics design tool, which we call *MELD*, for multi-scale electrodynamics. MELD allows the user to compose a "virtual optical bench," where micro- or integrated-optical components can be laid out in a

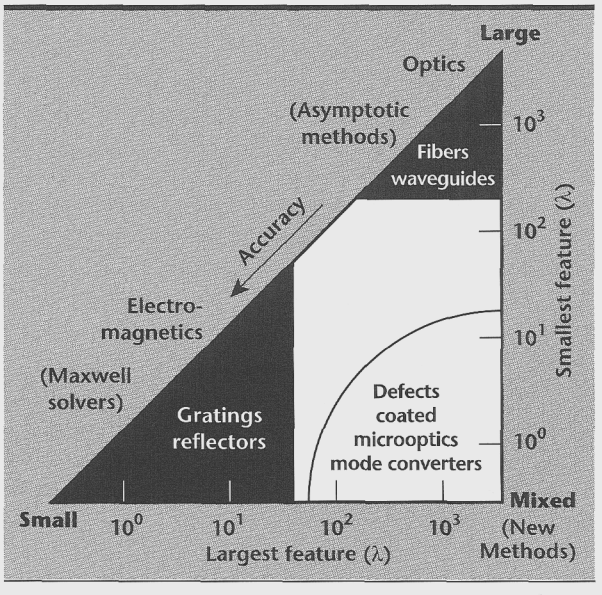

Figure 1. Classification of photonics devices. In terms of largest and smallest feature size, photonics devices can be classified as optically large, optically small, or optically mixed.

modular fashion. Each component is modeled using the most appropriate numerical method, and MELD provides a seamless interface between them.

Simulation in MELD begins when the user assembles an optical bench and "shoots light" from a source, such as a laser diode. Each module has one or more ports that can be connected to ports of other modules. MELD then propagates the light through the system, passing the transmitted field through the ports from one module to the next while keeping track of the reflected light. The optical field and intensities can be viewed at any port of the system. **Figure 2** shows the MELD 2-D layout for modeling an interferometer system.

Progress

In FY-97 we made a number of important advances in MELD to bring the project to its conclusion. These fall into three principal, but overlapping, areas: software, physics, and applications.

Software. We decided to rewrite the bulk of the underlying code using object oriented design in C++ ("new MELD"). Because of its modular structure, each photonics module in MELD is naturally treated as an object, which allows a great deal of reusable code and greatly simplifies the introduction of new modules. Further, in FY-97 we generalized the virtual optical bench to allow 2-D layout, thus enabling modeling of important 2-D configurations, such as Michelson or Mach-Zender interferometers (**Fig. 2**). The previous version of MELD allowed only uniaxial propagation of light.

We also added optimization and scanning routines in FY-97. These allow MELD to perform automatically typical design calculations, such as maximizing coupling efficiency (light throughput) as a function of any system parameter; for example, transverse off-set of the source.

A final but essential software accomplishment was documentation. In anticipation of MELD's use outside of our group, we have created a basic user's manual for MELD[1] so the novice user can navigate the program.

Physics. The physics in MELD is embodied in the optical module algorithms. MELD now involves thirteen modules: aperture, free space, thin lens, spherical coated lens, coated dielectric plate,

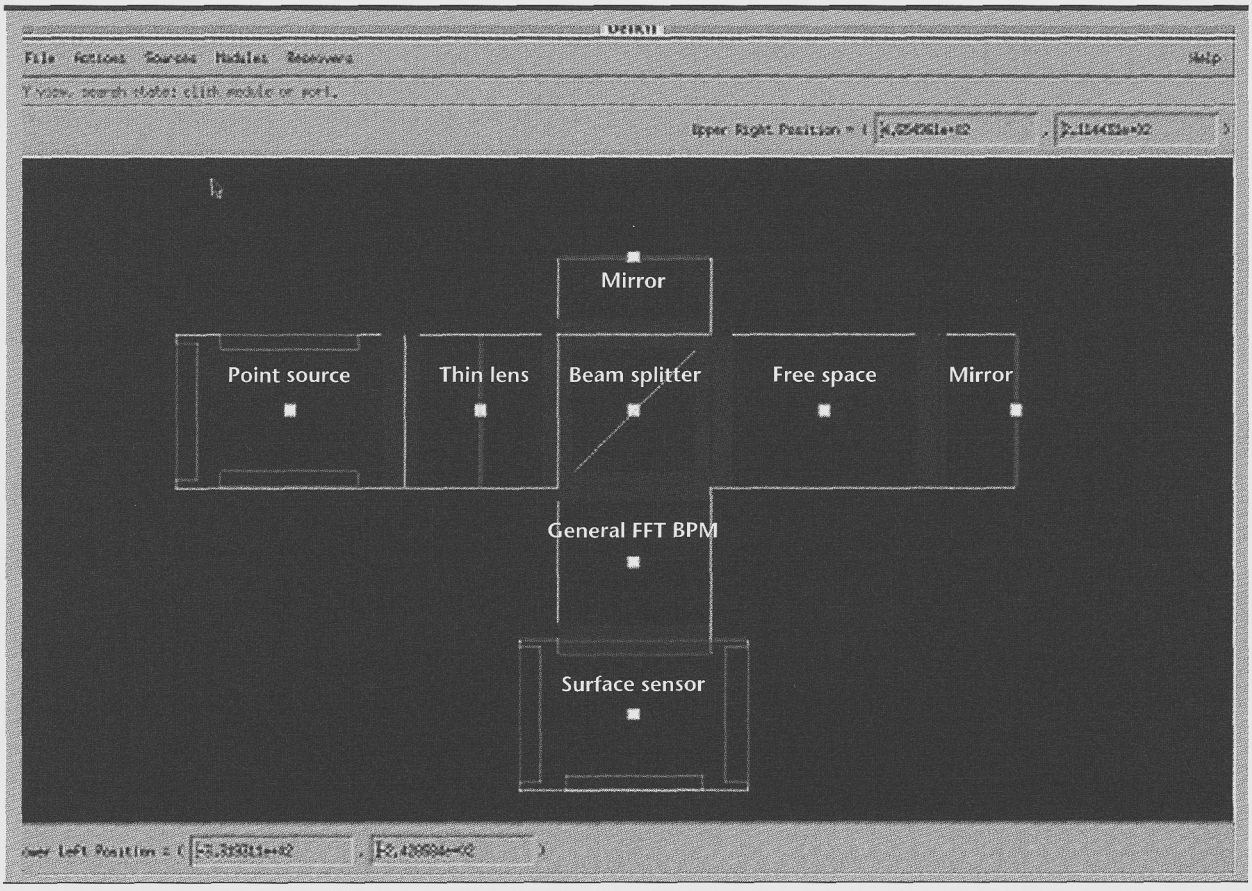

Figure 2. Two-dimensional layout of an interferometer in MELD.

directional coupler, mirror, phase plate, beam-splitter, ray-trace, general fast Fourier transform (FFT) BPM solver, FDTD Maxwell Solver, and transformer.

The BPM module solves the Helmholtz equation for optically large waveguiding structures. This module includes a full 3-D layout editor (written by us) for the system. The transformer is a "passive" module that interpolates fields from one grid to another. Most of these modules were added in FY-97. The code framework for the FDTD and ray-trace modules were developed in FY-97, but they are not yet fully implemented in the new MELD.

The ray-trace algorithms under development in the MELD project deserve further explication, since

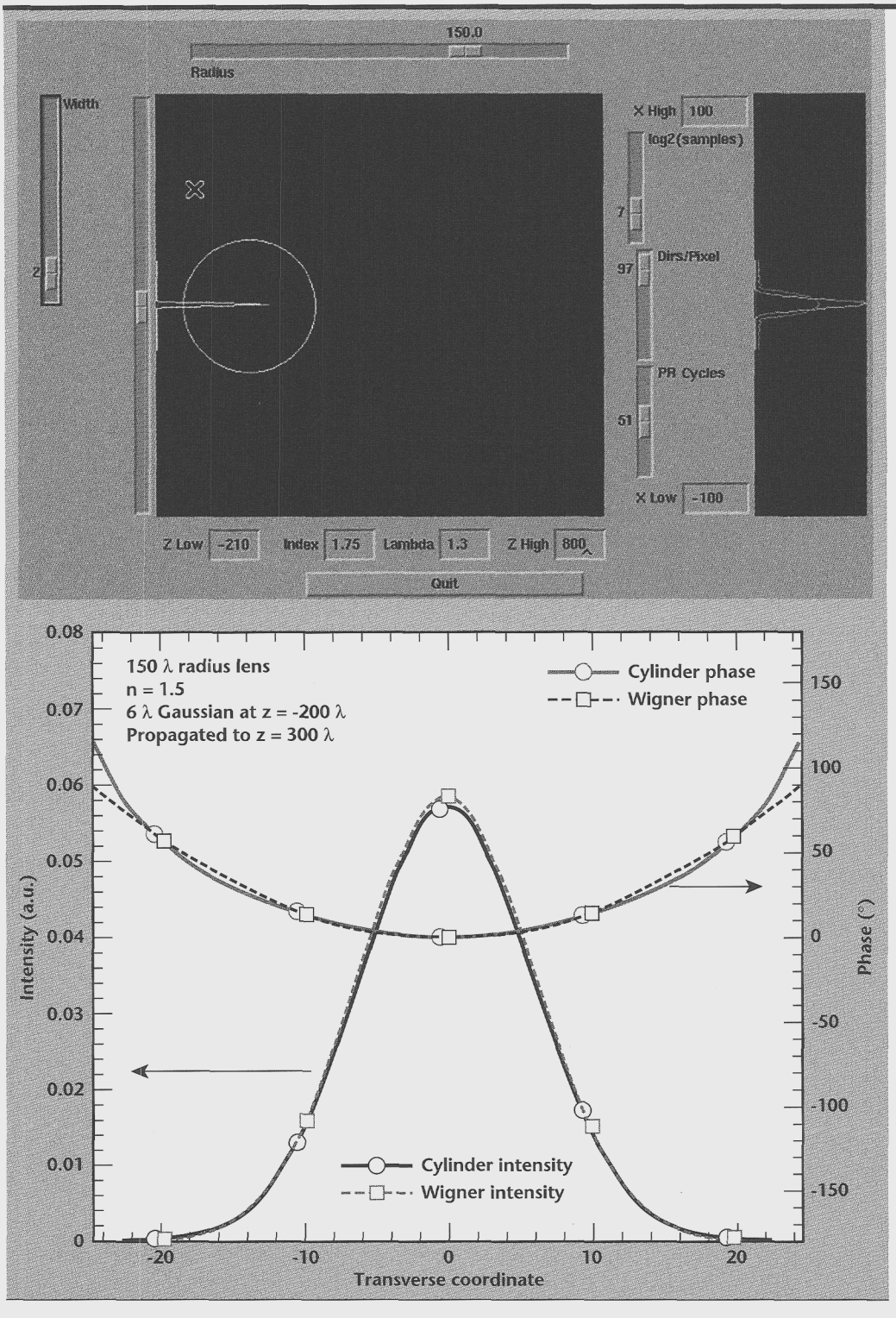

Figure 3. Accuracy of the Wigner method. A beam is propagated through a cylindrical lens very accurately. Curves marked "cylinder" are the exact solution. The user interface for the code is also shown.

they manifest the multi-scale spirit through the interface between ray and wave optics. Ray optics is usually a good approximation when the propagation medium is slowly varying on a wavelength scale. However, traditional ray optics cannot capture diffraction.

In FY-97 we developed and implemented an approach to ray optical propagation that allows us to calculate intensity and phase and, within a certain level of approximation, diffraction effects. The motivation for this work is the desire to model optically large elements, possibly with little symmetry, where diffraction effects may be important.

Our approach uses a set of rays distributed in both position and angle, called the Wigner distribution[2]. To propagate an optical beam, we first calculate the Wigner distribution from the complex field; it is equal to the Fourier transform of the two-point field correlation function of the field. We then simply propagate the Wigner distribution through the optical system from an input (source) plane to an output plane where we want to calculate the field. In practice, we propagate the rays backwards, since it is more convenient to know where a ray ends up than where it starts.

By projecting the output ray distribution in position (near field) and angle (far field), we can recover the phase of the field. This last step is accomplished using an iterative algorithm (Gerchberg-Saxon) which is identical to a technique used in the design of phase plates for LLNL's National Ignition Facility (NIF)[3]. Remarkably, then, we obtain both amplitude and phase information from the field from ray-tracing alone.

We illustrate the accuracy of the method in **Fig. 3**. Here we show the intensity and phase of a beam that has been propagated through a cylindrical lens using the Wigner method, compared with an "exact" calculation using an expansion in Bessel functions. The agreement is excellent, indicating that the method is potentially very valuable for treating aspherical surfaces, which are very difficult to model in any other way. This method is not yet implemented in a MELD module, but will be added in FY-98. It is now implemented in a stand-alone GUI-driven program (see **Fig. 3**).

Applications. We have had an ongoing relationship with Hewlett-Packard (HP) Laboratories, who continue to use MELD in the design of mode converters, components used to transform the optical mode size in a single-mode device to match that of a dissimilar device, thus increasing the coupling and relieving alignment tolerances. Optimal design of mode converters is an important issue, since a major limitation to the widespread use of photonic systems is the high cost (both in an economic and a performance sense) associated with this coupling.

HP has used MELD successfully to design a new mode-converter product line using ball lenses, an example of which is shown in **Fig. 4**, along with the MELD layout of the device package.

We have also created a World Wide Web interface to SPHERE, a subset (stand-alone module) of MELD which can be used for the mode-converter design. In FY-97 we also developed the capability to model arbitrary input fields, and this was used by HP to incorporate a realistic model of a novel laser diode design.

We have emphasized the uniqueness of MELD in being able to calculate, very accurately, coupling efficiencies for ball lens mode converters where other commercial software could not,[4–6] and to integrate different length-scale algorithms in a single package. Our results have been recognized through a 1997 award sponsored by *Research and Development* magazine as one of the one hundred most technologically significant new products of the year.[7]

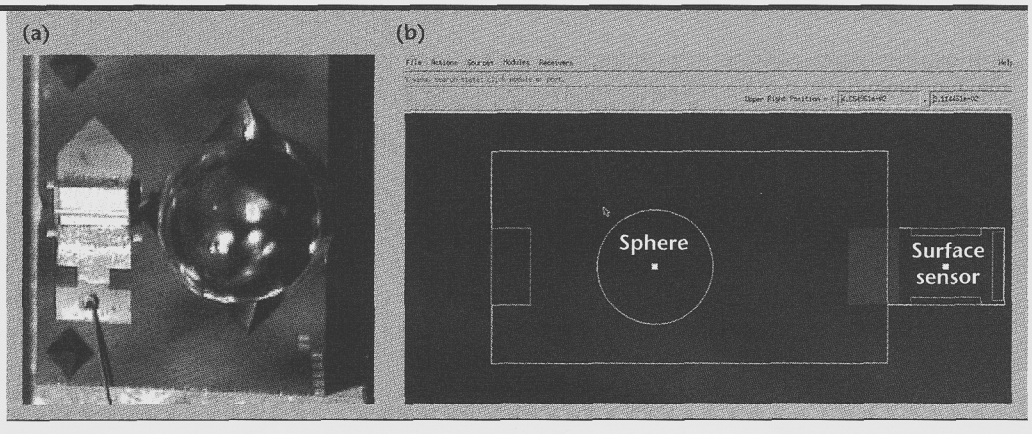

Figure 4. The HP-designed mode-converter package (a), designed using MELD. The package includes a laser diode and 750-μm-diameter ball lens on a silicon submount; (b) shows the MELD GUI-layout of the device.

Future Work

While the two-year effort is now complete, MELD is certainly not a closed-end project, for two reasons. First, the existing code can always be improved: some capabilities we would like to see are not yet implemented to our satisfaction, such as the FDTD solver and the ray-trace module. Second, new modules can and should be added to MELD. Their selection will be driven by applications. Furthermore, to be widely accessible, the code should be ported to other platforms. MELD currently runs on UNIX workstations using MOTIF graphics. We are exploring options to commercialize the code and fund the additional improvements.

References

1. Kallman, J. S., and R. P. Ratowsky (1997), *Introduction to Multiscale ELectroDynamics (MELD)*, in press.

2. Wolf, E. (1978), "Coherence and Radiometry," *J. Opt. Soc. Am.* **68**, pp. 6–17. and M. Bastiaans (1997), "Application of the Wigner distribution function in optics," *The Wigner Distribution: Theory and Applications to Signal Processing*, W. F. G. Mecklenbräuker, Ed., North-Holland.

3. Dixit, S. N., M. D. Feit, M. D. Perry, and H. T. Powell (1996), "Designing fully continuous phase screens for tailoring focal plane irradiance profiles," *Opt. Lett.*, **21**, pp. 1715–17.

4. Ratowsky, R. P., L. Yang, R. J. Deri, J. S. Kallman, and G. Trott (1997), "Laser diode to single-mode fiber ball lens coupling efficiency: full-wave calculation and measurements," *Applied Optics*, **2005**, pp. 3435–3438.

5. Ratowsky, R. P., L. Yang, R. J. Deri, J. S. Kallman, and G. Trott (1995), "Ball lens reflections by direct solution of Maxwell's equations," *Opt. Lett.*, **20**, p. 2048.

6. Yang, L., K. W. Chang, G. Trott, R. P. Ratowsky, R. J. Deri, and J. S. Kallman (1995), "Micro-size ball lenses for micro-optics: theory and experiment," *Photonics West, San Jose, CA*, SPIE Vol. **2687**, January.

7. 1997 R&D 100 Awards, *Research and Development*, September, Vol. **39**, (10), p. 41.

Peter J. Raboin, Thrust Area Leader

The Computational Mechanics thrust area is a vital and growing facet of the Mechanical Engineering Department at Lawrence Livermore National Laboratory (LLNL). This work supports the development of computational analysis tools in the areas of structural mechanics and heat transfer. Over 75 analysts depend on thrust area-supported software running on a variety of computing platforms to meet the demands of LLNL programs.

Interactions with the Department of Defense (DoD) High Performance Computing and Modernization Program and the Defense Special Weapons Agency are of special importance as they support our ParaDyn project in its development of new parallel capabilities for DYNA3D. Working with DoD customers has been invaluable to driving this technology in directions mutually beneficial to the Department of Energy.

Other projects associated with the Computational Mechanics thrust area include work with the Partnership for a New Generation Vehicle (PNGV) for "Springback Predictability" and with the Federal Aviation Administration (FAA) for the "Development of Methodologies for Evaluating Containment and Mitigation of Uncontained Engine Debris."

Spurred on by the increasing demand for computational analyses and process simulation tools, code development activities increased this past year as parallel DYNA3D entered into the "production" environment for the first time. With access to ASCI MPP computers, ever larger and more complex simulations were completed. Analysis times have been dramatically reduced as parallel processing on the IBM SP2 has scaled up the compute speed of DYNA3D by as much as a factor of 27 over the Cray YMP. Typical simulations within the last year included weapon transport safety, earthquake analyses of bridges, buildings and laser-support systems, knee-injury modeling, blast effects calculations, automobile crashworthiness, underground shock simulations and metal forming manufacturing.

In this report for FY-97, there are five articles, detailing three code development activities and two projects that synthesized new code capabilities with new analytic research in damage/failure and biomechanics. The articles this year are 1) Energy- and Momentum-Conserving Rigid-Body Contact for NIKE3D and DYNA3D; 2) Computational Modeling of Prosthetics: A New Approach to Implant Design; 3) Characterization of Laser-Induced Mechanical Failure Damage of Optical Components; 4) Parallel Algorithm Research for Solid Mechanics Applications Using Finite Element Analysis; and 5) An Accurate One-Step Elasto-Plasticity Algorithm for Shell Elements in DYNA3D.

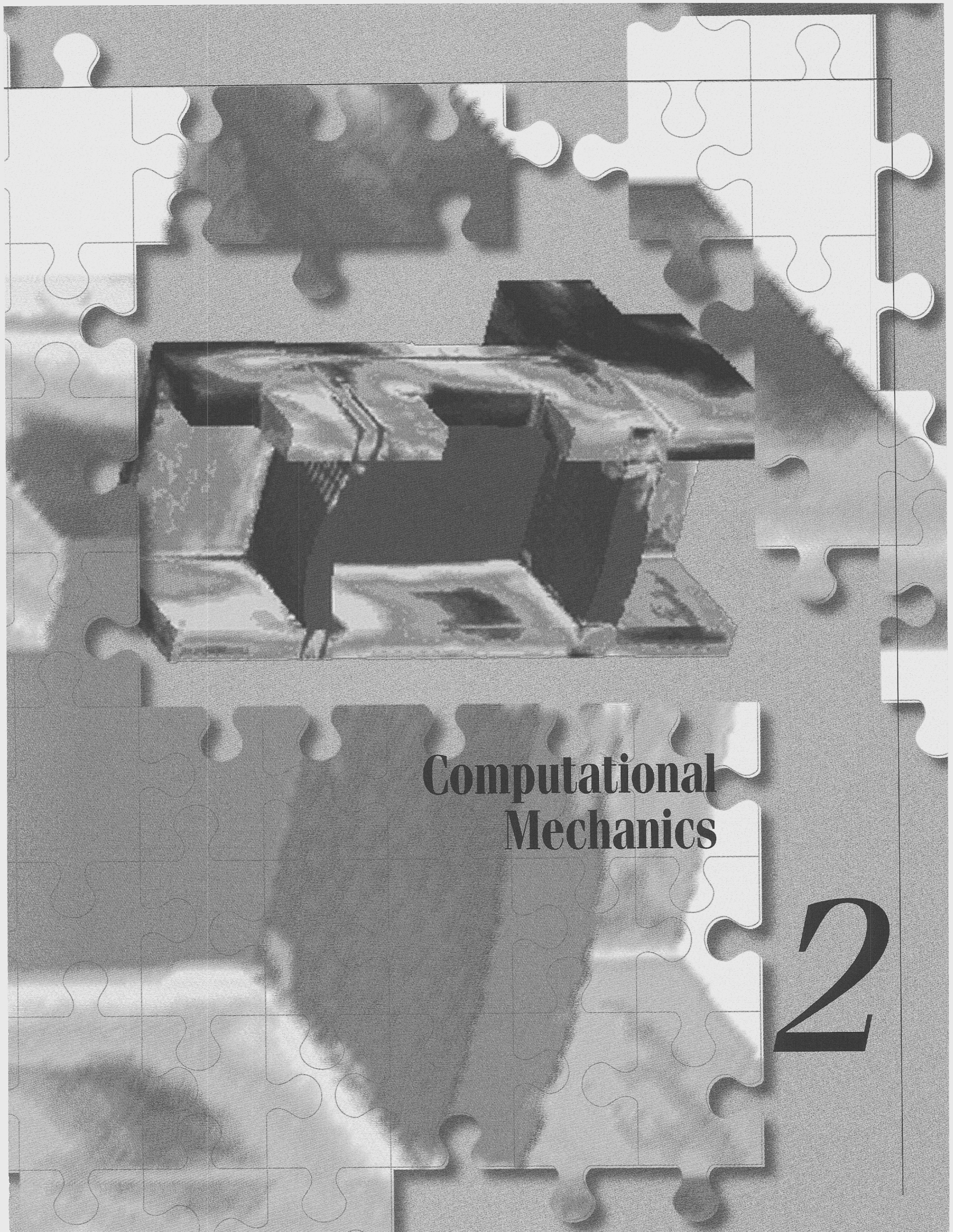

Computational Mechanics

2

2. Computational Mechanics

Overview
Peter J. Raboin, Thrust Area Leader

Energy- and Momentum-Conserving Rigid-Body Contact for NIKE3D and DYNA3D
Michael A. Puso and Edward Zywicz *2-1*

Computational Modeling of Prosthetics: A New Approach to Implant Design
Karin Hollerbach, Scott A. Perfect, and Harry E. Martz *2-5*

Characterization of Laser-Induced Mechanical Damage of Optical Components
Douglas R. Faux *2-11*

Parallel Algorithm Research for Solid Mechanics Applications Using Finite Element Analysis
Carol G. Hoover, Daniel C. Badders, Anthony J. De Groot, and Robert J. Sherwood *2-17*

An Accurate One-Step Elasto-Plasticity Algorithm for Shell Elements in DYNA3D
Jerry I. Lin *2-25*

Energy- and Momentum-Conserving Rigid-Body Contact for NIKE3D and DYNA3D

Michael A. Puso
Defense Technologies Engineering Division
Mechanical Engineering

Edward Zywicz
New Technologies Engineering Division
Mechanical Engineering

During long-time simulations of rigid body dynamics, especially with contact, conservation of momentum and energy is directly related to time-step size for both implicit and explicit formulations. For example, numerical simulation of a rigid ball bouncing inside a rigid box will always eventually go unstable if the time step is too large, or come to a stop if the time step is appropriately small. Consequently, we have implemented algorithms for rigid body dynamics with contact that can exactly conserve linear momentum, angular momentum, and energy, independent of the time step. The algorithms are inherently implicit and have been implemented in NIKE3D and DYNA3D. In addition, rigid-body smoothing has been incorporated into NIKE3D and DYNA3D for spherical rigid-body contact.

Introduction

The rigid material idealization is often exploited in finite element analyses to save computational time, since rigid materials do not require constitutive evaluations and vastly reduce the number of degrees of freedom in the problem. Yet, the algorithms for integrating rigid-body equations of motion can be somewhat more complicated than those for deformable solid elements, due to the presence of angular momentum. Furthermore, in an explicit setting, no critical time step naturally arises to maintain stability, unlike in the case of deformable elements.

In the past, with DYNA3D the user would have to guess at a particular time step for problems with rigid bodies. In NIKE3D, the rigid-body dynamics algorithms were not unconditionally stable. The inclusion of contact in these rigid-body problems would exacerbate the time step problem since contact penetrations have a tendency to drive energy (algorithmically) into the system.

Even with a stable time-step size, contact problems will dissipate energy (algorithmically) and cause free-body contact problems to eventually lose all momentum and energy. To solve these problems, an exact energy- and momentum-conserving algorithm has been developed and implemented into DYNA3D and NIKE3D for rigid-body dynamics. This algorithm can be shown to be unconditionally stable in the energy sense.[1]

In addition to the new conserving integration algorithm, a new method has been implemented to represent rigid spherical components in NIKE3D and DYNA3D. It allows spherical surfaces, defined by rigid materials, to roll or slide smoothly instead of "bumping," as is usually encountered with discrete faceted surfaces and traditional contact algorithms. The energy-conserving algorithms along with spherical smoothing can be used for understanding rolling problems, such as ball bearings.

Progress

A rigid-body dynamics algorithm,[2] has been implemented into NIKE3D and DYNA3D. This required the modification of the time integration schemes already used.[3,4] This integration method was extended in our work to include the effects of contact resulting in an exact energy- and momentum-conserving algorithm for rigid-body dynamics with contact. In fact, two different formulations have been developed.

The method implemented into NIKE3D is a penalty-based formulation which is similar to the current contact algorithms, in that the contact force

is proportional to the gap distance. This method enforces the so called "consistency condition," in that it mitigates the gap distance between the slave node and master surface. By enforcing the consistency condition, relatively large time steps can be used. Consequently, this algorithm is well suited for NIKE3D.

Since conservation algorithms use the midpoint rule, NIKE3D was modified for the generalized Hilber-Hughes-Taylor integration algorithm (also known as the *alpha* method). This method is a generalization of NIKE3D's Newmark integration rule. The *alpha* method can perform mid-point integration for energy conservation, or apply algorithmic damping by appropriate specification of integration parameters.

The method implemented into DYNA3D is a Lagrange multiplier method which uses a predictor step to anticipate contact, and a corrector step to apply forces that enforce the appropriate gap velocity. Because only the gap velocity is considered, the velocity constraint should be activated at or near the point of incipient contact. This requires small time steps and is well suited for DYNA3D.

The new contact algorithms were also modified for the rigid spherical contact idealization. This will allow them to capture the effect of smooth rolling of spherical bodies. Currently, only the spherical contact algorithm is available in the energy- and momentum-conserving form for NIKE3D. DYNA3D has the new algorithms implemented for both general and spherical contact, and also includes the effects of friction.[5]

Formulation

The basic theory[2] was generalized to address contact. This required the appropriate definitions and time integration of contact forces. First, the notions of discretized energy and momentum conservation are defined, then the individual algorithms for NIKE3D and DYNA3D that satisfy these conservation principles are presented.

Consider the free-body motions (that is, no applied forces) of N rigid bodies with contact. Using the mid-point rule, the discretized equations of motion, in momentum form, for the i-th body are given by:

$$\boldsymbol{p}^i_{n+1} - \boldsymbol{p}^i_n = \boldsymbol{f}^i_{n+1/2}\Delta t \quad \boldsymbol{h}^i_{n+1} - \boldsymbol{h}^i_n = \bar{\boldsymbol{R}}^i \times \boldsymbol{f}^i_{n+1/2}\Delta t \quad (1)$$

where $\boldsymbol{p}^i_n = M^i \boldsymbol{v}^i_n$ is the linear momentum at time t_n; $\boldsymbol{h}^i_n = \boldsymbol{I}^i_n \cdot \omega^i_n$ is the angular momentum; v is the velocity of the center of mass; ω is the rotation rate; $\boldsymbol{f}$ is the contact force; and $\bar{\boldsymbol{R}}$ is the appropriately defined moment arm, measured from the center of mass. Conservation of the discretized system linear and angular momentum is represented by:

$$\sum_{i=1}^{N} \boldsymbol{p}^i_n = \boldsymbol{P}, \qquad \sum_{i=1}^{N} \boldsymbol{X}^i_n \times \boldsymbol{p}^i_n + \boldsymbol{h}^i_n = \boldsymbol{H} \quad (2)$$

where $\boldsymbol{P}$ and $\boldsymbol{H}$ are constants, and $\boldsymbol{X}$ is the location of the center of mass. Energy conservation is given by:

$$T_n + U_n = E,$$

$$\text{where} \quad T_n = \frac{1}{2}\sum_{i=1}^{N} \boldsymbol{p}^i_n \cdot \boldsymbol{v}^i_n + \boldsymbol{h}^i_n \cdot \omega^i_n \quad . \quad (3)$$

The constant E is the total system energy, and U is some stored potential energy (U is non-zero when contact is made in the penalty method, but is always zero in the Lagrange multiplier method).

In general, time-stepping methods satisfy **Eq. 1**, but **Eqs. 2** and **3** are only satisfied in the limit as $\Delta t \to 0$. By using "algorithmic" definitions for $\boldsymbol{f}$ and $\bar{\boldsymbol{R}}$ and the integration rules given in Reference 2, the conservation laws, **Eqs. 2** and **3**, can be satisfied to some tolerance, yielding an unconditionally stable algorithm.

For the penalty method, an algorithmic definition of the gap is used in place of the exact gap. The algorithmic gap is given by the recursion:[6]

$$g^d_{n+1} = g^d_n + \bar{\boldsymbol{v}} \cdot \left(\left(\boldsymbol{x}^s_{n+1} - \boldsymbol{x}^s_n \right) - \left(\boldsymbol{x}^m_{n+1} - \boldsymbol{x}^m_n \right) \right) \quad (4)$$

where $\bar{\boldsymbol{v}}$ is the contact normal; $\boldsymbol{x}^s$ represents the position of the slave node; and $\boldsymbol{x}^m$ is the closest point projection of the slave node onto the master surface. This "dynamic" gap is a second order approximation to the actual gap. The contact force is given by

$$\boldsymbol{f} = p\bar{\boldsymbol{v}} \quad ,$$

$$\text{where} \quad p = \frac{1}{2}\frac{U_{n+1} - U_n}{g^d_{n+1} - g^d_n}$$

$$\text{and} \quad U = \begin{cases} k\left(g^d\right)^2 & \text{if } g < 0 \\ 0 & \text{otherwise} \end{cases} \quad . \quad (5)$$

The nodal points on both the slave and master surfaces of the rigid bodies are calculated at a modified position given by:

$$\bar{\boldsymbol{x}} = \frac{1}{2}\left(\boldsymbol{X}_{n+1} + \boldsymbol{X}_n\right) + \frac{1}{2}\frac{\tan\left(|\theta|/2\right)}{|\theta|/2}\left(\boldsymbol{R}_{n+1} + \boldsymbol{R}_n\right) \quad (6)$$

where $\boldsymbol{X}$ is the position of the center of mass; $\boldsymbol{R}$ is

the position to the node from the center of mass; and θ is the compound rotation from the n to n+1 position. From the nodal positions given by **Eq. 6**, the contact normal, $\bar{v}$, and the moment arm, $\bar{R}$, are calculated.

In the Lagrange multiplier method, an explicit "predictor" step is taken, in which no contact forces are applied. From the predictor step nodal positions, penetrated nodes are identified, and moment arms, R_p, and contact normals, $\bar{v}$, are calculated. The contact force is now:

$$f = \lambda \bar{v} \tag{7}$$

where λ is the unknown Lagrange multiplier. Using the predicted normals, the following algorithmic moment arms for respective slave and master nodes are used to conserve angular momentum:

$$\bar{R}^s = R_p^s + \left(\left(X_n^s - X_n^m\right) + \left(R_p^s - R_p^m\right)\right)/2$$

$$\bar{R}^m = R_p^m - \left(\left(X_n^s - X_n^m\right) + \left(R_p^s - R_p^m\right)\right)/2. \tag{8}$$

The Lagrange multiplier is calculated such that the following gap velocity constraint is enforced:

$$\bar{n} \cdot \left(\Delta v^m - \Delta v^s\right) = 0 \tag{9}$$

where Δv is the algorithmic velocity jump of the slave/master node from time n to n + 1, and is given by:

$$\Delta v = V_{n+1/2} + V_{n-1/2} +$$

$$\left(\exp(\theta)\omega_{n+1/2} + \omega_{n-1/2}\right) \times \bar{R}. \tag{10}$$

Here V is the velocity of the center of mass, and the matrix exp is the exponential map.[2] In the limit as $\Delta t \to 0$, the rotation, exp (θ), tends toward the identity matrix, and the continuum result is recovered for an elastic collision.[7]

The above algorithms are particularized to spherical contact by appropriately modifying the contact gap and normal calculations for the spherical surfaces.

Examples

In the first example, NIKE3D is used with rigid spherical smoothing. A 0.274-kg/m^3 solid ball is placed within a 0.743-kg/m^3 spherical shell **(Fig. 1)** and given an initial velocity of 1 m/s in the *y* direction, such that the inner ball rolls smoothly in the *y-z* plane. Because the system is entirely free, linear and angular momentum of the system is conserved (see **Fig. 2**). In fact, the energy and angular momentum are conserved within machine precision even after 2000 iterations.

In the second example, the Lagrange multiplier method in DYNA3D is used to model two slender (50 m × 1 m × 1 m) rigid bars impacting. The initial *x* velocity of the left bar is 1 m/s, and the right bar is at rest. **Figure 3** shows the rigid bars

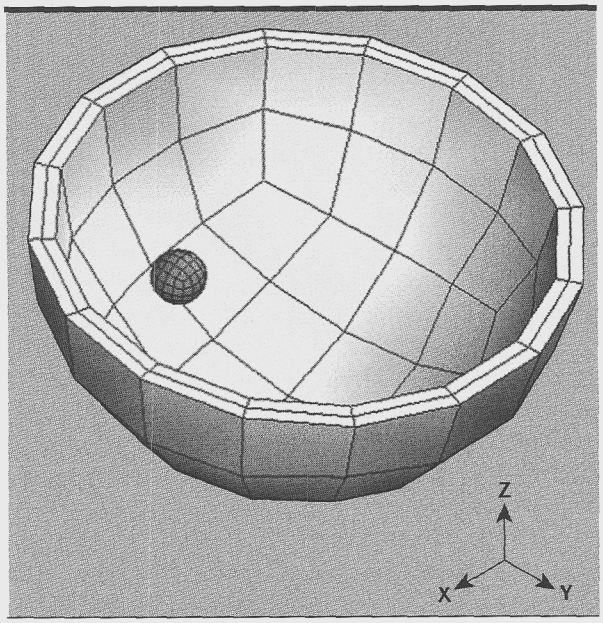

Figure 1. Ball inside spherical shell. Only the bottom half of the shell is shown.

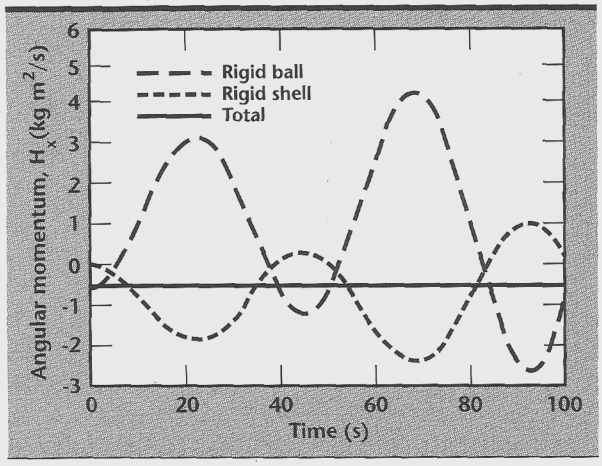

Figure 2. Angular momentum in the x direction for rigid ball and rigid shell.

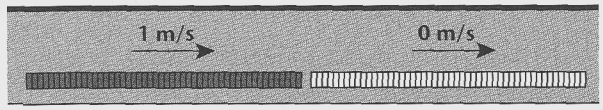

Figure 3. Initial conditions for impacting rigid rods.

separated by 0.01 m. **Figure 4** shows the displacement vs time of the rigid bars. Unlike the penalty method, the Lagrange multiplier method eliminates penetration, and is generally superior to the penalty method.

Future Work

It remains to implement the energy-conserving contact algorithms into the general contact algorithms for NIKE3D (rigid and deformable). Continued testing and work is needed for both the DYNA3D and NIKE3D implementations to increase robustness.

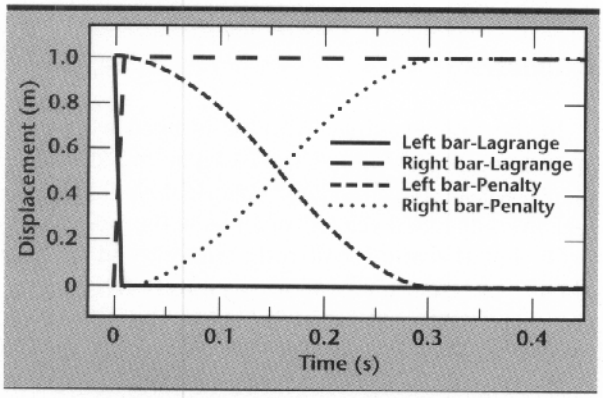

Figure 4. Displacement of impacting rigid rods.

References

1. Richtmyer, R. D., and K. W. Morton (1967), "Difference Methods for Initial Value Problems, Second Edition," *Interscience*, New York, NY.

2. Simo, J. C., and K. K. Wong (1991), "Unconditionally Stable Algorithms for Rigid Body Dynamics That Exactly Preserve Energy and Momentum," *Int. J. Num. Meth. Eng.*, **31**.

3. Puso, M. A. (1996), "Implicit Rigid Body Static and Dynamic Analysis with NIKE3D," *Thrust Area Report*, University of California, Lawrence Livermore National Laboratory, Livermore, CA, (UCRL-ID-125471).

4. Benson, D. J., and J. O. Hallquist (1986), "A Simple Rigid Body Algorithm for Structural Dynamics Programs," *Int. J. Num. Meth. Eng.*, **22**.

5. Zywicz, E., and M. A. Puso (1997), *A General Predictor-Corrector Solver for Explicit Finite-Element Contact*, University of California, Lawrence Livermore National Laboratory, Livermore, CA, (UCRL-JC-128410).

6. Armero, F., and E. Petocz (1997), *Formulation and Analysis of Conserving Algorithms for Dynamic Contact Impact Problems*, University of California, Berkeley, CA, (UCB/SEMM-96/10).

7. Kane, T. R., and D. A. Levinson (1985), *Dynamics: Theory and Applications*, McGraw Hill, San Francisco, CA.

Computational Modeling of Prosthetics: A New Approach to Implant Design

Karin Hollerbach
Institute for Scientific Computing Research
Center for Applied Scientific Computing
Computations

Scott A. Perfect
New Technologies Engineering Division
Mechanical Engineering

Harry E. Martz
Manufacturing and Materials Engineering Division
Mechanical Engineering

We are applying finite element techniques to computer-aided design (CAD) models of prosthetic implants, to 1) calculate implant kinematics and regions of high stress within certain implant materials; and 2) make design recommendations to improve performance and reduce the likelihood of failure. In the process of working with industry to achieve these goals, we have developed finite element models of several human joints, as well as prosthetic joint implants (or joint replacements).

Introduction

We are applying finite element analysis to the design and evaluation of joint replacement prostheses. Total joint replacement has become a major industry and will expand dramatically as our population ages and our life expectancy increases. The present joint replacement market is served by an inadequate product, frequently requiring revision surgeries. Today's implants may fail to reproduce normal joint kinematics, or they may exhibit material failure at the articular interface or at the bone-implant interface. Implant failure frequently results from a lack of understanding of human joint biomechanics and an inability to quantitatively assess the effects of implant geometry and material modifications on the biomechanics of the implanted joint.

Finite element modeling of joints with implants offers an improved approach to implant design and an opportunity to evaluate designs before they are manufactured or surgically implanted. This is an attractive alternative to current methods that use only expensive, time-consuming experimental testing, where retrieved implants serve as a post-failure demonstration of poor design strategies.

Non-linear 3-D finite element modeling and analysis are powerful tools for the evaluation and design of joint replacement prostheses. We are using this technology to model several different implant designs and to perform non-linear, 3-D, large-displacement analysis that replicates loads that would be experienced by the prosthetic implant *in vivo*.

Material failure is common in implant designs containing polyethylene components. Wear and fatigue are correlated with the pattern and magnitude of stresses experienced by the material. Orthopedic implant materials, especially polyethylene, have non-linear stress/strain relationships. Polyethylene wear occurs primarily in sub-surface regions, which cannot be adequately modeled in 2-D analyses. In addition, implants are 3-D and experience forces in all dimensions in the patient. Fully non-linear 3-D, modeling tools can produce more accurate results than the linear 2-D, analyses.

Progress

In our implant analyses, we are applying finite element techniques to computer-aided design (CAD) models of prosthetic implants, to 1) calculate

implant kinematics and regions of high stress within certain implant materials; and 2) make design recommendations to improve performance and reduce the likelihood of failure. In the process of working with industry to achieve these goals, we have developed finite element models of several human joints, as well as prosthetic joint implants (or joint replacements).[1]

The analysis code used in our research is Lawrence Livermore National Laboratory's (LLNL) NIKE3D, a non-linear, implicit, 3-D finite element code developed for studying dynamic, finite deformations. Articular contact algorithms in NIKE3D are based on a master/slave approach that provides general multi-body contact capability, including sliding with contact, gaps, and friction, as needed. Contact algorithms, a key feature in orthopedic modeling where the primary areas of interest are near the contacting articular surfaces and near the bone-implant interface, use the penalty method, in which a penalty is generated when interpenetration between contacting surfaces is calculated.

In analyzing the prosthetic implants, we have created finite element models of three thumb carpometacarpal joint prostheses and one knee prosthesis. From Initial Graphics Exchange Specification (IGES) we obtained format descriptions generated by the orthopedic industry using CAD tools. Using TrueGrid (XYZ Scientific Applications, Inc.), we meshed the 3-D surfaces of the implants into a set of eight-node solid (hexahedral) elements that closely approximated the surface descriptions. Mesh generation was performed manually, to allow for fine control of mesh quality, especially near contacting surfaces.

Data available in the orthopedic literature provided us with properties for the implant materials in the prosthetic models. The preliminary material model used for the polyethylene pieces was an elastic-plastic model. Numerical data obtained from Bartel[2] and De Heer[3] are shown in **Table 1**.

The thumb implant designs that were modeled include 1) a ball-and-socket joint with a polyethylene socket and a CoCr ball and stem; 2) a ball-and-socket joint with a Ti-backed polyethylene socket and a CoCr ball and stem; 3) an asymmetric saddle-shaped joint, in which the metacarpal component consists of a Ti stem with a polyethylene articular surface and a CoCr trapezial component; and 4) a similar but symmetric saddle-shaped joint.

Boundary conditions, defining net carpo-metacarpal joint forces for a specified set of commonly used grasps, were calculated based on simulations derived from a virtual five-link model of the thumb.[4]

Carpo-metacarpal joint reaction forces predicted by the five-link model are, for an applied load of 10 N: 188.5 N for key pinch, 241.1 N for screwdriver grasp, and 61.5 N for tip pinch. The joint reaction forces in pinch and grip are not perpendicular to the metacarpal, but are directed dorsally and radially (**Fig. 1**).

Non-linear 3-D finite element analyses of these models show articular surface and sub-surface stress patterns when the implants are loaded with forces representative of common grasping modes, such as key pinch, tip pinch, and screwdriver grasps. These loads are static and eccentric to the joint components. Metal-backed and unbacked polyethylene socket models varied in stress patterns and levels of maximum stress. The implant stress analyses appear to correlate with material failures observed clinically in the ball-and-socket designs. Both ball-and-socket designs were also compared to the newer design with an asymmetric saddle-shape. With similar eccentric loading, stress patterns varied between implant designs, and maximal stresses were lower in the asymmetric implant.

Simulation results of the saddle-shaped implants (**Fig. 2**) correlate with clinical findings and help to validate the modeling approach. As a result of its high failure rate, the ball-and-socket implant is now

Table 1. Numerical data for polyethylene material model.

Bartel		De Heer	
Plastic strain	Stress (MPa)	Plastic strain	Stress (MPa)
0.0	14.07	0.0	10.7
0.0108	22.05	0.00925	15.86
0.0363	27.06	0.01797	18.31
0.0910	29.52	0.0502	20.69
		0.0801	22.75
		0.2325	31.15
Elastic modulus	1016 MPa	Elastic modulus	571.6 MPa
Poisson's ratio	0.46	Poisson's ratio	0.45

used less frequently in the thumb. However, a geometrically similar design is commonly used in the hip, which represents one of the largest joint replacement markets.

In addition to the thumb prostheses, we have also analyzed a knee replacement. The objectives of this study, static simulations of knee implant loading, were to assess the effect of knee flexion angle and varus rotation angle on the stresses in an all-polyethylene tibial component, as a function of flexion angle and varus rotation angle. We have completed all simulations for both the cruciate-retaining and posterior-stabilized designs. Some representative stress calculations are shown in **Fig. 3**.

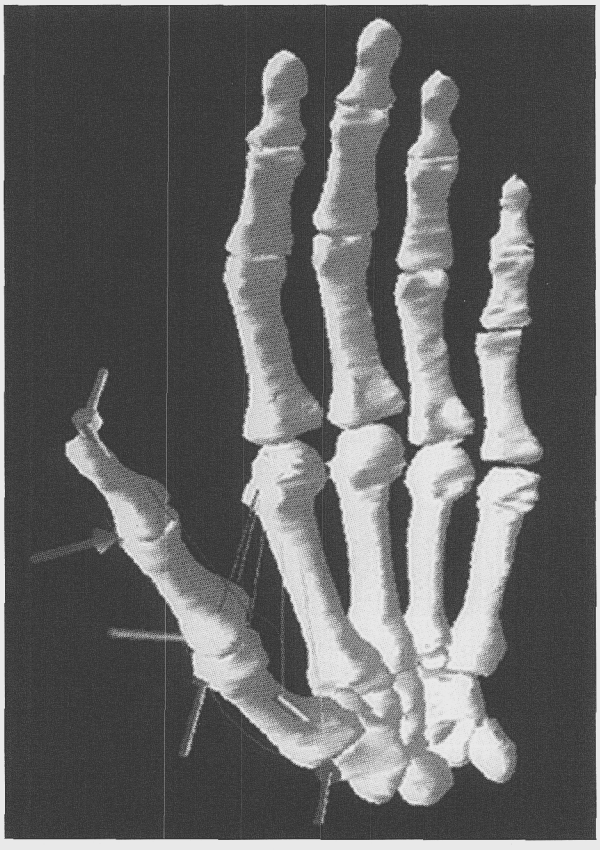

Figure 1. Biomechanics model used to calculate thumb carpo-metacarpal joint reaction forces for a key pinch and other grasps.

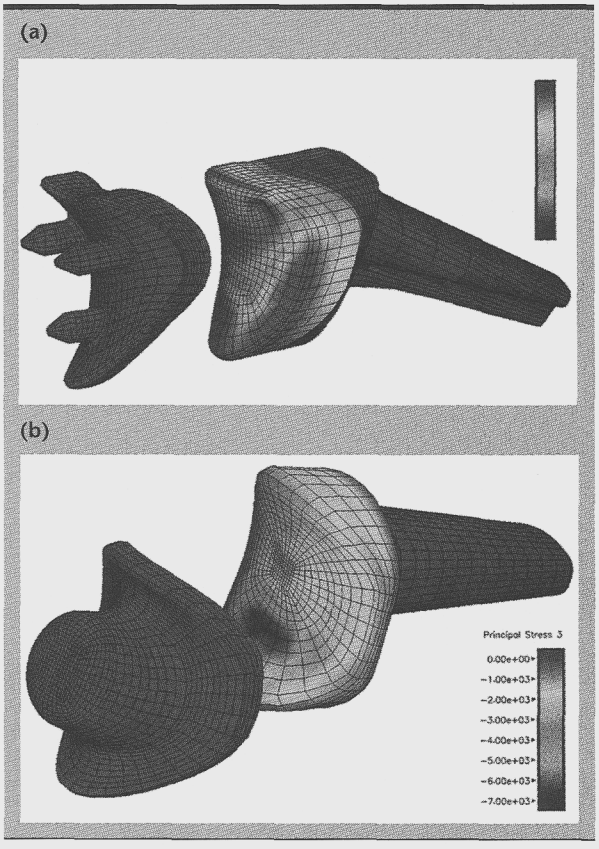

Figure 2. Finite element analyses of thumb carpo-metacarpal joint implants. Loading represents joint reaction forces experienced by the implants in a maximum key pinch grasp for (a) asymmetric saddle design, and (b) symmetric saddle design.

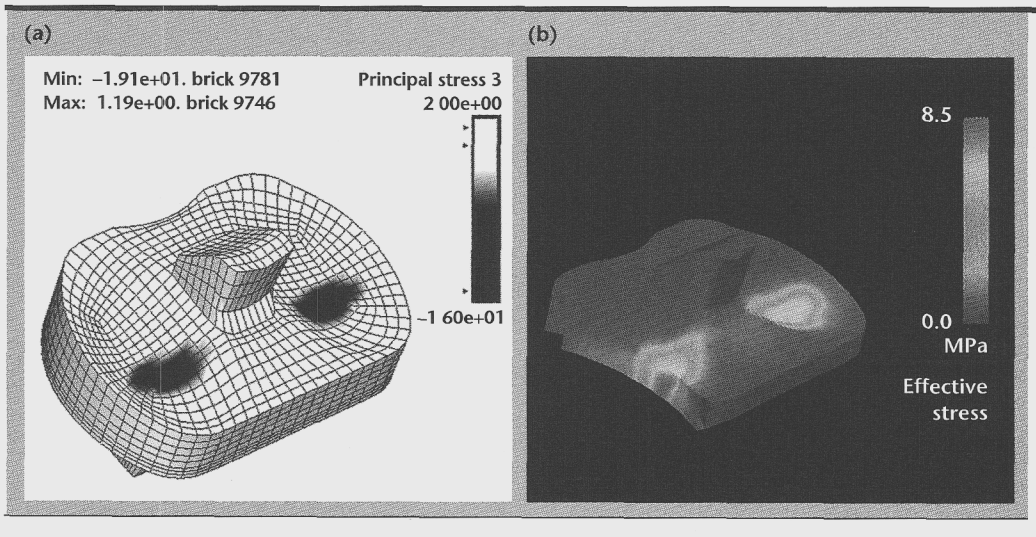

Figure 3. Finite element analysis of knee joint replacement with (a) principal stress at articular surface of polyethylene, and (b) cutaway view showing subsurface stress. Loading represents joint reaction force experienced by the implant in a straight leg stance.

Simulations of prosthetic joint implants without human joint models can provide predictive data on the mechanical performance of the implants. Integration of human joint with prosthetic joint models provides additional data for consideration in implant performance evaluation. With this in mind, we have developed several models of human joints, including a hand model and a knee model. In addition, we have developed a process by which we can acquire human joint data and process the data to create a new human joint model. The steps in this process are described in more detail below.

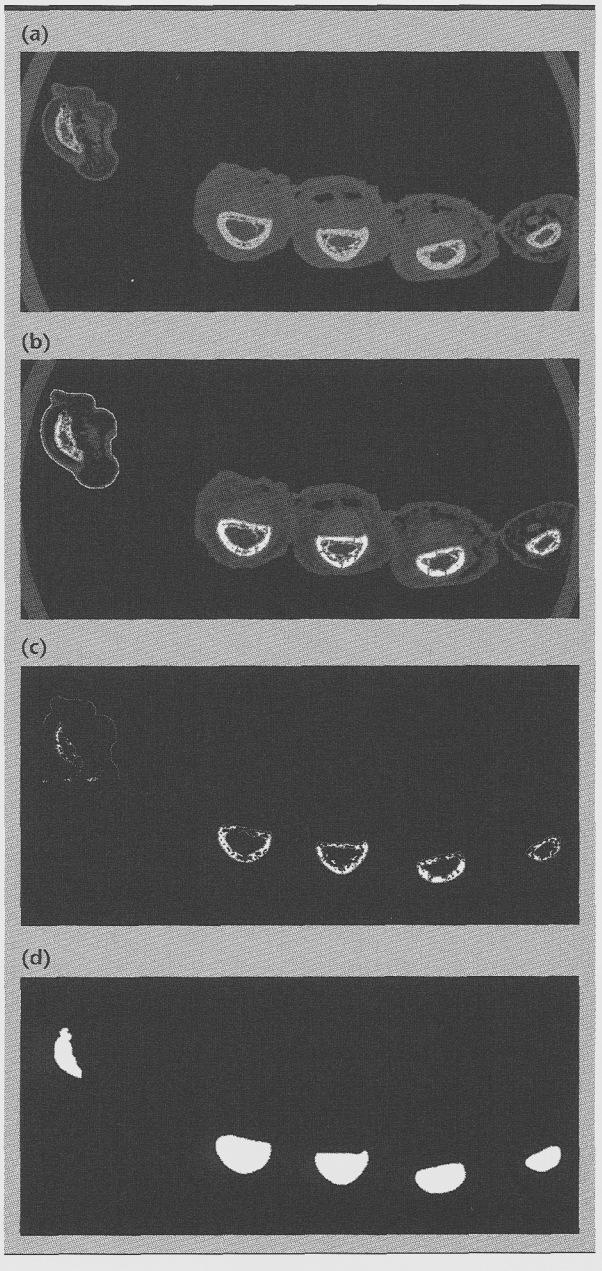

Figure 4. Segmentation of CT data: identification of bone tissues within a high-resolution, 3-D hand scan. A single slice is shown: (a) raw CT data; (b) bone outlines generated by automated edge detection; (c) partial manual correction of outlines; and (d) final bone identification overlaid on original CT data.

Developing a human joint model begins with scanning the joint to acquire geometrical data. Computed tomography (CT) scans are presently the best method to define the surfaces of bony material. CT scans are commonly used in medicine. However, scanners typically used in the medical field have a spatial resolution of up to 1 mm, which is not adequate for a precise definition of articular surfaces. We can achieve a higher resolution at LLNL, where we have scanned two cadaver hands and one knee, using the industrial scanners in the Non-destructive Evaluation group (NDE). Spatial resolutions of these scans have varied from 150 to 190 μm for the hand scans and approximately 280 μm for the knee scan.

While CT scans are good at defining bone surfaces, soft tissue geometries are more easily obtained using other scanning techniques, such as magnetic resonance imaging (MRI).

Collaborators at Massachusetts General Hospital (MGH) and the University of California at Davis (UCD) have provided several MRI datasets of patient knees (at MGH) and cadaver hands (at UCD), which we can use in conjunction with the CT data to help define exact attachment sites for soft tissues.

We have developed semi-automated CT processing software to convert CT images into 3-D surfaces. Segmentation of high resolution CT data is made difficult by the inhomogeneous trabecular structure of bones. Some level of human interaction is needed to fine-tune automatic segmentation results.

We have implemented tools that allow the user to visualize large data sets, manipulate color maps to display false colors, perform interactive thresholding, overlay the segmentation masks, save the corrected results, and create 3-D surfaces from the segmentation masks (**Fig. 4**). These 3-D surfaces are then meshed, and boundary conditions are applied, to set up the finite element simulations in the same way that the prosthetic implant analyses were performed. The loading (boundary) conditions and initial ligament tensions are determined from experiments performed in collaboration with our research partners at Louisiana State University Medical Center and from a model developed in collaboration with the GW Long Hansen's Disease Center.

Sample results from the human joint finite element analyses are shown in **Fig. 5**.

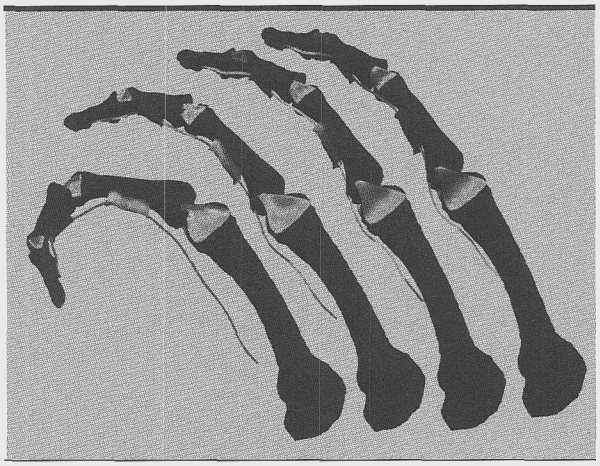

Figure 5. Finite element simulations of human joint articulation: flexion of index finger. Loading represents displacement of the tendon due to muscle contraction.

Future Work

Future work in this research project will be focused primarily on the integration of the human and prosthetic joint models, so that bone-implant interface analyses are possible. We will continue to work on the ball-and-socket and saddle designs for the thumb carpo-metacarpal joint and on the knee design. Most of our technical research progress in the upcoming year will be in developing these integrated models and in calculating the bone stresses resulting from the loads exerted by the implants on the bone.

In addition, model validation will form a key part of our work in the next year. The human knee and carpo-metacarpal joint models will be validated against experimental data. To maintain a manageable scope of work, our efforts are focused on specific aspects of the joint biomechanics that are relatively easy to access experimentally, such as joint kinematics (comparison with experiment and rigid body models), articular surface contact areas and stress patterns (comparison with experiment), and ligament stresses as a function of joint orientation (comparison with experiment).

For validation of implant models, we will compare contact stress calculations with experimentally determined values, where possible, and we will examine clinical data on the failure of one of the carpo-metacarpal joint implants. (Failure followed improper surgical insertion of the implant into the human joint).

Until now, we have worked with three orthopedic companies, (ExacTech, in Florida, ArthroMotion in Indiana, and Wright Medical in Tennessee) and with two orthopedic surgeons (Dr. A. Hollister, Louisiana State University Medical Center and Dr. K. Trauner, UCD). In the future, we expect to continue our research by expanding our interactions with these companies and with additional clinical and industrial partners.

Through clinical and industrial partnerships, we expect that our orthopedic research will become a self-sustaining research program at LLNL. To broaden our research interests and to augment contracts for analysis work with the orthopedic industry, we will also be pursuing external grant funding. Examples of related research application areas include simulations of fracture dislocations using the existing index finger model, population studies addressing ethnic-, gender-, and age-related differences in joint size and shape, and ergonomic simulations for tool design.

Additional future work involves the integration of our technology and experience into LLNL and other Department of Energy programs. For example, through NDE we are currently working with Knolls Atomic Power Laboratory to use our image processing, meshing, and modeling tools to analyze their systems. In this process, we have trained staff at NDE in the use of the segmentation and meshing codes, so that they may be used to perform inspections of CT scanned parts at Knolls. In addition, we will make our modeling results available to Health Services at LLNL and provide input on ergonomic device design teams, based on our hand simulations.

References

1. Hollerbach, K, S. Perfect, and E. Ashby (1997), "Computational Biomechanics: Finite Element Analyses of Human and Prosthetic Joints (video)," Lawrence Livermore National Laboratory, Livermore, CA, for the Department of Energy.

2. Bartel, D. L., J. J. Rawlinson, A. H. Burstein, C. S. Kanawat, and W. F. Flynn, Jr. (1995), "Stresses in polyethylene components of contemporary total knee replacements," *Clin. Orthop. and Related Research,* **317**, pp. 76–82.

3. De Heer, D. C (1992), *Stresses in Polyethylene Tibial Components for Total Knee Arthroplasty.* Master's thesis, Purdue University, School of Mechanical Engineering, West Lafayette, IN.

4. Giurintano, D. G, A. M. Hollister (1995), "Force Analysis of the Thumb for a Five-link System," *Med Eng Phys,* **17**, pp. 297–303.

Characterization of Laser-Induced Mechanical Damage of Optical Components

Douglas R. Faux
Defense Technologies Engineering Division
Mechanical Engineering

The goal of this research is to quantify by numerical techniques the effects of surface and sub-surface defects on damage initiation and growth in high-power laser optical components. The defects include laser absorbing spots (such as surface particulate contamination), and surface damage regions (such as micro-cracks and voids), which are present due to environmental exposure and fabrication processes. Our work here focused on three sources of particle contamination that can cause damage to optical components: front-surface; back-surface; and sub-surface. The DYNA2D code was used to model the growth of damage in the glass substrate.

The damage in the glass substrate as a result of front-surface particle contamination was found to be dependent on the magnitude of the pressure pulse applied to the particle and the initial area of contact between the particle and glass substrate. The pressures generated from a back-surface particle being blown off the surface provided sufficient loading to severely damage (crack) the glass substrate. A sub-surface cerium oxide particle showed a strong surface interaction that influenced the formation and direction of the cracking that ultimately resulted in the blow-out of the damaged material, leaving a relatively clean crater in the glass.

Introduction

The Beamlet spatial filter failure caused significant damage to the laser and a month of down-time. Experimental evidence indicates that particulate contamination on the lens surface or embedded below the surface may have been the precursor to failure.

A failure scenario is the following: a particle on the back surface is irradiated by laser light, creating a hot expanding plasma which then imparts a severe pressure loading on the glass surface, and creates micro-cracks and unacceptable damage. For the National Ignition Facility (NIF) at Lawrence Livermore National Laboratory (LLNL) to set cleanliness and surface finish requirements, we must determine the particle contamination size that results in critical damage morphologies after laser irradiation.

Particulate contamination on optics can act as an obscuration in the beam, or as a local initiation site for laser damage. An on-going experimental program, initiated in FY-96 and funded by NIF, is looking at damage morphologies on optical surfaces contaminated with particles of well-controlled size and composition.

To improve our understanding of damage initiation and growth, a modeling effort, complementing the experimental work, was initiated in FY-96. The modeling group is a multidisciplinary LLNL team with representatives from NIF, Physics, the Laser Program, and Mechanical Engineering.

The Physics staff is responsible for formulating theoretical models of the problem with emphasis on plasma physics, laser/matter interaction, and radiation transport. The Laser Program is using LASNEX to model the laser interaction with surface particulate and plasma formation, and to calculate the magnitude of the surface pressure pulse on the optic. Mechanical Engineering staff are using DYNA2D[1] to investigate the optic response to the surface pressures calculated from LASNEX and to investigate front-surface particulate contamination and sub-surface particulate contamination.

Progress

DYNA2D Brittle Damage Models

Four brittle damage models were incorporated into DYNA2D for modeling dynamic impact events with brittle materials, such as ceramics and glasses.

Three of the brittle damage models implemented use a scalar damage parameter to track cumulative damage, while the fourth incorporates a tensor damage via the explicit tracking of 3-D cracks within an element.

For the three scalar damage models, the constitutive response of undamaged material is treated with either an isotropic-elastic-plastic or a Steinberg-Guinan high-rate elastic-plastic flow rule. Failed material is treated with a piece-wise linear definition of yield stress vs pressure. The transition between undamaged and fully damaged material is accomplished through the evolution of the scalar damage parameter, D.

The three scalar damage models differ in their evolution equations for D. The shear modulus, yield strength, and pressure are transitioned between the undamaged values and fully-damaged values as D goes from 0 to 1. The three scalar damage models are the modified Tuler-Butcher[2] damage model, the modified Cagnoux-Glenn brittle damage model,[3,4] and the Steinberg-Tipton brittle damage model.[5]

The tensor damage model incorporated into DYNA2D to calculate the brittle damage response of glass is a modified Rubin-Attia 3-D crack damage model.[6] Fracture is modeled in a continuum sense by introducing a symmetric tensor, e^v, which denotes void strain. The void strain is determined by restricting the traction vector that is applied on a fracture surface.

The model allows the formation of up to three orthogonal fracture surfaces, which are normal to the right-handed orthonormal set of unit vectors characterizing the fracture triad. Compressive yielding and tensile failure are each treated separately. Compressive failure involves the evolution of a scalar damage variable, and tensile failure involves the formation of three fracture surfaces and the evolution of a void strain.

The 3-D crack damage model is used for problems where the directionality of the damage is more critical in matching experimental results. A hardened 440 stainless steel sphere with 0.05 cm diameter impacted against an optical quality fused silica glass surface at 305 m/s. The experimental damage morphology was a hemispherical sub-surface fracture region surrounded by a smaller, heavily fractured inner "plastic" region, and, in some cases, with a few Herzian cone cracks extending somewhat further into the target. The experimentally measured outer

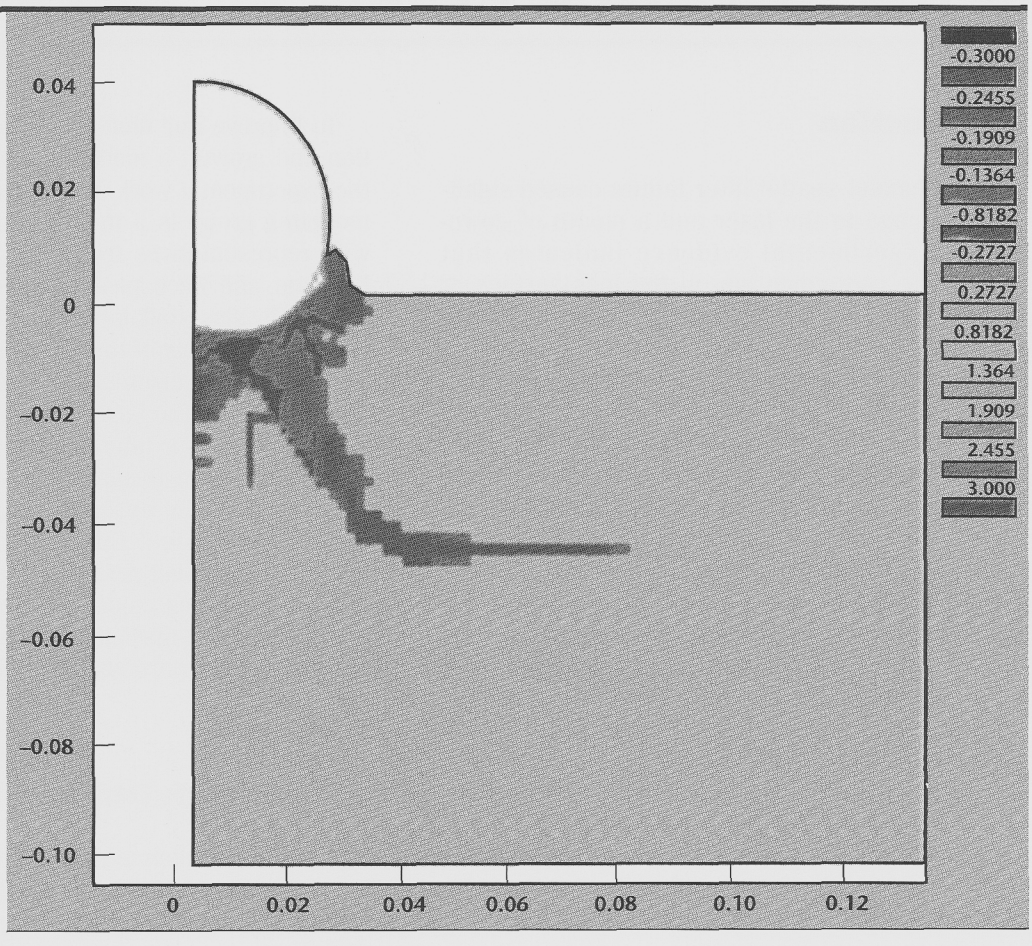

Figure 1. Steel ball impacts fused silica at 305 m/s. The fringe of damage is at 80 μs.

fracture diameter was 0.165 cm; the inner, more fractured region, had a diameter of 0.08 cm; and the depth of the fractured region was 0.10 cm.

Figure 1 shows the steel ball impact analysis 80 μs after impact, displaying fringes of element damage states. Strong evidence of Herzian cone cracks is observed on the plot, as is the compressive "plastic" fracture region beneath the steel ball. The conical crack grows at a semi-apex angle of 30°, then moves horizontally. The maximum fracture diameter is 0.162 cm, compared to the experimental value of 0.165 cm. The inner "plastic" fracture region is 0.07 cm in diameter, compared to the experimental value of 0.08 cm. The depth of the damage is 0.05 cm, indicating a less than hemispherical damage region.

A complete description of these models and their applications to ceramic and glass damage can be found in an earlier report.[7]

Front-Side Particle Contamination

If a metal particle is on the front side of an optic and is hit with a laser, a pressure pulse due to the laser light absorption on the surface of the particle will be transmitted through the particle and into the glass substrate. An aluminum spherical particle, 100 μm in diameter, was placed in contact with a silicon oxide substrate. Initial contact was assumed to be a 40° apex angle. A 150-kbar, 4-ns full-width half-maximum (FWHM) Gaussian pressure pulse was applied to the surface of the sphere with a cosine squared pressure distribution. The Steinberg-Guinan constitutive law, Mie-Gruneisen equation of state, and Tuler-Butcher failure criteria for spall were used to model the behavior of the aluminum particle. The silicon oxide substrate was modeled with the Modified Rubin-Attia 3-D crack damage model and a linear polynomial equation of state.

The damage in the glass begins at the outer contact points where shear stresses develop first. The damage grows into the substrate, then connects to the subsurface damage (12 μm below the surface) where the shear stresses reach their maximum. Damage then continues to expand in a semi-circular

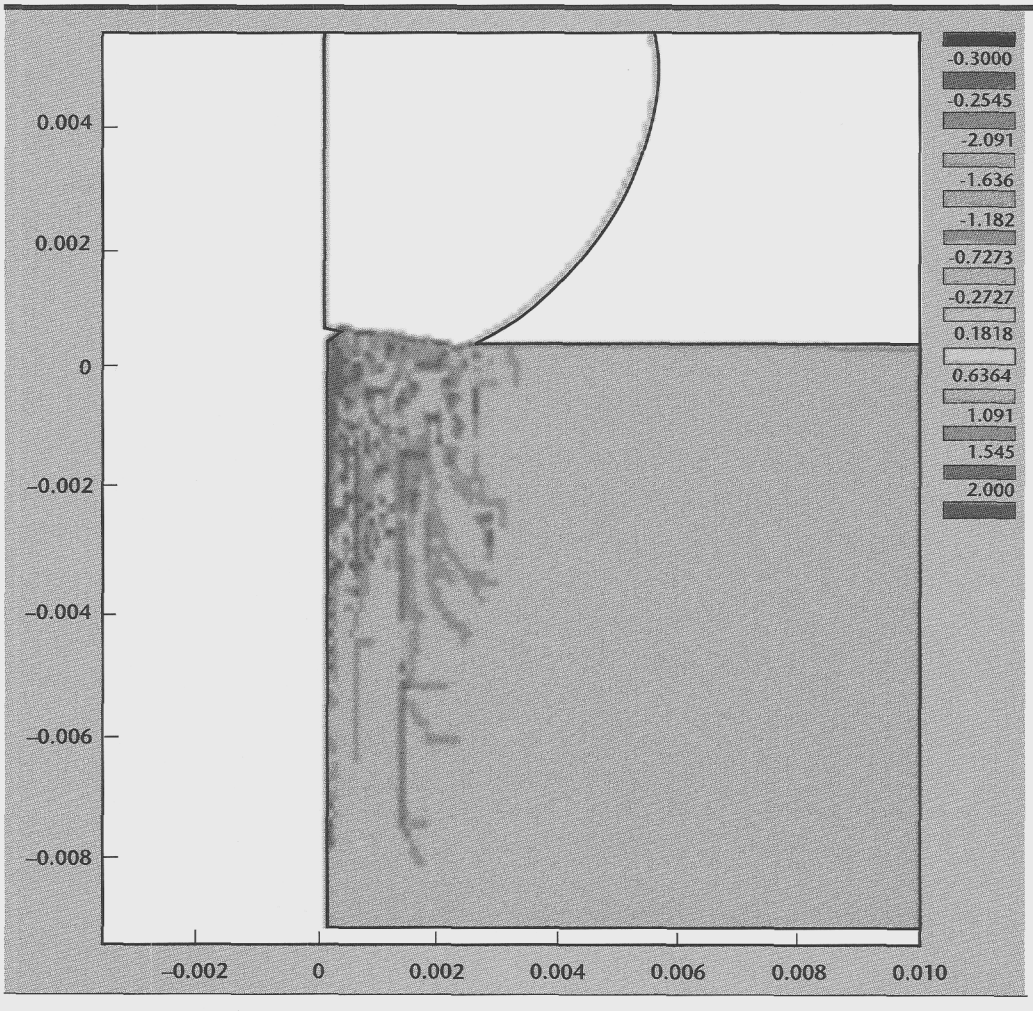

Figure 2. Aluminum sphere 100 μm diameter, 40° contact angle, 150 kbars, 4-ns FWHM Gaussian Pulse; time = 50 ns. The fringe of damage is in glass substrate.

fashion with visible fingers of damage emanating from the main sub-surface damage region (**Fig. 2**). The aluminum particle separates from the substrate and the gap grows until the damaged glass expands and fills the gap. Significant damage of the glass occurs to a depth of 40 μm, with fingers of damage growing to 80 μm deep. The diameter of damage is 70 μm.

Back-Side Particle Contamination

Back-surface particle contamination of optics components involves a particle on the back surface being irradiated by laser light, creating a hot expanding plasma, which then imparts a severe pressure loading on the glass surface and creates microcracks and unacceptable damage. To determine the pressure loading on the glass surface, LASNEX was used to model the formation of the plasma and its subsequent pressure loading of the glass. An aluminum disc 100 μm in diameter and 5 μm thick was placed on the backside of a silicon oxide substrate. A 18-J/cm^3 Gaussian pulse, 3-ns FWHM, was applied to the optic. Pressure as a function of time and radius at the solid/liquid interface (0.1 eV) was obtained from the LASNEX calculation.

To facilitate the transfer of pressure data from LASNEX to DYNA2D, a table look-up feature was incorporated into DYNA2D to apply this time- and spatially-varying pressure history to a virgin glass substrate. A DYNA2D model, 400 μm in diameter and 300 μm deep, was generated to apply the pressure histories. Nonreflecting boundary conditions were used to simulate a semi-infinite block. A pressure boundary surface from a radius 0 to 80 μm was specified on the semi-infinite block and the table look-up feature was used to apply the pressures as a function of radius and time. The silicon oxide substrate was modeled with the modified Rubin-Attia 3-D crack damage model.

The pressure pulse starts out in a rectangular pattern, but dispersion causes the pulse to spread out spherically. Damage behind the main pressure pulse causes pressure concentrations to occur. Damage begins at the outside radius of the disc where shear stresses are maximum. Damage follows the pressure pulse, then begins to move out in finger-like cracks at ~45° (**Fig. 3**). Damage is measured to a depth of 120 μm, with a diameter of 170 μm.

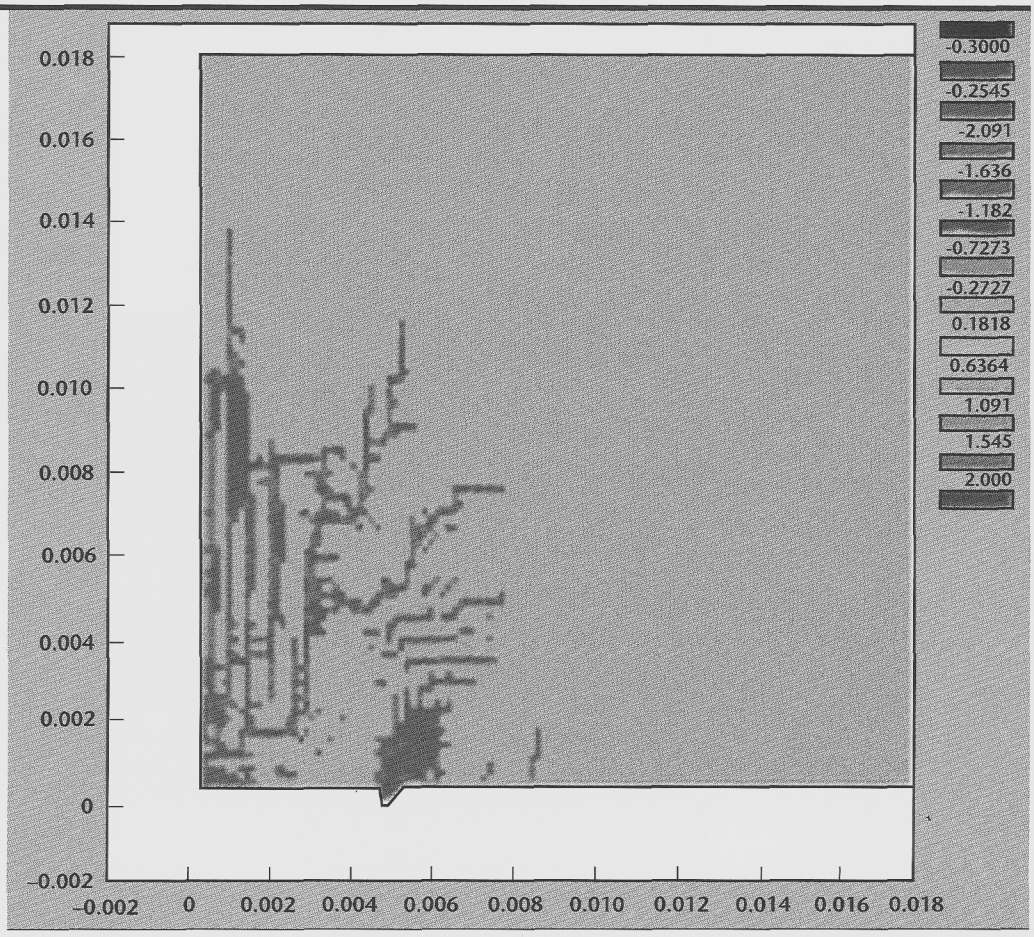

Figure 3. Aluminum disc 100 μm diameter, 5 μm thick on silicon oxide back surface; 18 J/cm^3 Gaussian Pulse, 3-ns FWHM. The fringe of damage is at time = 60 ns.

Sub-Surface Particle Contamination

Sub-surface particle contamination of the optics has been shown to cause unacceptable damage after irradiation. It has been postulated that cerium oxide particles, left over from the polishing process, are absorbing energy, expanding and causing small craters on the glass surface. DYNA2D was used to investigate this phenomenon by explicitly modeling the cerium oxide particle and the glass substrate. Energy was deposited into the particle allowing it to expand and damage the glass substrate. It was assumed that the glass around the cerium oxide particle does not absorb light and heat up.

The cerium oxide particle modeled was a 100-nm-diameter particle, 300 nm deep in a silicon oxide substrate. A linear polynomial equation of state with energy dependent bulk modulus and Gruneisen gamma was used for the cerium oxide particle. The silicon oxide substrate was modeled with the modified Rubin-Attia 3-D crack damage model.

Energy was deposited into the cerium oxide particle at a constant rate for 3 ns. Pressure in the cerium oxide particle builds up to approximately 36 kbars at 1.8 ns, then the glass begins to damage and the cerium oxide particle expands and relieves pressure. At 1.0 ns, the initial compressive wave has reached the upper surface and reflected back as a tensile wave which initiates damage at the 90° location. At 1.9 ns, tensile waves reflected off the surface have created a spall plane near the surface and the damage is growing down toward the particle. At 2.0 ns, the glass around the particle is undergoing compressive failure as the crack is growing out and toward the surface (**Fig. 4**). The surface damage grows down and converges with the particle. At 2.9 ns, the conical crack emanating from the 90° location on the particle has reached the surface, and one would expect the material within the damaged region to be blown off (**Fig. 5**).

Future Work

Different particle shapes were not addressed for the front-surface contamination study, but would also play an important role in understanding the transfer of pressure into the glass substrate, resulting in its damage. Irregular-shaped particles would absorb laser light differently, and subsequently load the glass substrate in a non-uniform manner.

The back-surface contamination study should be enhanced to look at different particle shapes and

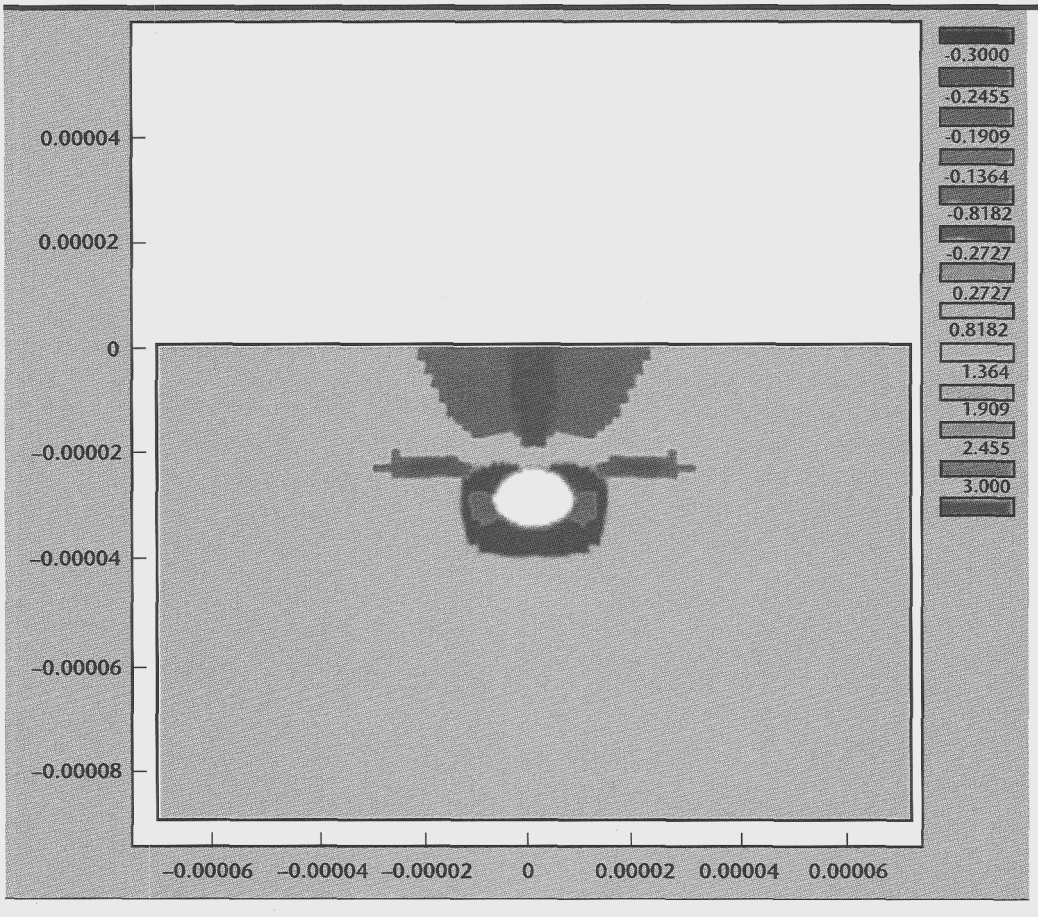

Figure 4. Cerium oxide particle 100 nm diameter, 300 nm deep in silicon oxide substrate. The fringe of damage is at time = 2.0 ns.

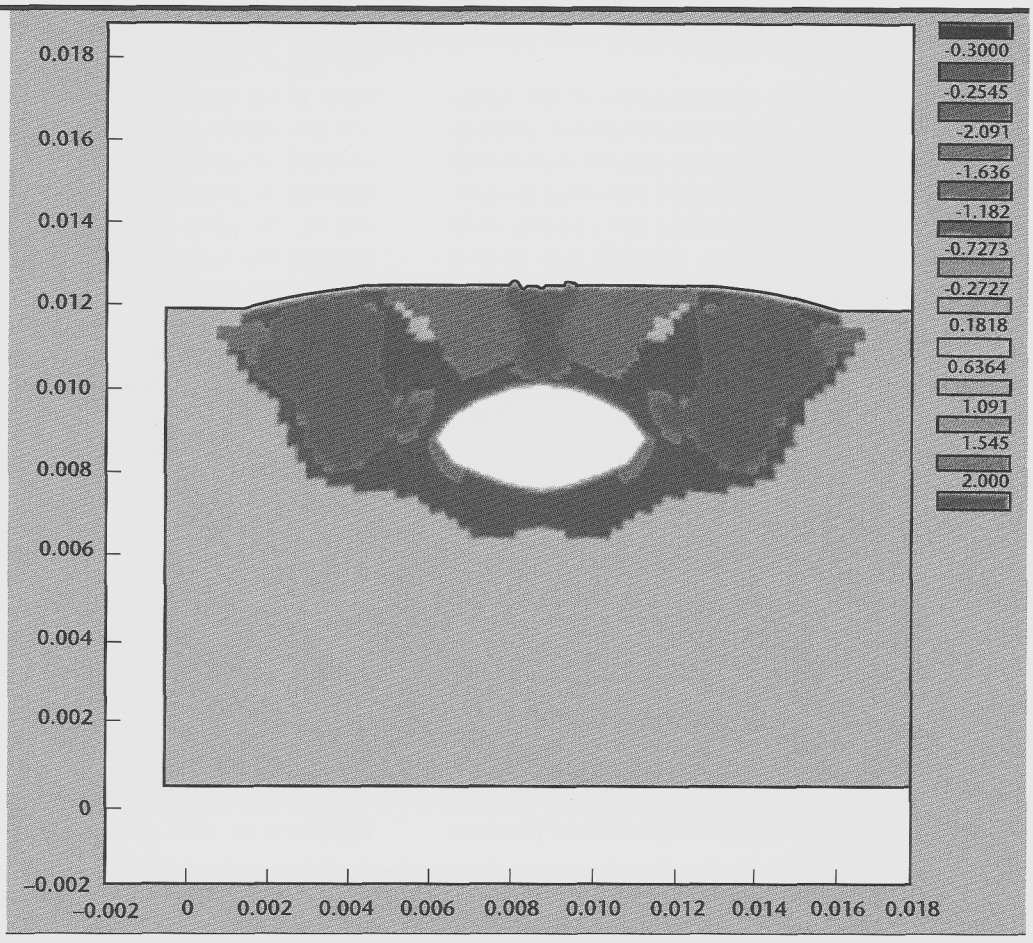

Figure 5. Cerium oxide particle 100 nm diameter, 300 nm deep in silicon oxide substrate. The fringe of damage is at time = 2.9 ns.

materials. The particle shape and material would significantly affect the formation of plasma and subsequent loading on the glass substrate.

Sub-surface particle size variations were not addressed here, but would also play an important role in understanding the formation of craters in the surface of the glass. For the cases investigated here, the crater was at a depth such that surface interaction influenced the formation and direction of the damage (cracking). Additional depths should be looked at, to find out where this surface interaction diminishes. In those cases, a more accurate definition of the equation of state of the cerium oxide particle is needed to handle the solid/liquid/vapor transition. Also a more accurate energy deposition scheme would be needed.

References

1. Whirley, R. G., B. E. Englemann, and J. O. Hallquest (1992), *DYNA2D A Nonlinear, Explicit, Two-Dimensional Finite Element Code For Solid Mechanics User Manual*, Lawrence Livermore National Laboratory, Livermore, CA, April, (UCRL-MA-110630).

2. Tuler, F. R., and B. M. Butcher (1968), "A Criterion for the Time Dependence of Dynamic Fracture," *Int. J. Fracture Mechanics,* December, Vol. **4**, (4).

3. Cagnoux, J. (1984), "Phenomenological Model of Pyrex Glass Fracture," *J. De Physique,* Col C5, suppl au no. 8, Tome 46.

4. Glenn, L. A., B. Moran, and A. S. Kusubov (1992), *Modeling Jet Penetration in Glass*, Lawrence Livermore National Laboratory, Livermore, CA, April, (UCRL-JC-103512).

5. Steinberg, D. J., and R. E. Tipton (1994), *A New Fracture Model for Ceramics*, Lawrence Livermore National Laboratory, Livermore, CA, March, (UCRL-JC-116953).

6. Rubin, M. B., and A. V. Attia (1990), *A Continuum Tensile Failure Model With Friction*, Lawrence Livermore National Laboratory, Livermore, CA, August, (UCRL-ID-104759).

7. Faux, D. R. (1997), *Brittle Damage Models in DYNA2D,* Lawrence Livermore National Laboratory, Livermore, CA, September, (UCRL-ID-128520).

Parallel Algorithm Research for Solid Mechanics Applications Using Finite Element Analysis

Carol G. Hoover and Daniel C. Badders
Defense Technologies Engineering Division
Mechanical Engineering

Anthony J. De Groot and Robert J. Sherwood
Defense Sciences Engineering Division
Electronics Engineering

Two important methods for treating parallel contact for explicit finite element methods are described. Using parallel computers, performance enhancements for small, medium, and large engineering models have resulted in tremendous turnaround improvements for design calculations.

Introduction

Significant advances in the development of new contact algorithms and partitioning techniques have led to scaleable production applications using ParaDyn, the parallel version of DYNA3D. This has resulted in several benefits to our engineering design programs at Lawrence Livermore National Laboratory (LLNL).

First, calculations are now performed in a day or less for problems which previously ran over several weeks. Next, new models are being generated for mesh sizes between one million and ten million elements. This is an order of magnitude larger than the largest models possible in the past. Finally, longer time simulations (problems running for a few million steps) for small- to moderate-sized problems are now possible on both distributed and shared memory systems using the message-passing paradigm implemented in ParaDyn.

A successful strategy for parallel implementation of the explicit finite element method used in DYNA3D (ParaDyn) was described in an earlier report.[1] The method is based on dividing the finite element mesh among the processors, and executing ParaDyn on the individual subdomains. This is a message-passing parallel model, with nodal point data identified as the shared data between processors.

The algorithms for calculating internal deformations involve only one communication step, which occurs when the element stress gradients are scattered to the nodal points that are shared. A more difficult problem is to calculate the contact forces needed to prevent penetration at a material interface and include those in the communication step.

Contact occurring in applications can be characterized by whether the problem involves predictable motion of surfaces or whether large deformation and motion on the grid results in arbitrary interactions among the surfaces in the problem.

In the first case, contact is treated by defining pairs of surfaces that are expected to interact with each other, and the search for material interpenetration can be limited to neighborhoods on these surfaces. We refer to this as "local" contact. The more general case occurs for problems in which the motion of the surfaces is arbitrary. In this case a localization technique for detecting contact, referred to as "bucketing," is used. Bucketing is simply the construction of an Eulerian grid of boxes (in one, two, or three dimensions) and the assignment of the surface nodes to the buckets.

An example of arbitrary contact is a ball rolling on a plane. A novel aspect of our original implementation of a parallel algorithm for arbitrary contact was the notion of using more than one partitioning for the problem, one for the finite-element deformation calculations and a second one for the contact calculations. This idea of using two partitions for the same problem is needed also for local contact algorithms.

Conceptually, there are several useful ideas for implementing parallel algorithms for local contact. One idea is to allocate each surface pair entirely to one processor, and to distribute the set of all surface

pairs among as many processors as possible. There is no additional communication among processors (due to contact) using this method, because the contact is assumed to occur only between points on surfaces that were defined as a pair.

A second approach is to extend the bucketing methods used in arbitrary contact to the local contact algorithms. Then the parallel implementation would involve allocating the buckets to processors. In this case, communication occurs for contact calculations in buckets that are on the boundary of a processor.

Yet a third method is to allocate surface pairs to processors, and, for the contact calculation, choose a coordinate system with one surface fixed and the other moving. Again, this algorithm requires additional communication for contact as the moving surface crosses the boundary of a processor. Each of these methods involves the development of techniques for partitioning objects, and data structures for connecting the contact calculations with the full mesh partitioning. We describe the implementation of the first method for local contact in ParaDyn in the "Progress" section of this report.

The automatic contact algorithm in DYNA3D was developed to implement arbitrary contact and to eliminate the need for the time-consuming task of surface definition for large models. The original algorithm has been improved and made much more robust in the last few years.[2]

The current algorithm is designed also to more efficiently search for contact with new options. For example, boxes defined on the grid can be used to limit the domain for the automatic contact application. Boxes are further augmented by the implementation of multiple automatic contact definitions, giving more flexibility to the analyst modeling complex problems. Finally, materials can be selected for inclusion or exclusion from a specific automatic contact definition.[3]

The steps in the automatic contact algorithm include 1) an algorithm for generating the faces on every surface in the regions defined for the contact; 2) bucketing methods to localize the search for contact onto a coarse grid; 3) a local search to find contact nodes and penetrated facets; and 4) a contact force calculation.

Our first implementation of parallel contact[1] was developed in the automatic contact algorithm because it treated the general case for arbitrary contact and it incorporated many contact types into a single algorithm. Bucketing methods make the algorithm particularly compatible with parallel computing methods. We report on progress in developing the latest version of the algorithm in the section below.

Progress

This section emphasizes advances in our parallel algorithm research, followed by a discussion of some of the parallel production calculations simulated with the ParaDyn program. It concludes with progress on other projects that are part of the broader activities covered in our parallel algorithm development efforts.

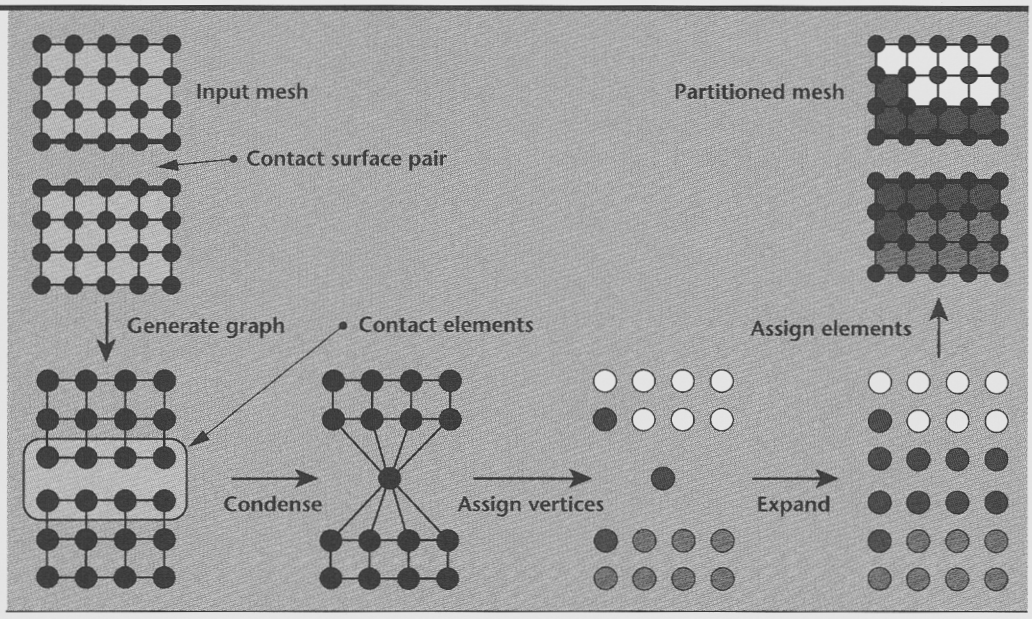

Figure 1. Illustration of the five logical steps used to allocate a contact surface pair to a processor. We condense the vertices associated with contact before giving the graph to METIS, to ensure that all elements involved in contact are in the same processor.

Combined Mesh/Boundary Partitioning Method for Local Contact

There are two conceptual and developmental steps in the implementation of our new algorithm for local contact. The first step is a technique for ensuring that a contact surface pair is allocated fully to a processor, and at the same time, distributing all pairs of surfaces among the processors for efficient load balancing. This partitioning step is implemented in preprocessing software, which provides many tools for mesh and boundary partitioning.[4]

The second step is to implement changes in ParaDyn so that the method applies to penalty contact methods, Lagrange contact, and other special purpose algorithms for nodes in contact with surfaces.

We use the METIS software[5] to partition our meshes. The METIS algorithms use graph-based methods in which a graph has vertices and interconnecting edges. For finite element meshes, we identify the vertices with the elements in the problem and the edges with the nodes shared between elements.

Once the graph is generated (in this case the graph is the element-to-element connectivity matrix), the METIS algorithms find an optimal division of the graph corresponding to the number of processors in the problem. Since two partitions are needed for the problem, the contact surfaces must be identified, and a connection made to the partition for the full mesh.

The new idea needed to allocate the surface pairs to processors is based on the notion of condensing a contact surface pair into a "super element," containing all of the elements having a facet on either of the surfaces. Each element has a vertex weight determined by its element type. Each super element has a vertex weight equal to the number of elements condensed, and an edge weight corresponding to the total connectivity of the nodes on the surface. This idea is represented in **Fig. 1**.

Next, the graph for the mesh is replaced by a graph with the super elements and the remaining elements in the mesh. The result is partitioned with METIS. This is a very advantageous approach because it automatically finds an optimal load balance among the partitions, including the super elements. Another advantage is that all of the required shared node communication for both the contact forces and the deformation forces is known in advance at this preprocessing step.

Preprocessing software which automatically partitions boundary conditions and allocates the surface pairs identified for the parallel local contact has been a significant software development effort in the last year. Six new preprocessing tools have been developed to fully implement the needed capability. In addition, we have made extensive modifications to the program for generating the partition file, and this has increased the speed by over an order of magnitude for some problems.

The memory requirements for our software have been sufficiently reduced so that all of the problems of current interest can run with considerably less than 2 GB of memory. METIS still requires more than 2 GB of memory for one problem of interest.

Finally, work is in progress to implement fully dynamic memory allocation for the dual generation program. The pay-off for this code development effort has been an automated software system that has effectively enabled a full range of production models for parallel calculations.

Additional work was necessary in ParaDyn to most efficiently implement this method for local

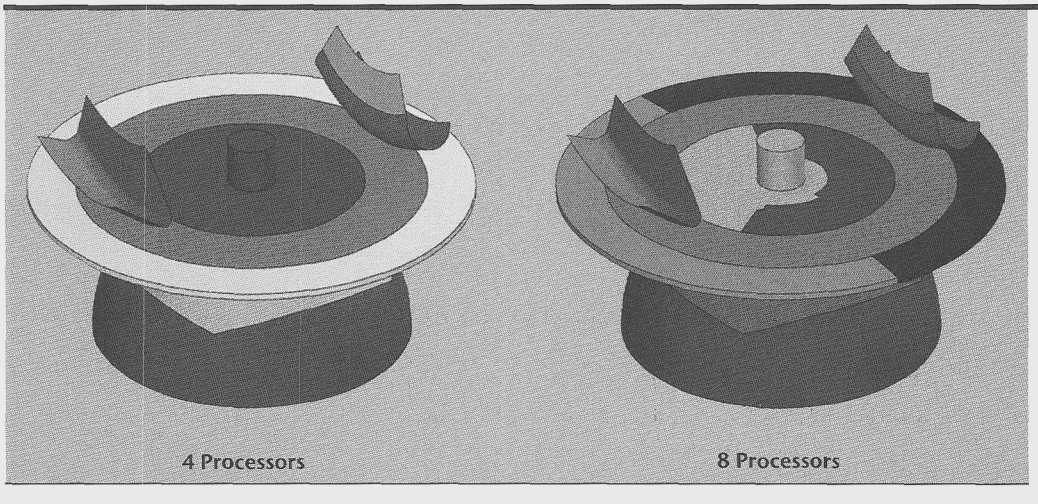

Figure 2. Illustration of metal-forming application in which a spinning plate is formed by two rollers of different size and shape. The shading shows the partitioning for four and eight processors, with the surface ring under the rollers fully contained in one processor.

contact. For example, a re-ordering of the algorithm so that the communication step followed the calculation of the Lagrange contact forces has resulted in one, rather than two communication steps. Results for parallel contact using both penalty and Lagrange methods have been checked for agreement with single processor results.

Partitioning with local contact surfaces for two different models is shown in **Figs. 2** and **3**. These examples demonstrate visually that this combined mesh/contact partitioning method results in a reasonable division for both models. The effectiveness of the partitioning can also be analyzed quantitatively.

METIS provides a balance statistic which takes on a value of 1.0 for a well-balanced calculation. In practice, we find that balance numbers between 1.0 and 1.1 provide a reasonable partition. Another check for the partitioning quality is to inspect the first few lines of the partition file. This gives the statistics for the allocation of the elements and nodes to the processors, as well as the number of shared nodes.

It is clear conceptually, and verified with the performance statistics for our production applications, that for a fixed problem size the maximum number of processors for an efficient calculation may be limited by the size of the largest contact surface. A variation of our algorithm to increase the maximum number of processors is to split large contact surfaces among one or more neighboring processors. We are currently investigating algorithms of this kind.

Parallel Automatic Contact Algorithm

Parallel arbitrary contact is treated in ParaDyn with a geometric partitioning of the contact surfaces into one-dimensional strips. The direction of the strips is determined dynamically and is the coordinate direction with the longest length which contains contact surface nodes. The strip widths are adjusted to equalize roughly the number of contact nodes allocated to a strip, and each strip is associated with a processor. Because the contact is arbitrary, new buckets are computed every ten time steps during the calculation. At these same times, the partitioning strips used in the parallel algorithms are recalculated and the contact buckets are redistributed among the processors. The use of these techniques localizes the contact search and load balances the parallel calculation.

The addition of new capabilities, such as boxes and multiple automatic contact, has necessitated a review and rewriting of the data structures and storage for the parallel algorithm. Although signif-

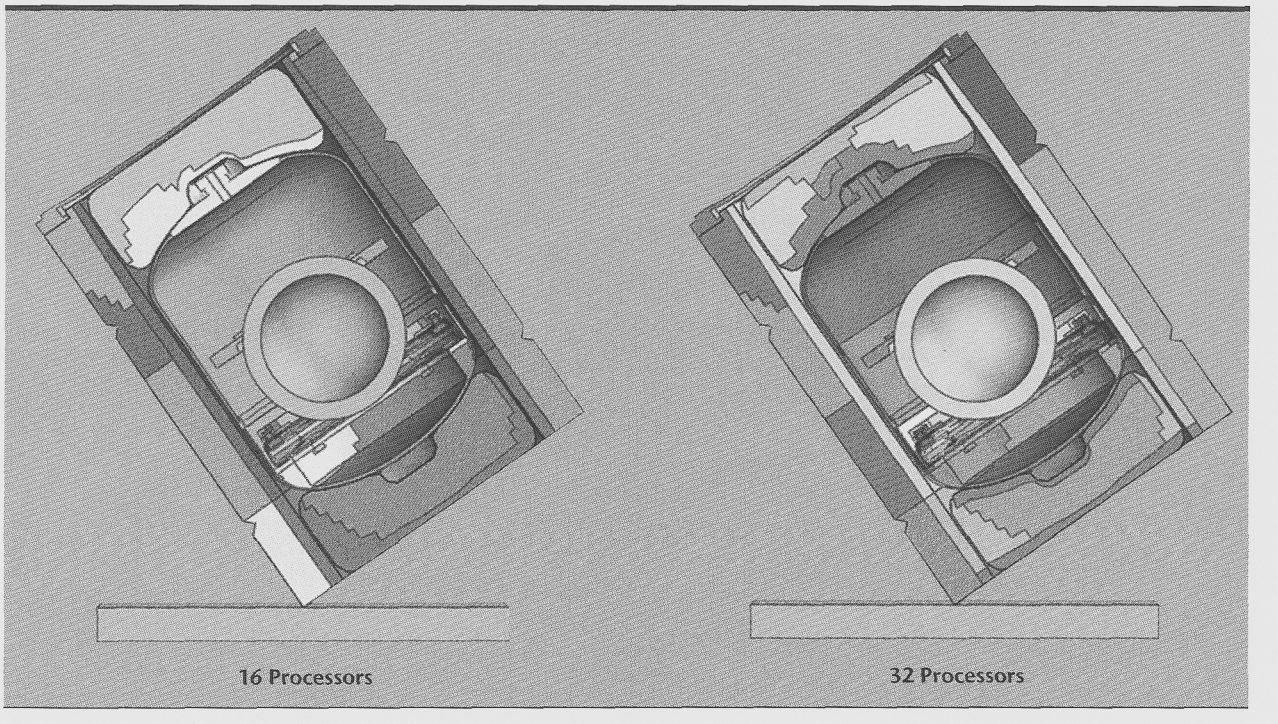

Figure 3. Illustration of the combined mesh/contact partitioning for a shipping container application. The problem included 27 contact surface pairs.

icant work is still in progress in this activity, recently we were successful in running the crash worthiness benchmark using the parallel automatic contact algorithm The calculation was noteworthy because the use of parallel computers made it possible to run the problem for a much longer simulation time than the previous simulation on a serial computer.[6] This progress is a tribute to both the robustness of our new algorithm modifications, and the performance enhancements provided by parallel computers.

Parallel Applications and Performance

ParaDyn is currently running on several parallel computers available at LLNL, and also on the parallel computers provided by the Department of Defense (DOD) High-Performance Computing and Modernization Program through the Major Shared Resource Center (MSRC) at the U.S. Army Engineer Waterways Experiment Station (WES) in Vicksburg, Mississippi. These include 256-processor IBM SP-2 systems; a 128-node (256-processor) Meiko CS-2 system; a 256-processor T3E and a 256-processor T3D; a 32-processor Origin 2000; 12- and 16-processor Power Challenge Arrays; and 10-processor DEC Alpha SMP workstation clusters.

The range of production applications that have been simulated on these systems varies from a very small (fewer than 5000 elements) spin-forming application run for more than two million time steps, to large-scale applications with more than a million elements. The following are highlights of some of the applications run with ParaDyn.

One of the first very large calculations with ParaDyn was an advanced design concept studying shock interactions with an underground target. This calculation modeled a shock at some distance from a target and required sufficient zoning in the region of the shock interface to represent the physics. This resolution resulted in a model with 2.5 million zones.

The performance on several parallel systems using up to 256 processors is shown, along with the partitioned mesh, in **Fig. 4**. This initial proof-of-concept application did not include contact in the model. Subsequent calculations with contact surfaces using either the local algorithms or the automatic contact algorithm are expected to scale as well as this original model.

Two mid-sized models were particularly beneficial to the W87 Life Extension Program by providing parameter studies in production runs which previously took too long to meet design schedules.

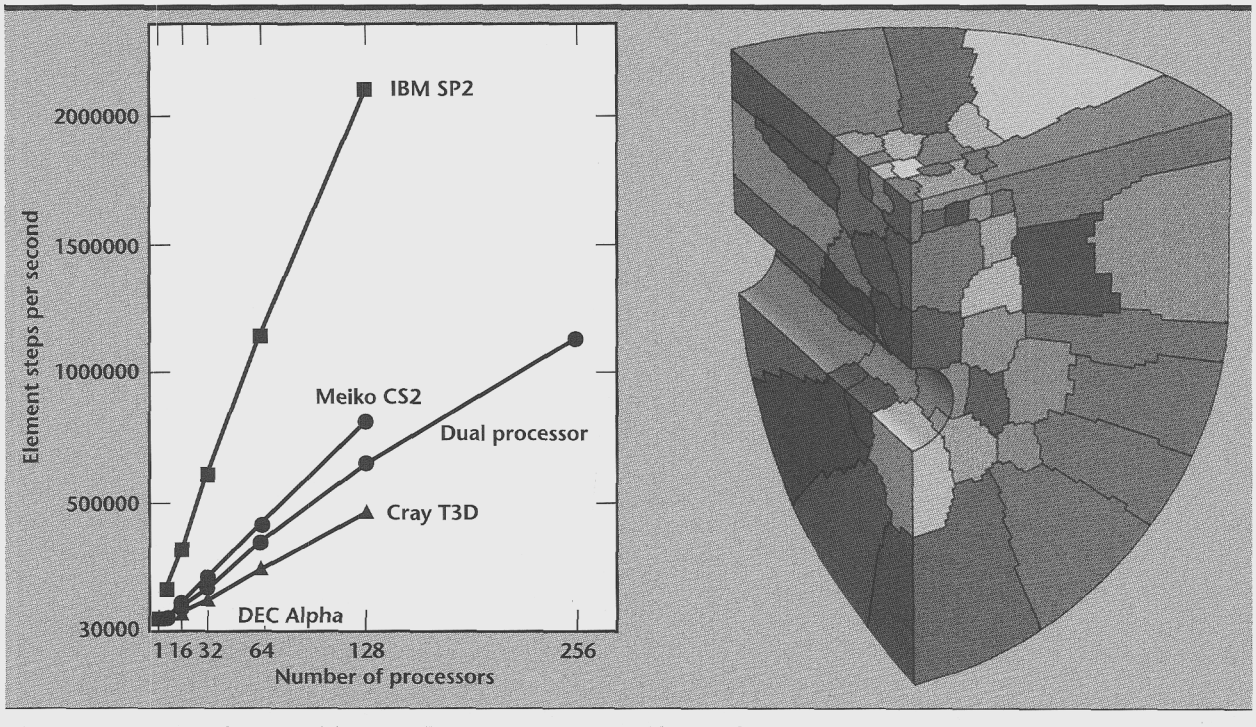

Figure 4. ParaDyn performance (a) for a million-zone problem. Problems in the multi-million element class will benefit from computers with larger numbers of processors and faster processor speeds. Illustrated in (b) are the automatic mesh partitioning results for this million-zone problem.

Figure 5 shows the performance and model input for these applications. In the first case (**Fig. 5a**), each ParaDyn production calculation was processed in half a day, where previously the same calculation would have required 27 days. Prior to the availability of parallel computers, this model would have been at the limit of the capabilities of the serial computers.

The model in **Fig. 5b** was the benchmark driving the ideas designed into our new local contact algorithm. The collaboration with the analyst resulted in a re-definition of the sliding surface interfaces at the mesh generation step to better fit the parallel algorithm. The optimal number of processors for an efficient parallel calculation was improved by a factor of four after the parallel local contact algorithm was available.

The adoption of MPI, a message-passing interface standard, plus our highly optimized domain-partitioning techniques, now makes it possible to run ParaDyn very efficiently on a symmetric multiprocessor (SMP) workstation, such as the DEC/8400 450-MHz Alpha system. Because the processors on an SMP are generally the fastest technology available, these systems are very promising parallel computing platforms for an entirely different class of problems, the small- to medium-sized problems with requirements for longer time simulations.

One application illustrating this is a spin-forming model with only 4800 elements. The partitioned mesh is shown in **Fig. 2**. The model was run for 1.1 s in 2.3 million time steps. The problem ran in 34 h on four DEC processors, compared to 96 h on a single DEC processor. Finally, this use of optimized partitioning methods with message-passing most likely results in better performance on an SMP than other types of parallelism, such as compiler directives.

Our collaborative DOD project with WES has broadened the range of applications that have been simulated with ParaDyn. **Figure 6** shows an example of their activities. Their largest model has been an application with 3.5 million elements.

Graphics and I/O

Several tasks in graphics and I/O software development needed for a parallel visualization tool are ongoing. The file-combining capability for parallel runs has been incorporated into the GRIZ visualization tool. This, plus the installation of the single processor version of GRIZ on the parallel computers, was a very valuable capability enhancement for the analysts. The new mesh I/O library (Mili) software is being added to DYNA3D/ParaDyn, and modifications have been added to GRIZ to provide the read capability for Mili files.

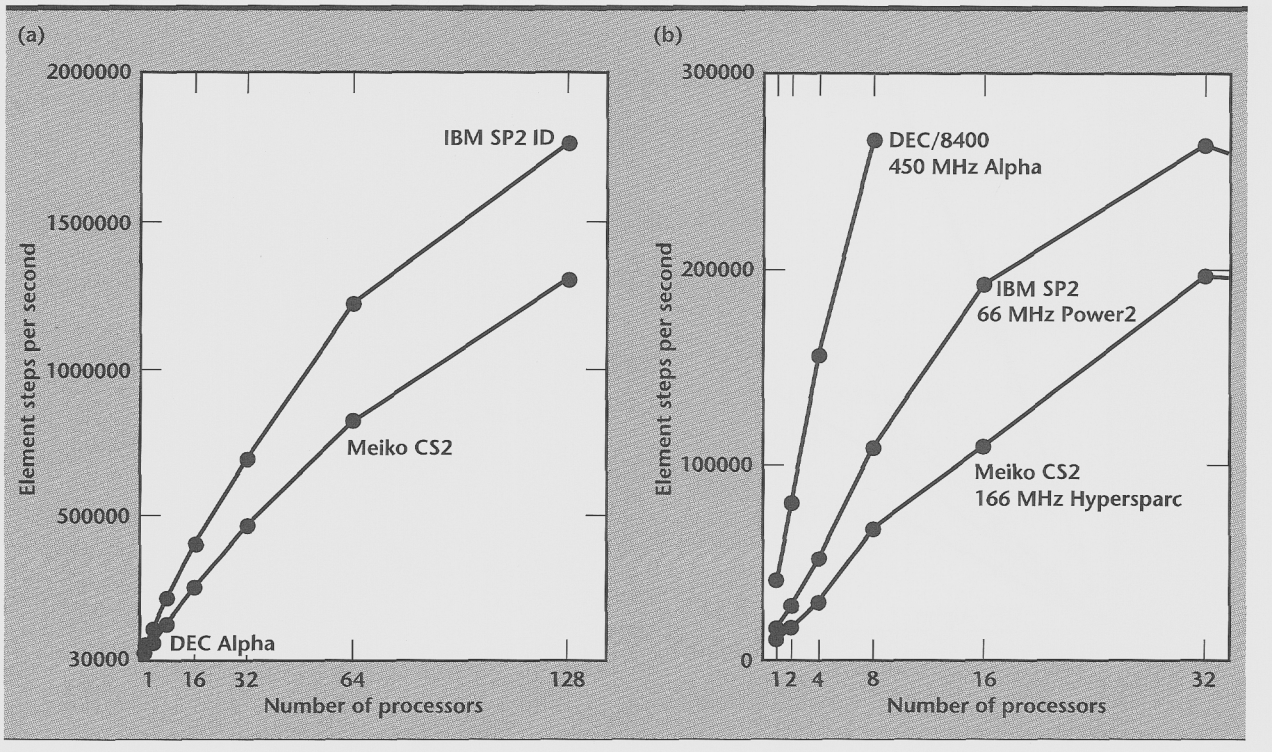

Figure 5. Performance data for two moderate-sized weapons applications. In (a) the mesh included 100,000 elements with 30 slide surfaces, containing a total of 20,000 nodes; (b) shows the performance for the shipping container application of Figure 3. The problem input specified 50,000 elements, 27 contact surfaces, 28,000 contact-related elements, and 3,200 elements in the largest contact surface pair.

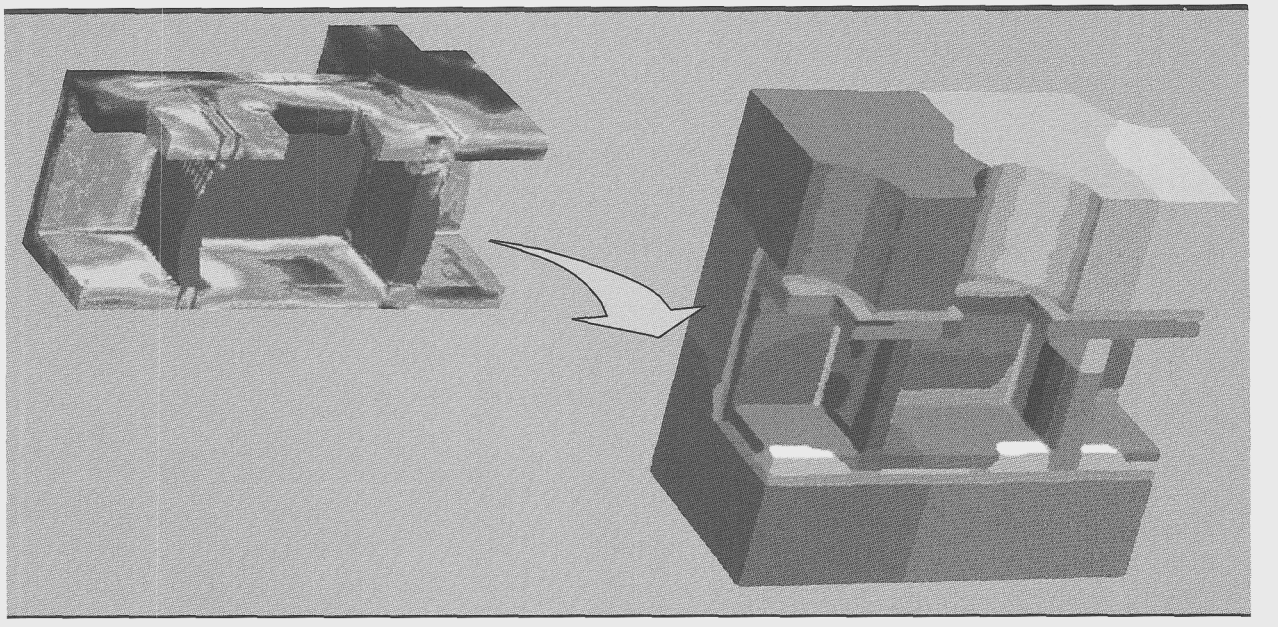

Figure 6. Model representing the loading of a structure by air blast and fragments. The simulation corresponds to experiments conducted at the U.S. Army Engineer Waterways Experiment Station, in collaboration with the Defense Special Weapons Agency. The results (a) show extensive rebar and concrete damage. The mesh (b) is partitioned for 32 processors.

Parallel Implicit Algorithms

We conducted a summer project to evaluate linear solvers for symmetric sparse matrices, to determine their potential use in a parallel version of the NIKE3D program. Our findings indicate that new solver strategies, iterative as well as direct, will be needed. Furthermore, most of the more important NIKE3D applications will require new solver techniques (for example, multi-grid methods), and will involve very challenging mathematical research.

Future Work

The code development in ParaDyn will continue to focus on optimizing the parallel algorithms which we currently have developed. We anticipate adding one more local contact algorithm either to fill in the capability which is not treated in the automatic contact, or to provide an alternate method for optimizing the performance for local contact.

Parallel algorithm development for NIKE3D will steadily increase, particularly as mathematical research moves forward in the area of multi-grid methods, and as we pursue the sub-structuring methods developed by Charbel Farhat from the University of Colorado.

Acknowledgments

Research grants from the LDRD Program and the Weapons Program at LLNL have provided the opportunity for this parallel project to mature to a production capability. The multi-million element problems run at LLNL are possible because of computers and grants provided by the Accelerated Strategic Computing Initiative (ASCI). Additional support for the ParaDyn Project has been provided by the DOD High Performance Computing and Modernization Program through a Common HPC Support Software Initiative (CHSSI) project, and a coordinated grant from the Defense Special Weapons Agency (DSWA). We gratefully acknowledge this support and the excellent collaborations with the DOD that have resulted from it.

Figure 6 was provided by the Waterways U. S. Army Engineer Experiment Station in Vicksburg, Mississippi.

References

1. Hoover, C. G., A. J. De Groot, J. D. Maltby, and R. J. Procassini (1995), *ParaDyn-DYNA3D for Massively Parallel Computers*, Lawrence Livermore National Laboratory, Livermore, CA, (UCRL-53868-94).

2. Zywicz, E. (1997), private communication, Applied Mechanics Group, Lawrence Livermore National Laboratory, Livermore, CA.

3. Whirley, R. G. and B. E. Engelmann (1993), *DYNA3D: A Nonlinear, Explicit, Dimensional Finite Element Code for Solid and Structural Mechanics—User Manual*, Lawrence Livermore National Laboratory, Livermore, CA, (UCRL-MA-107254 Rev. 1).

4. Hoover, C. G., D. C. Badders, A. J. De Groot, and R. J. Sherwood (1997), *Parallel Algorithm Research for Solid Mechanics Applications Using Finite Element Analysis*, Lawrence Livermore National Laboratory, Livermore, CA, (UCRL-ID-125471).

5. Karypis, G. and V. Kumar (1995), *METIS: Unstructured Graph Partitioning and Sparse Matrix Ordering System*, University of Minnesota, Department of Computer Science, Minneapolis, MN, (http://www.cs.umn.edu/~karpis).

6. Schauer, D. A., C. G. Hoover, G. J. Kay, A. S. Lee, and A. J. De Groot (1996), *Crashworthiness Simulations with DYNA3D*, Transportation Research Board, (Paper No. 961249).

An Accurate One-Step Elasto-Plasticity Algorithm for Shell Elements in DYNA3D

Jerry I. Lin
Defense Technologies Engineering Division
Mechanical Engineering

In the explicit finite element code DYNA3D, shell elements are treated as assemblages of plane stress laminae, hence the algorithms for the plane stress constitutive calculations play a significant role in the robustness and efficiency of the elements. A one-step algorithm is presented to find the analytical solution for the stress state of a von Mises lamina.

Compared to the existing iterative algorithms in DYNA3D, the proposed method is more efficient and easier to vectorize since no iterations are required. It also offers the same accuracy as the existing methods, and is far superior to other non-iterative schemes, such as the Stress Scaling Algorithm. Both isotropic and kinematic hardening laws can be accommodated, and rate-dependent material characteristics can be easily implemented.

Introduction

Advances in modern computers and developments in computational technologies in recent years have made detailed dynamic analyses of complex structures possible. Thin-walled or shell-type segments often exist in these structures, and usually are modeled by shell or membrane elements. Under impulsive loadings, such as those generated by explosive blast, ballistic impact, vehicle crash, or mechanical forming of metals, many of the shell structures exhibit strong non-linearities. To account for the material non-linearities, elasto-plastic constitutive models must be implemented in the analysis programs.

In explicit finite element codes, unlike their implicit or static counterpart, constitutive evaluation at the element level makes up a major part of the computational cost. To make feasible the simulation of a non-linear transient event, which often includes tens to hundreds of thousands of elements, and requires tens to hundreds of thousands of time steps in many applications, speedy constitutive evaluation is of critical importance. In addition to the efficiency issue, the possible existence of highly non-linear material behavior and severe element deformation necessitates reliable stress calculations, to avoid error accumulation through excessive time steps. Because of these two considerations, the constitutive algorithms adopted in modern explicit finite element codes must be both fast and accurate to be of any practical use.

Most of the elasto-plasticity constitutive algorithms can be categorized in two classes: iterative and one-step. Iterative methods solve non-linear equations through iterations, and one-step methods use a procedure that first predicts a trial stress state, then returns it to the yield surface, approximately.

As expected, iterative methods are, in general, more accurate, but time-consuming, whereas one-step methods are relatively fast, but less accurate.

DYNA3D[1,2] includes both an iterative method[3,4] and an one-step method[5] in its constitutive library. The one-step algorithm is an adoption of a radial scale-back algorithm.

Because of the inefficiency of fully iterative algorithms in a vectorized code environment, a compromised fixed three-iteration version of the iterative algorithm was also added to DYNA3D. The fixed three-iteration algorithm simply executes the iterative procedure three times and stops, disregarding convergence status. This allows the iterative loop to be unwrapped, which leads to vectorization.

Note that the most widely used shell element[6] in DYNA3D is based on the Mindlin Theory. Hence, the plane stress state means that only $\sigma_{ZZ} = 0$, and non-zero transverse shear stresses, that is, σ_{XZ} and σ_{YZ} are considered in constitutive calculation.

In this work, an analytic solution to the constitutive equations for a von Mises material with infinitesimal strain increments is presented. This procedure is directly applicable to DYNA3D because of the inherent small time step size in explicit finite

element codes. Strain increments in a DYNA3D run for applications such as ballistic impact, penetration simulation, vehicle crash, and metal forming range from 10^{-7} to 10^{-4}. Our study shows that the strain increments of this size are small enough to be considered infinitesimal for stress increment evaluation purposes.

Progress

The Elasto-Plastic Algorithm for Shell Elements

Given the strain increments, the current stresses, the current strains, and the material properties, a constitutive algorithm in an explicit time-marching scheme must find the corresponding stress increment. Let us consider a material that is isotropic within elastic limit, and exhibits isotropic/kinematic hardening behavior beyond yielding. Furthermore, the material follows the von Mises yield criterion and the associated flow rule. At a given material point, that is, an element integration point in finite element analysis, **Eqs. 1** to **4** must be satisfied.

Hooke's Law:

$$d\underline{\sigma} = \underline{C}\left(d\underline{\varepsilon} - d\underline{\varepsilon}^{\,p}\right) \tag{1}$$

The Flow Rule:

$$d\underline{\varepsilon}^{\,p} = \dot{\lambda}\frac{\underline{a}}{\left\|\underline{a}\right\|} \tag{2}$$

The Hardening Law:

$$d\bar{\sigma} = \beta H d\bar{\varepsilon}^{\,p} \tag{3a}$$

$$d\underline{\alpha} = 2(1-\beta)H\frac{\dot{\lambda}}{\left\|\underline{a}\right\|}\left(\underline{\sigma} - \underline{\alpha}\right) \tag{3b}$$

The Yield Condition:

$$f\left[\left(\underline{\sigma} + d\underline{\sigma}\right) - \left(\underline{\alpha} + d\underline{\alpha}\right)\right] = \left(\bar{\sigma} + d\bar{\sigma}\right)^2 \tag{4}$$

where

f	is the yield function,
$\underline{C}$	the elastic constitutive matrix,
H	the plastic modulus,
$d\underline{\sigma}$	the stress increment,
$d\underline{\varepsilon}$	the strain increment,
$d\underline{\varepsilon}^{\,p}$	the plastic strain increment,
$d\underline{\alpha}$	the back stress increment,
$d\bar{\sigma}$	the effective stress increment,
$d\bar{\varepsilon}^{\,p}$	the effective plastic strain increment,
$\underline{\sigma}$	the current stress,
$\underline{\alpha}$	the current back stress,

and

$$\underline{a} = \frac{\partial f}{\partial \underline{\sigma}} \quad \text{the plastic flow vector.} \tag{5}$$

Underlined entities represent vectors or tensors, and $\left\|\underline{a}\right\|$ stands for the magnitude of vector $\underline{a}$.

Eqs. 1 to 4 are directly applicable to infinitesimal strain increments. Because of the inherent small time steps in an explicit calculation, our study shows that these equations can be applied effectively to the finite strain increments in a time step. Combining **Eqs. 1 to 4** results in a quadratic algebraic equation for the proportional coefficient $\dot{\lambda}$. Solving $\dot{\lambda}$ and substituting it into these equations yields the desired quantities, such as $d\underline{\sigma}$ and $d\underline{\alpha}$.

This algorithm has been implemented in DYNA3D, and the sample problems in the next section demonstrate its effectiveness.

Examples and Comparison

Two examples are used to compare the proposed and existing algorithms. The first example is a rigid blunt projectile impacting a frame-supported plate; the second a vehicle hitting a u-shaped rigid post. For the first example, only a quarter of the model was analyzed, because of the symmetry about two axes. These problems are chosen because they are shell-dominated models and exhibit high material non-linearities. The results produced by the fixed three-iteration scheme, which is designated as the default algorithm in DYNA3D, is used as a benchmark for accuracy as well as efficiency comparison in the validation process. **Figures 1 and 2** show the final deformation.

Two runs were made for each example, one by the proposed algorithm, the other by the DYNA3D default scheme. Only results by the proposed method are presented in the figures since there is no appreciable difference in the deformation shapes between the two runs.

To monitor the comparison more closely, key quantities such as nodal velocities and displacements and element effective stress at critical or sensitive locations were also examined for both problems. Sampling spots for the first example include the center point of the target plate and a

Table 1. Efficiency comparison for projectile impacting a plate.

	Overall CPU (s)	Constitutive evaluation CPU (s)
Proposed algorithm	947	120
Fixed 3-iteration algorithm	1093	256
CPU saving	13%	53%

Table 2. Efficiency comparison for vehicle crashing into a u-post.

	Overall CPU (s)	Constitutive evaluation CPU (s)
Proposed algorithm	8337	1070
Fixed 3-iteration algorithm	9316	2046
CPU saving	11%	48%

point on the diagonal line just outside the direct impact zone. Sampling spots for the second example are points on the fenders, where local shell buckling took place, and spots on the front bumper, where the direct impact occurred. Again, no significant differences were observed, hence no specific graphs are presented here.

Since both algorithms offer almost identical results, the superior computational efficiency of the proposed algorithm surely makes it more appealing than the default algorithm. **Tables 1 and 2** summarize the CPU time comparison on a DEC-Alpha workstation.

A rate increase of about 50% was achieved for both problems on constitutive evaluation. With other time-consuming features, such as contact slidelines and various other constitutive models, taken into account, the overall CPU saving is still at a significant level of more than 10%.

Future Work

Although intended for shell elements, the proposed algorithm can be extended to general 3-D continuum elements. It can also be modified to accommodate other similar materials, such as rate-dependent elasto-plastic materials and thermal elasto-plastic materials. These are the areas to explore in future years.

Reference

1. Whirley, R. G., and B. E. Engelmann (1993), *DYNA3D: A Nonlinear, Explicit, Three-Dimensional Finite Element Code for Solid and Structural Mechanics - User Manual,* University of California, Lawrence Livermore National Laboratory, Livermore, CA, (UCRL-MA-107254).

2. Whirley, R. G., J. O. Hallquist, and G. L. Goudreau (1988), *An Assessment of Numerical Algorithms for Plane Stress and Shell Elastoplasticity on Supercomputers,* University of California, Lawrence Livermore National Laboratory, Livermore, CA, (UCRL-99690).

3. Krieg, R. D., and S. W. Key (1976), "Implementation of a Time Dependent Plasticity Theory into Structural Computer Programs," *Constitutive Equations in Viscoplasticity: Computational and Engineering Aspects,* ASME, New York, NY, Vol. **20**, p. 125.

4. Hughes, T. J. R., and E. Hinton, Eds. (1986), "Finite Element Methods for Plate and Shell Structures," *Element Technology,* Pineridge Press International, Swansea, United Kingdom, Vol. **1**, p. 394.

5. Key, S. W., Z. E. Beisinger, and R. D. Krieg (1978), *HONDO II: A Finite Element Computer Program for the Large Deformation Dynamic Response of Axisymmetric Solids,* Sandia National Laboratory, Livermore, CA, (SAND78-0422).

6. Belytschko, T., J. I. Lin, and C. S. Tsay (1984), "Explicit Algorithms for the Nonlinear Dynamics of Shells," *Computer Methods in Applied Mechanics and Engineering,* **42**, pp. 225–251.

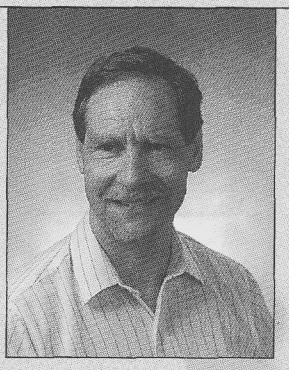

Raymond P. Mariella, Jr., Thrust Area Leader

The Microtechnology thrust area conducts activities for the Lawrence Livermore National Laboratory (LLNL) missions of global security, global ecology, and bioscience. Our efforts are associated with devices, instruments, or systems that require microfabricated components, including micro-electromechanical systems (MEMS), electronics, photonics, microstructures, and microactuators.

All of our microtechnology work revolves around our microfabrication facility. In all work, we have close collaborations with the various LLNL programs, ensuring that we select those areas for our attention that offer the greatest leverage to LLNL.

Our work is driven principally by the applications of our internal programs, and, to a lesser extent, by external applications. For both of these we must have interdisciplinary teams to deliver complete solutions to the problems. Our recent successes in analytical instrumentation reflect our broad, interdisciplinary base and the cross-fertilization that results from all of the personnel sharing their capabilities and ideas with each other.

The Center for Microtechnology continued to grow in FY-97. The more than 60 people working in this thrust area have training as shown in the following figure:

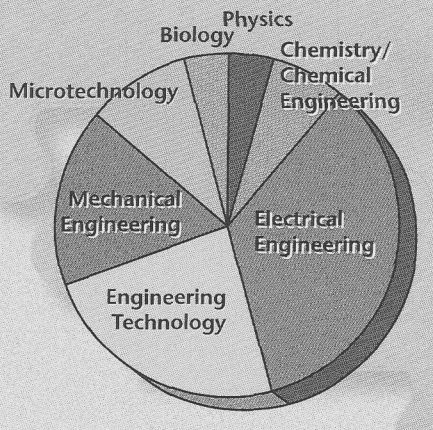

We continue to show a very high rate of return on investment. Over the last year, with a total budget of over $13M, including approximately $0.5M of technology-base projects, we have successfully performed collaborations with industry. We have had one instrumentation project for performing automated, multi-chamber, real-time polymerase chain reaction for DNA amplification funded by the Defense Intelligence Agency. One microtechnology project in collaboration with University of California, Santa Barbara (UCSB) researchers successfully produced the first GaN laser in the United States.

In the fall of 1996, we took our flow cytometer (invented under Engineering TechBase funds) to the Joint Field Trials (JFT) in Dugway, UT, for the open competition and scored the best performance ever recorded there for detection of the Anthrax simulant (Bacillus globigii).

Overall, numerous small technology-base investments in microtechnology have paid off this year:

1) outstanding results at JFT III with the LLNL flow cytometer, miniFlo;
2) highest performance hand-held gas chromatograph built;
3) automated PCR system at Dugway PG for the Navy port/airbase ACTD;
4) LLNL electrophoresis system with etched/bonded plates—a future keystone in the Department of Energy's Joint Genome Institute/Human Genome Project in LLNL's Biology and Biotechnology Research Program;
5) $1M DARPA funding for dielectrophoresis technology;
6) $1M CRADA signed using shape-memory-polymer release mechanism in medical applications;
7) $2.2M external funding for optical interconnects in partnership with the Photonics Program;
8) highly visible multi-$M CRADA with Intel Corporation and other semiconductor houses for EUV lithography (the Microtechnology Center is being expanded to accommodate this work); and
9) collaboration with UCSB and the country's first GaN laser.

As the applications for microtechnology grow, we continue to perform the technology-base activities for LLNL and external partners and stay in a leadership position, both nationally and world-wide.

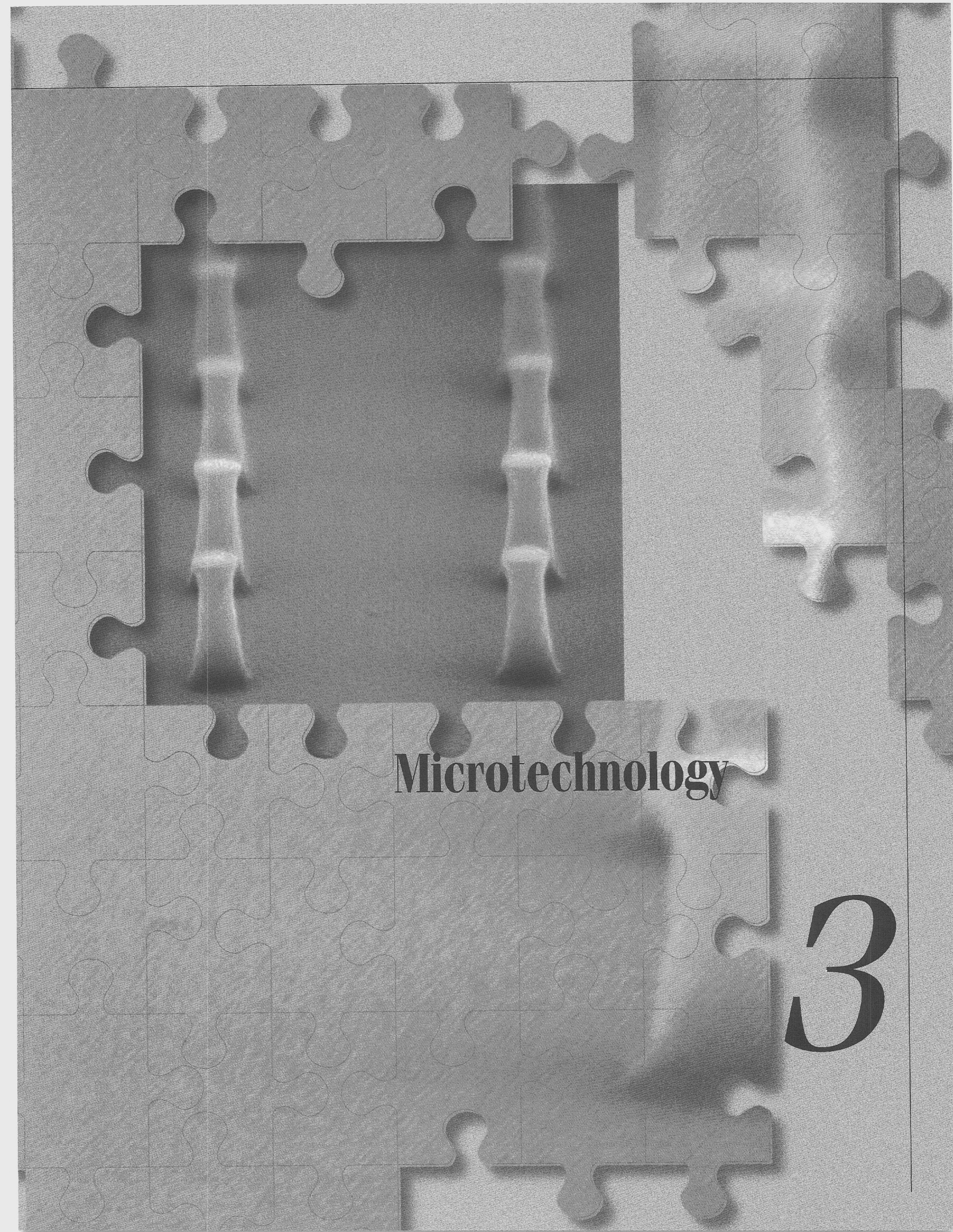

Microtechnology

3

3. Microtechnology

Overview
Raymond P. Mariella, Jr., Thrust Area Leader

Gas and Vapor Preconcentrator
Conrad N. Yu, Jackson C. Koo, and Norman F. Raley 3-1

Compliant Silicon Nitride Cantilever Beams for Atomic Force Microscope Applications
Dino R. Ciarlo 3-3

Sub-Micron Lithography
Dino R. Ciarlo 3-5

Complementary Metal-Oxide Semiconductor Electronics and Micro-Electro-Mechanical Systems
Charles F. McConaghy and Abraham P. Lee 3-7

Monolithic High-Performance Three-Dimensional Coil Inductors for Wireless Communication Applications
Vincent Malba, Darrin J. Young, Jia-Jiunn Ou, Anthony F. Bernhardt, and Bernhard E. Boser 3-11

Vertical-Lasing Semiconductor Optical Amplifiers
Jeffrey D. Walker and Sol P. Dijaili 3-17

Field-Emission Cathode Micro-Electro-Mechanical System Technology for Sensors, Diagnostics, and Microelectronics
Jeffrey D. Morse, Jackson C. Koo, Robert T. Graff, Alan F. Jankowski, and Jeffrey P. Hayes 3-21

Blue Laser Diode Process Development
Glenn A. Meyer, Gregory A. Cooper, Stacy L. Lehew, and Steven DenBaars 3-25

Laser Transceiver for Safeing Applications
Charles F. McConaghy and Karla G. Hagans 3-31

Gas and Vapor Preconcentrator

Conrad N. Yu, Jackson C. Koo, and Norman F. Raley
Engineering Research Division
Electronics Engineering

We have investigated multiple-fine-hole and slot-structures on silicon wafers as gas and vapor preconcentrators for the portable gas chromatograph (GC) application. Our calculation and test results indicated that the surface areas of these structures are too small to be useful. We plan to redesign these devices for the portable GC application.

Introduction

A gas and vapor preconcentrator is commonly used in ordinary GCs to increase their detection capability and sensitivity. For this case, we have to make the preconcentrator not only miniature, but also compatible with the fabrication technique of the portable GC. In short, we need to produce these preconcentrators by micro-electro-mechanical systems (MEMS) technology.

Progress

From our early experiments, we measured several parameters of the portable GC: the gas flow velocity, V, was about 5 cm/s; the sample signal duration, T, about 10 ms; and the diameter, D, of the separation column, 100 μm. From these numbers, we calculate the gas sample size, v, required for the portable GC ($v = \pi VT(D/2)^2$) to be 4 nL. The injection duration in the portable GC is required to be the same as the sample signal duration, 10 ms.

For a sample preconcentrator, sample gas will first have to be adsorbed on its surface. A material with a large surface area is required. Nano-porous silicon has a high specific surface area, about 100 to 600 m^2/cm^3, but is somewhat limited in robustness. We chose to first investigate silicon membrane structures in several different sizes, with multiple fine holes and slots. The specific surface areas of these devices is quite a bit lower, with values ranging from 0.2 to 0.3 m^2/cm^3.

The primary structure first investigated is shown in **Fig. 1**. The total size of the membrane of the devices is 1 mm × 1 mm × 50 μm. The total surfaces, S, are calculated to be from 10 to 15 mm^2.

To calculate or estimate the amount of adsorbed monolayer of gas sample, we used water as an example. The diameter of a water molecule is 2.5 Å; the total adsorbed water volume, v(w), is 37.5×10^{-10} cm^3. Since the surface water density, d, is 1 g/cm^3, there are n = v(w)d/18 = 0.21 nmoles of water. At high temperature, under standard pressure, the steam volume becomes 4.67 nL.

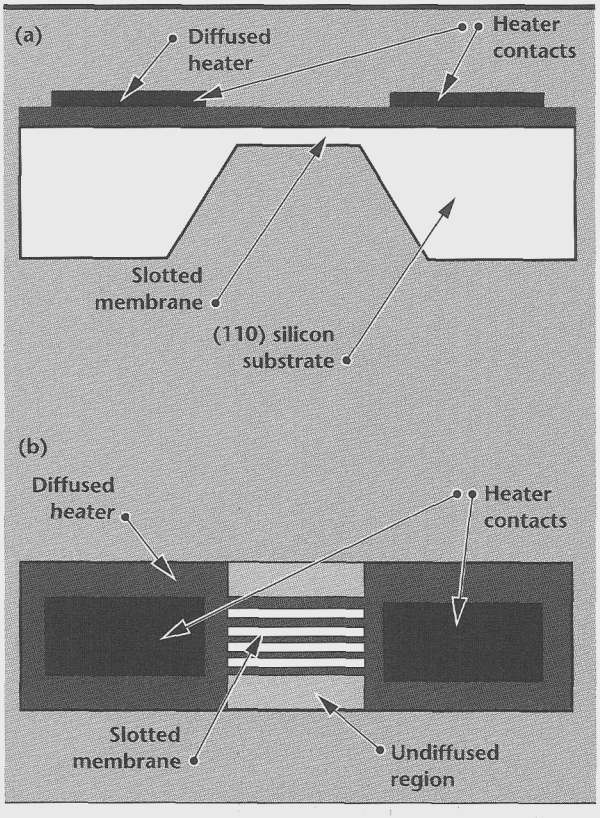

Figure 1. Schematic illustration of two silicon membrane structures: (a) with holes, and (b) slotted.

The top surfaces of these silicon membranes are phosphorous-doped to achieve a diffused heater with a surface resistance of 18.6 Ω per square. Two metal electrodes are placed on each side of the same top surfaces of the membranes. Resistances of these devices are measured, with values typically more than 70 Ω. To evaporate the amount of adsorbed material within 10 ms, we have to increase the device temperature within this duration above the evaporation temperature, in general, around 100 °C.

To ensure the localization of the heating, we fabricated these devices again by placing the electrodes on the opposite sides of the silicon membranes. Their resistances were measured to be somewhat less than 50 Ω. The weight of the silicon membrane is calculated to be 110 μg; its heat capacity is 0.7 J/g K. Because of the small amount of adsorbed sample molecules, and because of the good insulation characteristics of air without convection, heat loss due to adsorbed molecules and the surrounding air can certainly be neglected. Due to the small cross-sectional area and the short duration, we also neglect the heat conducting out of the membrane region in our calculation of heating power. The heating power required can then be shown to be 0.8 W.

To ensure rapid temperature rise, we applied a 12-V power supply directly onto these devices. The heating power was about 4 W. The temperature of the device increased quite rapidly. Direct temperature measurement, however, is quite difficult, due to the small membrane size. For the adsorbed gas samples, we expected to observe the evaporating steam from its surface, the effect of expansion of the heated gas in a small volume, or some acoustic effect.

However, in our tests, no visible emission of gas, steam, or acoustic effect was observed, with or without small paper cover. The amount of gas or steam generated seemed to be much smaller than what is calculated.

In practice, because the sample concentrator needs to be in a certain size enclosure, and because the sample gas produced needs to have higher pressure than that in the separation column, to inject the sample gas into the separation column in 10 ms, the volume required in a portable GC should be one or two orders of magnitude more than what is calculated. In other words, the steam volume due to the monolayer-adsorbed water molecules is too small for the portable GC application.

In summary, we have designed and fabricated silicon membrane structures with various holes and slots. Our calculation and test results showed that the gas volumes generated from monolayer adsorption are too small to be useful. We have to redesign these devices for the GC application.

Future Work

From the above experimental results, we think the basic approach of the preconcentrator is sound, but the total available surface area may need to be adjusted. We also need to consider and develop the preconcentrator concurrently with an injector or a sniffer. They may have to be considered and designed together as a unit. There may also be other materials and coatings to be considered in future fabrication.

Compliant Silicon Nitride Cantilever Beams for Atomic Force Microscope Applications

Dino R. Ciarlo
Engineering Research Division
Electronics Engineering

Silicon nitride cantilever beams were fabricated for use in Atomic Force Microscopes. Depending on their design, these beams can be more compliant than those commercially available. This gives experimenters another source for these cantilever beams when the force exerted on their sample needs to be kept to an absolute minimum.

Introduction

There is a proliferation of Atomic Force Microscopes (AFMs) at Lawrence Livermore National Laboratory (LLNL). These instruments analyze surfaces or material on surfaces by dragging a sharp stylus across the surface and monitoring the position of this stylus. The monitoring is done optically or with a piezo-resistive sensor.

The instruments can achieve Angstrom-level vertical resolution, and are used extensively in microfabrication, by biologists and by most surface scientists.

Normally, the manufacturer of the AFM offers a variety of styluses, depending on the application. They are usually small cantilever beams made of silicon or silicon nitride, with sharp points on one end. Occasionally an experimenter requires a stylus with a compliance (flexibility) not available from the manufacturer. This proposal describes styluses fabricated from our low-stress silicon nitride process.

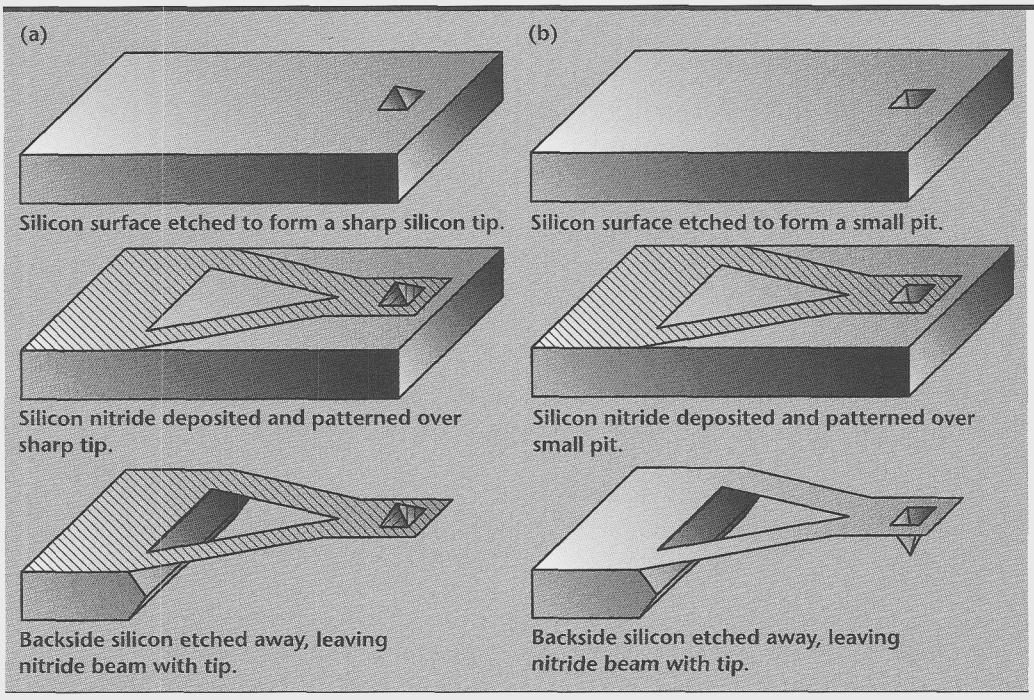

Figure 1. Fabrication sequence for two types of silicon nitride cantilever beams for AFM applications.

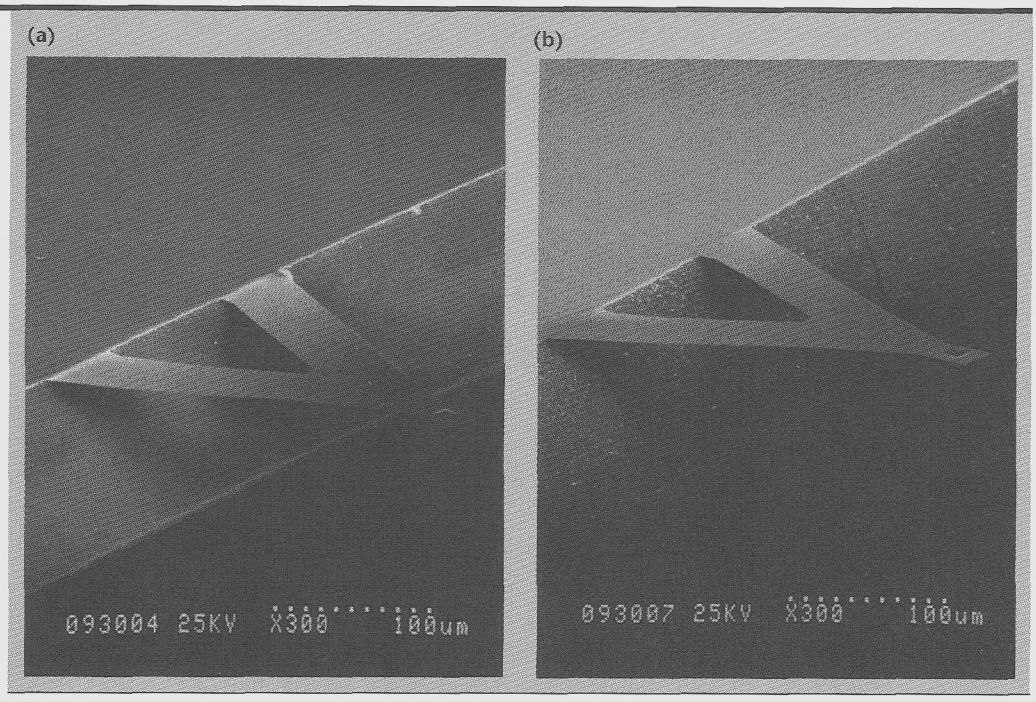

Figure 2. SEMs of silicon nitride cantilever beams, 500 nm thick and 200 µm long. The sharp point on the end of the cantilever extends upward in (a) and downward in (b).

Progress

We fabricated compliant silicon nitride cantilever beams of two designs, as illustrated in **Fig. 1**. Both used 200-µm-thick silicon wafers, with double-sided polished (100) surface orientation, and 50-mm diameter. In the first design, a small, four-sided pyramid was first etched through a small silicon nitride square mask into the surface of the wafer, using an anisotropic wet etch (potassium hydroxide). This pyramid was then covered with a 500-nm-thick film of our low-stress (300 MPa) silicon nitride. The silicon was then etched away from the back of the wafer to release the suspended cantilever beam, 500 nm thick.

In the second design, a sharp silicon point was first formed by etching the silicon surface that had been covered with a small silicon nitride mask. We used an isotropic etch (hydrofluoric-nitric-acetic). This point was then coated with the same low-stress silicon nitride. As before, the silicon was then etched away from the back of the wafer to release the 500-nm-thick cantilever beam.

Figure 2 shows SEMs of the results. Each cantilever is supported by a silicon holder with overall dimensions of 3.5 mm × 1.5 mm. This is close to the part size used by several AFM vendors. On each 50-mm-diameter silicon wafer, we fabricated 90 separate devices, changing the shape of the cantilever in groups of five. The shortest cantilever is 100 µm long, while the longest is 500 µm.

Apparently there is no stress gradient through the thickness of our nitride, because the cantilevers are very straight and flat. Some care had to be taken during the rinse after the etch to prevent the cantilever beams from collapsing from capillary action. Of the two types of cantilevers fabricated, the one shown in **Fig. 2a** is more practical, since the silicon holder does not limit the size of the sample to be measured. For the cantilever shown in **Fig. 2b**, the sample size needs to be comparable to the length of the cantilever beam. There are ways to eliminate this limitation by using wafer-to-wafer silicon bonding.

Future Work

These new cantilever beams should be tested in a real instrument. Since a wide variety of beam lengths and shapes were fabricated, it is likely that an optimum design can be selected. If not, these tests would supply enough information to optimize the design during the next fabrication run.

Sub-Micron Lithography

Dino R. Ciarlo
Engineering Research Division
Electronics Engineering

We continued to investigate the use of phase shift masks to improve the lithography performance of a commercial wafer stepper. Our effort this past year concentrated on the use of double exposure schemes to print small diameter columns in photo-resist, on anti-reflection coatings, and on the installation of the lithography simulation program known as Sample3D from the University of California, Berkeley (UCB).

Introduction

In previous work, we reported on the improvement of the lithography capability of a 1X Ultratech wafer stepper by the use of phase shift masks.[1] Line-widths were printed in positive photo-resist that were 0.2 µm wide, using a system with a specified minimum resolution of 0.7 µm.

Phase-shift masks adjust the phase of the UV radiation going through the mask to take advantage of interference effects. In the type used in this work, the phase of the electric field is shifted by 180° for adjacent sections as the radiation exits the mask. The exposure energy arriving at the wafer plane is proportional to the square of the magnitude of the electric field. Therefore, this exposure energy is positive on both sides of the phase-shift edge, but it has a true zero value at the edge. This leads to a very narrow line of unexposed resist.[1] As in the past, all our experiments were performed at Ultratech Stepper, in San Jose, California, using their SATURN 1X stepper.

Progress

During this past year, we experimented with double exposure schemes to print small diameter posts. The advantage of this scheme is that it allows one to print small diameter posts without having to have small features on the mask. For example, we used a phase-shift mask consisting of parallel lines that were 2 µm wide. The phase-shifts of these lines alternated between 0° and 180°.

If this mask is first printed in one direction at a reduced intensity, and then printed again after being rotated by 90°, the result is an array of small diameter columns located at the intersection of the edges in the two exposures.

An SEM of such an experiment is shown in **Fig. 1**, demonstrating that an array of sub-micron diameter posts can be printed from a mask consisting only of 2-µm-wide lines.

A critical parameter in these experiment is the exposure intensity required. For our experiments we use the JSR 500 positive resist, with a nominal

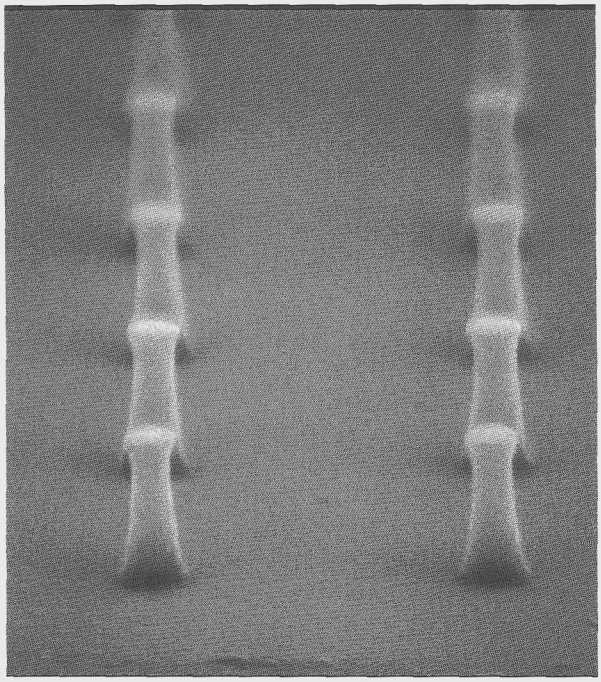

Figure 1. Photo-resist posts, 0.3 µm in diameter, printed using the double exposure of a phase-shift mask. Center-to-center spacing is 2 µm.

thickness of 1 µm. The minimum i-line (365 nm) UV energy required to clear this resist is 100 mJ/cm^2. The two exposures used in **Fig. 1** were both 75 mJ/cm^2.

We also experimented with anti-reflection coatings (ARC). Most of our initial results were obtained on bare silicon wafers coated with photo-resist. A more practical application is to print resist images on a silicon wafer that has been coated with a metal. We used a 60-nm coating of cobalt for our experiments, and found that the smallest feature that could be printed using phase-shift masks, was about 0.8 µm, as compared to 0.2 µm, printed on bare wafers.

This is most likely caused by the change in reflectivity of the cobalt, as compared to the bare silicon. A couple of experiments were tried with a commercial ARC, having a thickness of 200 nm. The results were not very different, meaning that the thickness of the ARC layer, or perhaps the type of ARC layer needs to be changed.

Finally, we successfully installed the UCB lithography simulation program, called Sample3D, on our UNIX work station to help guide and understand our lithography experiments. This is a powerful simulator that allows one to simulate the resist profiles resulting from various exposure tools and different resists. Input to the program consists of the mask design, a description of the exposure tool and the photo-resist parameters. The output is an aerial image of the exposure energy at the wafer plane and a three-dimensional image of the developed photo-resist pattern.

Future Work

Through the combined efforts of The Advanced Microtechnology Program (AMP) in Lawrence Livermore National Laboratory's Laser Directorate and Electronic Engineering Technology Division, a 5X wafer stepper has been purchased, and will be installed in the MicroTechnology Center early in FY-98. Our plans are to apply the advanced lithography techniques we have developed to this new tool.

References

1. Ciarlo, D. R., and D. R. Kania (1996), "Phase-Shift Lithography," *Engineering Research, Development and Technology FY96 Thrust Area Report,* Lawrence Livermore National Laboratory, Livermore, CA, (UCRL 53868-96).

Complementary Metal-Oxide Semiconductor Electronics and Micro-Electro-Mechanical Systems

Charles F. McConaghy and Abraham P. Lee
Engineering Research Division
Electronics Engineering

The goal of this technology-base project at Lawrence Livermore National Laboratory (LLNL) has been to build the infrastructure in electronics support for our micro-electro-mechanical systems (MEMS) activity in the Microtechnology Center. Included in our goal is the ability to fabricate electronics at the chip level, and meld this with the MEMS device. A secondary purpose of this project has been to develop capacitive positioning electronics for use with a MEMS moveable mirror.

Introduction

We generally require electronics to use MEMS devices in real applications. Devices such as the gas chromatograph, the miniature polymerase chain reaction (PCR), or moveable mirrors, all require electronics before they can be put into a functional system. The electronics can be completely external to the MEMS device, but it is desirable to have some functions integrated, or co-located, to reduce parasitic capacitance as well as physical size. Further advantages might be in power saving, ease of fabrication, and more functionality to the end user.

Two Approaches to Integration

One method of incorporating electronics is to have a completely integrated process, an approach used by Analog Devices and Sandia National Laboratories. The completely integrated process has both complementary metal-oxide semiconductor (CMOS) electronics and MEMS devices fabricated on the same chip. Therefore, both electronic processing for devices such as amplifiers and switches, and mechanical processing for devices such as proof masses and comb drives, take place in the fabrication procedure. Because the electronic and mechanical devices reside on the same physical piece of silicon, these processes must be carefully tailored to meet the constraints of both types of devices. Often trade-offs must be made, in the type of electronic or mechanical devices that can be fabricated.

A second approach is to fabricate the electronics and MEMS devices separately, and to bond them together afterwards. The advantage of this approach is that the processing can be optimized for each type of device. For example, sub-μm CMOS can be easily combined with deep-etched MEMS structures. The disadvantage is that the devices then need to be bonded together. Parasitic capacitance might also be slightly higher, because longer interconnects may be needed to mate the two types of devices. However, because of the flexibility and the ability to use outside resources such as the Berkeley Sensor and Actuator Center (BSAC, Berkeley, California), MOSIS (University of Southern California), and the MEMS Technology Application Center (MCNC, North Carolina), this is the approach we have taken to meet our objectives.

Progress

The Micro-Mirror Project

A related project, to fabricate a miniature moveable mirror by MEMS, was chosen as the demonstration MEMS project that would use the CMOS electronics. The MEMS mirror, a 1-mm square piece of polysilicon that moves 1200 nm, in and out of the plane of the silicon substrate, was designed as a replacement for large piezo-driven phase-shifting mirrors. The voltage levels to drive this mirror are less than 10 V. However, the mirror movement is slightly non-linear. When used in one arm of an interferometer, the movement of the mirror causes phase-shifting of the light, which translates to movement of fringes in the interferometer. It is desirable to have the movement of the mirror and the resulting fringes as linear as possible.

Capacitive position sensing

Capacitance is used in many MEMS devices, such as accelerometers and pressure sensors, to determine position or amount of movement. Typically, one plate of the capacitance sensor is formed by the moveable structure, with the other plate formed by the substrate or some fixed structure, such as the anchored part of a comb drive. Therefore, as the moveable part changes position, the capacitance varies inversely with displacement. This assumes a parallel plate approximation for the capacitance, which is a reasonable assumption in the case of our micro-mirror. Actual capacitance values range from femptofarads to a few picofarads.

One of the challenges in capacitive sensing is to separate the sense capacitor signal from the often larger parasitic capacitances of the MEMS structure. For example, the mirror sense capacitance is about 2 pf, whereas the capacitance of the bottom sense plate to the substrate is on the order of 50 pf. Clever circuit topologies that involve keeping the voltage across the parasitic capacitances near zero, minimize the impact of the parasitics.

One circuit that we tried initially used a switched current approach, where a current source was applied to the sense capacitor for a known time, depositing a known amount of charge, which resulted in a voltage proportional to the sense capacitor value. Although this technique worked, it required that voltages on the order of a few volts be present on the capacitor. Voltages greater than 1 V on our large-area sense capacitor caused an electrostatic force which was directly opposite to the force of the comb driver force, and tended to interfere with the movement of the mirror.

A second capacitive-sensing technique, shown in **Fig. 1**, uses a very low-amplitude high-frequency signal (well above the mechanical frequency of the mirror) to sense the change in the capacitance impedance as the position changes. The detector uses synchronous detection to filter out all but the probe signal.

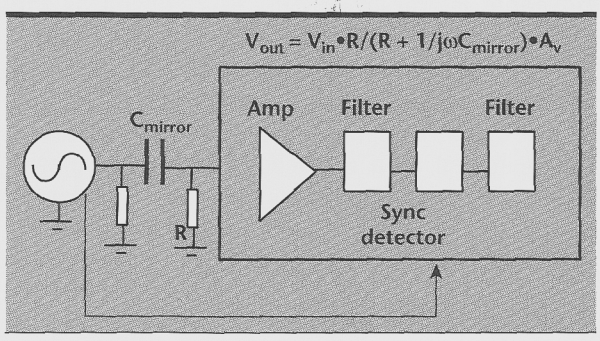

Figure 1. Capacitive sensing circuit using a low-amplitude high-frequency probe signal.

The circuit of **Fig. 1** was first implemented on a 1-in.-×-1-in. surface mount board that contained all the electronics and the MEMS mirror. The electronics system was useful as a diagnostic of the mirror movement. The circuit showed that the mirror had response times of 20 ms and 200 ms for upward and downward movement, respectively. In addition, the sense circuit showed the linearity of mirror movement as a function of drive voltage.

One additional piece of information that the circuit yielded was the starting position of the mirror. The calculated values of capacitance, based on a simple model for two parallel plates separated by 2 μm, did not agree with the measured starting capacitance. This led to optical measurements of the mirror with a Zygo interferometer, which showed that the mirror plate was somewhat bowed from stresses induced by the supporting MEMS springs.

The conclusion was that the amount of bowing was not completely predictable, thus making absolute distance measurements with the capacitance sensor not easily obtainable. However, even with the bow, the mirror movement still follows the inverse relationship with capacitance, thus making the relative position obtainable. Therefore, the capacitance can be used for linearization of movement, since the absolute position is not necessary for this application.

Figure 2 shows the capacitance signal as the micro-mirror is driven over a distance of 1200 nm. In one case the mirror is driven by a linearization look-up table; in the other, by a ramp. There is a 1/d dependence in both cases.

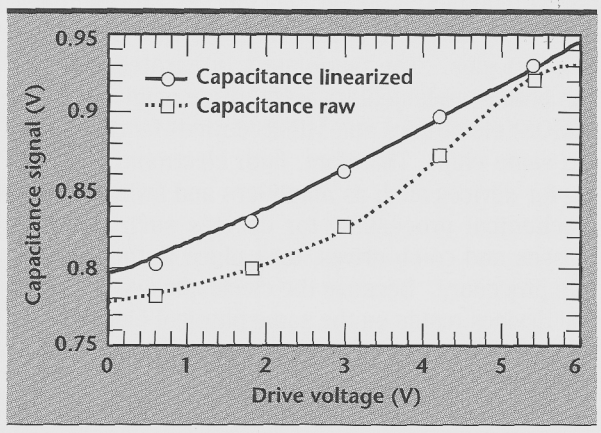

Figure 2. Capacitance signal as the micro-mirror is driven over a distance of 1200 nm.

MOSIS CMOS Chip

MOSIS is an electronic chip foundry that has specialized CMOS processes that range from sub-µm to 2-µm gate lengths. The advantage to using such a foundry is that the CMOS process is well-maintained and characterized. The second advantage is price. For small volume, the total fabrication cost for research chips is $600. The prices vary with size and processing requirements, but the cost is kept low by sharing the same silicon wafer with other users from around the country. Third, MOSIS runs on a set schedule, with delivery times as short as two months.

A second generation of the capacitive sensor circuit was implemented at the chip level in CMOS. The CMOS chip, although not entirely identical to the circuit in **Fig. 1**, contained most of the components, including the high-speed amplifiers and detector. The filters are implemented off-chip at this time. The frequency was chosen as 455 kHz, to match readily available filters. Many operational amplifier designs have very little gain at this frequency. The amplifier design was similar to that described by Saether.[1] This particular design was implemented in 2-µm CMOS, and has gain to well beyond 10 MHz.

The goal was to have each amplifier achieve a voltage gain of at least 10 at 455 kHz. Higher gains would then be realized by a cascade of 10× gain blocks. The gain-setting resistors were implemented in polysilicon. Although resistor formation using polysilicon is not highly accurate, the actual process values were within 10% of design values, which was close enough for this application.

The circuit was designed using SPICE for circuit simulation. Actual model parameters for the n- and p-channel transistors were taken from the MOSIS data base of a previous 2-µm analog CMOS run. The actual layout was done using MATLAB on a Macintosh to generate the layouts for the various size transistors.

The MATLAB code generated all layers for each transistor. These layers consist of the n-well, polysilicon, active area, contact holes, two levels of metalization, and vias. The output of the MATLAB code was compatible with the KIC code which was used for layout. KIC is a UNIX code that resides on the LLNL Engineering computer TRINITY, and was used to manually place the MATLAB-generated cells, as well as manually route the on-chip wiring. The KIC output was converted to CIF format and sent electronically to MOSIS. The submission process is highly streamlined and tuned, since MOSIS has been doing this work for a number of years.

Figure 3a shows a picture of the completed chip. This chip had three amplifiers, a synchronous detector, and some test structures. A comparison of simulated and measured gain of the amplifiers is shown in **Fig. 4**. The frequency response is quite close to the prediction. The gain of the two-stage amplifier was supposed to be 40 dB, but was closer to 31 dB, because of some additional resistance in the input structure for the first amplifier. This is now understood and can be easily changed on the next iteration. The closeness of the modeled results gives confidence that more ambitious designs can be handled in the future.

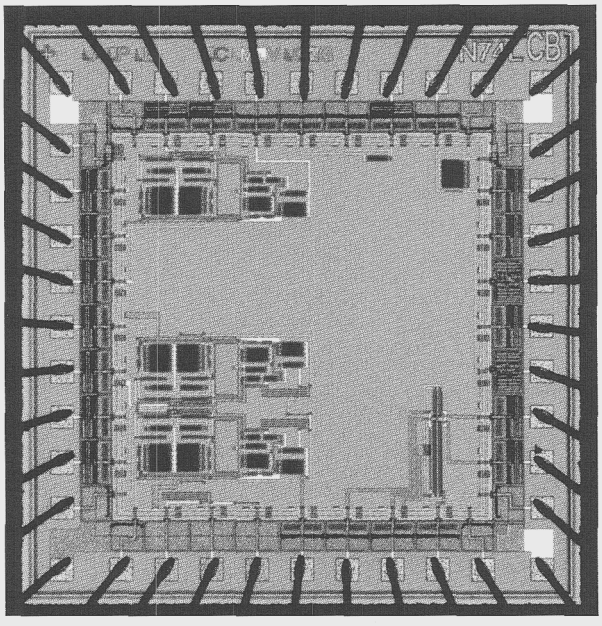

Figure 3. Photograph of MOSIS chip designed to measure capacitance position sensors in MEMS devices.

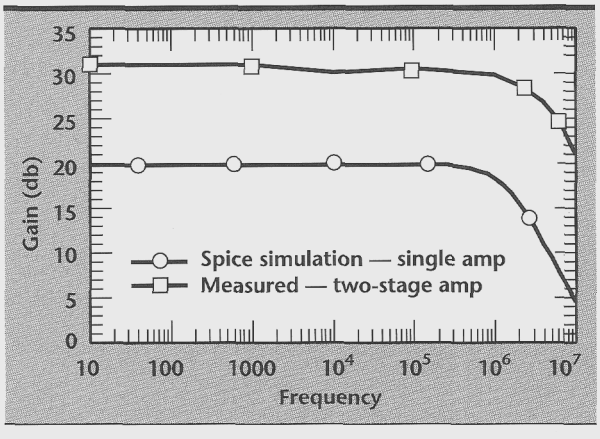

Figure 4. Comparison of measured gain vs frequency for a two-stage amplifier fabricated by MOSIS, with a simulation of the single-stage version. The predicted and measured frequency responses are quite close.

Future Work

At this time the current chips are wire-bonded. It is planned that some flip-chip techniques can be used in the future for mating these with the MEMS devices. It is also planned that other types of chips will be fabricated in the coming year to support new MEMS projects in wireless sensors, as well as existing projects in gas chromatography.

Acknowledgment

We would like to acknowledge D. Hadley for the layout and construction of the surface mount electronics for the capacitive sense electronics.

Reference

1. Saether, T., C. Hung, Z. Qi, M. Ismail, and O. Aaserud (1996), "High Speed, High Linearity CMOS Buffer Amplifier," *IEEE Jour. Solid-State Circuits*, Vol. **31**, (2), Feb., pp. 255–258.

Monolithic High-Performance Three-Dimensional Coil Inductors for Wireless Communication Applications

Vincent Malba
Engineering Research Division
Electronics Engineering

Anthony F. Bernhardt
Physics and Space Technology Directorate

Darrin J. Young, Jia-Jiunn Ou, and Bernhard E. Boser
Department of Electrical Engineering and Computer Sciences
University of California, Berkeley, California

An on-chip 3-D RF coil inductor is proposed as a key component to implement monolithic wireless transceivers. The device achieves a substantially superior performance compared to conventional spiral inductors, and is amenable to monolithic integration in a standard IC process, due to its low thermal budget. Experimental devices fabricated on a standard silicon substrate (10 Ω-cm) achieve a 2.6-nH inductance with a peak quality-factor (Q) of 13 at 900 MHz. The Q-factor is limited by a lossy adhesive used in the fabrication. In a modified process without adhesive in the coil area, a 4.8-nH inductor achieves a peak Q-value of 30 at 1 GHz. High-Q inductors with 8 nH and 13.8 nH have also been fabricated.

Introduction

Increasing demands for wireless communications motivate a growing interest in low-cost, monolithic personal communication transceivers. High-performance RF inductors are the key components for implementing critical building blocks, such as low-noise RF voltage-controlled oscillators (VCOs), low-loss impedance-matching networks, passive filters, and inductive loads for power amplifiers. Critical parameters include inductance value, quality factor (Q), and self-resonant frequency.

Many cellular communication systems, such as AMPS and GSM, operate around 1 GHz and require inductance values on the order of 5 nH, Q of at least 10, and a self-resonant frequency well in excess of the operating frequency. However, such high-performance inductors are not available in current silicon IC technology. Therefore, the integration of these devices has become the key task for realizing monolithic wireless transceivers.

Conventional aluminum spiral inductors fabricated on standard silicon substrates achieve Q-factors around 3 at 1 GHz.[1,2] Two issues contribute to the limited Q-factor: eddy currents in the substrate and metal resistive losses. The first problem can be addressed in part by removing the silicon substrate underneath the inductor, leading to a Q of around 5,[3] or a Q close to 10 at 1 GHz by using copper traces on a sapphire substrate.[4] While improving the Q-value, sapphire substrates are incompatible with standard IC processes.

Progress

In this paper, a new solution, based on a 3-D coil inductor is proposed. The 3-D micro-structure minimizes the device capacitive coupling to the substrate and eddy current loss. Thick copper traces reduce the series resistance, thus ensuring a high Q. Because of the low processing temperature, the inductor can be fabricated on top of wafers with completed electronics without affecting the characteristics of active devices. This is particularly crucial in RF applications, where the availability of the most recent IC technology is a critical competitive advantage.

Monolithic 3-D Coil Inductor

Figure 1 shows the schematic top and cross-sectional views of a 3-D two-turn coil inductor. The device consists of 5-μm-thick copper traces electroplated around an insulating core with a 650-μm × 500-μm cross-section. Compared to spiral inductors, this geometry minimizes the coil area that is in close proximity to the substrate, and hence minimizes the eddy current loss, resulting in a maximized Q-factor and self-resonant frequency of the device.

Copper is selected as the interconnect metal because of its low sheet resistance, critical for achieving a high Q-factor. The skin depth at 1 GHz determines the optimal metal thickness of 5 μm. The 50-μm metal width represents a compromise between the interconnect resistance and capacitance to the substrate. A 50-μm line spacing is used in this conservative design to avoid processing difficulties.

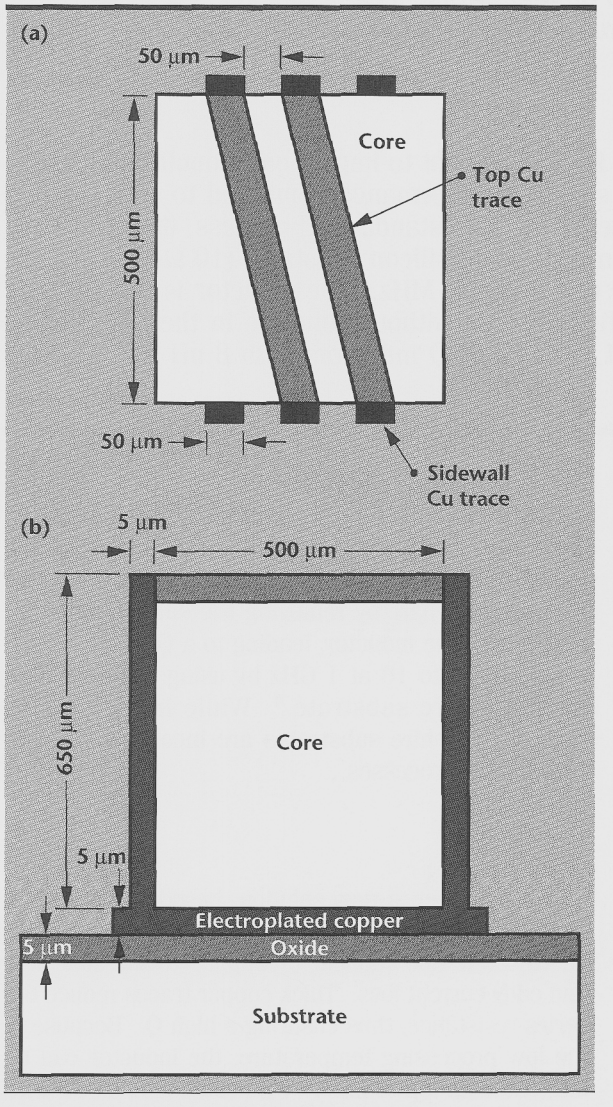

Figure 1. Schematic of 3-D coil inductor, showing (a) top view, and (b) cross-sectional view.

Alumina is used as the core material because of its negligible loss tangent at high frequencies,[5] a key parameter to ensure a high Q-factor. The core width of 500 μm is found experimentally to be the minimum that avoids tilting during attachment to the bottom copper traces. Its height is limited by the thickness of a commercially available alumina sheet.

A typical RF transceiver uses inductances on the order of 5 nH. For the current fabrication, devices with one, two, and four turns are designed to achieve 5 nH, 8.5 nH, and 13.5 nH, respectively.

Fabrication Process

Figure 2 illustrates the process flow. First, the wafers are passivated with 5-μm or 10-μm low-temperature oxide (**Fig. 2a**). Then the bottom traces of the inductors are fabricated. For this purpose, 50-nm titanium and 300-nm copper seed layers are sputtered and covered by an 8-μm-thick electroplated resist. The electroplating method is chosen because it can conformally deposit a thick resist on a complex surface such as an inductor core.

The patterns of the bottom metal traces are transferred photolithographically (**Fig. 2b**). This step is followed by selective electroplating of the 5-μm copper traces. To prevent oxidation, the copper is passivated with two 100-nm layers of electrolytic nickel and gold (**Fig. 2c**). Finally, the photoresist and copper/titanium seed layer are removed with a wet etch, leaving the bottom metal traces of the inductor on the substrate (**Fig. 2d**).

The core of the inductor is formed from an alumina sheet. The sheet is first covered with a 75-μm-thick electrically insulating thermoplastic adhesive film and then diced into 500-μm-wide strips. A 2% width accuracy has been achieved by using a thin diamond grit blade on a commercial dicing saw. The strips are then centered on the bottom copper traces and baked for 30 s at 170 °C to cure the adhesive (**Fig. 2e**).

To fabricate the copper traces on the side and the top of the alumina core, the same process is used as for the bottom traces (**Fig. 2f**). However, the resist is exposed with a 3-D maskless direct-write laser lithography tool.[6] After developing the laser-exposed resist, 5-μm-thick copper traces are electroplated at the sides and on the top of the alumina core. The completed inductor coil is illustrated in **Fig. 2g**.

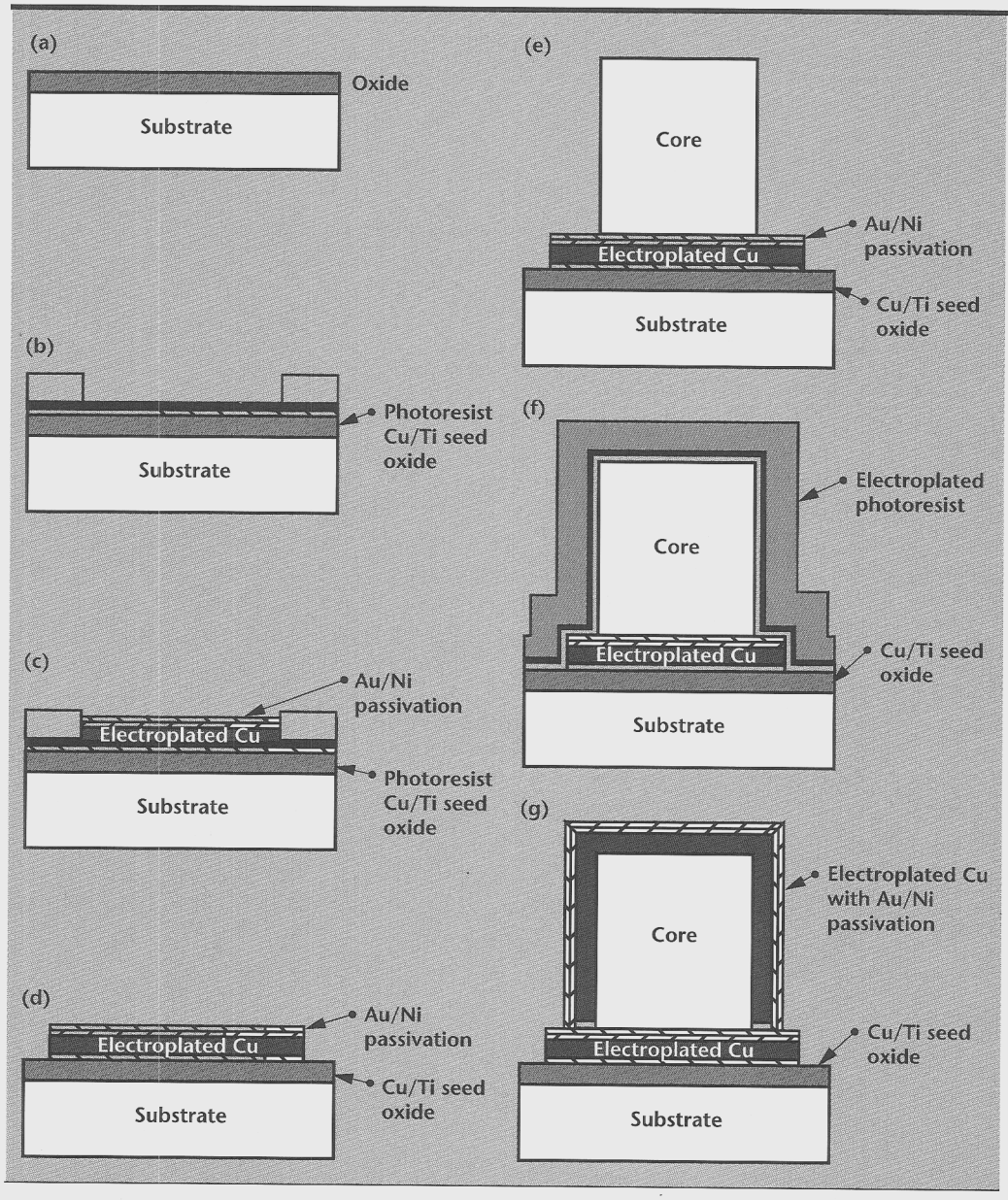

Figure 2. Fabrication process flow.

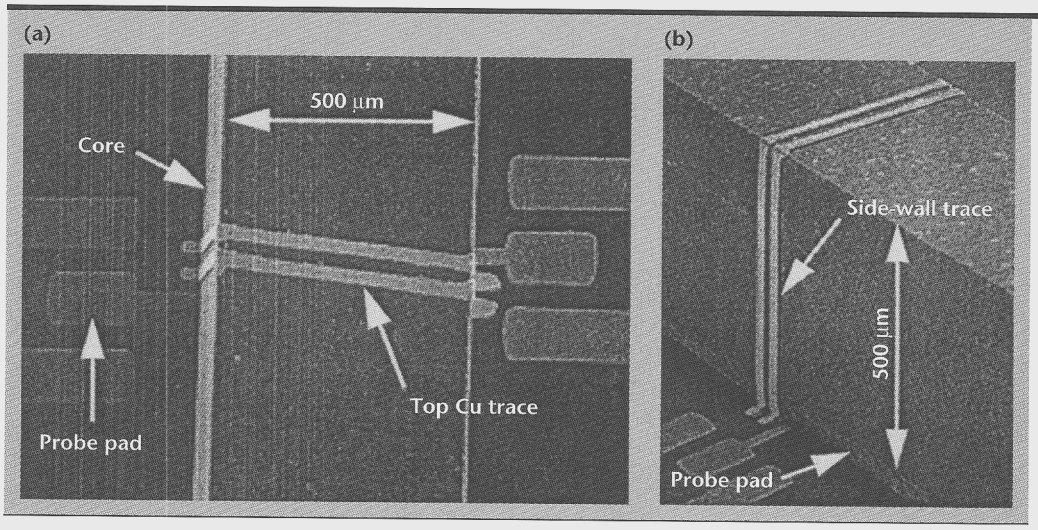

Figure 3. SEM of a two-turn coil inductor, showing (a) top view, and (b) side view.

Experimental Results

Figure 3 shows an SEM of a two-turn inductor on a standard silicon wafer with a 5-μm oxide layer above the substrate. The coil area above the substrate is approximately 250 μm × 500 μm, comparable to that of a typical spiral inductor of the same value.

The two-port S-parameters of the device are obtained with an HP8719 network analyzer. **Figure 4** shows the measured Q and the inductance value as a function of frequency after de-embedding the parasitics from the probe pads. The inductance is 2.6 nH, with a peak Q of 13 around 900 MHz. This Q-value is substantially higher than previous published results; however, the inductance is lower than the simulated value of 8.5 nH. Loss in the adhesive at high frequencies is suspected as the reason. This interpretation would also explain the rapid decrease of Q for frequencies above 1 GHz. A higher inductance (3.9 nH) is measured for inductors fabricated on a high-resistivity silicon substrate (1 kΩ-cm), but no improvement in Q at 1 GHz. Loss in the adhesive is again suspected as the reason.

Inductors recently fabricated with a modified process that does not use an adhesive inside the coil area achieve an improved performance. A two-turn inductor on a high-resistivity silicon substrate achieves 8 nH inductance with a Q of 16 at 900 MHz. These results closely match the simulated values. **Figure 5** presents an SEM of inductors with one and four turns.

Measurement results for these devices are shown in **Figs. 6** and **7**, and demonstrate a record Q of 30 at 1 GHz for a single turn device. The resonant frequencies for the devices are more than 4 GHz, well above the operating frequency of interest.

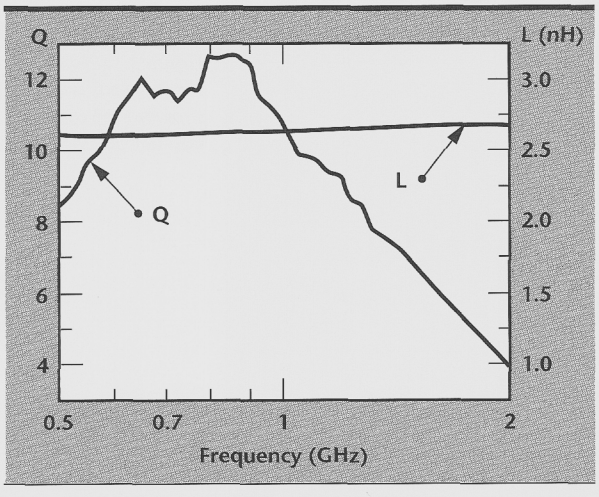

Figure 4. L and Q vs frequency for a two-turn inductor.

Conclusions

Compared to conventional aluminum spiral inductors, the proposed 3-D copper coil inductors achieve a substantially superior performance, with Q-values up to 30 at 1 GHz. These elements are critical for reducing the off-chip component count, lowering power dissipation, and improving the performance of personal RF communication devices such as cellular phones. While initial devices have been fabricated on bare silicon wafers, all fabrication steps are compatible with standard IC technology, thus allowing monolithic integration of active devices with high-Q inductors.

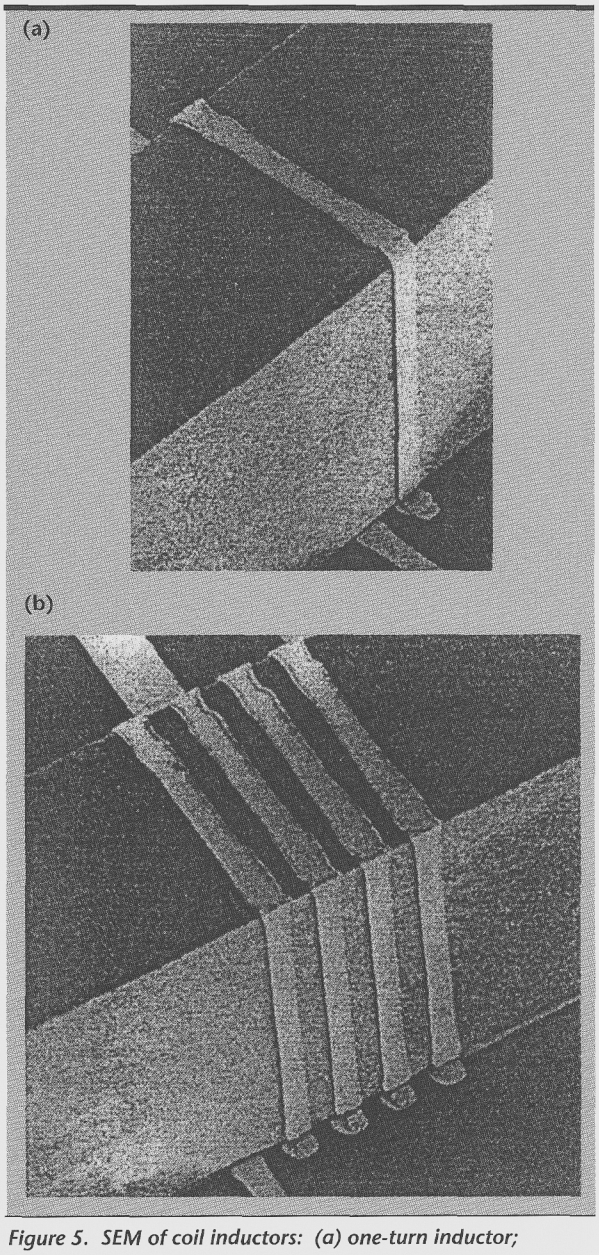

Figure 5. SEM of coil inductors: (a) one-turn inductor; (b) four-turn inductor.

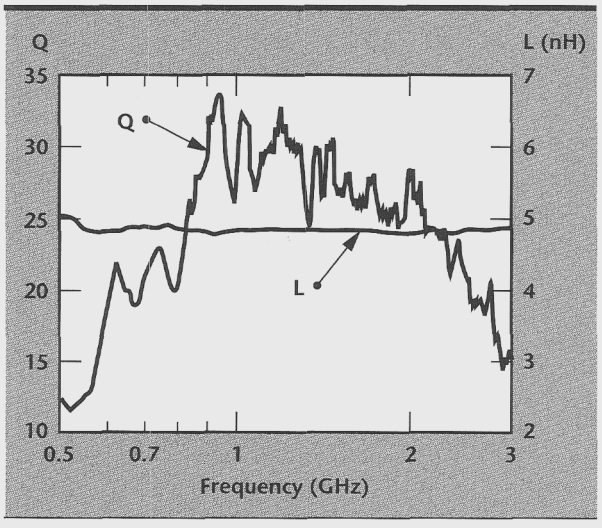

Figure 6. L and Q vs frequency for a one-turn inductor.

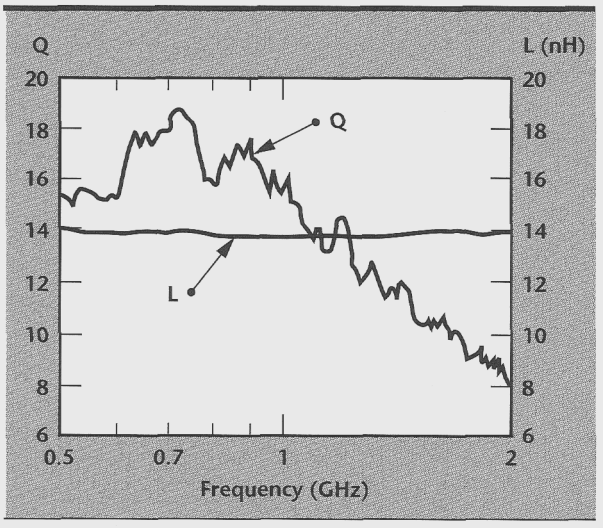

Figure 7. L and Q vs frequency for a four-turn inductor.

Acknowledgment

The authors wish to thank C. Harvey, L. Evans, and R. Graff for helpful suggestions and processing assistance. Certain fabrication steps were carried out in the University of California, Berkeley, Microfabrication Laboratory.

References

1. Nguyen, N. M, and R. G. Meyer (1990), "Si IC-compatible inductors and LC passive filters," *IEEE Journal of Solid-State Circuits,* August, Vol. **25**, (4), pp. 1028–1031.

2. Burghartz, J. N., M. Soyuer, and K. A. Jenkins (1996), "Microwave inductors and capacitors in standard multilevel interconnect silicon technology," *IEEE Transactions on Microwave Theory and Techniques,* January, Vol. **44**, (1), pp. 100–104.

3. Chang, J. Y-C., A. A. Abidi, and M. Gaitan (1993), "Large suspended inductors on silicon and their use in a 2-μm CMOS RF amplifier," *IEEE Transactions on Electron Device Letters,* May, Vol. **14**, (5), pp. 246–248.

4. Burghartz, J. N., B. C. Edelstein, K. A. Jenkens, and C. Jahnes (1996), "Monolithic spiral inductors fabricated using a VLSI Cu-damascene interconnect technology and low-loss substrate," *IEDM Tech. Dig.,* pp. 96–99.

5. Nakayama, A., and K. Shimizu (1994), "An improved reflection wave method for measurement of complex permittivity at 100 MHz - 1 GHz," *IECE Transactions Electron,* April, Vol. **E77-C**, (4), pp. 633–638.

6. Malba, V., V. Liberman, and A. F. Bernhardt (1997), "Fabrication of a DRAM cube using a novel laser patterned 3-D interconnect process," *Proceedings of the International Conference on Multichip Modules,* April, pp. 160–165.

Vertical-Lasing Semiconductor Optical Amplifiers

Jeffrey D. Walker and Sol P. DiJaili
Engineering Research Division
Electronics Engineering

We have established the design, growth, and fabrication of the first vertical-cavity laser diodes developed at Lawrence Livermore National Laboratory (LLNL). These lasers, the first single-mode vertical-lasing amplifiers ever built, were used to demonstrate gain-clamped vertical-lasing semiconductor optical amplifiers that operated at a wavelength of 0.85 μm. They have a chip gain of 17 dB, and a threshold current of 100 mA, which is a factor of four lower than previously demonstrated devices.

Introduction

Optical amplifiers are used to make up for propagation and splitting losses in fiber-optic networks. They can provide an optical gain on the order of 30 dB; in other words, they can boost the intensity of light traveling through them one thousand times.

There are two basic types of optical amplifiers, the erbium-doped fiber amplifier (EDFA), and the semiconductor optical amplifier (SOA). The SOA has many potential advantages over the EDFA, including size, cost, power, speed, and wavelength agility. However, the EDFA is now used in commercial systems because of problems that have existed with current SOA technology. The fundamental problem that has prevented the use of SOAs in commercial applications is cross-talk, which arises from gain variations in the amplifier and causes distortion of signals as they travel through the device.

The purpose of this project was to establish the usefulness of an LLNL-patented technology that solves the cross-talk problem in SOAs. The solution is to use a vertical-lasing field to clamp the gain in the SOA, and thereby eliminate the cross-talk problem. Previous proof-of-principle demonstrations of this vertical-lasing SOA (VLSOA) device showed the basic effect of cross-talk reduction in this structure.[1] However, the previous work had several deficiencies, including high operating current, a multi-mode SOA waveguide, and operation at the wrong wavelength for commercial applications. This report demonstrates the first low-operating-current, single-mode, 0.85-μm wavelength VLSOAs.

Progress

A sketch of the VLSOA is shown in **Fig. 1**. It is basically a long and narrow vertical-cavity surface-emitting laser (VCSEL) that lases vertically and amplifies laterally. VCSELs are a relatively new type of laser diode that emit light vertically out of the top of the semiconductor wafer, as compared to conventional laser diodes that emit light laterally out of the side of the wafer. Compared to conventional edge-emitting laser diodes, VCSELs are extremely complex and high-precision devices that are difficult to fabricate.

In the first phase of this project, we demonstrated the first VCSELs that were designed, grown and fabricated at LLNL. These VCSELs were designed to operate at a wavelength of 0.85 μm, and they are similar to those found in the literature,[2] except that the cavity region is expanded, and a graded index section is inserted to provide vertical

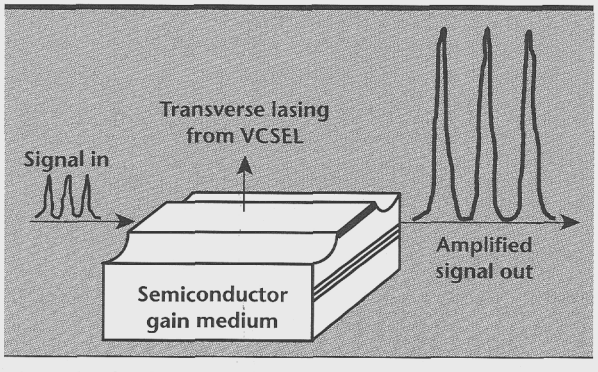

Figure 1. Sketch of VLSOA.

waveguiding for the SOA mode. The lasing threshold current for a 5-μm-×-200-μm device was 100 mA.

Once we established the capability to fabricate VCSELs, we were able to apply this technology toward development of a VLSOA. In this second generation VLSOA, we were able to demonstrate a single-mode device by adding single-mode vertical and lateral index confinement for the SOA mode. In the vertical direction, a conventional VCSEL is a poor waveguide because the average refractive index of the mirror is greater than that of the optical cavity. For this reason, the light traveling in the SOA would be expected to leak out of the cavity region and into the mirror cladding.

In the present structures, this problem was solved by extending the VCSEL cavity region to be a number of wavelengths thick, and adding a graded-index waveguide region around the quantum wells. In the lateral direction, waveguiding was achieved by reducing the waveguide width from 20 μm in the first generation devices down to 5 μm, and by maintaining a lateral index step on the order of 0.1%. Reduction in the width of the structure had the additional advantage of greatly reducing the threshold current of this second generation device.

To facilitate measurement, the gain of the VLSOA devices was determined by measuring the amplified spontaneous emission (ASE) power as a function of current.[3] **Figure 2** shows the gain vs current plot for a 200-μm-long second generation VLSOA structure. The data is collected with the device active side up, and without heat sinking. Because of the lack of adequate heat sinking, the device was operated pulsed, with a 1% duty cycle. Using this measurement technique, the gain shows the effects of clamping above 100 mA injection current. While the gain is not completely flat in the clamped region, this data differs greatly from that of a conventional SOA, for which the ASE power would be expected to continue to increase rapidly to a saturation point of typically 30 dB gain. The reason the gain is not completely flat is attributed either to unclamped regions along the waveguide where the VCSEL is not lasing, or to collection of stray ASE light generated outside of the SOA waveguide. From **Fig. 2**, the clamped chip gain of the VLSOA is about 17 dB. The threshold current for the gain clamping of 100 mA is four times lower than that of the first generation devices that have thresholds of 400 mA, for devices with similar chip gain.[1]

The VLSOA devices were fabricated with windows in the top VCSEL mirror to allow the observation of the VCSEL light during operation. **Figure 3** shows the overlapping VCSEL and SOA optical spectrum for the VLSOA of **Fig. 2**. This plot was generated by collecting the ASE light emitted from the SOA waveguide with a multi-mode fiber, and simultaneously collecting VCSEL light emitted vertically out of the top of the device with a second fiber. The two fibers were then combined with a fiber coupler and the data was observed using a Hewlett Packard optical spectrum analyzer. The data in **Fig. 3** was collected at 120 mA current injection in the gain-clamped region of operation. The reason the VCSEL spectrum does not go off-scale is that only a small fraction of the VCSEL power was collected.

The combined VCSEL/SOA spectrum, shown in **Fig. 3**, was used to observe the behavior of the

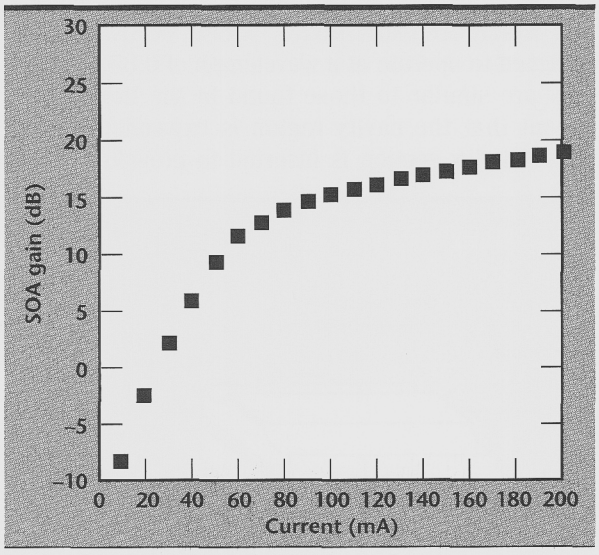

Figure 2. Gain as a function of current for a VLSOA device.

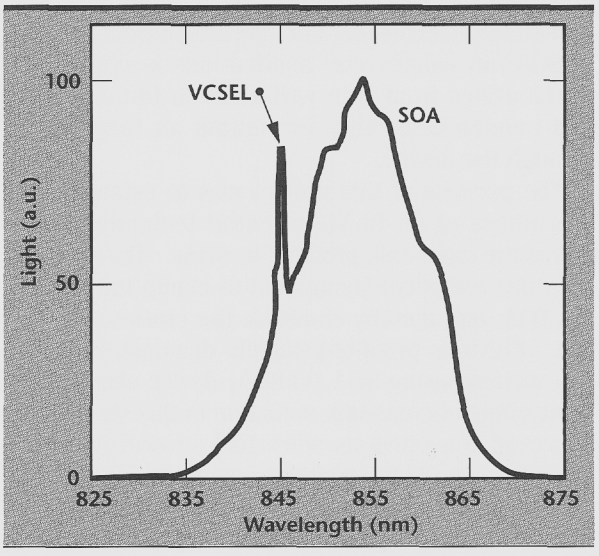

Figure 3. Combined VCSEL/SOA optical spectrum.

VLSOA device. As expected, as the injection current increased, the current at which the VCSEL begins to lase is consistent with the observation of gain clamping of the SOA. **Figure 3** also shows that in these devices, the VCSEL wavelength is blue-shifted from the peak of the gain spectrum. Because the gain medium is homogeneously broadened, the gain is expected to be clamped independent of the VCSEL wavelength. However, in future devices it may be desirable to move the VCSEL wavelength closer to the gain peak to further reduce the threshold current for gain clamping.

In summary, this work represents the first VCSELs fabricated at LLNL, the first single-mode VLSOA, the first 0.85-μm VLSOA, and the first low-threshold-current VLSOA. A gain-clamped amplifier was presented, with a chip gain of 17 dB, and a clamping threshold current of 100 mA. Additional work will be required to extend the operating wavelength to the communications wavelengths, 1.3 and 1.55 μm, and to further refine the design and fabrication of these devices.

Acknowledgments

The authors would like to acknowledge the diligent efforts of W. Goward, H. Petersen, and P. Stephan.

References

1. Walker, J. D., F. G. Patterson, S. P. DiJaili, and R. J. Deri (1996), "A gain-clamped, crosstalk free, vertical cavity lasing semiconductor optical amplifier for WDM applications," *Integrated Photonics Research Conference, Boston, MA*, **IWD1-1**, April 29–May 2.

2. Walker, J. D., D. M. Kuchta, and J. S. Smith (1991), "Vertical-cavity surface-emitting laser diodes fabricated by phase-locked epitaxy," *Appl. Phys. Lett.*, **59**, p. 2079.

3. DiJaili, S. P., J. D. Walker, F. G. Patterson, and R. J. Deri (1996), "Thermally robust optical semiconductor devices using AlGaInAs grown by molecular beam epitaxy," *LLNL Engineering Research, Development and Technology FY96 Thrust Area Report,* Lawrence Livermore National Laboratory, Livermore, CA, (UCRL 53868-96), **3**, pp. 29–33.

Field-Emission Cathode Micro-Electro-Mechanical System Technology for Sensors, Diagnostics, and Microelectronics

Jeffrey D. Morse, Jackson C. Koo, and Robert T. Graff
Electronics Engineering Technologies Division
Electronics Engineering

Alan F. Jankowski and Jeffrey P. Hayes
Materials Science and Technology Division
Chemistry and Materials Sciences

We have investigated field-emission devices for applications in sensors, diagnostics, and microelectronics. Field-emission devices micromachined from silicon and molybdenum have been fabricated and tested. Experimental results have shown that the presence of nitrogen gas molecules for pressures up to 1 mTorr has only a moderate impact on device emission performance, and has no long term effect on device operation. These results demonstrate that field-emission cathodes can potentially be used in sensors applications where gas ionization by electron impact is desirable, or other applications in which the field-emission device is exposed to less than ideal vacuum conditions.

Introduction

A substantial level of interest from Lawrence Livermore National Laboratory (LLNL) programs, government agencies, and the private sector has been generated to use miniature electron sources for a variety of applications, including ion gages, ion cells, cathodes for x-ray sources, and radiation hard microelectronics.

In most cases, a solid-state field-emission cold cathode would replace a thermionic emitter, or filament. Of these applications, several stand out as having significance for LLNL programs and Department of Energy (DOE) directives. These include radiation hard vacuum microelectronics; electron sources for miniature x-ray sources having remarkably small spot sizes for imaging, diagnostics, and instrumentation; field-emission cathodes (FECs) as an electron source for an ion cell in a portable mass spectrometer,[1] and as an ion cell detector for potential use in gas chromatography.[2]

The last application, which is the focus of this report, requires critical understanding of micro-electro-mechanical (MEMs) systems design, along with integration of field-emission devices, to realize a new micro-sensor technology. The advantage is that a low cost, micro-miniature, gas-molecule detector sub-system technology can be realized, with improved sensitivity over existing detectors. Furthermore, this ion cell can be integrated for specific application to gas chromatography systems. This technology would support industrial and environmental programs for the monitoring of toxics, pesticides, and petroleum products. In these applications parts-per-billion sensitivity is required in compact, portable systems.

At present gas-molecule detection schemes consist of several approaches, including helium ionization detection (HID), electron capture detection (ECD), both of which are highly sensitive (many parts per billion), and thermal conductivity detectors (TCD), with sensitivity limited to a few parts per million.

The ECD is more selective, being limited to sample molecules having sufficient electron capture cross-sections, such as pesticides and PCBs. ECDs therefore are useful in environmental monitoring applications. HIDs are more universal in the range of gas sample molecules that can be detected. This system implements a windowless photo-ionization system in which a carrier gas (helium or doped helium) is ionized by pulsed discharge. The UV

radiation then propagates to the detection region where it ionizes the sample gas without exciting the carrier gas. The free electrons are then collected by an electrode with a current peak corresponding to the sample molecule. Presently, these high sensitivity detection systems suffer from the need for a pulse discharge or radioactive source to generate ionizing UV radiation.

Unfortunately, these approaches are neither desirable nor conducive to micro-miniaturization, low cost, and high performance.

Progress

Gated field-emission, cold-cathode electron sources were evaluated as an improved means to generate electrons that could subsequently be used as an ionization source. The concept is illustrated in **Fig. 1**. Field-emission devices are cathode structures that are formed to atomically sharp tips which are in the proximity of an extraction, or gate electrode. By applying a positive voltage to the gate electrode with respect to the cathode, electrons are emitted into the vacuum above the gate, where they are swept away by the anode electric field. The efficiency of the field-emission process depends on the gate-to-tip spacing, the shape of the tip, and the effective work function of the tip material.

The potential advantages of field-emission devices as an electron source are improved efficiency, addressability and control, no heating of surrounding areas, and faster turn-on. Furthermore, field emitters are made using standard microfabrication processes, thus are more conducive to implementation into arrays, specific cathode designs, and integration with other microfabricated components.

These advantages can impact the performance of an ionization source in several ways. First, the FEC is controlled by a gate electrode, therefore is electrically addressable, and uses only a fraction of the power of filaments or pulse discharge electrodes. Field-emission devices can be integrated within the gas microflow system to directly ionize the sample gas, or be used in a manner to generate UV photons by ionizing a carrier gas, such as helium. The UV photons subsequently ionize the sample gas molecules. Thus, field emitters enable more flexibility and lower power usage in the ionization and detection scheme.

An FEC array was designed having an active emission area ranging from 25 μm × 100 μm (800 emitters) to 100 μm × 200 μm (10,000 emitters). **Figure 2** illustrates the fabrication sequence for making a gated FEC device using the Spindt cathode technique.[3–5] Using a proprietary lithographic technique developed at LLNL, gate-to-tip spacings of <0.1 μm have been achieved, as illustrated in **Fig. 3**. Process development consisted of several iterations of this sequence to optimize problems associated with adhesion of thin films, uniformity of emitters, gate hole diameter, pattern transfer, and gate-to-cathode leakage current. While most of these issues have been addressed and resolved, the issue of gate leakage current remains problematic.

A vacuum test station has been assembled to characterize the FECs at pressures on the order of 10^{-7} Torr. The test apparatus includes a fixture on which the FEC is mounted and electrical leads attached. The anode is then positioned to within 0.5 mm of the cathode array to collect any electrons that are emitted. Vacuum testing of these devices has demonstrated field-emission current turn-on with less than 50 V applied to the gate electrode.

As previously mentioned, a limitation of devices fabricated is the excessive gate leakage current

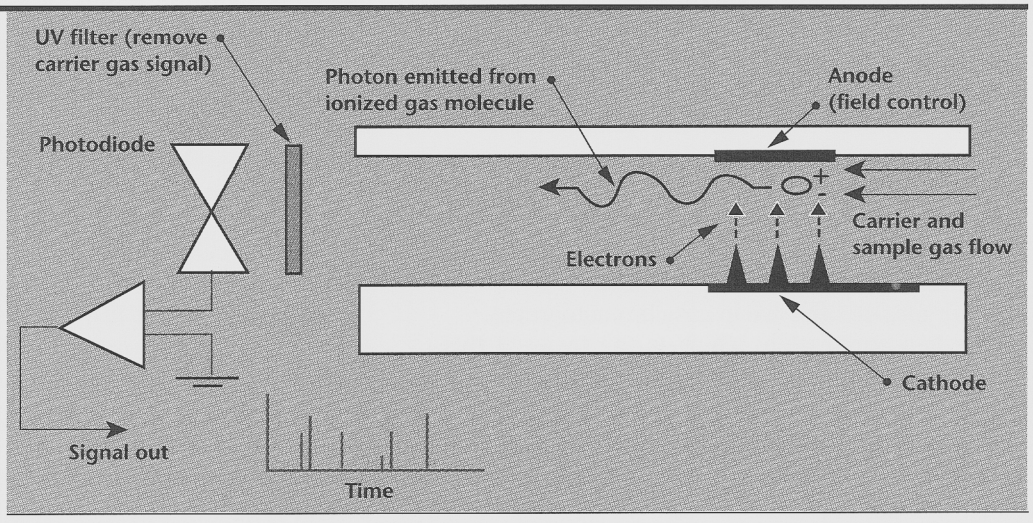

Figure 1. Schematic of ion cell concept with integrated field-emission devices.

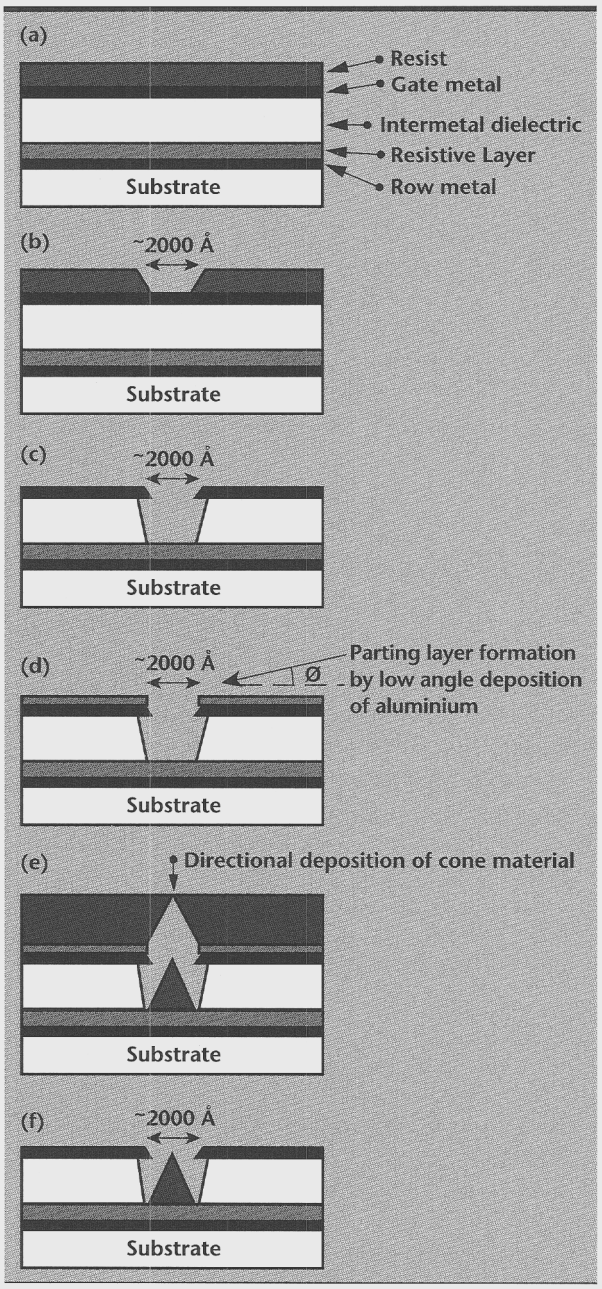

Figure 2. Cross-sectional schematic diagram of field-emission cathode fabrication process sequence: a) initial stack of thin film layer with resist deposited on top; b) patterning of resist by lithographic techniques to form gate structure; c) etching of the gate metal through the mask and the cavity in the intermetal dielectric; d) field-emitter tips formed by depositing a parting layer; and e) directional deposition of the tip material. The final emitter structure (f) is formed after lifting the parting layer from the gate metal.

which is orders of magnitude greater than the emission current, as illustrated in **Fig. 4**. This problem is being addressed, and is likely a result of contamination in the intermetal dielectric, or metal, shorting the tip directly to the gate electrode. Further iterations should resolve this problem. The impact on

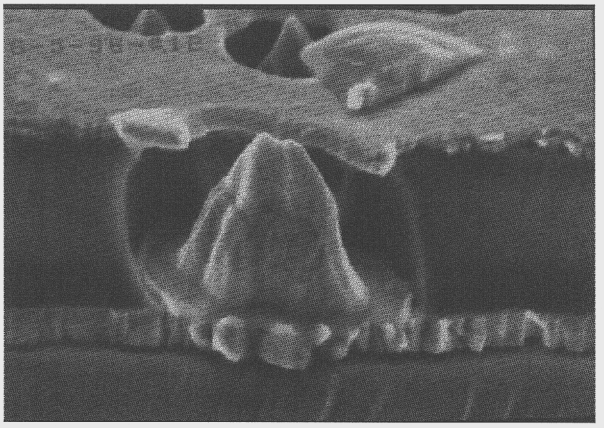

Figure 3. Gated field-emission cathode fabricated using sequence shown in Figure 1. Gate diameter for this device is 2000 Å.

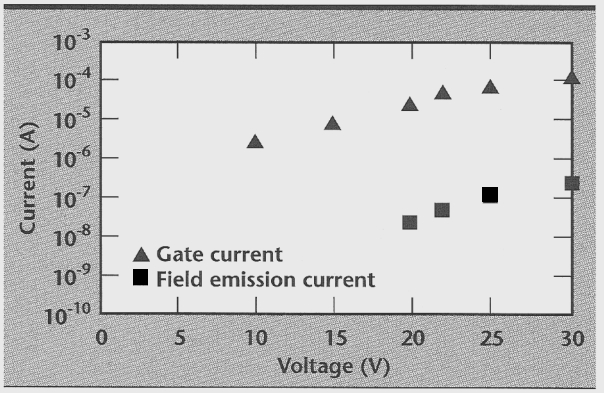

Figure 4. Current/voltage characteristics for field-emission cathode array. Current, measured at anode with 1.5 kV applied, and gate electrode, are illustrated as a function of gate-to-cathode voltage.

device performance is that the FEC will burn out when the gate current reaches some value, on the order of 100 µA, thus limiting the field-emission current to about 50 nA. Other solutions to this problem include an integrated ballast resistor, which in effect will minimize the impact of shorting due to point defects.

Arrays of ungated, silicon field emitters were fabricated and tested. The silicon tips were created by patterning a silicon nitride mask on heavily doped, n-type silicon. The silicon was then isotropically etched, undercutting the nitride mask, until the silicon formed a relatively sharp point. The silicon tip arrays are illustrated in **Fig. 5**.

The silicon field-emitter array was mounted on the test fixture, and positioned in the vacuum test chamber, with an anode spacing of approximately 500 µm above the tips. Field-emission current was then monitored as the anode voltage was increased. These characteristics were monitored as the pressure was increased by introducing nitrogen to the chamber.

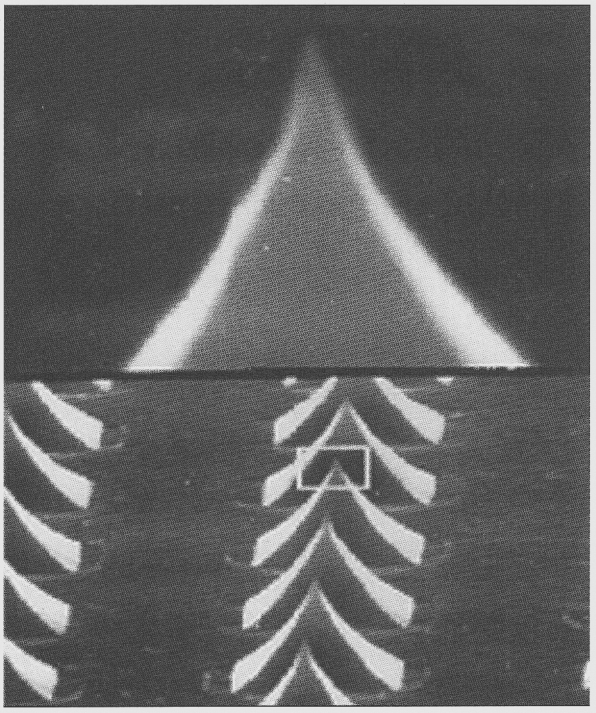

Figure 5. Scanning electron micrograph of silicon field-emission tip arrays.

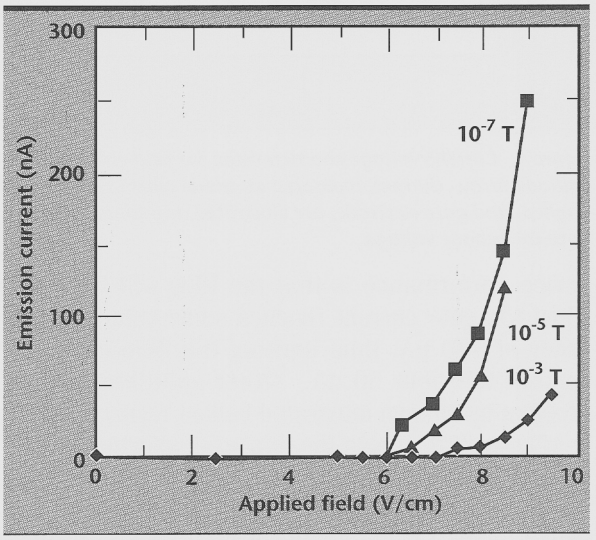

Figure 6. Experimentally measured current/voltage characteristics of silicon field-emitter tip array with varying nitrogen pressure.

The performance of the silicon emitter array at various pressures is illustrated in **Fig. 6**. We observed that the relative field-emission current decreases at higher pressures, likely resulting from increased scattering of the emitted electrons with the gas molecules. Upon further inspection of the silicon tip array after testing, we observed no physical damage to the devices.

Future Work

Ionization sources are finding increased uses for a variety of applications. Efforts to further evaluate the performance of field-emission devices in non-ideal vacuum, and higher gas flow conditions are continuing, to understand the optimal design and performance for this application. Once completely evaluated, field-emission devices can be integrated with microflow components, to realize a MEMS-based micro-analytical instrument for detection and identification of trace chemical species.

References

1. Spindt, C. A. (1992), "Microfabricated field-emission and field-ionization sources," *Surface Science,* North Holland, **266**, pp. 145–154.

2. Snyder, A. P., C. S. Harden, A. H. Brittain, M-G. Kim, N. S. Arnold, and H. L. C. Meuzelaar (1996), "Portable Hand-held Gas Chromatography/Ion Mobility Spectrometry Device," *Analytical Chemistry,* February, Vol. **65**, (3), pp. 299–306.

3. Spindt, C. A., I. Brodie, L. Humphrey, and E. R. Westerberg (1976), "Physical properties of thin-film field-emission cathodes with molybdenum codes," *J. Appl. Phys.*, **47** (12), p. 5248.

4. Spindt, C. A., C. E. Holland, P. R. Schwoebel, and I. Brodie (1996), "Field-Emitter-Array Development for Microwave Applications," *J. Vac. Sci. Technol. B,* **14** (3), p. 1986.

5. Bozler, C. O., C. T. Harris, S. Rabe, D. D. Rathman, and M. A. Hollis (1994), "Arrays of Gated Field-Emitter Cones Having 0.32-μm Tip-To-Tip Spacing," *J. Vac. Sci. Technol. B,* **12** (2), p. 629.

Blue Laser Diode Process Development

Glenn A. Meyer
New Technologies Engineering Division
Mechanical Engineering

Gregory A. Cooper and Stacy L. Lehew
Electronics Engineering Technologies Division
Electronics Engineering

Steven DenBaars
Photonics Group
University of California, Santa Barbara

We have developed a dry etching process for fabricating optical quality laser mirrors with parallel facets on gallium nitride (GaN)-based materials. The process uses a chemically-assisted ion beam etching technique, with a Xe-ion beam and chlorine gas (Cl_2). Laser mirrors dry etched at Lawrence Livermore National Laboratory (LLNL) on an InGaN/GaN laser device grown at the University of California, Santa Barbara (UCSB) recently demonstrated lasing under pulsed power at room temperature, emitting at a wavelength of 419 nm.

Introduction

Semiconductor laser diodes have found widespread use in many commercial applications owing to their small size, high efficiency, low cost, and high reliability. While reliable and efficient semiconductor lasers presently operate in the visible (630 nm) to IR (2000 nm) wavelength range, it has proved to be considerably more challenging to demonstrate useful laser diodes at shorter wavelengths. The ability to produce green, blue, and near-ultraviolet laser diodes would allow full color displays, and would enable very high-density optical memory storage for CD-ROMs.

Currently, lasers that read data in CD players use gallium arsenide (GaAs) diodes which emit red light at a wavelength of 780 nm. The readable data density could be increased by a factor of four if the spot size is reduced using shorter wavelength blue laser diodes, emitting light in the 460 nm wavelength range. High-power laser diodes in this wavelength range would also allow new laser diode-pumped solid-state laser systems to be realized.

The Ti:sapphire laser is a widely used solid state laser because of its wide tuning range, from 670 nm to 1070 nm, and its ability to generate femtosecond pulses. However, the short pump wavelength of this material involves the use of a separate laser to generate the required pump intensity. This is usually done with large Ar-ion lasers, or frequency doubled Nd:YAG or Nd:YLF lasers. A laser diode-pumped tunable Ti:sapphire laser would eliminate the need for a separate pump laser module. Blue laser diodes would also eliminate the need for frequency doubling crystals in certain systems, thus reducing laser system complexity, enhancing reliability and boosting efficiency.

Blue laser diodes could find applications in a host of areas as diverse as information storage, RGB displays, submarine communications, bio-warfare detection systems, materials processing, biotechnology, and laser surgery. They can also be pump sources for new solid state and dye laser systems.

Light emitting diodes (LEDs) are much simpler devices to fabricate than laser diodes. The light emitting structure of the two devices is similar where light is emitted at the junction between n-type and p-type semiconducting materials. In LEDs, the light that is generated at the junction passes through the transparent semiconductor layers and leaves the device. In laser diodes, some of the light is reflected by mirrors back into the light generating

region and is amplified. The mirrors are fabricated out of the semiconductor diode material itself. The intensity of light emitted from a laser diode is much higher than that emitted from an LED.

Several years ago the first blue-green LEDs were produced using ZnCdSe-based materials. Unfortunately, their reliability is intrinsically poor, and it is unlikely that this system will ever produce the requisite commercial/military lifetimes (> 10,000 h of operation).

Alternatively, there has been considerable progress in the AlGaInN material system. AlGaInN exhibits high thermal conductivity and thermal stability, and covers the wavelength range of 250 to 600 nm. The progress has been so compelling that commercial blue GaN LEDs have already replaced blue SiC LEDs, due to their higher brightness and efficiency. It is expected that the conventional yellow/green LEDs may soon be replaced as well.

At UCSB multiple quantum well (MQW) InGaN LEDs have also been fabricated, and emit bright blue to green direct-gap luminescence peak wavelengths of 450 nm and 550 nm. The luminescence peaked at 450 nm and the external quantum efficiency was 4.5% for the MQW structure at 20 mA.[1] High peak power output of 55 mW was measured under a pulsed condition of 1 A, for 3 μs pulse width, which is almost twice as bright as commercially available LEDs from Nichia Chemicals Ltd., Japan.

In 1996, S. Nakamura at Nichia, demonstrated the first current injection InGaN/AlGaN laser diode, emitting at 417 nm.[2] S. Nakamura has now achieved lifetimes of more than 1000 h for an InGaN MQW structure laser diode emitting at 390 to 440 nm, operating CW at room temperature.[3] In 1997 M. Mack, A., and Abare S. DenBaars succeeded in growing, fabricating, and testing a current injection InGaN/GaN laser diode, thus making UCSB the first university to demonstrate a 419-nm blue laser diode at room temperature.[4] The UCSB laser diode consisted of a 10-InGaN-MQW active region grown on c-plane sapphire substrates with uncoated reactive ion etched (RIE) facets.

Under pulsed operation, lifetimes exceeding 6 h have been demonstrated with peak powers as high as 17.6 mW and threshold current densities as low as 12.7 kA/cm^2. To date, only eight research groups in the world have produced blue, current injection GaN laser diodes: Nichia, Fujitsu, Toshiba, Cree, USCB, Sony, Xerox, and HP/Meijo University.

One important step in the manufacture of laser diodes or advanced electro-optic devices is the fabrication of mirrors that provide the optical feedback necessary for lasing. Mirrors for laser applications require vertical, smooth sidewalls. Although high-quality laser mirrors in conventional laser diode material (cubic GaAs) can be fabricated by cleaving on the {100} crystal planes, this method does not work well with the hexagonal crystal structure of GaN. It is thus necessary to develop other methods to fabricate the laser mirrors for GaN.

Dry etching techniques have been perfected at LLNL, and by several other research groups around the world, to produce facets and mirrors on GaAs opto-electronic devices. These processes use an ionized reactant to remove material from the surface of the device by a combination of chemical and/or mechanical processes. The chemically-assisted ion beam etching (CAIBE) technique has become the dominant technique to fabricate facets and mirrors on opto-electronic devices in AlGaAs/GaAs heterostructures.[5,6]

Other researchers using RIE, electron cyclotron resonance discharge, and CAIBE have demonstrated effective etching of GaN. One group[7] achieved GaN etch rates of greater than 50 nm/min by RIE in silicontetrachloride plasmas ($SiCl_4$, 1:1/$SiCl_4$,:Ar, and 1:1/$SiCl_4$:SiF_4) at a bias voltage of 400 V. However, over-cut etching of the sidewall, which resulted in tapered sidewalls, was observed.

CAIBE of GaN using an argon ion beam in hydrogen chloride gas (HCl)[8] and Cl_2[9] shows promise as a method to fabricate laser facets and mirrors. Near-vertical sidewall profiles were achieved on GaN using an Ar-ion beam energy of 500 eV at 0.9 mA/cm^2 under flowing HCl at 10 sccm at 300 °C.[8] Etch rates as high as 210 nm/min have been observed. However, the GaN etch surface following CAIBE in both Cl_2 and HCl at elevated temperatures of 300 °C was roughened and decorated with round "potholes."

At lower temperatures of 20 °C, smoother surfaces were observed with comparable etch rates but the sidewalls were slightly sloped.[9] One group[10] reported similar roughened $In_{0.5}Ga_{0.5}N$ surface morphology following Cl_2 etching using the electron cyclotron resonance (ECR) discharge technique. By adding sulfur hexafluoride (SF_6) or H_2 to the Cl_2 discharge, smoother surface morphologies were obtained. It was suggested[10] that with increasing H_2 or SF_6 concentrations in a Cl_2 discharge, the N atoms are more efficiently removed from the sample surface. Since H_2 is known to passivate dopants in other semiconductor devices,[11] the Cl_2/SF_6 chemistries may have an advantage over H_2/SF_6 chemistries, due to the absence of H_2.

The objective of this project is to develop a dry etching process for the fabrication of optical quality laser mirrors in GaN-based laser diode devices.

This requires parallel (90°) laser mirrors with smooth sidewalls (<50 nm roughness).

Progress

During FY-97 a collaboration between UCSB and LLNL was established for the development of processes necessary to fabricate GaN-based blue laser diodes. Our primary objective was to develop dry etching techniques for the fabrication of laser mirrors on GaN-based materials. Our research focus is on the quality of the dry-etched laser mirror, and not on the etch rate of the GaN. Research at UCSB focused on device design and GaN crystal growth, and provided the necessary materials for the dry etching experiments at LLNL.

As of September 1997, vertical etching of single crystal GaN was demonstrated at LLNL using CAIBE, with a Xe-ion beam and Cl_2 (**Fig. 1**).

Using existing equipment located in LLNL's MicroTechnology Center, we have evaluated CAIBE using the following gases: Cl_2, H_2, SF_6, and carbon tetrafluoride (CF_4). The etcher consists of an 8-in. ion gun from Commonwealth Scientific Corp., Alexandria, VA with a water cooled rotary stage. The reactive gases are introduced via nozzles directed at the sample.

Initial research focused on the patterning technology necessary to define the areas to be etched. This requires straight, smooth, photoresist lines and a masking material that will be resistant to corrosive ions. Due to the optically transparent nature of the GaN, techniques were developed to reduce the negative effects of internal reflections during photoresist exposure. Anti-reflective coatings of tungsten were found to be very effective in reducing internal reflections, resulting in accurate pattern replication. A bottom anti-reflective coating material from Clariant Corporation, Summerville, NJ was found to be effective as well in reducing internal reflections during photoresist exposure.

Most researchers are presently using Ni as a mask for reactive ion etching of GaN. Since nickel is very resistant to reactive gases, the patterning of Ni is typically performed by ion milling or by a photoresist lift-off process. However, the fabrication of a Ni mask with pattern definition required for the laser mirror (straight, smooth mask lines) was found to be extremely difficult under the stringent time constraints of this project. Our limited work on Ni-masking resulted in unsatisfactory line definition with rough sidewalls.

Plasma-resistant photoresist was found to be the best masking material for the laser mirror fabrication process, since it provided the best quality pattern replication with adequate resistance to the reactive gases used in this study. Etch selectivity of the GaN to the photoresist ranged from 4:1 to 2:1 for Xe beam voltages of 500 and 1000 V, respectively.

Gas mixtures of Cl and SF_6, at ratios of 10:1 and 2:1, were found to produce poor quality, rough, sloped (over-cut) sidewalls. No enhancement of etch rate or sidewall smoothness due to the addition of SF_6 to Cl_2 was observed as has been suggested.[10]

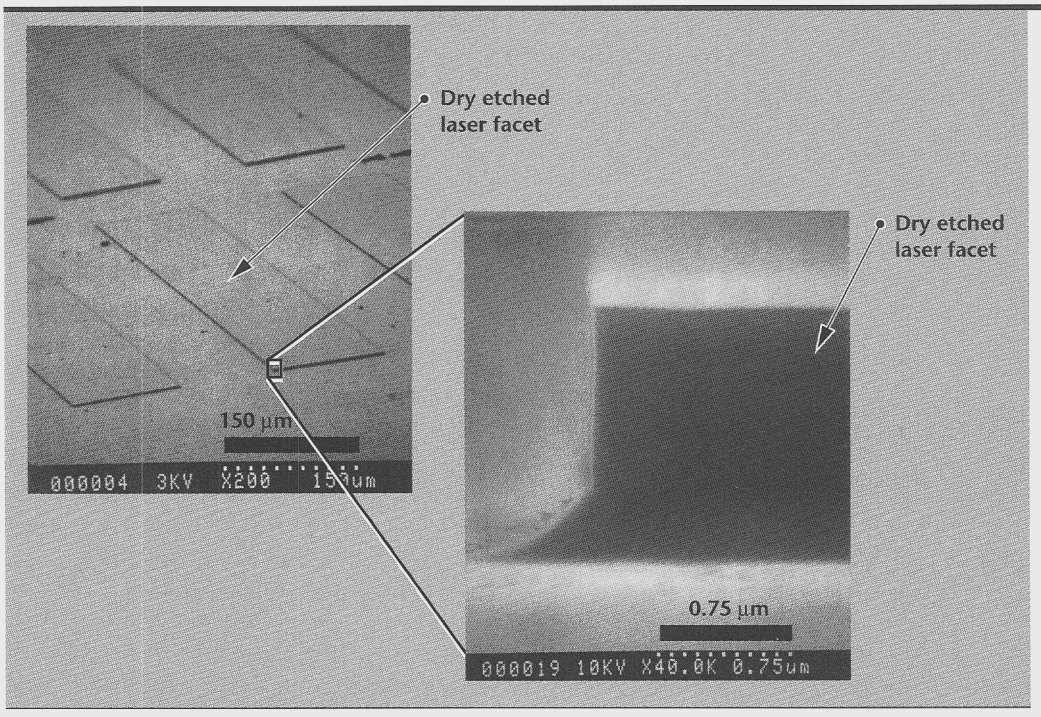

Figure 1. Scanning electron microscope (SEM) images of a GaN etched laser facet formed by chemical assisted ion beam etching (CAIBE) at the LLNL MicroTechnology Center using a 800-eV xenon ion (Xe) beam in a Chlorine (Cl_2) ambient. Note the vertical smooth sidewalls.

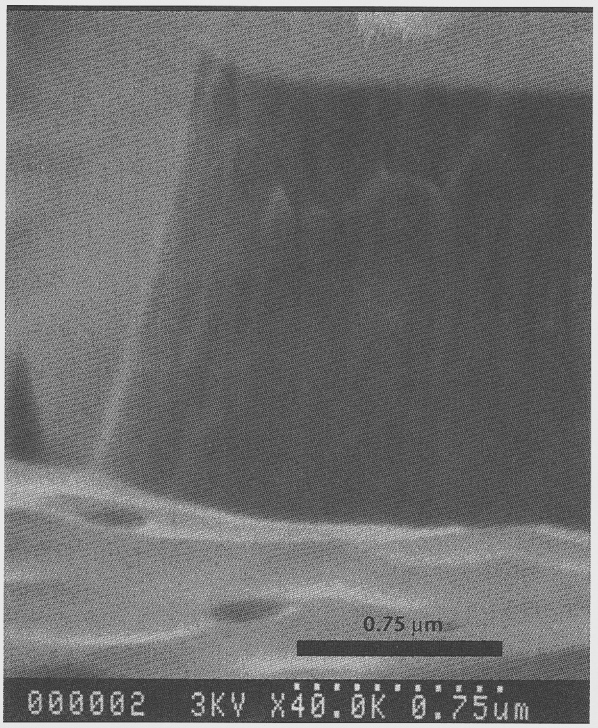

Figure 2. Scanning electron microscope (SEM) image of the corner of a GaN etched laser facet formed by chemical assisted ion beam etching (CAIBE) at the LLNL MicroTechnology Center using a 500-eV xenon ion (Xe) beam in a 10:1 chlorine (Cl_2) carbon tetrafluoride (CF_4) ambient. Note the rough morphology, sloped (over cut) sidewalls.

Cl and CF_4 gas mixtures, at ratios of 10:1 and 2:1, were found to produce rough sloped sidewalls as well (**Fig. 2**).

An enhancement in the sidewall smoothness morphology was observed, however, with the addition of 2% H to Cl. To date, our best quality vertical etching has been achieved by CAIBE using a 800-eV Xe beam in a Cl_2 ambient, achieving vertical walls with smooth sides at etch rates of 900 Å/min (**Fig. 1**). The enhanced sidewall smoothness and vertical etching was achieved by increasing the Xe beam voltage from 500 to 800 eV at beam current densities of 0.2 mA/cm^2 with a Cl_2 flow rate of 20 sccm with stage rotation. Stage rotation is useful in minimizing ion milling etch artifacts which produce sloped walls even at normal beam incidence.

Laser mirrors dry etched at LLNL on an InGaN/GaN laser device grown at UCSB recently demonstrated lasing under pulsed power at room temperatures, emitting at a wavelength of 419 nm. This demonstrates that our dry etch process developed for the fabrication of laser mirrors in GaN works. In addition, the recently developed dry etch process shown in **Fig. 1** should further enhance the efficiency of UCSB InGaN/GaN laser device.

Acknowledgments

The authors wish to thank H. Peterson, W. Goward, and S. Dijaili for technical discussions and assistance in the development of the GaN dry etching process. In addition, special thanks to M. Mack and A. Abare at UCSB for growing the GaN crystals used for the study, and congratulations to them for successfully demonstrating a blue emitting InGaN/GaN laser diode.

References

1. Kozodoy, P., A. Abare, M. Mack, K. Sink, S. Keller, U. Mishra, S. Keller, S. DenBaars, and D. Steigerwald (1997), "MOCVD growth of high output power InGaN MQW LEDs," *Materials Research Society Proceedings, San Francisco, CA*, D8.18.

2. Nakamura, S., M. Senoh, S.-I. Nagahama, N. Iwasa, T. Yamada, T. Matsushita, H. Kiyoku, and Y. Sugimoto (1996), "InGaN multi-quantum-well structure laser diodes grown on MgAl2O4 substrates," *Appl. Phys. Lett.*, **68** (15), pp. 2105–2107.

3. Nakamura, S. (1997), "III-V Nitride-based Blue/Green LEDs and LDs," *24th ISCS, San Diego, CA*, Sept.

4. Mack, M. P., A. Abare, M. Aizcorbe, P. Kozodoy, S. Keller, U. K. Mishra, L. Coldren, S. DenBaars (1997), "Characteristics of Indium-Gallium-Nitride Multiple-Quantum-Well Blue Laser Diodes Grown by MOCVD," *J. Nitride Semicond., MRS Internet,* Res. **2**, p. 41, (http://nsr.mij.mrs.org/2/41/).

5. Goward, W. D., H. E. Petersen, and S. P. Dijaili (1996), *Chemically Assisted Ion Beam Etching (CAIBE) of Precision High Quality Laser Facets on AlGaAs Quantum Well Multilayer Structures*, Lawrence Livermore National Laboratory, Livermore, CA, (UCRL-ID-124399).

6. Scherer, A., J. L. Jewell, Y. H. Lee, J. P. Harbison, and L. T. Florez (1989), "Fabrication of microlasers and microresonator optical switches," *Appl Phys. Lett.*, **55**, p. 2724.

7. Adesida, I., A. Mahajan, E. Andideh, M. Asif Khan, D. T. Olsen, and J. N. Kuznia (1993), "Reactive ion etching of gallium nitride in silicon tetrachloride plasmas," *Appl. Phys. Lett.*, **63** (20), pp. 2777–2779).

8. Ping, A. T., I. Adesida, and M. Asif Khan (1995), "Study of chemically assisted ion beam etching of GaN using HCl gas," *Appl. Phys. Lett.*, **67** (9), pp. 1250–1252).

9. Adesida, I., A. T. Ping, C. Youtsey, T. Dow, M. Asif Kahan, D. T. Olson, and J. N. Kuznia (1994), "Characteristics of chemically assisted ion beam etching of gallium nitride," *Appl. Phys. Lett.*, **65** (7), pp. 889–891).

10. Pearton, S. J., C. R. Abernathy, and F. Ren (1994), "Dry patterning of InGaN and InAlN," *Appl. Phys. Lett.*, **64** (26), pp. 3643–3645.

11. Gendron, F., L. M. Porter, C. Porte, and E. Bringuier (1995), "Hydrogen passivation of donors and acceptors in SiC," *Appl. Phys. Lett.*, **67** (9), pp. 1253–1255).

Laser Transceiver for Safeing Applications

Charles F. McConaghy
Electronics Engineering Technology Division
Electronics Engineering

Karla G. Hagans
Defense Sciences Engineering Division
Electronics Engineering

The purpose of this work has been to construct an electro-optic equivalent to a weapons safeing, arming, and detonation subsystem. The laser transceiver is a very important portion of this subsystem. An additional objective has been to evaluate the use of opto-electronics in weapons safeing applications.

Introduction

In this project, we have focused on replacing or re-inventing some of the safeing and arming functions with opto-electronics. It is believed that opto-electronics provides an extra degree of safety and security. Our design involved a fiber-based link to replace all wires and provide a high degree of electrical isolation, enhancing weapons safety. A schematic drawing of the transceiver and how it fits into the overall system is shown in **Fig. 1**.

The main functions of the transceiver are threefold. First, the transceiver receives optically modulated data via fiber and transforms it to electrical signals, which are then demodulated by electrical logic. Second, the transceiver module takes electrically-modulated data from the logic circuit and modulates it optically onto a fiber. The third function provided by the transceiver block is power generation. The electrical power to run the digital logic, as well as the transmitter and receiver, is provided by optical means. A fiber fed by a high-power laser diode is used to bring power to the transceiver. A special power converter chip converts this optical power to electrical power and acts much like a battery.

Progress

Laser Transceiver Construction

The laser transceiver is composed of elements fabricated in dissimilar technology. For example, the laser diode and power converter are both fabricated in GaAs, while the receiver chip is fabricated in Si. In addition, both GaAs parts, although fabricated in the same type of material, use substantially different processing.

These parts were fabricated by three separate commercial sources and then packaged at Lawrence Livermore National Laboratory (LLNL) into a single compact package. Although it is theoretically possible to integrate the transmitter, receiver, and power converter into one common substrate, this would have required a large research effort, and was well beyond the scope of our work. Therefore, we found it more expeditious to obtain separate, well-optimized parts from different vendors and to combine them with advanced packaging and fiber pigtailing techniques.

A large portion of the packaging is dominated by the fiber pigtails, so not much space-saving would be gained by a single integrated chip, as compared to three separate chips, as was used in this transceiver. The only difficulty with using separate parts is in identifying commercial sources willing to sell these devices in chip form.

Description of Individual Sub-Components

Both light emitting diodes (LEDs) and vertical cavity laser diodes (VCSELs) were tried for the transmitter. Although both worked, the VCSELs coupled much more efficiently to the fiber. The LEDs coupled 2 μW of optical power into the fiber for 15 mA of drive current. In contrast, the VCSELs coupled 200 μW of power into the fiber for 8 mA of drive current. The beam pattern from the VCSELs is quite circular, with a low divergence of about 8°. On the other hand, the LEDs emit light into a hemisphere, making it difficult to collect into a fiber unless a lens is used.

Horizontal fiber pigtailing was chosen to minimize package height, as well as to maximize the strain relief of the fibers. Because the fibers are horizontal, either the chips had to be mounted vertically, or some means of turning the light had to be used if the chips were mounted horizontally. The latter is the method chosen for pigtailing all three devices.

An easy method of turning the light is simply to polish the optical fibers at a 45°-angle and allow the light to bounce off the angled face. It was originally anticipated that the angled surface would have to be metalized to improve reflectivity, but almost all the light reflects off the glass/air interface, since the angle is steep enough for total reflection. The angled fiber technique was used for the fibers that pigtailed the VCSEL and the receiver chip. The only disadvantage to this approach is that the light must propagate through the cylindrical side wall of the fiber, which causes some unintentional lensing of the light.

The receiver chip is a Si device that consists of a sensor integrated with an amplifier and circuitry to generate a digital logic level output. The receiver is very sensitive and can be switched on and off with as little as 2 μW of optical power. This chip, however, does require 5V of supply voltage at a minimum of 10 mA of current drain.

The interconnection to the power source is shown in **Fig. 1**. The current drain of this chip increases proportional to the optical power that is incident on the receiver. Therefore, to minimize drain, the optical power should be only slightly above threshold.

The most unique and challenging device in the laser transceiver module is the power converter. This device acts like a constant current source with the current level set by the optical power of the incident laser light.

Power converters come in different voltage ranges achieved by variations of the series and parallel hook-ups of the array of individual cells. A 6-V device was chosen for our application since it was sufficiently high to meet the voltage requirements of both the receiver and the logic. The active area of the power converter is a 1.5-mm-diameter circle. (A 3.0-mm device was used in a later package.)

The efficiency of the power converter is 40% if the device is well heat-sinked. Current levels in excess of 100 mA at 5 V with 2 W of optical illumination were desired.

It was found experimentally that, to achieve maximum performance with these power converters, optical beam quality and positioning were critical. The maximum current is determined by the cell within the array that has the lowest optical power. Therefore, it is imperative to have all cells illuminated within the same power. One method is to use the Gaussian beam that comes out the end of a cleaved fiber. The fiber end has to be back far enough to illuminate the entire cell, but not so far back that it overfills the array. If the fiber is too close to the array, current limits may result from saturation of the power converters.

The saturation problem is handled by spreading the power over a larger area (3.0 mm, vs 1.5 mm). The 45°-fibers were found to be inadequate for giving the uniformity of illumination required by these power converters. A better method to turn the light involved the use of specially fabricated Si turning mirrors. These mirrors were anisotropically etched in Si and Au-coated. An equally effective scheme involved the use of miniature prisms attached to the end of the fiber with UV-cured epoxy. Both of these schemes gave good beam patterns on the power converters.

A 28-pin leadless chip carrier was chosen to mount all three components. This package, designed to mount electronic chips, is a .450-in.-square package that is only .060 in. tall. It is

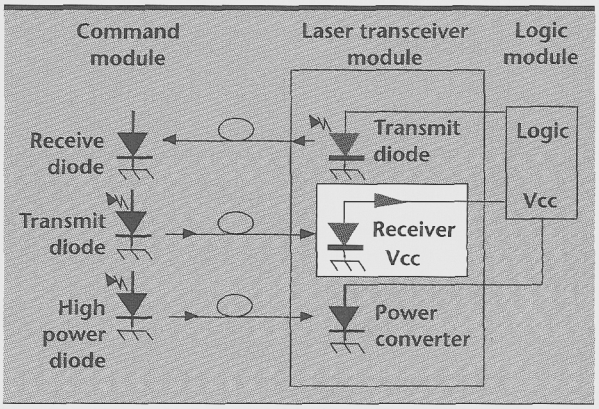

Figure 1. Laser transceiver module consisting of a transmit laser diode, receiver chip, and power converter chip.

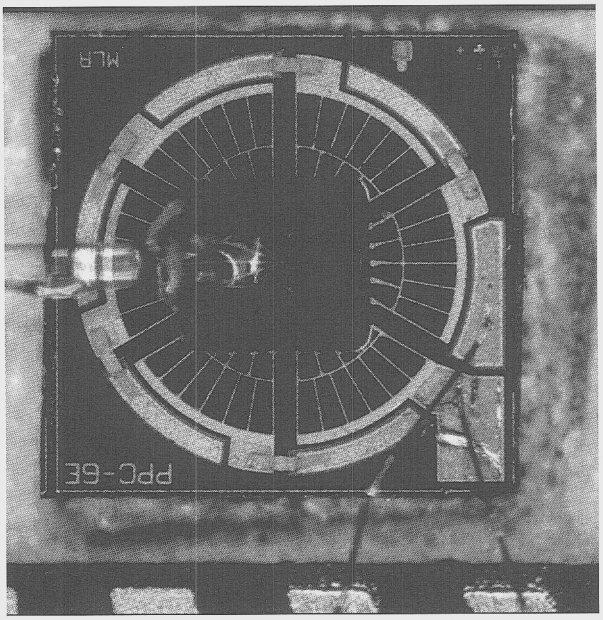

Figure 2. Power converter illuminated by fiber, with prism turning arrangement.

compatible with surface mounting, so it can be mounted easily on the same board as the logic. To mount optical fibers to this package, some modifications were made by precision sawing. These saw cuts allowed the fibers to protrude from the side of the package. Additional saw cuts were used to mount light shields between each of the sections of the package. **Figure 2** shows one of the power converters with a fiber pigtail attached by means of the miniature prism.

One of the main difficulties in achieving the full-current output of the power converter was getting the correct spacing between the prism and the power converter chip. For the 1.5-mm power converter, the maximum power was achieved with the prism spaced 2.5 mm away. This spacing required that the top of the package be modified to accommodate the extra space needed to illuminate the power converter. A completely packaged laser transceiver module is shown in **Fig. 3**.

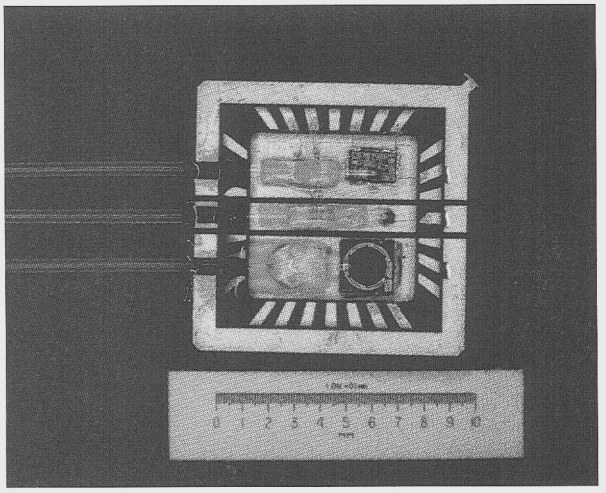

Figure 3. Completely packaged laser transceiver (less top and light shields). The receiver is at the top of the package, the VCSEL in the middle, and the power converter at the bottom. Three optical fibers exit the left side of the package.

Future Work

The main issue in this work was achieving the 100+ mA of current from the power converter. Future work will concentrate on new logic designs that require less current. The high-current power converters take more space, and the goal is to minimize the space of this module. Other improvements in the future would be to add optical switches to minimize the possibility of inadvertently powering the power converter.

Acknowledgments

The authors would like to thank G. Jacobson for help with all aspects of the project, from procuring parts to testing modules. We would also like to thank P. Stephan for his precision in mounting and bonding the individual components. Finally, we would like to thank R. Becker of Integrated Optical Circuit Consultants for his help in design and assembly of the modules.

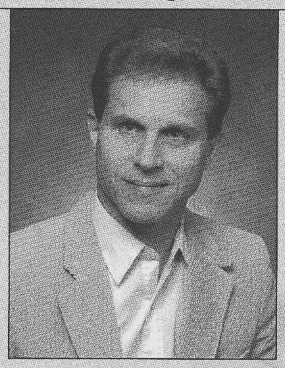

Kenneth L. Blaedel, Thrust Area Leader

The mission of the Manufacturing Technology thrust area at Lawrence Livermore National Laboratory (LLNL) has been to have an adequate base of manufacturing technology, not necessarily resident at LLNL, to conduct our future business.

Our specific goals were (1) to develop an understanding of fundamental fabrication processes; (2) to construct general purpose process models that have wide applicability; (3) to document our findings and models in journals; (4) to transfer technology to LLNL programs, industry, and colleagues; and (5) to develop continuing relationships with the industrial and academic communities to advance our collective understanding of fabrication processes.

In support of this mission, two projects are reported here, each of which explores a way to bring higher precision to the manufacturing challenges that we face over the next few years. The first, "A Spatial-Frequency-Domain Approach to Designing a Precision Machine Tools," is an overall view of how we design machine tools and instruments to make or measure workpieces that are specified in terms of the spatial frequency content of the residual errors of the workpiece surface. This represents an improvement of an "error budget," a design tool that saw significant development in the early 1980's, and has been in active use since then. The second project, "Micro-Drilling of ICF Capsules," is an attempt to define the current state in commercial industry for drilling small holes, particularly laser-drilling. The report concludes that 1-μm-diameter holes cannot currently be drilled to high aspect ratios, and then defines the engineering challenges that will have to be overcome to machine holes small enough for NIF capsules.

Looking to the future, the Engineering Directorate is implementing a new technology plan, which calls for transitioning the thrust areas into centers. One such center will be in precision engineering and will serve to further focus our manufacturing efforts on precision, as well as to merge the different projects into a more comprehensive and cohesive effort. The Precision Engineering Center will play a more active role in directly enabling the success of LLNL programs, and will bring focus to Engineering's investment in technology development.

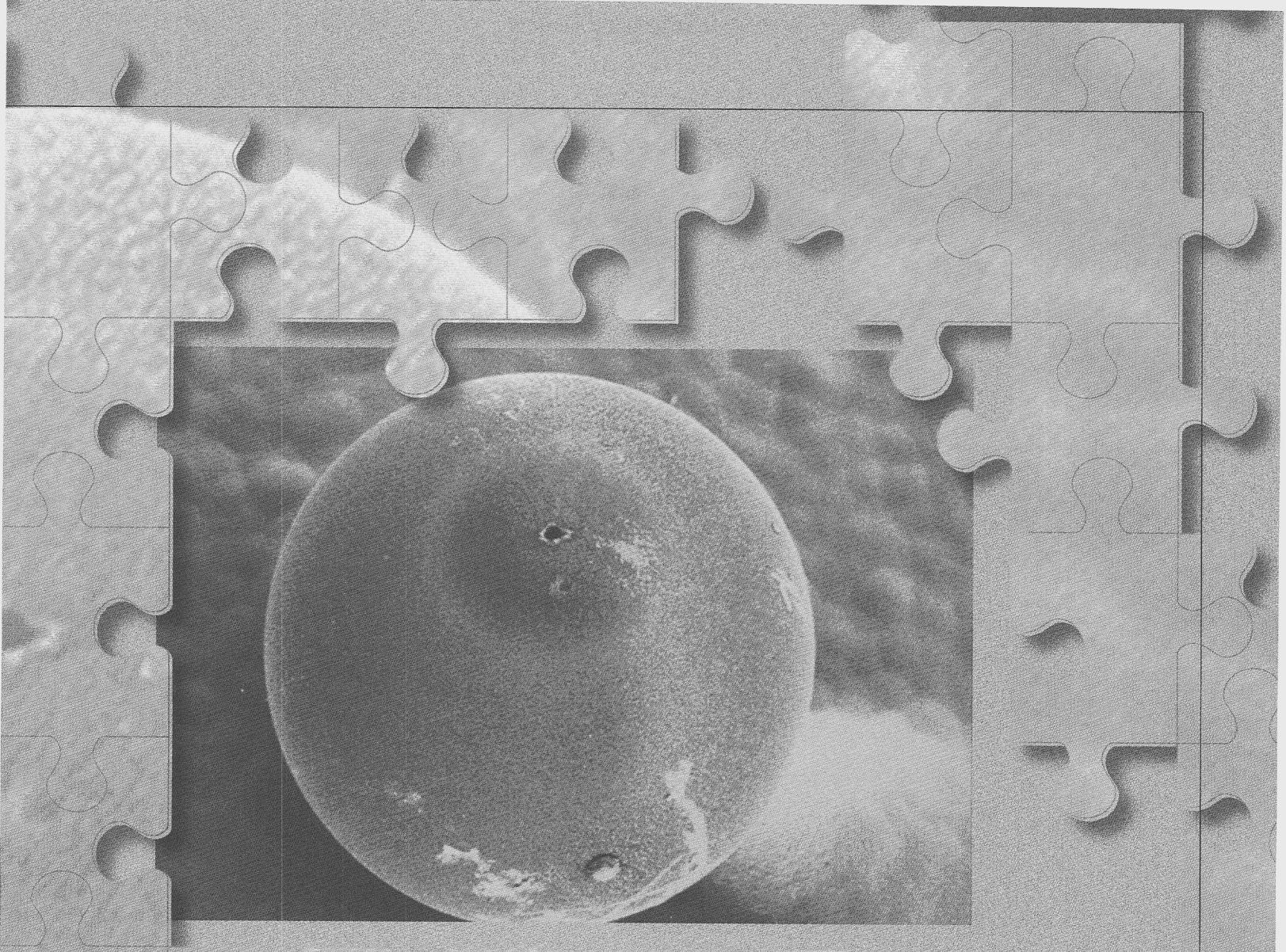

Manufacturing Technology

4

4. Manufacturing Technology

Overview
Kenneth L. Blaedel, Thrust Area Leader

A Spatial-Frequency-Domain Approach to Designing Precision Machine Tools
Debra A. Krulewich *4-1*

Micro-Drilling of ICF Capsules
Steven A. Jensen *4-13*

A Spatial-Frequency-Domain Approach to Designing Precision Machine Tools

Debra A. Krulewich
Manufacturing and Materials Engineering Division
Mechanical Engineering

The goal of this project is to develop a new error budgeting methodology for designing machine tools and motion control systems that can meet increasingly stringent tolerances. This new approach quantitatively accounts for the spatial and temporal frequency content of the error sources during a machining process and estimates workpiece error in terms of power spectral density (PSD). In our methodology, the amplitude and frequency content of the contributing error terms are appropriately summed. Compared to the traditional approach, this method is better able to handle the dynamics of the machining, producing a mapping of the PSD onto the machined workpiece. During FY97, three key technical issues have been analyzed: 1) identifying and characterizing elemental error terms that contribute to the net error; 2) developing a combinatorial rule to sum the elemental error terms; and 3) developing a frequency domain transfer function of the machining process to map the PSD onto the machined workpiece.

Introduction

Increased precision in manufacturing is being demanded by Lawrence Livermore National Laboratory (LLNL) programs, in areas ranging from National Ignition Facility (NIF) optics[1] manufacturing and Inertial Confinement Fusion (ICF) target positioning, to the production and alignment of optics for extreme ultra-violet (EUV) lithography.[2] Other LLNL areas that drive unique requirements for precision include the machining of diffractive optical systems, the fabrication of ICF targets,[3] and the manufacture of weapons components.

The precision-to-cost ratio is another metric that relates to a wide variety of industrial mechanical systems, such as automotive engine components, but has a special significance at LLNL where an increased interest in tighter tolerances is matched by the need to lower program costs. Minimizing technical risk is another issue that defines manufacturing goals for programs that cannot tolerate yield factors less than 100%, such as in fabricating components for the nuclear weapons program.

This project will significantly improve the process of formulating an error budget for a manufacturing, positioning, or measurement system. Error budgets provide the formalism to account for all sources of uncertainty in a process, and sum them to arrive at a net prediction of how 'precisely' a manufactured component can meet a target specification. The error budgeting process drives decisions regarding the conceptual design of the system and choice of components and sub-systems, and enables a rationale for balancing precision (performance), cost, and risk.

The basic procedure of preparing an error budget begins by considering the amplitudes of all terms that contribute to the error motion of a machine.[4–10] These are summed using a combinatorial algorithm[11–13] that produces an estimate of the net displacement error in a given direction. This net error can be compared to a mechanical specification, or further related to a workpiece by considering the machining operation and its associated transfer function. Once the error budget is transformed to relevant workpiece coordinates, it can be compared to a specified workpiece tolerance.

This methodology is quite successful when the desired errors in tool positioning are characterized by a single number, designated by either an rms or peak-to-valley value. However, recent specifications for advanced optical systems are being posed in terms of the spatial frequency content of the residual errors imparted to the optical wavefront. This requirement directly maps back to specifications for workpiece accuracy posed in terms of the power spectral density (PSD)[14] of the workpiece surface errors. Similarly, the ability of the physics

community to better model implosion events is leading to manufacturing specifications for structural weapons components in terms of the spatial frequency of the residual errors on the surface.

Based on these requirements, it is no longer acceptable to specify manufacturing or machine tool tolerances in terms of a single number that spans all temporal and spatial frequencies. Current efforts to embrace the frequency aspects of error budgeting typically divide the frequency spectrum into a small number of bins, such as figure, ripple, and finish, and then perform an error budget summation within each of those bins. This may be acceptable when the manufacturing specifications can be simplified to 2 to 3 frequency bins. However, this approach does not satisfy the demand for a continuous PSD of the dimensional errors on the machined part.

The goal of this project is to develop a new error budgeting methodology for designing machine tools and motion control systems that can meet increasingly stringent tolerances. This new approach quantitatively accounts for the spatial and temporal frequency content of the error sources during a machining process and estimates workpiece error in terms of PSD.

Figure 1 shows the proposed error budget flowchart that uses frequency information for the error sources. Similar to the traditional approach, the error sources, S, couple to the machine via mechanisms, C, resulting in displacements, Δ. These displacements are not converted to a single number, but are transformed into PSDs for each of the elemental errors; for example, PSD_{1x}. The elemental PSDs are then summed using an appropriate combinatorial algorithm, which has been defined during FY-97 and will be described in detail in the next section.

The results of this summation are the net PSDs for each relevant machine coordinate and their probability density functions. With this information, confidence intervals around the expected errors can be determined. The final box on the flowchart of **Fig. 1** is a transfer function, T_{ij}, which accounts for the frequency response of the machining operation, and yields the error spectrum that would be produced on the workpiece.

Progress

We have proposed to test the hypothesis that the composite PSD of the dimensional errors on a workpiece can be predicted by appropriately combining the PSDs of the machine's elemental errors. The practical consequence of this hypothesis is that a machine tool could be designed for meeting a programmatic PSD specification. We have made significant progress toward this goal during the first part of FY-97.

The project tasks are broadly divided between analysis and validation experiments. During FY-97, we have concentrated our efforts on analysis. Key technical issues include: 1) identifying and

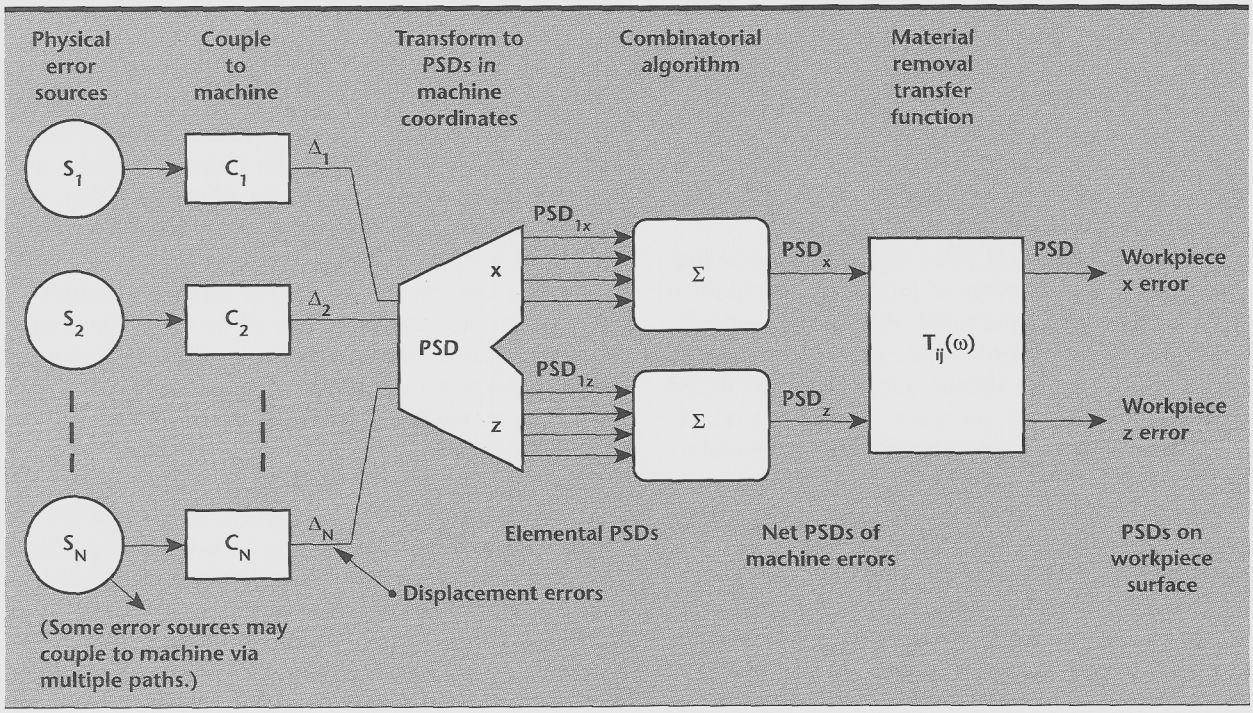

Figure 1. Proposed error budget flowchart using frequency information for the error sources.

characterizing elemental error terms that contribute to the net error; 2) developing a combinatorial rule to sum the elemental error terms; and 3) developing a frequency domain transfer function of the machining process to account for the dynamics during cutting. Progress on these issues will be discussed in detail.

We began the project by reviewing PSD requirements for a variety of programs, including the manufacture of ICF targets and KDP crystals for NIF, and structural weapons components for the Life Extension Programs. We also performed a literature search to identify current work in this area. We located many papers discussing traditional error budget methodology and combinatorial rules, but no papers were found that specifically addressed frequency domain error budgeting techniques. We did not locate anyone who has studied the distribution of particular elemental error terms, nor their frequency content. Furthermore, we did not locate any sources that discussed how to sum elemental error PSDs to predict a net PSD.

While much current research involves the study of cutting dynamics, all work is based on time domain simulations, and we did not locate any sources that discussed a frequency domain transfer function for machining processes.

Identifying and Characterizing Elemental Error Terms

We have begun to identify and characterize the elemental error terms that contribute to the net error. The identification of elemental errors will be similar to the traditional error budgeting methodology, and the results of the literature search are valuable. However, we must also determine characteristic frequency and mean amplitudes of these elemental errors, along with the expected distribution about the mean. These two aspects of the elemental errors are depicted in **Fig. 2**.

We must be able to relate the specific shape of each elemental PSD to our knowledge of that error. For example, since the thermal capacitance of the machine is large, thermal errors will produce relatively low spatial frequency errors. If the machine has encoder feedback, we would expect a positioning error at a spatial frequency of once per revolution of the leadscrew. Each elemental error will have a mean PSD, depicted in **Fig. 2a**, and a distribution about the mean representing the apparently nonrepeatable component of this error, depicted in **Fig. 2b**.

We must know the distribution and spread of the PSD about the mean, so we use the appropriate combinatorial rule. We will relate the distribution and spread back to our knowledge of the particular error. For example, the leadscrew positioning error spread will be related to the resolution of the feedback mechanism.

To study the frequency and amplitude content of elemental errors, we measured the positioning error of a moving axis on a T-base lathe. Results are shown in **Fig. 3** in both the spatial domain and frequency domain. Since this machine uses encoders for feedback, we see a very apparent once-per-revolution error of the leadscrew. Note that a machine with scales or laser feedback would not exhibit this error. Surprisingly, we saw a very high frequency error that occurred 320 times every

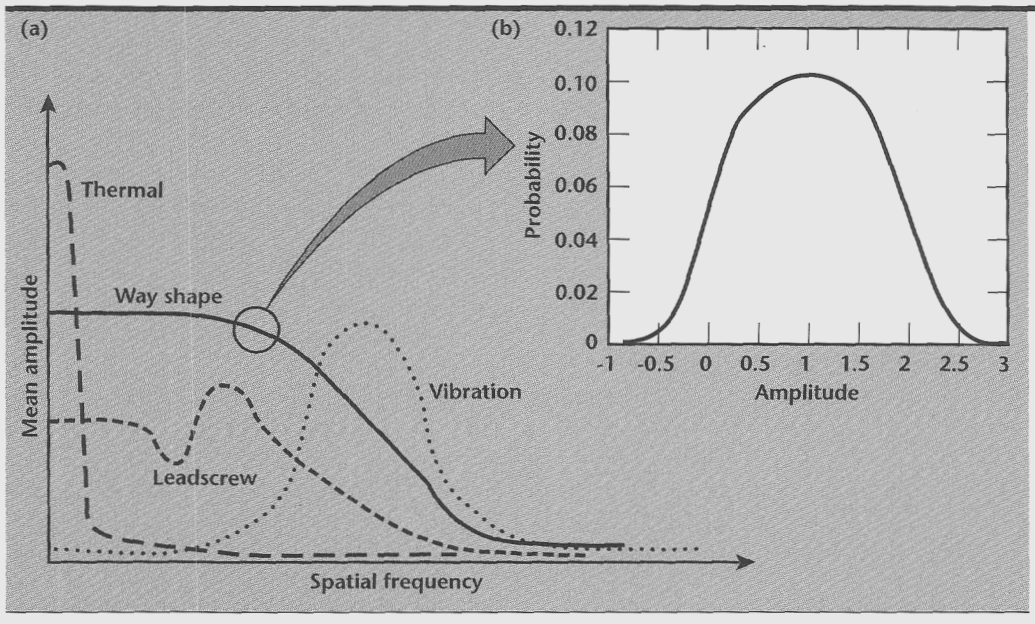

Figure 2. Two aspects of the elemental errors: (a) characteristic frequency and amplitude of four elemental errors, and (b) distributions of the errors about the mean.

revolution of the leadscrew. We are working with Moore, the manufacturer of this machine to identify the source of this error. We believe it is related to the position interpolation procedure of either the machine or the laser measurement system we used to measure the positioning error.

Since the amplitude of this high frequency error is relatively large, a significant amount of aliasing errors occur when the sample rate is not set high enough. From a practical standpoint, it is time-consuming to acquire this finely-spaced data. Conventional measurement procedures take data when the machine is stopped. The machine moves to the new measurement location, stops, and then the measurement is acquired before the machine moves to the next measurement location.

It requires an unreasonable amount of time to acquire data across the full travel of the machine at a sampling rate high enough to avoid aliasing. Furthermore, time-domain filtering cannot be used to prevent aliasing errors since the machine is not moving at a constant rate. Therefore, we are developing a new measurement procedure that will acquire data on the fly, not requiring the machine to stop at each measurement location. (See the section on Future Work for a description of this measurement procedure.)

On the same T-base lathe, we measured the repeatability of both a positioning error and angular pitch error of a moving axis on a T-base lathe. We found that the angular error non-repeatability was smaller than the resolution of our measuring instrument. This is an important observation which we hope to generalize upon. It may be that certain angular errors can be considered knowns rather than random variables. We also found that the non-repeatable component of the positioning error was much smaller than the repeatable component, and the distribution was near to Gaussian, as shown in **Fig. 4**. We also measured the repeatability at

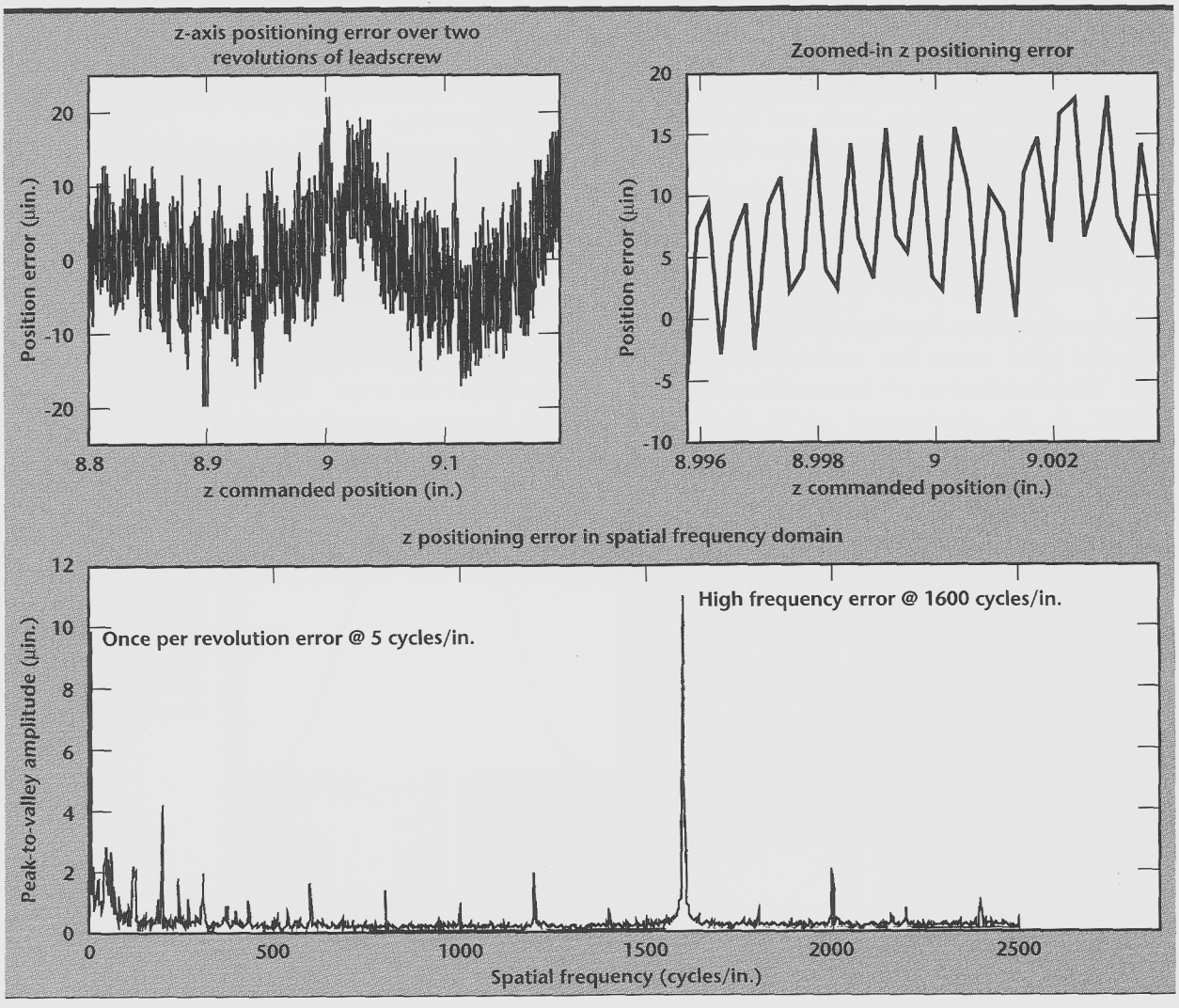

Figure 3. Frequency and amplitude content of an axis positioning error.

different locations along the moving axis and found that the variance is dependent on the position.

Developing a Combinatorial Rule to Sum the Elemental Error Terms

We have developed a combinatorial rule for the addition of elemental PSDs. We have analytically shown that the mean resulting PSD is the sum of the elemental PSDs at each discrete frequency.

However, as a design constraint we are interested in the worst case rather than the mean expected resulting PSD. The worst case scenario would occur if each elemental PSD was simultaneously at a maximum. This could be found by adding the Fourier transforms of the elemental PSDs, and then finding the PSD of the net Fourier transform. When considering sinusoidally varying signals, this would only occur if every elemental error were in phase with the others, and the non-repeatable components of the errors were also at a maximum.

From a statistical standpoint, this scenario is practically impossible. To put practical confidence intervals around the net PSD, it is necessary to determine the distribution and variance of the total PSD as well as the mean PSD.

To determine the net PSD probability distribution function, we considered each elemental PSD to be generated by a sinusoidally varying signal of known amplitude but unknown, uniformly distributed phase. The resulting net PSD probability density function approaches an exponential distribution described by

$$p_{PSD} = \frac{1}{\overline{PSD}} e^{-\frac{PSD}{\overline{PSD}}},$$

$$\overline{PSD} = \sum_i PSD_i ,$$

where

$\overline{PSD}$ = mean net PSD,

PSD = net PSD,

p_{PSD} = probability density function of the net PSD, and

PSD_i = i-th elemental PSD.

The probability density function can now be integrated to determine an upper bound on the net PSD given a confidence interval, α. The upper bound is then

$$PSD_{\max} = -\overline{PSD}\ln(1-\alpha).$$

For a 95% confidence limit, the maximum is approximately three times the mean, and for a 99% confidence limit, the maximum is approximately 4.6 times the mean. This is significantly less than the worst case, when all the errors are in phase. For example, if 25 errors of equal amplitude were summed, the worst case net PSD would be more than eight times larger than the 95% confidence limit, and more than five times larger than the 99% confidence limit.

The spatial frequency domain requirements we have seen are in terms of the power spectral density, so we have concentrated our efforts on determining the distribution of the PSD. However, there may be applications that specify frequency domain errors in terms of the Fourier transform (proportional to the amplitude) rather than the PSD (proportional to the square of the amplitude). We have also determined the probability distribution function for the net Fourier transform, which is directly calculable from the net PSD distribution.

The above results assume that the magnitudes of the elemental PSDs at each frequency are known. In reality, the magnitudes are also random variables with unique distributions at each frequency. This complicates the analysis to the point that it is not feasible to analytically solve for the net PSD distribution.

We have consulted with two professors from the University of California at Berkeley and were advised that in complex situations as this, we should resort to a Monte Carlo simulation. Similar statistical techniques have also been used for tolerance analysis of optical systems.[15] As a tool, we built a Monte Carlo simulation that sums points on the PSD at discrete frequencies. At each frequency, the total

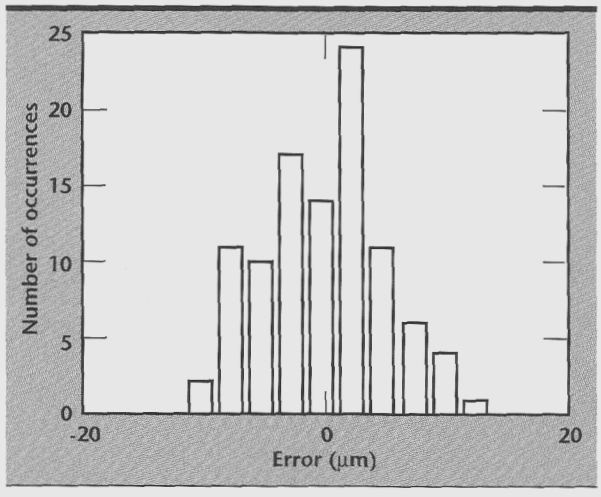

Figure 4. Positioning error repeatability.

error is generated by the sum of sinusoidal elemental errors of known amplitude probability distribution functions and random, uniformly distributed phase shifts. The simulation can be run through 50,000 iterations in less than 30 s.

Figure 5 shows a histogram of the error predictions from 50,000 iterations of the Monte Carlo simulation. In the simulation, 25 errors with amplitude of one and zero variance, and uniformly distributed phases are summed. Since the variance is zero, we can predict the distribution analytically using the exponential distribution.

In the case where the variances of the elemental errors are zero, there is no need to run the Monte Carlo simulation, and the results can be accurately determined using the analytical exponential distribution. This similarity between the histogram and the line shows that the Monte Carlo simulation is working properly.

The Monte Carlo simulation has demonstrated that we must understand the typical distributions of the non-repeatable components of the elemental errors. We found that the particular form of the distribution might not be that critical. For example, if the variance is small in comparison to the mean, the results of the simulation are not significantly different if we assume either uniformly distributed or normally distributed elemental errors. However, as the variance becomes larger, the elemental distributions become more important.

We expect that many of the errors will have small variances in comparison to the mean, or, in other words, the repeatable component of the error will be significantly larger than the non-repeatable component. Therefore, it is critical for us to know the band (minimum to maximum) of the error rather than the exact distribution of the error.

We made a comparison between this new method and the conventional approach at certain spatial frequency bins specified in an error budget for a fly-cutting machine at LLNL.[16] We found that the new method produces similar results for each frequency. This is reassuring since the conventional approach has been shown to produce reasonable predictions. These results are summarized in **Table 1**. The new error budget will have the additional capability of

Table 1. KDP error budget 99.8% confidence limit results.

Frequency bin	Conventional approach	New approach
Roughness	8.70 nm	9.99 nm
Waviness 1	7.45 nm	8.24 nm
Waviness 2	10.54 nm	11.04 nm
Waviness 3	20.95 nm	22.05 nm

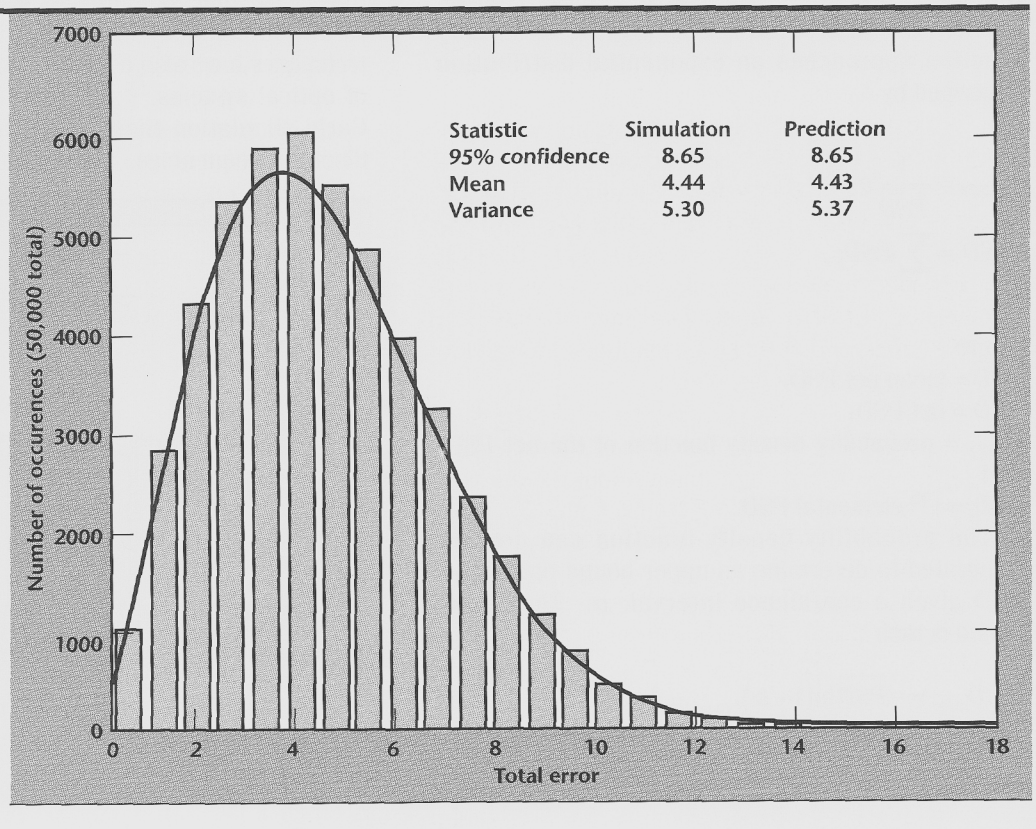

Figure 5. Histogram of total error predictions from 50,000 iterations of the Monte Carlo simulation. The plot represents a summation of 25 independent sinusoidal errors with amplitude of one. The line shows the analytical solution.

predicting the full spectrum of errors, rather than single value estimates for the four frequency bins (that is, roughness, waviness 1, waviness 2, and waviness 3).

Developing a Frequency Domain Transfer Function of the Machining Process

The traditional error budget combines the elemental errors of the machining process to predict the motion of the tool in free space. During machining, the tool is in contact with the workpiece. If the machine had no compliance, a one-to-one transfer between the motion of the tool and the resulting surface on the part would occur in a diamond turning process. However, the machine and machining process have some compliance and damping. In actuality, errors that occur at the machine resonance may be amplified by the dynamic process.

Other errors may actually be entirely filtered and not show up on the machined workpiece. We must therefore determine the transfer function between the motion of the tool in free space and the resulting error on the part.

There is much current research in the field of cutting dynamics. However, since the cutting process is highly non-linear, all the research is focused on time-domain simulations of the cutting process. For this project, we don't want to rely on a complex time-domain simulation to produce the transfer function. Instead, our strategy is to make simplifying assumptions that will allow us to develop a frequency-domain transfer function.

We assume that the depths of cut are small, and that the tool will remain in contact with the workpiece for the entire process. We also assume that there are no form errors on the initial part. We also will not be machining at conditions that will excite the resonant modes of the machine, so we are not concerned with the highly non-linear behavior of chatter. We feel that these assumptions are valid for precision machining operations.

We have divided the cutting model development into two phases. The purpose of the first phase is to verify the concept of a frequency-domain approach to representing the machine transfer function using a simple model. The second phase will include a complex turning model, where all the elemental errors will contribute to the final errors on the part. The second phase will be addressed in FY-98 and will be discussed in the next section.

During the first phase, a simple orthogonal cutting model was selected, where only spindle errors and machine dynamics will contribute to the resulting workpiece errors. A cutting model simulation has been written to produce the transfer function between the tool motion and the resulting errors on the workpiece. Inputs to this simulation include the modal parameters of the machine. We have measured the modal properties of the machine.

A sample transfer function is shown in **Fig. 6**. Note that this is not the actual transfer function that we will use, because the gain is actually dependent on the amplitude of the error, the mean depth of cut, and the frequency due to non-linearieties in the process. Therefore, after we measure the spindle error amplitudes and frequencies, we can generate the true transfer function for this process. During FY-98 we will validate this approach by measuring the spindle errors and machining an actual part. (See the next section for details.)

The output of the transfer function is the motion of the tool while it is in contact with the part. In combination with the feed-rates of the axes, we can generate the amplitude and frequency content of the resulting errors on the part in the direction of the tool motion. However, this does not predict the errors during a turning process "across the lay," that is, perpendicular to the direction of the tool. Since the errors in both directions are relevant to workpiece specifications, we are also developing a procedure to determine the amplitude and frequency content of the residual errors perpendicular to the path of a tool during a turning process.

To determine the amplitude and frequency content of the tool motion, we use the output from the transfer function which predicts the frequency and amplitude content of the tool motion while it is in contact with the part. Next, the tool motion is sampled by the reciprocal of the feed-rate, where the feed-rate units are distance per revolution and the reciprocal units are revolutions (or cycles) per distance. Note that the units of the spatial-domain frequency (cycles per

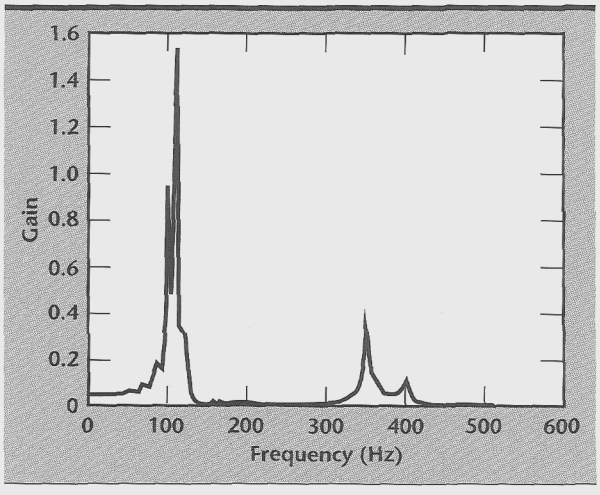

Figure 6. Machining process transfer function for Phase 1.

distance) are the equivalent to time-domain frequency units of Hz (cycles per second).

When the frequency of the tool motion is less than one half the sampling frequency, the sampling procedure is fairly straightforward. Since sampling is a multiplication process in the time domain, this is equivalent to a convolution process in the frequency domain. However, when the frequency of the tool motion is greater than one half the sampling frequency, unavoidable aliasing occurs. We must then determine the apparent frequency and amplitude content of the aliased signal.

For example, if the frequency of the tool motion is an integer of the sampling rate, the sampled signal will appear to have only a DC off-set. (See **Fig. 7** for a relationship between the frequency of the error and the apparent frequency after aliasing.) During FY-98 we will further investigate this relationship.

The nominal surface finish generated when the machine has no errors has some amplitude and frequency content, caused by the shape of the tool. For a tool with a flat profile, the nominal surface finish would be flat; however, most tools have a round profile, creating surface finish errors at spatial frequencies of once per feed-rate, and higher harmonics. Previous work has investigated the nominal surface finish and, based on geometry, the nominal peak-to-valley surface error across the lay is

$$PV = \frac{f^2}{8R}$$

f	=	feed-rate (distance/revolution)
R	=	tool radius (distance)
PV	=	peak-to-valley error (distance).

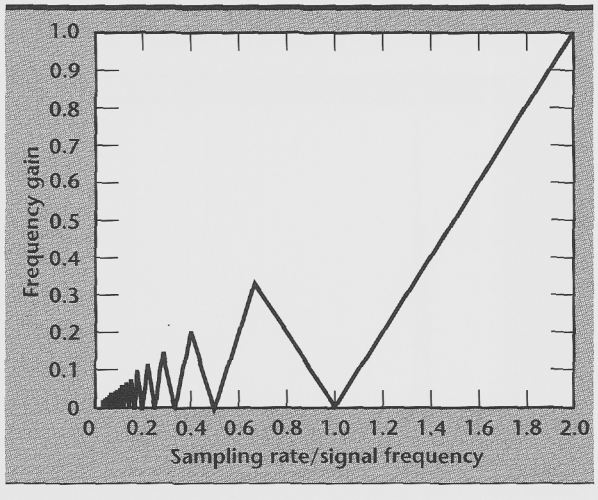

Figure 7. Apparent frequency gain after aliasing.

We have started to investigate how the nominal frequency content and the error frequency content add to produce the final errors on the part. **Figure 8** shows the nominal surface finish and the surface finish when the tool motion is given a sinusoidal error at a single frequency. The error motion has a filtering effect on the surface finish. These surface finishes are shown in the frequency domain in **Fig. 9**.

During FY-98, we plan to show that the frequency content of the actual surface can be attained by appropriately adding the aliased frequency content of the error motion and the frequency content of the nominal surface. This will be discussed in more detail in the following section.

Future Work

Identifying and Characterizing Elemental Error Terms

In actual usage of the error budget, it is not possible to measure all the errors on a new machine before the machine has been built. Therefore we need a procedure to predict the frequency and amplitude content of the elemental errors from the physical properties that create the error.

To develop this procedure, we will fully characterize the frequency and amplitude content of many of the significant elemental errors that contribute to the net error on a T-base lathe. We will relate the form of the elemental error to physical sources that create the error. We will create generalizations that will provide a methodology for predicting the frequency and amplitude contents of the elemental errors to the physical sources.

We will develop a new measurement capability, a high speed data acquisition system that triggers off position so our measurement data is evenly spaced in position. This is necessary so our spatial frequency domain calculations based on digital Fourier transform (dft) techniques are correct. To accomplish this, a laser interferometer will measure position in line with the measured error, and we will trigger off the laser interferometer. We have purchased the appropriate hardware in FY-97 and will design and implement this system in FY-98.

Developing a Combinatorial Rule to Sum the Elemental Error Terms

This task was completed in FY-97. The procedure will be summarized and incorporated into the full error budget procedure.

Developing a Frequency-Domain Transfer Function of the Machining Process

We have divided this task into two phases. The purpose of the first phase is to verify the concept of a frequency-domain approach to representing the machine transfer function using a simple model.

During FY-97, a time-domain cutting simulation was written to produce the frequency-domain transfer function (see previous section).

In FY-98, we will measure the spindle error motion that contributes to the error on the machined part. This error motion will be input into the time-domain simulation to produce the frequency-domain transfer function. From the transfer function and the motion of the tool in free space, we will predict the resulting frequency and amplitude content of the surface finish of an orthogonally turned part. We will then machine an actual part, measure the surface finish, and compare the prediction to the measurement.

The second phase will include a complex turning model, where all the elemental errors will contribute to the final errors on the part. We have contracted Northwestern University to establish a methodology for determining frequency-domain transfer functions of cutting processes during machining.

Northwestern's tasks include developing a generalized methodology to determine the frequency-domain transfer function, and one case study that applies this methodology to one particular machining operation. The machining process used for verification of the model will be a turning procedure of a hemispherical part. Northwestern will provide a transfer function along the direction of the tool path.

We will perform this machining operation and characterize and sum the elemental errors during the machining process to determine the frequency content of the tool motion in free space. Using the transfer function developed by Northwestern, we will predict the frequency and amplitude content of the residual errors on the machined part. We will

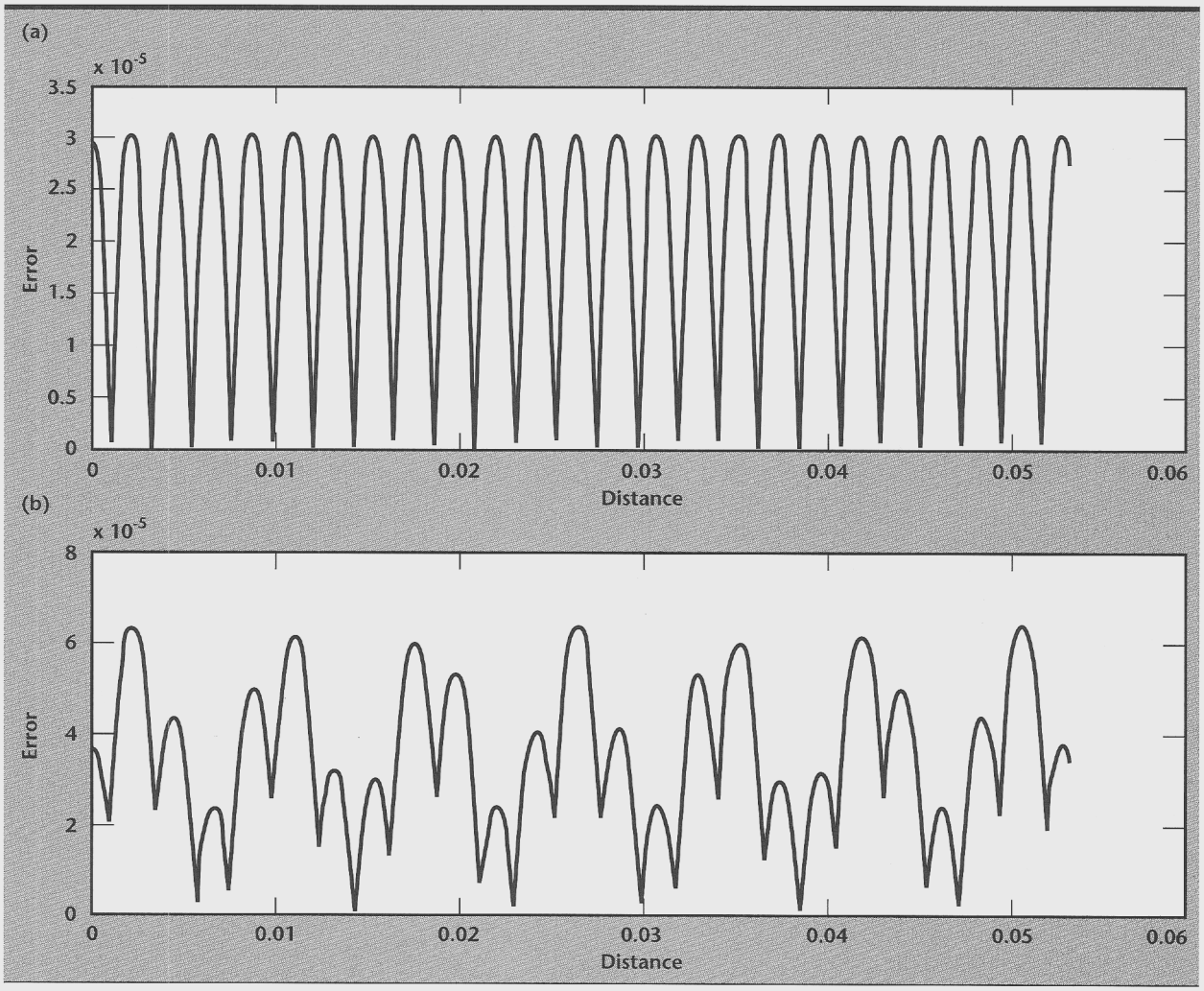

Figure 8. Nominal surface finish (a) and actual surface finish (b) of turned part perpendicular to tool motion.

measure the frequency content of the surface finish of the machined part and the measurements will be compared to the prediction.

Note that the machine that we will use to create the hemispherical testpiece will be the same machine that will be fully characterized to study the elemental error terms.

We also need to predict the frequency and error content of the residual errors perpendicular to the motion of the tool. During FY-98, we plan to show that the frequency content of the actual surface can be attained by appropriately adding the aliased frequency content of the error motion and the frequency content of the nominal surface (See previous section for more details). We have written simulation that creates the surface errors on a part given the tool geometry, feed-rate, and error motion of the tool. Our hypothesis is that the resulting errors on the part can be determined by appropriately filtering the simple addition of the aliased frequency content of the error motion and the frequency content of the nominal surface. Using the simulation, we will develop this relationship. We will then predict the surface finish of the machined part perpendicular to the tool motion and compare the prediction to measured values off the machined part.

Integration

The last effort will be to put each task in the error budget together into a usable procedure. This includes procedures to 1) identify and predict the frequency and amplitude characteristics of the elemental errors; 2) sum elemental errors to predict

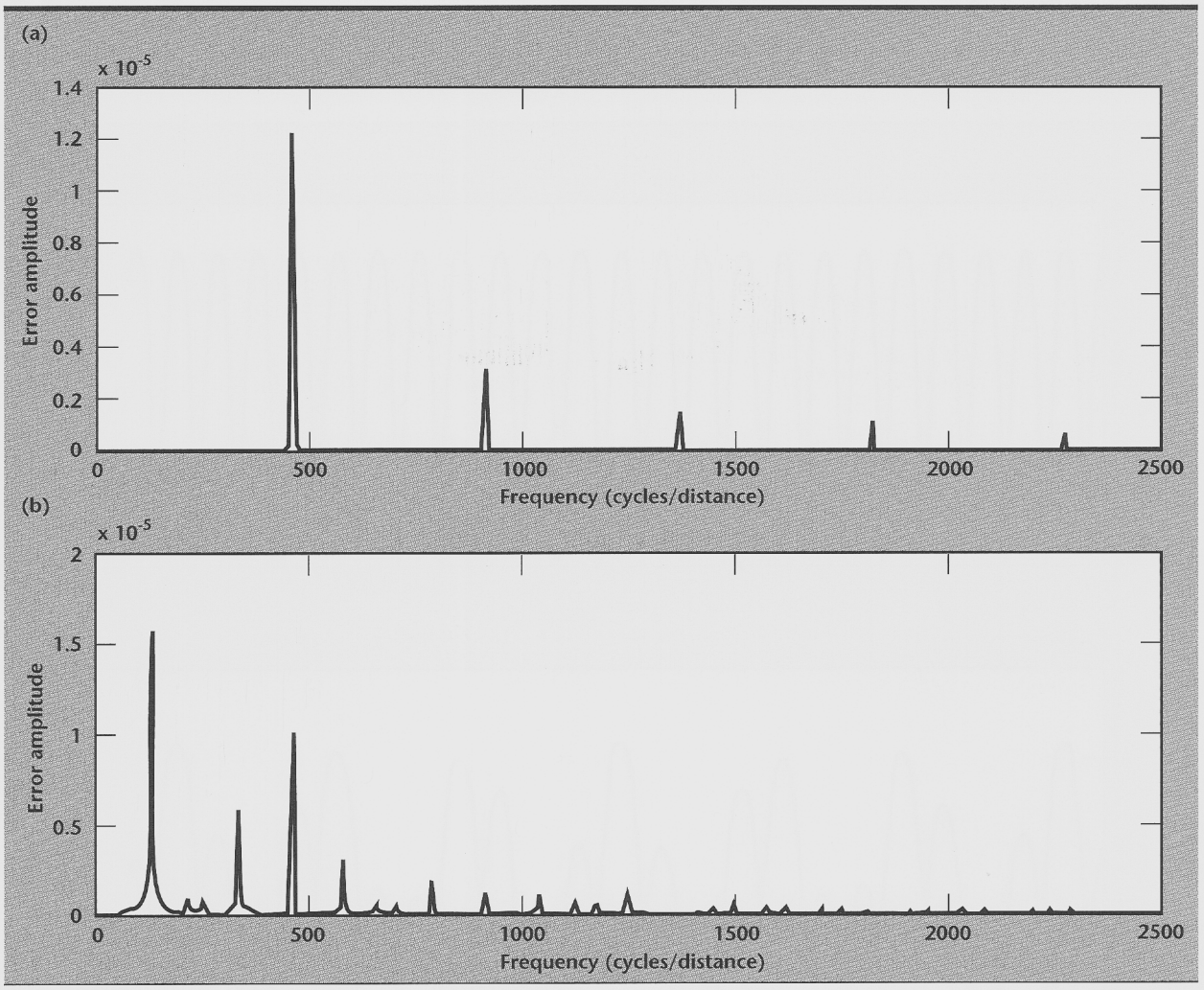

Figure 9. Frequency content of the nominal surface finish (a) and actual surface finish (b) of turned part perpendicular to tool motion.

the frequency and amplitude content of the tool motion in free space; 3) develop a frequency-domain transfer function between the motion of the tool in free space and the motion of the tool while it is in contact with the part during machining; 4) predict the frequency and amplitude content of the surface finish of the part along the direction of the tool; and 5) predict the frequency and amplitude content of the surface finish of a part perpendicular to the direction of the tool.

References

1. Aikens, D. M. (1995), "The origin and evolution of the optics specifications for the National Ignition Facility," *Optical Manufacturing and Testing*, V. J. Doherty and H. Philip Stahl, Eds., SPIE Vol. **2536**, pp. 2-12 .

2. Church, E. L. and P. Z. Takacs (1994), "Specification of the Figure and Finish of EUV Mirrors in Terms of Performance Requirements," *OSA Proceedings on Extreme Ultraviolet Lithography*, F. Zernike and D. T. Atwood, Eds., Vol. **23**, pp. 77-82.

3. Lawrence Livermore National Laboratory, Livermore, CA, UCRL-52000-95-4 (1995), "Creating Microsphere Targets for Inertial Confinement Fusion Experiments," pp. 1-9.

4. Donaldson, R. R. (1980), "'Error Budgets,' in Machine Tool Accuracy," *Technology of Machine Tools: A Survey of the State of the Art by the Machine Tool Task Force*, R. Hocken, Ed., Vol. 5 (9).

5. Dorndorf, U., V. Kiridena, and P. Ferreira (1994), "Optimal Budgeting of Quasistatic Machine Tool Errors," *Journal of Engineering for Industry, Transactions of the ASME*, Vol. **116** (1), pp. 42-52.

6. Gee, A. (1994), "'Error-Budgeting' for High Performance Positioning in Ultra-Precision Manufacture," *IEE Colloquium (Digest) IEE Computing and Control Division Colloquium on Precision Motion Control in Robotics and Machine Drives*, November, **226**, pp. 3/1-3.

7. Slocum, A. H. (1992), *Precision Machine Design*, Prentice Hall, Princeton, NJ.

8. Thompson, D. C. (1989), "The Design of an Ultra-Precision CNC Measuring Machine," *39th CIRP General Assembly, Trondheim*, Norway, August.

9. Treib, T. (1987), "Error Budgeting—Applied to the Calculation and Optimization of the Volumetric Error Field of Multiaxis Subsystems," *Annals of the CIRP*, Vol. **36** (1), pp. 365-368.

10. Zakovorotny, V., I. Ladnik, and S. Dhande (1995), "A Method for Characterization of Machine-Tools Dynamic Parameters for Diagnostic Purposes," *Journal of Materials Processing Technology*, Vol. **53**, pp. 588-600.

11. Shen, Y., and N. Duffie (1993), "Comparison of Combinatorial Rules for Machine Error Budgets," *CIRP Annals*, Vol. **42** (1), pp. 619-622.

12. Shin, Y., and Y. Wei (1992), "A Statistical Analysis of Positional Errors of a Multiaxis Machine Tool," *Precision Engineering*, Vol. **14** (3), pp. 139-146.

13. Spotts, M. (1975), "The Combination of Uniform Probability Curves in Engineering," *ASME Design Engineering Technical Conference*, Washington, DC, September.

14. Bendat, Piersol, J. M. Elson, and J. M. Bennett (1995), "Calculation of the power spectral density from surface profile data," *Applied Optics*, **34** (1), pp. 201-208.

15. Wilkinson, E., J. Green, and D. Sahnow (1994), "Tolerance analysis of the Far Ultraviolet Spectroscopic Explorer (FUSE): a statistical approach," *Proceedings of SPIE—The International Society for Optical Engineering X-Ray and Ultraviolet Spectroscopy and Polarimetry, San Diego, CA*, July, Vol. **2283**, pp. 261-264.

16. Moore Tool Company, Inc. (1995), "Diamond Turning Machine for KDP Crystal Manufacturing," *Conceptual Design Report*, November.

Micro-Drilling of ICF Capsules

Steven A. Jensen
Manufacturing and Materials Engineering Division
Mechanical Engineering

We have investigated the commercial capability of micro-drilling in terms of the current limits to precision, quality, and aspect ratios attainable. The motivation behind this study is to determine the feasibility of drilling a small hole in the National Ignition Facility fusion capsules, suitable for filling with the intended fuel mixture. The challenge of accomplishing this task is that the hole to be drilled must have a very high aspect ratio (up to 100 to 1, or beyond), and be drilled in such a manner that it does not become a major structural defect or perturbation to the overall capsule. From the information available, it does seem feasible to create micro-holes suitable for filling. Based on preliminary investigations, however, it does not seem likely that a commercial company will be able to produce these holes.

Introduction

The National Ignition Facility (NIF) at Lawrence Livermore National Laboratory (LLNL) will require spherical shell targets about 2 mm in diameter, with ablator shell thickness between 100 and 150 μm. These targets will be filled with a deuterium-tritium (DT) fuel mixture, and ultimately struck from all directions, simultaneously and uniformly, by sufficient radiant energy to vaporize or ablate the outer capsule shell, which will then expand in a rocket-like blow-off. This rapid expansion of the ablator drives the inner portion of the capsule inward, compressing and heating the DT fuel contained inside. By the end of the implosion, the fuel core reaches a high enough density and temperature to initiate nuclear fusion.

The shape and symmetry of the compressed fuel during implosion is critical to capsule performance. Irregular or non-uniform compression of the DT fuel could create conditions that fall short of complete ignition. The uniformity and smoothness of the ablator shell plays a significant role in the proper compression of the DT fuel. For this purpose, the capsules need to be made with as few structural defects or surface perturbations as possible. Currently the required surface roughness for these capsules is on the order of 10 nm rms, or less.

Progress

We have studied the micro-drilling process in terms of current limits to processing quality and aspect ratios for fusion capsules.

Capsule Fabrication and Design

There are three approaches being pursued for an ablator capsule. The first approach, and most direct, is to machine two hemi-shells from bulk material and bond them together. The second approach involves coating a hollow mandrel (possibly in some chemical vapor deposition (CVD) process, or by sputtering), and then drilling a small hole in the capsule, suitable for filling. Once filled, this hole would be plugged or welded shut. The third, and most current, method for capsule fabrication involves sputtering a hollow polymer mandrel (polystyrene 3 to 6 μm thick), which is then diffusion-filled.

Several materials were originally chosen as candidates for the ablator shell, among which were B, B_4C, B_9C, CH, and doped Be. Doped Be was eventually chosen because it offers advantages in lower density, better hydrodynamic stability, reduced drive temperatures, faster sputtering rates, and overall strength characteristics.[1] The hollow mandrels are sputter-coated with the doped Be using

three magnetron sputter guns and a piezoelectric-driven bounce pan, which is used to help ensure a uniform coating.

The bounce pan is electrically isolated, so that, if desired, a voltage bias can be applied. By applying a voltage bias, the morphology and grain structure of the deposited Be can be altered. This becomes important when attempting to diffusion-fill the capsules. Ideally, the capsules would be diffusion-filled at or near room temperature; however, this requires that the porosity of the capsule be near 10%. The downside to this is that as the porosity increases, so does the over all surface roughness, and a porosity of 10% does not meet the surface roughness requirements of less than 10 nm rms. By applying a voltage bias, the morphology of the deposited Be becomes more compact and less porous, which leads to better surface roughness values.

However, current efforts to diffusion-fill these less porous capsules have not been successful. Attempts have been made at using elevated temperatures to aid the diffusion-filling process, but these elevated temperatures tend to melt the inner polystyrene mandrel. Furthermore, even when using a voltage bias, current efforts have not produced a capsule having the required surface roughness of 10 nm rms or less (50 nm rms has been the best). This suggests that even in the event that the capsules can be diffusion-filled, some type of post-processing, such as micro-polishing, may be required to improve surface finish of the deposited films.

Micro-Drilling of Capsules

The advantages to using a micro-hole as a means to fill the capsules are as follows:

1) It will be much easier to attain the required surface roughness if the grain morphology is more tightly packed (hence non-porous). Currently, capsules are sputter-coated to be somewhat porous so they can eventually be diffusion-filled. This limits the quality of the surface roughness attainable. If there existed a small hole suitable for filling, the ablator shell would not need to be porous at all.
2) Porous capsules that are capable of being diffusion-filled are just as capable of leaking. To prevent this, the capsules are over-filled and then cryogenically handled up until they are positioned at the center of the target chamber. If a suitable micro-hole could be drilled, filled, and then sealed in a non-porous capsule such that there were no leaking, the need for cryogenic handling from the time of fill would be eliminated. This would ultimately add flexibility to the process and would represent a significant saving in cost.

We looked at several methods of creating micro-holes. One method is to mechanically drill the holes using a very small drill bit. The drawback to this method is that mechanical drill bits are limited in size to, at absolute best, 12 to 15 μm in diameter. Furthermore, mechanically drilled holes of this size are limited to, at best, a 5 to 1 aspect ratio.

Another method would be to electroplate around a post made of polymethal methacrylate, or some other polymer that would eventually be dissolved away, leaving a hole. This method does allow for very straight and small holes having a high aspect ratio and good quality, but electroplating Be is not currently done.

A third method would be to use a chemical etching process to create the hole, but, as with mechanical drilling, the aspect ratios would be limited.

Still another method, and relatively new, would be to use supersonic waves. This technique, which is still in the research and development stages in Japan, uses a small hard metal tool (about 4 μm in diameter), and some small diamond powder abrasive (0.25 μm grit size), in conjunction with supersonic waves, to chisel away small fragments of material. It is not yet known if this technique is suitable for metals, since it has been tested only on glasses and ceramics.

Finally, the holes could be created using a laser drilling process. The information in this report will focus on the issues related to the laser drilling approach to creating micro-holes. More specifically, it will define the current limitations to commercially drilled holes and outline possible solutions by which work at LLNL can possibly overcome these limitations.

Commercial Vendors

To determine the status of the commercially available technology for laser drilling, several companies specializing in small hole technology were contacted and consulted on holes that they were able to produce. Although eight companies were contacted, only three claimed to have the ability to commercially produce holes less than 5 μm in diameter, having relatively high aspect ratios. Those companies are Resonetics (New Hampshire), Lenox Lasers (Maryland), and Oxford Lasers (Massachusetts).

Two of these vendors (Resonetics and Lenox Lasers) were chosen to drill holes in samples for evaluation purposes. SEM photographs of a few sample holes drilled by these companies, are shown in **Fig. 1**.

Challenges Associated with Micro-Drilling

There are some significant challenges to be resolved using the laser drilling approach. First of all, the laser technology for drilling very small precision holes, on the order of 5 μm in diameter or less, is still in its infancy. Most commercial vendors do not have the equipment or expertise to drill holes this small. Work is currently being done in this area, including at LLNL. However, this work is not yet able to consistently produce micro-holes in a conventional manufacturing setting.

The first fundamental limitation to producing very small micro-holes is the diffraction limit of the optical system. The governing equation for the attainable spot size diameter of the laser beam is given by:

$$\text{dia} = 1.27 \cdot f\# \cdot \lambda$$

where f# is the f-number, defined as the focal length divided by the diameter of the optic (L/D), and λ is the wavelength of the laser beam. For a given wavelength the only way to reduce the spot size is to reduce the f-number. Optics having a low f-number have high resolution and produce small spot sizes, but at the expense of having a limited range of material penetration. Conversely, optics having a larger f-number are able to penetrate to higher depths, but at the expense of a limited hole size diameter. Having a laser with a very short wavelength becomes critical to producing very small holes having a high aspect ratio.

In the commercial field, excimer lasers are most often used to produce small holes. These lasers typically have a wavelength of 247 nm. Realistically, this needs to be smaller if holes on the order of 1 to 2 μm in diameter are to be drilled.

The other two major problems associated with drilling small precision holes, as they relate to the NIF capsules, are the taper angles associated with high aspect ratio holes, and thermal damage to the substrate. These key limitations are outlined below.

Taper Angle. Because the ablator shell of the capsule is between 100 and 150 μm thick, and the desired holes are to be less than 5 μm (ideally 1 to 2 μm) in diameter, the holes must have a very high aspect ratio (up to 100 to 1). Drilling high-aspect

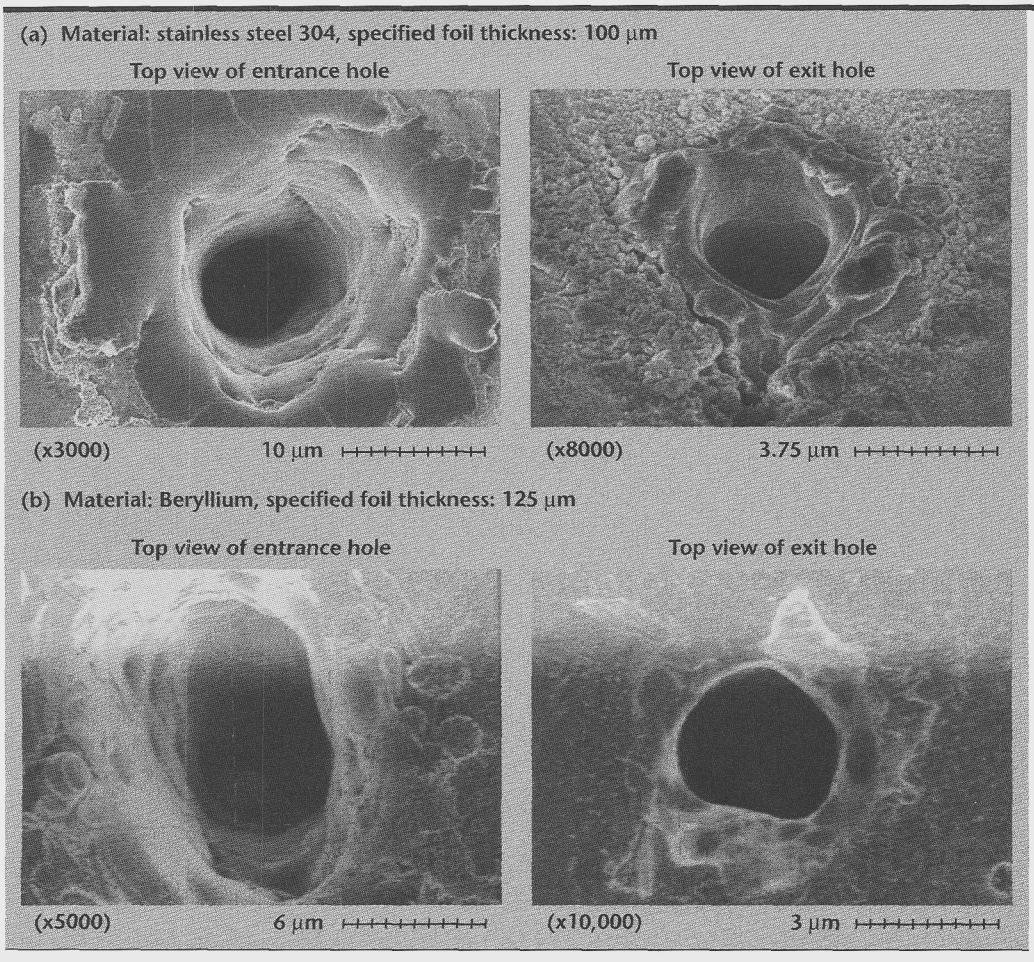

Figure 1. SEM photographs of holes drilled by commercial vendors, (a) Lenox Lasers, and (b) Resonetics.

ratio holes in and of itself is difficult, but drilling them straight without any taper or angular deviance is a much tougher task. Most laser drilling techniques produce holes which have a slight nominal taper angle. (In actuality the holes have a cross-sectional appearance similar to that of an inverted wine bottle.) Commercial taper angles typically range between 4° or 5°, at best, and 10° or 12° for relatively clean holes having minimal thermal damage. A schematic showing this taper angle is depicted in **Fig. 2**.

Because of this taper angle, the entrance diameter will be larger than the exit diameter, and can become quite significant for high aspect ratio holes. Assuming an exit hole diameter of 1 μm and an ablator shell thickness of 100 μm, the entrance hole diameter would range between approximately 8 μm, at best, and as much as 22 μm. A hole entrance diameter of this size starts to become a major structural perturbation in the capsule shell.

The generated taper comes as a result of a combination of effects. Some researchers have attributed the taper to the spatial intensity distribution of the focused laser beam (shaped similar to Gaussian distribution) and light reflected off the side walls. Resonetics recently finished a project funded by NASA, where they attempted to make a particular excimer laser beam 10 times more coherent than previously possible. It was anticipated that this would reduce the taper angle, creating a straighter hole.

However, the results seemed to indicate that it had little or no effect on the taper angle. Since then, they speculate that it is more of a function of thermal heating and diffusivity into the surrounding lattice structure, and the direction and flow of the melt products. This view is also shared in part by other researchers at LLNL. This is best described in the following section on thermal effects.

Generally speaking, micro-holes are created by either evaporative or melt expulsion, or brittle materials spallation. Which one of these mechanisms dominates the process depends on the material and the processing parameters used. Overall, these mechanisms determine the geometrical shape of the resulting hole, and the extension and geometry of the heat and mechanically affected zones (**Fig. 3**).

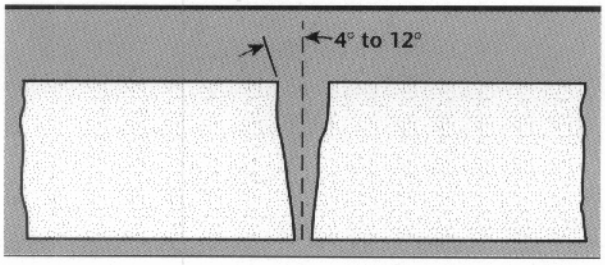

Figure 2. Taper angle of typical commercial laser-drilled hole.

Figure 3 represents a typical view of the laser drilling process in a metallic substrate. Evaporative expulsion takes place when surface material is superheated to the gas or plasma state. This type of drilling is referred to as true thermal ablation. The amount of thermally ablated material is typically very small for most commercial drilling operations, due to longer pulse lengths (nanosecond regime or longer).[2–4]

The larger part of the pulse energy is used to heat up the material until ablation starts at the end of the pulse. As a consequence, most of the beam energy is lost, due to heat conduction into the bulk material. Material that is at a temperature just below the superheated gaseous state remains molten. The molten material is expelled due to the ablation and plasma pressure. This has adverse effects on the geometry of the hole. The larger entrance hole is more than likely attributed to erosion of the side walls from the expulsion of melt products.

The SEM photographs in **Fig. 1** show samples of entrance and exit holes drilled in stainless steel and beryllium.

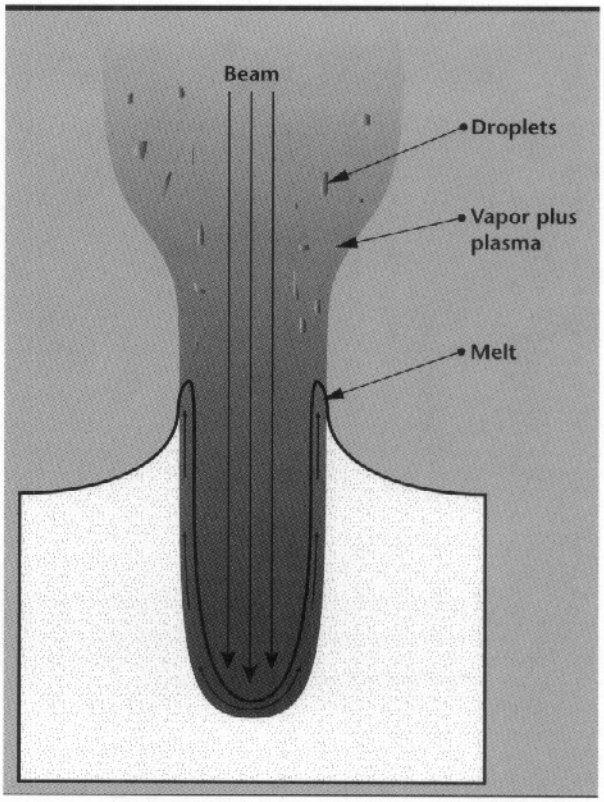

Figure 3. Schematic of typical view of the laser drilling process in a metallic substrate.

For the particular application of drilling holes in an ablator capsule, the taper will need to be reduced to angles ideally below 3° to 4°, which, for a 1-μm exit hole in a 100-μm-thick substrate would give an entrance hole diameter ranging between approximately 4 μm and 8 μm.

Thermal Effects. The majority of all laser-drilled micro-holes, commercial or non-commercial, are made by literally burning a hole through the metallic substrate. The hole is mostly created by the expulsion of molten material, which leads to the formation of dross, thermal re-cast layers, and thermal cracking. Equally present, but not always visible, is the formation of dislocations, slip planes, and residual stresses. All of these adversely affect the overall integrity of the capsule and could lead to conditions that fall short of complete ignition.

The SEM photographs in **Fig. 4** show some extreme cases of thermal damage associated with laser drilling holes in stainless steel foil samples. Stainless steel is one of the worst materials to laser-drill, due to its inhomogeneity, which produces more than average amounts of dross and re-melt. Holes drilled in highly homogenous materials, and having a relatively small grain size, produce cleaner holes with less dross and re-melt. Such materials include tungsten, tantalum, molybdenum, and beryllium.

Laser Drilling of ICF Capsules

In view of the problems associated with laser-drilling, a "best effort" approach was taken to drill holes in some actual sample target capsules using commercial capabilities. The idea was to try and drill as small a hole as was commercially available, while minimizing the thermal effects by using as short a laser pulse length as possible.

Target capsules approximately 500 μm in diameter with a wall thickness of about 17 μm were sent from LLNL to Resonetics. Three holes were drilled in three separate targets using an excimer laser having a wavelength of 193 nm. The optical set-up had a recorded diffraction limit of 6 μm. The other important parameters were as follows: laser energy, 550 mJ; demagnification, 16.5; and measured fluence, 43 J/cm^2. SEM photographs of two of the drilled holes are shown in **Fig. 5**.

The photographs do show some thermal re-melt layers, but, overall, the heat-affected zone is not overly large in comparison to the hole diameter. These photographs also show the columnar and porous structure of the sputtered, beryllium surface of the targets. Although these targets had a wall thickness of only 17 μm, far less than what will eventually be needed, the holes do show some promising signs of being used as a filling orifice. If a laser set-up capable of femtosecond pulses were used to drill the holes, and if the diffraction limit of the laser set-up were lowered to 2 to 3 μm, the holes would be much cleaner and smaller, as described in following section.

Femtosecond Laser Ablation

As stated earlier, the creation of holes in metallic substrates is done by either melt expulsion or evaporative expulsion, also known as true thermal ablation. In a true thermal ablative process, the material is converted from a solid state to a vapor or plasma state very rapidly. This then either evaporates or, ideally, would be extracted through the use of a vacuum.

True thermal ablative processes require very short pulses of energy, on the order of femtoseconds. Theoretically, when the laser energy interacts with a material, it is first deposited into the free electrons, which rapidly cool by transferring this energy to the lattice structure. The cooling of

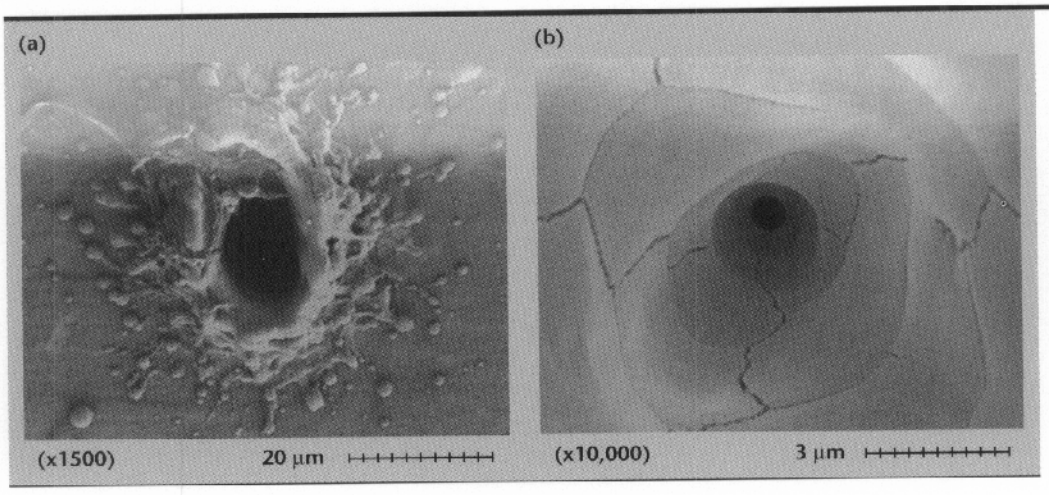

Figure 4. SEM photographs showing extreme cases of thermal damage associated with laser-drilled holes in stainless steel: (a) top view of entrance hole, showing dross and re-melt; and (b) inside view, showing thermal cracking.

the electrons and transfer of energy happens on the order of 1 ps, which is much longer than the laser pulse duration (when operating in the femtosecond regime).

If the energy transferred is above the evaporation threshold for the particular material, then the lattice material is converted from the solid phase to the vapor and plasma phase. This happens so rapidly that thermal diffusion into the target is negligible, so there is very little heating of the surrounding areas.[4–8] Therefore, there is virtually no re-melt, thermal cracking, or generated dross, because of the absence of the liquid phase.

The SEM photograph in **Fig. 6** shows a hole drilled in 100-μm-thick steel, using a short pulse laser (that is, a femtosecond laser).[7] Although the hole is quite large in diameter, it does show the advantages of using a short pulse laser to minimize thermal damage to the substrate. The pulse lengths used to drill the hole were on the order of 200 fs.

The use of femtosecond technology is relatively new, and commercial vendors typically do not have lasers capable of generating these pulse lengths. Commercial vendors typically have excimer-type lasers, which can produce pulse lengths as short as 20 ns, but usually no shorter. In fact, the shortest pulse length used to drill the holes in the previously shown SEM photos was approximately 25 ns.

Currently, micro-holes drilled using femtosecond technology are limited to research and development facilities. There are several femtosecond lasers at LLNL.

Micro-holes drilled using pulse lengths in the nanosecond regime more than likely will not produce high enough integrity holes to meet the stringent NIF requirements for the target capsules. Laser pulses on the order of nanoseconds are too long, resulting in significant heat transfer to the surrounding lattice structure, causing re-melt, and thermal cracking of the material, as evidenced in the SEM photographs.

It should be pointed out that, even using a femtosecond pulse laser, there are still the issues of aspect ratio and taper angle. For the most part, only thermal effects will be eliminated. Preliminary studies have shown that even femtosecond pulsed lasers create a taper angle, and that it is not much better than the taper angles associated with longer pulse lasers.

New research suggests that using a flat-top beam will help reduce this, but it is not known just how much of an effect it will have on very small holes

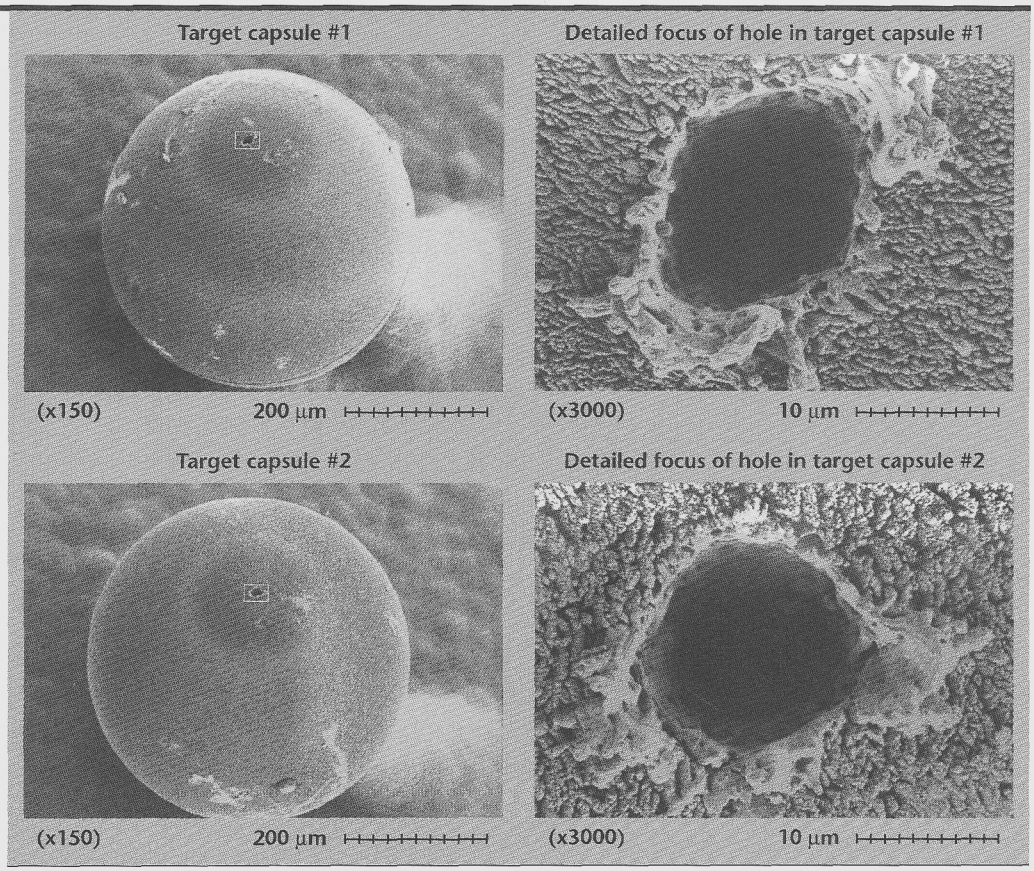

Figure 5. SEM photographs of laser-drilled holes in two sample target capsules, (a) and (b).

with a high aspect ratio. The ablation process, when using a femtosecond laser, is mostly dependent on the intensity of the beam and the material properties. During drilling, an energy field is created in the walls and results in current conduction. This leads to a loss of energy through the side walls. The smaller and deeper the hole is, the more energy is lost through the side walls. When the intensity of energy gets too low, stalling occurs where no material is ablated.

Efforts are being made at LLNL to drill holes in either beryllium foil or actual target capsules using femtosecond laser pulses. We have the means to drill in a vacuum and have created holes using a flat-top beam. We have not yet attempted to drill small high-aspect ratio holes. Initial projections are that drilling a 1-μm-diameter hole 100 μm deep, without any taper, would be virtually impossible, but that drilling a 3- to 5-μm-diameter hole approximately 50 μm deep with very little taper, could probably be done with a minimum number of problems. Once the holes have been drilled, they can be photographed and compared to the holes already drilled using nanosecond pulse lengths.

Conclusions

From the information available, it does seem feasible to create micro-holes suitable for filling. Based on preliminary investigations, however, it does not seem likely that a commercial company will be able to produce these holes. SEM photos of commercially-drilled holes show an excessive amount of thermal damage due to laser pulse lengths of relatively long durations (nanoseconds or longer). Furthermore, most commercial companies are not equipped with the appropriate lenses and laser set-up to drill <5-μm-sized holes, because the current demand is not high enough.

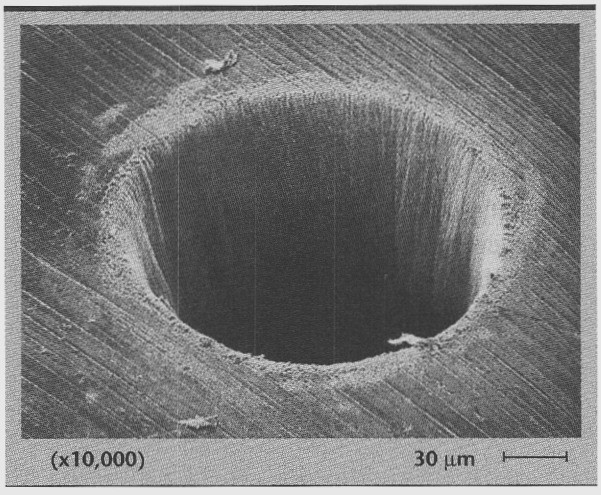

Figure 6. SEM photograph of hole drilled in 100-μm-thick steel, using a femtosecond laser.

Initial studies indicate that using a laser capable of femtosecond pulses may help to eliminate the thermal damage caused by longer pulse length lasers and could prove beneficial in creating holes in ICF target capsules suitable for filling. Efforts are being made to have preliminary sample holes made at LLNL. Although not delineated in this report, studies are currently on-going to address the issues of sealing the holes, once drilled, and then polishing the capsules to produce the necessary surface finish required.

References

1. Korner, C., R. Mayerhofer, M. Hartmann, and H. W. Bergmann (1996), "Physical and material aspects in using visible laser pulses of nanosecond duration for ablation," *Applied Physics A*, **63**, pp. 123–131.

2. Luft, A., A. Franz, J. Emsermann, and J. Kaspar (1996), "A study of thermal and mechanical effects on materials induced by pulsed laser drilling," *Applied Physics A*, **63**, pp. 93–101.

3. Stuart, B. C., M. D. Feit, A. M. Rubenchik, B. W. Shore, and M. D. Perry (1995), "Physical Review Letters," March, Vol. **74** (12), pp. 2248–2251.

4. Chichkov, B. N., C. Momma, S. Nolte, F. von Alvensleben, and A. Tünnermann (1996), "Femptosecond, picosecond, and nanosecond laser ablation of solids," *Applied Physics A*, **63**, pp. 109–115.

5. Ihlemann, J., A. Scholl, H. Schmidt, and B. Wolff-Ronke (1995), "Nanosecond and femtosecond excimer-laser ablation of oxide ceramics," *Applied Physics A*, **60**, pp. 411–417.

6. Preuss, S., A. Demchuk, and M. Stuke (1995), "Sub-picosecond UV laser ablation of metals," *Applied Physics A*, **61**, pp. 33–37.

7. Momma, C., B. N. Chichkov, S. Nolte, F. von Alvensleben, A. Tünnermann, H. Welling, and B. Wellegehausen (1996), "Short-pulse laser ablation of solid targets," *Optics Communications*, August, Vol. **128**, pp. 101–109.

8. Stuart, B. C., M. D. Perry, A. M. Rubenchik, J. Neev, S. Herman, H. Nguyen, P. Armstrong, and L. B. DaSilva (1997), "Femtosecond Laser Materials Processing," *CLEO, Glen Arm, MD.*

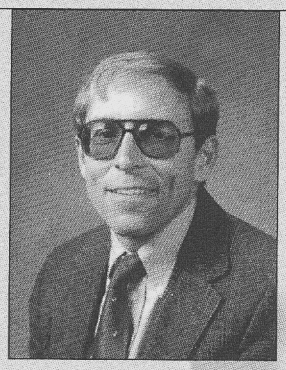

Donald R. Lesuer, Thrust Area Leader

During FY-97, work within the Materials Science and Engineering thrust area was focused on material modeling. Our motivation for this work is to develop the capability to study the structural response of materials as well as materials processing.

These capabilities have been applied to a broad range of problems, which support many programs at Lawrence Livermore National Laboratory. Recent examples of structural response problems studied include material fracture (such as interface failure), damage in laser optics, the response of weapons components (such as high explosives) and the failure of composite materials. For materials processing, typical problems studied include metal forming, laser processing, casting, and heat treating.

To improve our ability to model material behavior, much of our work involves developing new material models and failure models, as well as applying the codes to new problems. Most investigations involve experimental studies to gather basic information on material response and to validate codes or material models. Projects are inherently multi-disciplinary, involving several investigators with expertise in materials and mechanics.

Our thrust area studies for FY-97 are described in the following three articles: 1) Evolution of Anisotropic Yield Behavior; 2) Modeling of She Localization in Materials; and 3) Modeling of Casting Microstructures and Defect

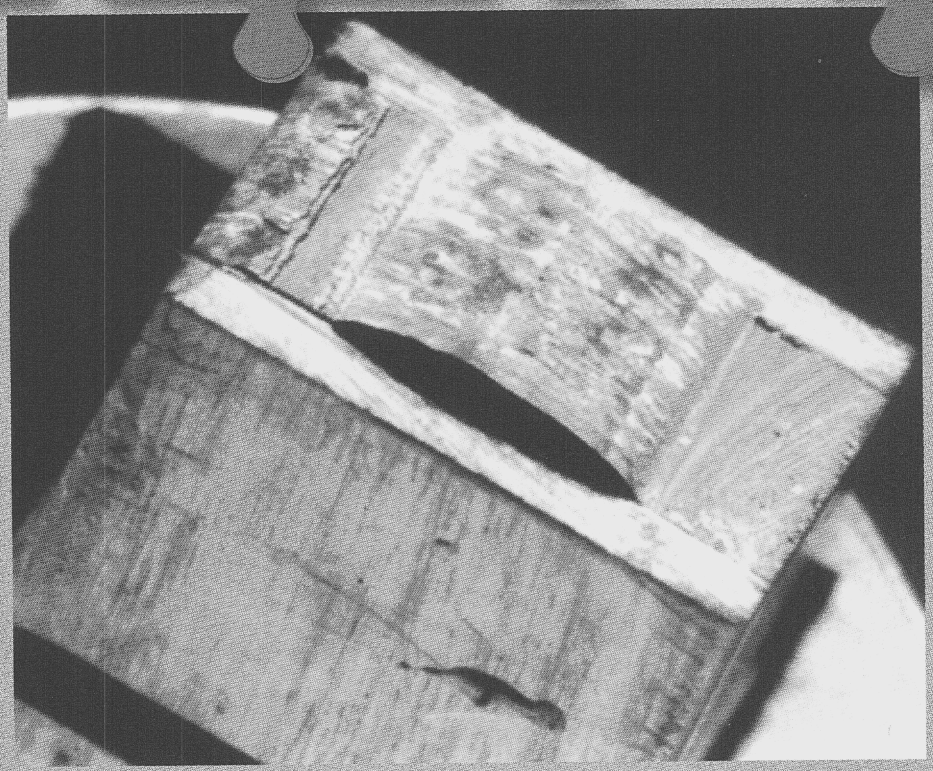

Materials Science and Engineering

5

5. Materials Science and Engineering

Overview
Donald R. Lesuer, Thrust Area Leader

Evolution of Anisotropic Yield Behavior
Daniel J. Nikkel, Jr., Arthur A. Brown, and James Casey 5-1

Modeling of Shear Localization in Materials
Donald R. Lesuer, Mary M. LeBlanc, Robert A. Riddle, and Bert R. Jorgensen 5-7

Modeling of Casting Microstructures and Defects
Arthur B. Shapiro and J. Del Eckels 5-13

Evolution of Anisotropic Yield Behavior

Daniel J. Nikkel, Jr.
Manufacturing and Materials Engineering Division
Mechanical Engineering

Arthur A. Brown and James Casey
University of California
Berkeley, California

We have developed an experimental capability for measuring the yield behavior of elastic-plastic materials under multiaxial loading conditions. This enables us to determine the multi-dimensional yield surface of the material, both in its initial state and as it evolves during large inelastic deformations. This surface, and its functional representation, is an essential component of the constitutive theory for non-linear anisotropic elastic-plastic materials. Experimental data provided by this facility aids the development of more physically realistic and complete models for materials undergoing large inelastic deformations.

Introduction

Generally speaking, polycrystalline metals subjected to loads or deformations initially exhibit elastic (reversible) behavior. However, if the deformation or loads become large enough, the material begins to exhibit plastic behavior (that is, there is no longer a one-to-one correspondence between stress and strain, the stress response is path dependent, and residual—plastic—deformations remain after external loads are removed.) This gives rise to the theoretical idealization of an elastic-plastic material, and in particular, the notion of a yield function,[1]

$$f\left(s_{kl}, e^{p}_{kl}, k, \ldots\right) = g\left(e_{kl}, e^{p}_{kl}, k, \ldots\right) \quad .$$

This relationship, a key ingredient of the constitutive theory of elastic-plastic materials, describes the boundary between loads (or deformations) that produce only elastic behavior, and those that result in inelastic deformation (**Fig. 1**). Here, s_{kl} denotes the components of the stress tensor; e_{kl} denotes the components of the strain tensor; e^{p}_{kl} denotes the components of the plastic strain tensor; k is a scalar measure of work hardening; and the ellipses represent other inelastic state variables that may be present, depending on the constitutive theory.

For fixed values of the inelastic variables, the yield condition described by $f = 0$ (or $g = 0$) can be interpreted geometrically from the point of view of stress space (or strain space), the multi-dimensional space whose axes are the components of stress (or strain), as a surface that bounds the region in which only elastic behavior occurs (the elastic region). As long as the loading of the material is such that the current state is enclosed by the yield surface, the material responds elastically. But if the loading causes the current state to intersect the yield surface and try to move outward from this surface, inelastic behavior occurs and plastic deformation results. The current state never moves outside the yield surface, but instead the surface is pushed along with it, and may also change shape as the inelastic deformation increases.

Most plasticity models implemented into numerical codes assume a fixed shape of the yield surface (for example, elliptical). What distinguishes different models is how the yield surface evolves, for example by allowing it to rigidly translate or to change in size while maintaining its shape according to some strain- (or strain-rate- or temperature-) dependent hardening law. While the initial yield surface of isotropic materials may be reasonably represented by an ellipse, subsequent to even moderate plastic deformation, the shape of the yield surface in real materials can change significantly (**Fig. 1**). For this reason, simple representations of the yield function will be satisfactory only under very restrictive loading

conditions (for example, monotonic or uniaxial), and are totally inadequate for general multiaxial loading conditions, during which loads can reverse and change direction during the history of loading.

Motivated by these considerations, and the fact that the vast majority of experimental data available is for uniaxial (and generally monotonic) loading, we have developed an experimental capability to map out the yield surface at various fixed states of large inelastic deformation under multiaxial states of loading. By determining the yield surfaces on a single specimen at multiple fixed states, the evolution of the yield surface during plastic deformation can be observed, and better quantitative representations of the yield function and hardening characteristics of the material can be developed. This will lead to better constitutive equations for anisotropic materials undergoing large inelastic deformations.

Progress

The experimental determination of the yield surface of the material under two-dimensional loading is carried out by loading a specimen under multiaxial conditions and probing until the point of yield is reached, then backing off and probing in a different direction in stress space, until the entire surface is mapped out. A multiaxial MTS hydraulic test machine with an axial load capacity of ±50,000 lbf and ± 20,000 in.-lbf in torsion is used for these experiments.

Although it can operate in either load, strain, or displacement control modes, it was found best to carry out all testing in load control. For the small load and strain increments being used during yield surface probing, it was found that this method gave the best level of accuracy.

Preliminary tests showed that the ratio of load noise to load increment was significantly smaller than the ratio of strain noise to strain increment, and further, that displacement control was impossible, since the rotation increment corresponding to the desired rotation step size was more than a factor of 100 smaller than the noise in the rotation measurements.

There are three basic issues to be addressed in the development of this experimental capability: 1) specimen design and preparation; 2) automated control of the testing machine; and 3) experimental methodology for the determination of yield.

Specimen Design

A specimen to be used for mechanical behavior characterization should have a gage section where the state of stress and deformation during testing are homogeneous, as are the material properties. For axial and torsional loading, this suggests using a thin-walled tubular specimen. To map out the entire yield surface (in the two-dimensional axial-torsional sub-space of stress-space), it is necessary to subject the specimen to positive and negative torsional loads in combination with tensile and compressive axial loads.

Moreover, one must be able to apply a large enough stress to cause significant plastic deformation (up to 20%) for the full range of experiments under consideration. A thin specimen can be susceptible

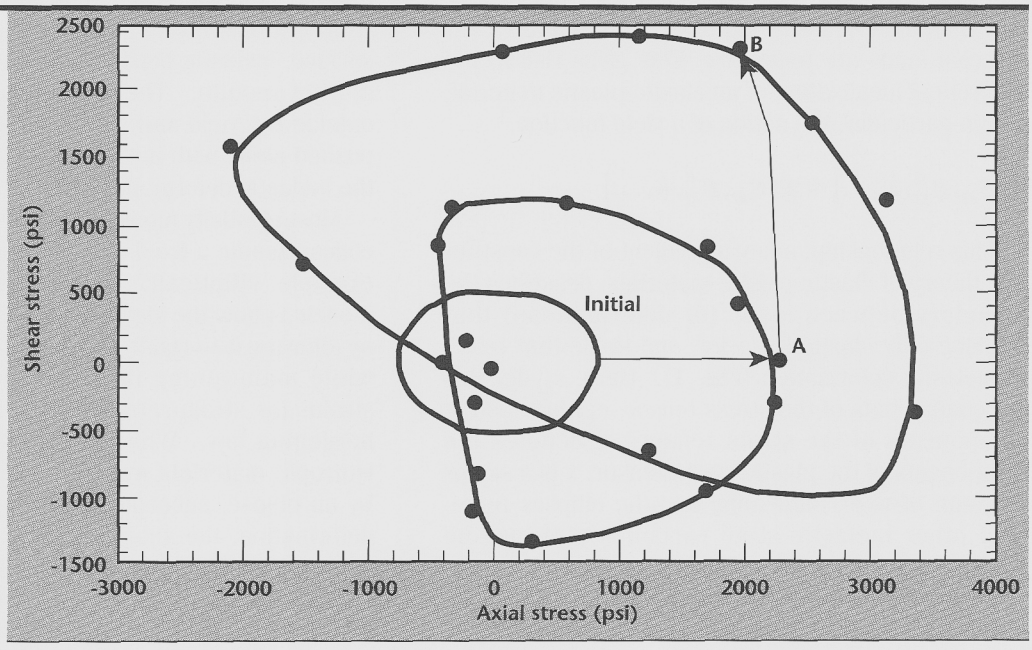

Figure 1. Initial yield surface, and measured points on two subsequent yield surfaces, for a single 1100 aluminum specimen. The subsequent yield surfaces for pre-loads to point A, and then to B, show significant deviation from an idealized ellipse, even though the strains involved are moderately small.

to buckling, and while making the specimen thicker makes it more resistant to buckling, this reduces the overall stress that can be applied to the material and compromises the homogeneity of the stress and strain state in the gage section during torsion.

In addition, it is desirable to make the overall specimen geometry compatible with other experiments making use of the machine so as to avoid redesign of fixturing.[2] Balancing these contrasting goals, a specimen geometry was arrived at, consisting of a circular cylinder 9 in. long (4 in. gage length), 2 in. inside diameter, with a 0.1-in. wall thickness. These specimens were machined out of thicker walled stock of 1100 aluminum, and the ends were potted with conical sections of epoxy to allow for gripping.

For the mechanical properties in the gage section to be sufficiently homogeneous, the microstructure of the specimen must be much finer than the wall thickness. This was accomplished through heat treatment. The first heat treatment tried, following Bell,[3] whose experiments we wished to compare ours with, resulted in extremely large grains that were unacceptable. The heat treatment process that was found to give the best grain structure followed Phillips[4]: heating to 650 °F in 15 min, and maintaining for 1 h, followed by furnace cooling. This resulted in equiaxed grains with an average size of 0.003 in.

Test Machine Control and Data Acquisition

The numerical control of the test machine and the data acquisition are coordinated via a custom application written in LabView II for this project. This program communicates with the test machine's load cells and receives input from four strain gages affixed to the specimen. Three of the strain gages are in a 45° rosette, bonded in the center of the gage length such that the center gage element is in the longitudinal direction, and the other two elements are aligned at 45° to each side of the longitudinal axis.

One extra axial strain gage is placed diametrically opposite to the rosette and is used to check that the specimen is properly aligned and that no bending occurs during testing. The data inputs to the LabView program are the test machine's axial force, axial stroke, torsional load, and rotation, along with conditioned signals from the strain gages. The operator can specify end states (either as loads or displacements), as well as ramp rates of force and torque (or stroke and rotation) for getting from one fixed state to the next. Up to four different sets of cross-plotted output data are simultaneously presented, to visually observe the nature of the material behavior (**Fig. 2**).

Experimental Methodology for Determination of Yield

The surface that we are trying to map is the yield surface at an arbitrary fixed inelastic state. Ideally, all points on a given yield surface should be determined without inducing any further plastic deformation to the specimen. In practice, however, a point on the yield surface can only be determined by reaching, and slightly exceeding, the yield point.

The challenge therefore, in developing an experimental procedure for mapping the surface, is to do it in such a way that all the points necessary to characterize a given surface (probably a minimum of 10 points) can be located while changing the inelastic state (and hence the surface itself) as little as possible. The procedure that has been developed can detect yield without producing a plastic strain greater than 5×10^{-6}, with a good level of repeatability.

From whatever load state the specimen is currently in, a linear load path segment in stress-space is specified, and is carried out in step increments in which no component of stress changes by more than 50 psi. Under multiaxial loading conditions, to see yielding occur, it is necessary to watch multiple components of the response simultaneously.

Observing the raw stress/strain response for different directions is not sufficiently sensitive to determine yield as soon as is desired. Instead, prior to reaching the yield surface, data is taken during purely elastic behavior, then the path is retraced. A best linear fit to the stress/strain response is determined, and a new modified strain measure for each component direction of interest is defined as the actual strain minus the fitted linear elastic response.

When the load vs modified strain output is observed during the test, the point at which yielding begins to occur is much clearer (**Fig. 2**). Prior to reaching the proportional limit, the data points are on a nearly vertical line. When three successive data points (with 1-microstrain error bars) fall away from the abscissa in three out of the four load vs modified strain plots (corresponding to different strain-gage directions), the specimen is considered to have yielded, and a point on the yield surface is identified. The load is then reversed, taking the specimen back to a state within the yield surface, and a new end state is sought.

This process is repeated until a sufficient number of points have been located on the yield surface to characterize it. Once the yield surface for one inelastic state is so obtained, an excursion involving plastic deformation can be applied to the same specimen, and the process described above can be repeated to map the yield surface for the new inelastic state.

Figure 1 shows actual measured data from a single 1100 aluminum specimen, where the initial yield surface is shown, along with the measured surfaces after first applying a tensile stress of 2400 psi (point A, where the axial plastic strain is approximately 0.11%), and subsequently following a path along which both axial and torsional loads varied, to point B (where the axial plastic strain is approximately 0.96%, and the plastic shear strain is approximately 1.4%). Even with these moderately small strains, the deviation from an idealized elliptical yield surface is clearly seen.

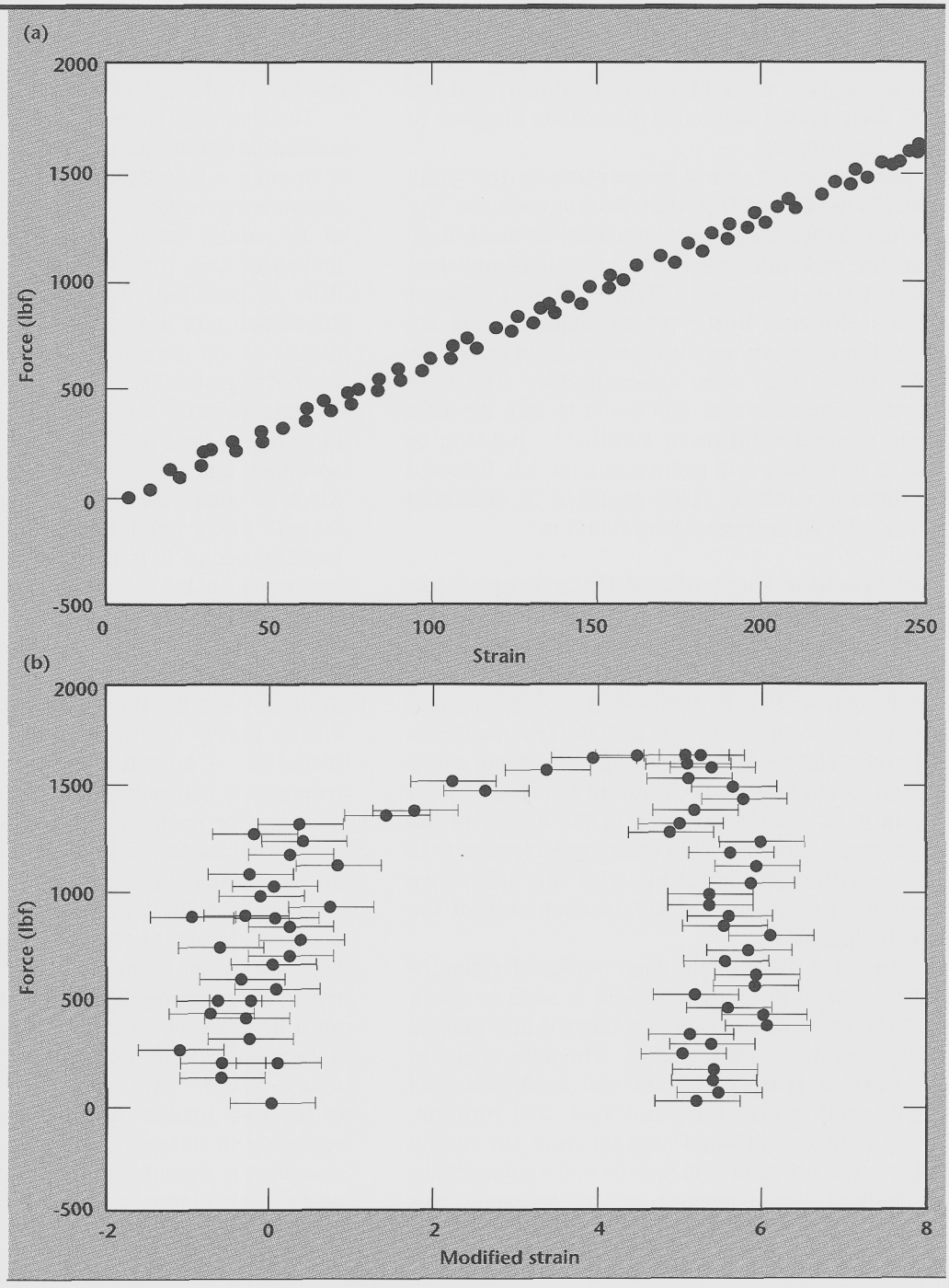

Figure 2. A typical cross-plot of output data during loading and unloading, showing (a) load vs strain; and (b) load vs the modified strain measure described in the text. The yielding of the material is more readily seen in the load vs modified strain plot. The operator must simultaneously observe four such plots, corresponding to different strain-gage directions, to ensure detection of yield for an arbitrary direction of loading.

Future Work

We now have the ability to conduct novel experiments in finite plasticity. At present, the procedure requires significant operator expertise and interaction. Speed of testing could possibly be improved by automating the yield surface probing and mapping process via some control algorithm. However, this may not be a practical possibility in the near term, since the output data needs to be interpreted with a great deal of judgment during testing.

We plan to use these experiments to aid in the development of better constitutive equations for non-linear plasticity. We plan to examine materials of particular programmatic relevance, such as tantalum, which is a target material for the Multi-Scale Material Modeling effort. These experiments can be used to test predictions of models coming out of the multi-scale approach.

We also plan to conduct experiments to address an open question in the continuum theory of finite plasticity, namely the correct identification of the plastic strain tensor in the context of general finite deformations.[5,6]

Acknowledgment

Contributions to this project from J. Casey result from work supported by a grant from the Solid Mechanics Program of the National Science Foundation, administered by the University of California, Berkeley. Part of the support for A. Brown's work, and material used during the development of the experimental procedure, were also provided through this grant.

References

1. Naghdi, P. M. (1990), "Critical Review of the State of Finite Plasticity," *J. of Appl. Math. and Phys.* (ZAMP), **41**, pp. 315-394.

2. Groves, S., R. Sanchez, and W. Feng (1991), *Multiaxial Failure Characterization of Composites*, Lawrence Livermore National Laboratory, Livermore, CA, (UCRL-JC-105244).

3. Bell, J. (1983), "Continuum Plasticity at Finite Strain for Stress Paths of Arbitrary Composition and Direction," *Arch. Rat. Mech. Anal.*, **84**, pp. 201-232.

4. Phillips, A., C. Liu, and J. C. Justusson (1972), "An Experimental Investigation of Yield Surfaces at Elevated Temperatures," *Acta Mechanica*, **8**, pp. 119-146.

5. Casey, J., and P. M. Naghdi (1992), "A Prescription for the Identification of Finite Plastic Strain," *Int. J. Engr. Sci.*, **30**, pp. 1257-78.

6. Casey, J., and P. M. Naghdi, (1992), "On the Identification of Plastic Strain at Finite Deformation," *Defects and Anelasticity in the Characterization of Crystalline Solids*, L. M. Brock, Ed., ASME AMD Vol. **148**, pp. 11-33.

Modeling of Shear Localization in Materials

Donald R. Lesuer and Mary M. LeBlanc
Manufacturing and Materials Engineering Division
Mechanical Engineering

Robert A. Riddle and Bert R. Jorgensen
Defense Technologies Engineering Division
Mechanical Engineering

The deformation response of a Ti alloy, Ti-6Al-4V, has been studied during shear localization. The study has involved well-controlled laboratory tests on a double-notch shear sample. The results have been used to provide a comparison between experiment and the predicted response using DYNA2D and two material models (the Johnson-Cook model and an isotropic elastic-plastic-hydrodynamic model). The work will serve as the basis for the development of a new material model that represents the different deformation mechanisms active during shear localization.

Introduction

Shear Localization

Shear localization is a common deformation and failure process that occurs when deformation is concentrated in a single macroscopic shear zone. It can occur in many materials at moderate and high strain rates due to localized, adiabatic heat production. Zener and Holoman[1] have estimated that during simple punching of a metal plate, the temperature increase in a shear band due to adiabatic heat production can be as high as 1000 °C. This increase in temperature produces thermal softening in the band and localization of plastic flow.

Shear localization is observed in many material processing operations, as well as during the in-service performance of materials. Typical material processing operations in which shear localization is observed include material cutting, numerous forming operations (such as rolling and forging), and material polishing.

In many cases, the success or failure of these processing operations is defined by shear localization. It is typically observed during the ballistic penetration and perforation of armor materials, the performance of munitions and explosive fragmentation, all problems of interest to programs at Lawrence Livermore National Laboratory (LLNL).

Despite its common occurrence and importance, shear localization remains poorly understood and is difficult to model accurately. Much of this difficulty arises from the large strains and adiabatic heat produced which, in turn, causes increases in temperature with resulting changes in material microstructure, material properties, and deformation mechanisms. Large changes in strain rate are also produced.

Progress

Material models that can adequately represent the deformation response during shear localization must account for large strains (and the resulting strain hardening or softening), as well as large changes in strain rate and temperature. Several models have been developed that can represent, to varying degrees, the high rate deformation response of materials. Examples include models by Johnson-Cook (JC),[2] Zerilli-Armstrong (ZA),[3,4] and Follansbee-Kocks (mechanical threshold stress model)[5]. Two of these models (JC and ZA) have been introduced into the DYNA codes. Of these two models, the JC model is much more widely used, primarily because of the availability of material constants in the constitutive equations.

The objective of this project is to critically assess the ability of existing material models to represent

the deformation response of materials during shear localization. We have done this using well-controlled laboratory experiments involving a double-notch shear sample. The experimental results have been compared with the predictions of the DYNA2D code using the JC model, as well as an isotropic elastic-plastic-hydrodynamic (EPH) model commonly used for large strain problems. The work will serve as the basis for the development of a new material model which represents the different deformation mechanisms active during shear localization.

Material Models

The formulation for the JC model is empirically based, and represents the flow stress with an equation of the form,

$$\sigma = \left[A + B\varepsilon^{n}\right]\left[1 + C\ln\dot{\varepsilon}^{*}\right]\left[1 - T^{*}\right], \qquad (1)$$

where σ is the effective stress; ε is the effective plastic strain; $\dot{\varepsilon}^{*}$ is the normalized effective plastic strain rate (typically normalized to a strain rate of 1.0 s^{-1}); T^{*} is the homologous temperature; n is the work hardening exponent; and A, B, C, and m are constants.

The values of A, B, C, n, and m are determined from an empirical fit of flow stress data (as a function of strain, strain rate, and temperature) to **Eq. 1**. For shear localization problems, we can assume that an arbitrary percentage of the plastic work done during deformation produces heat in the deforming material. For many materials, 100% of the plastic work becomes heat in the material. Thus, the temperature used in **Eq. 1** can be derived from the increase in temperature, according to the following expression:

$$\Delta T = \frac{\alpha B}{\rho c\left(n+1\right)}\varepsilon^{n+1}, \qquad (2)$$

where ΔT is the temperature increase; α is the percentage of plastic work transformed to heat; c is the heat capacity; and ρ is the density.

The EPH model uses an arbitrary effective stress/effective plastic strain curve, while a tensile cut-off pressure is defined for the principal stress spall criterion. A linear polynomial was chosen to define the hydrostatic equation of state. Material properties were derived from handbook data. The model is a popular choice for large strain plasticity problems. However, it does not account for strain rate or temperature effects and thus its accuracy for predicting deformation response during shear localization is largely unknown.

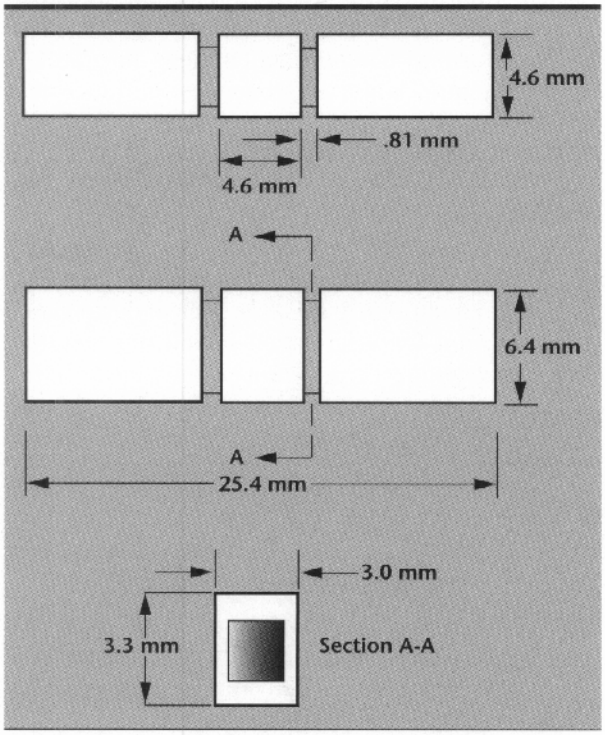

Figure 1. Double-notch shear specimen used in this study.

Experiments

The double-notch shear sample, which is shown schematically in **Fig. 1**, is designed to produce a homogeneous strain state of pure shear in the gage section of the sample at a reasonably constant displacement velocity. Deformation in the gage section becomes localized and adiabatic shear can result. The samples were loaded using a split Hopkinson pressure bar (SHPB) apparatus and data was obtained at strain rates of 10^{-3} to 10^{-4} s^{-1}. A schematic diagram of this apparatus is shown in **Fig. 2**.

In the SHPB tests, the strain histories for the incident ($\varepsilon_I(t)$) and transmitted ($\varepsilon_T(t)$) waves were measured and analyzed to determine the nominal shear stress/strain/strain-rate response of the sample during the shear test. The stress and strain-rate response were calculated from the following expressions:

$$\tau(t) = E\frac{A_o}{A}\varepsilon_T(t), \qquad (3)$$

and

$$\dot{\gamma}(t) = \frac{-2C_o}{L}\varepsilon_R(t), \qquad (4)$$

with

$$\varepsilon_I(t) + \varepsilon_R(t) = \varepsilon_T(t), \tag{5}$$

where $\tau(t)$ is the shear stress; E is the elastic modulus of the bar; A_0 is the cross-sectional area of the bar; A is the specimen shear area; $\dot{\gamma}(t)$ is the shear strain rate; C_0 is the longitudinal sound velocity in the bar; L is the gage length; and $\varepsilon_R(t)$ is the reflected strain in the bar. The resulting strain in the sample, $\varepsilon(t)$, was obtained by integrating the strain rate history:

$$\gamma(t) = \int_{t_0}^{t} \dot{\gamma} dt . \tag{6}$$

During FY-97, experiments and simulations of the double-notch shear experiment were done for a Ti alloy, Ti-6Al-4V. The tests were done at a number of different projectile velocities to get experimental results over a range of strain rates.

Results and Analysis

Modeling. Simulations of the experiment were performed using the finite element code DYNA2D and the two material models described above, the isotropic EPH model (number 10) and the JC model. The simulations were used as an aid in both specimen and experiment design, as well as to evaluate the material models.

For the specimen design studies, three notch configurations were considered. Additional details of the simulations and the results are available in other references.[6,7]

Previous studies[8,9] using the double-notch shear specimen have shown that significant plastic bending can occur in the sample, which can cause deviations from the desired strain state of pure shear. The finite element simulations show that these bending effects can be minimized with proper specimen design. The results showed that a specimen containing a square notch (with corner radius equal to .002 in.) on all four sides of the sample had the highest ratio of shear strain to bending, and thus was selected for the experimental work.

The resulting specimen, shown in **Fig. 1**, is a significant improvement over test sample configurations used by other investigators. Simulations were also done to show the influence of important experimental variables, such as projectile length, incident bar length and strain gage placement. Results here were a significant aid in experiment design and data interpretation.

The deformed configuration for a sample tested with a projectile velocity of 1000 in./s is shown in **Fig. 3**. The specimen is near the point of maximum deformation and bending in the specimen is evident. Contours of effective plastic strain are also shown and illustrate that deformation is concentrated in an arc through the gage section. Similar deformation patterns and failure modes were obtained for both the JC and the EPH material models. Post-test examination of tested samples confirms the predictions of the simulations and shows that deformation was concentrated in an arc through the gage section. However, the JC model predicts greater deformation for a given projectile impact velocity. This is primarily a result of the softening caused by temperature increases in the shear zone.

Experimental Results. Experiments were conducted over a range in strain rates from an average shear strain rate of 3.8×10^3 to 1.1×10^4 s^{-1}. The shear stress and shear strain were calculated

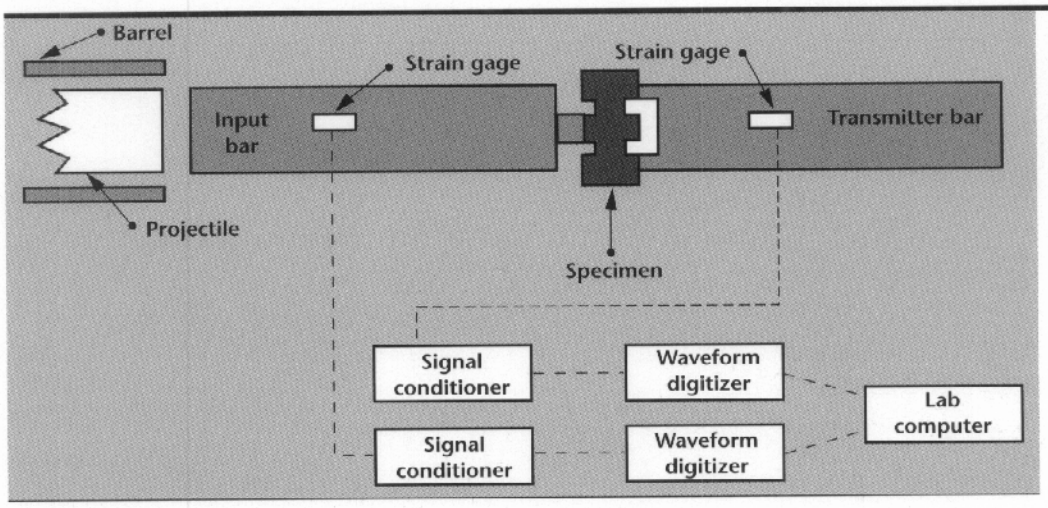

Figure 2. Schematic diagram of the split Hopkinson pressure bar apparatus used to load the double-notch shear specimen.

using **Eqs. 3, 4,** and **6**. The effective stress and effective plastic strain were then determined from the following expressions:

$$\sigma = \sqrt{3}\tau \tag{7}$$

and

$$\varepsilon_p = \left(\gamma - \tau/G\right)\Big/\sqrt{3}\,, \tag{8}$$

where σ is the effective stress; ε_p is the effective plastic strain; and G is the shear modulus. The effective stress/effective plastic strain response of the sample is shown in **Fig. 4** for a test conducted at 7000 s^{-1}. The adiabatic temperature rise in the sample is also shown in the figure. Sufficient flow localization occurred to promote ductile fracture with a shear strain of about .25 (effective plastic strain of about .14). Despite the limited strains-to-failure, a temperature increase in the sample of about 40 °C is expected.

Figure 5 shows a macro-photograph of a typical failed sample. Examination of samples deformed to strains near, but slightly less than, the failure strain showed cracks at the square corners of the gage section. The cracks resulted from the stress concentration at the corners and were the origins of failure. Final shear fracture occurred along an arc in the gage section due to intense plastic shear, which is consistent with the predictions of the finite element simulations shown in **Fig. 3**. The critical condition for shear fracture was obtained before significant thermal softening could be obtained.

The stress/strain response of the sample, as predicted by the simulation, was determined for an element in the center of the gage section. Calculations were done for both the EPH and the JC material models. The results are shown in **Fig. 4**, and compared against experimental data. The EPH model predicts flow stresses that are typically 200 to 300 MPa greater than those observed experimentally.

Figure 3. Simulation results showing the deformed configuration and contours of effective plastic strain for the double-notch shear test. Sample was loaded with a projectile velocity of 1000 in./s.

The calculations also predict a positive work hardening rate that is not observed experimentally. Some of these differences are due to the material model, which does not account for adiabatic heat, the resulting increase in temperature, and the decrease in strength. Experimental data available in the literature shows that the 40-°C increase in temperature observed here could lower the flow stress by about 100 MPa.[10] For the JC model, the predicted flow stress in the sample is about 100 MPa higher than that observed experimentally. Thus, the JC model shows closer agreement with experimental data than the EPH model. In addition, the JC model shows some thermal softening due to adiabatic heat production, which is consistent with experimental observations.

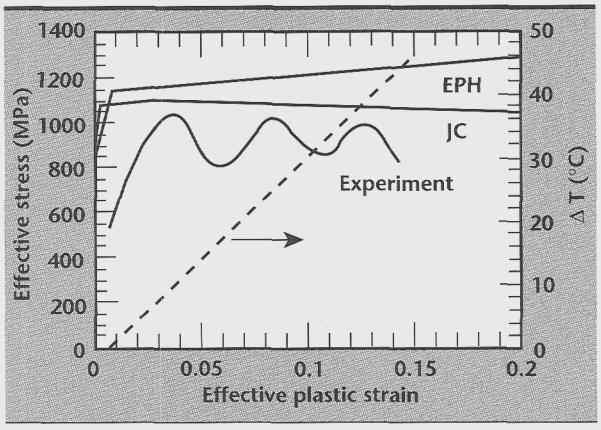

Figure 4. Simulation results and experimental data of effective stress vs effective plastic strain for the double-notch shear sample shown in Figure 1. Results are shown for both the Johnson-Cook and the elastic-plastic-hydrodynamic material models. Adiabatic temperature increase is shown in the figure. Deformation rate is 7000 s^{-1}.

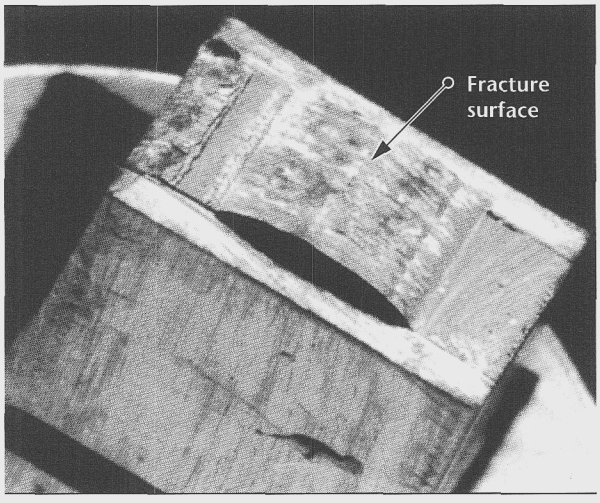

Figure 5. Macro-photograph of a typical fractured sample. The fracture surface is indicated. Final fracture occurred along an arc in the gage section due to intense plastic shear.

Summary and Conclusions

The deformation response of a Ti alloy, Ti-6Al-4V, has been studied during shear localization. The study has involved well-controlled laboratory tests involving a double-notch shear sample. The results have been used to provide a comparison between experiment and the predicted response using DYNA2D and two material models. The primary conclusions from the study are as follows:

1) The deformation of the double-notch shear specimen has been studied using finite element analysis and an optimal specimen design for obtaining shear stress/shear strain data at high rates has been established.
2) The simulations show that deformation is concentrated in an arc through the gage section. Post-test examination of fractured samples shows that the simulations for both the EPH and the JC material models can represent the macroscopic deformation and fracture patterns observed in the sample.
3) For the Ti-6Al-4V alloy studied, shear fractures were obtained with a shear strain of about .25. A temperature increase of about 40 °C is expected.
4) The EPH model predicted flow stresses that were 200 to 300 MPa higher than experimental data. The calculations also predicted a positive work hardening rate that is not observed experimentally.
5) The JC model predicts flow stresses in the test sample that are closer to experimental data than the EPH model. In addition, the model correctly predicts the thermal softening observed experimentally.

References

1. Zener, C., and J. H. Hollomon (1944), "Effect of Strain Rate Upon Plastic Flow of Steel," *Journal of Applied Physics,* January, **15**, pp. 22–32.

2. Johnson, G. R., and W. H. Cook (1983), "A Constitutive Model and Data for Metals Subjected to Large Strains, High Rates and High Temperatures," *Proceedings of the Seventh International Symposium on Ballistics,* The Hague, Netherlands, pp. 541–547.

3. Zerilli, F. J., and R. W. Armstrong (1992), "The Effect of Dislocation Drag on the Stress-Strain Behavior of FCC Metals," *Acta Metallurgica et Materialia,* **40**, p. 1803.

4. Zerilli, F. J., and R. W. Armstrong (1990), "Description of Tantalum Deformation Behavior by Dislocation Mechanics Based Constitutive Relations," *Journal of Applied Physics,* **68**, p. 1580.

5. Follansbee, P. S., and U. F. Kocks (1988), "A Constitutive Description of the Deformation of Copper Based on the Use of the Mechanical Threshold Stress as an Internal State Variable," *Acta Metallurgica*, **36**, p. 81.

6. Jorgensen, B. R. (1997), *Double-Notch Shear Test Analysis Using Johnson-Cook Material Properties*, Lawrence Livermore National Laboratory, Livermore, CA.

7. Jorgensen, B. R. (1997), *A Parametric Study of Double-Notch Shear Tests Using Finite Element Analysis*, Lawrence Livermore National Laboratory, Livermore, CA.

8. Harding, J. (1985), "Double-Notch Shear Testing and Punch Loading," *Metals Handbook—Mechanical Testing*, J. R. Newby, Ed., ASM International, Materials Park, Ohio, Vol. **8**, p. 228.

9. Harding, J., and J. Huddart (1979), "The Use of the Double-Notch Shear Test in Determining the Mechanical Properties of Uranium at Very High Rates of Strain," *Mechanical Properties at High Rates of Strain, 1979*, J. Harding, Ed., The Institute of Physics, London, United Kingdom.

10. Eylon, D., J. R. Newman, and J. K. Thorne (1990), "Properties and Selection: Nonferrous Alloys and Special-Purpose Materials," *ASM Handbook*, ASM International, Materials Park, Ohio, Vol. **2**, p. 638.

Modeling of Casting Microstructures and Defects

Arthur B. Shapiro
New Technologies Engineering Division
Mechanical Engineering

J. Del Eckels
New Technologies Engineering Division
Mechanical Engineering

We have developed and implemented a micro-model for uranium that uses experimental results to estimate nucleation and growth kinetics.

Introduction

Our interest in casting is linked to Department of Energy (DOE) efforts to reduce hazardous waste and scrap produced by metal component fabrication processes. Improved processes for manufacturing plutonium and uranium components, for example, can minimize scrap metal, contaminated waste, and possible radiation exposure, and reduce the cost of equipment and facilities.

Casting is an ancient art that has been a trial-and-error process for more than 4000 years. To predict the size, shape, and quality of a cast product, manufacturers typically cast full-size prototypes. If one part of the process is done incorrectly, the entire process is repeated until an acceptable product is achieved.

One way to reduce the time, cost, and waste associated with casting is to use computer modeling to predict not only the quality of a product on the macro-scale, such as distortion and part shape, but also on the micro-scale, such as grain defects. Modeling of solidification is becoming increasingly feasible with the advent of parallel computers.

There are essentially two approaches to solidification modeling. The first is that of macro-modeling, where heat transfer codes model latent heat release during solidification as a constant, based solely on the local temperature. This approach is useful in predicting large-scale distortion and final part shape. The second approach, micro-modeling, is more fundamental. The micro-models estimate the latent heat release during solidification using nucleation and grain growth kinetics. Micro-models give insight into cast grain morphology and show promise in the future to predict engineering properties such as tensile strength.

The micro-model solidification kinetics can be evaluated using first principles or experiments. This work describes an implementation of a micro-model for uranium that uses experimental results to estimate nucleation and growth kinetics.

Progress

Mathematical Formulation

The primary and most obvious phenomenon controlling casting is the transfer of heat from the cooling metal to the mold and surroundings. The present needs of many foundries are being satisfied by relatively simple heat conduction modeling that merely indicates regions of risk for shrinkage porosity. Using empirical information, foundry engineers successfully cast parts used in life-critical applications, such as jet engine turbine components.[1]

However, DOE's vision is to move from empiricism to science-based design.

Heat conduction analysis codes model latent heat release during solidification as a constant, based solely on the local temperature. The next step in solidification modeling is to make the latent heat a function of the solidification fraction, which depends on the nucleation rate and grain growth rate. **Equation 1** expresses an energy balance for a small volume of liquid, equating the change in internal

energy to heat lost by convection to the environment plus generation of latent heat during phase change:

$$\rho c \frac{dT}{dt} = -h \frac{A}{V}\left(T - T_\infty\right) + \rho L \frac{dV_s}{dt} \quad (1)$$

where V_s is the evolution of solid.

Equation 1 can be re-arranged to give the rate of change of temperature for the control volume:

$$\frac{dT}{dt} = -\frac{h}{\rho c}\frac{A}{V}\left(T - T_\infty\right) + \frac{L}{c}\frac{dV_s}{dt}. \quad (2)$$

The first term on the right hand side of **Eq. 2** reflects the effect of casting geometry (the ratio of the surface area of the casting to its volume) on the extraction of sensible heat; the second term takes account of the continuing evolution of latent heat of fusion during solidification. It can be seen from this equation that during solidification, heating will occur if the second term on the right of **Eq. 2** becomes greater than the first one. This is known as recalescence, and is shown graphically in **Fig. 1**.

V_s depends on the number of nucleation sites (N) and the grain growth rate (dR/dt), as shown in **Eq. 3:**

$$\frac{dV_s}{dt} = N 4\pi R^2 \frac{dR}{dt}\left(1 - V_s\right). \quad (3)$$

Micro-models estimate V_s during solidification using nucleation and growth kinetics. Several kinetic rate equations have been reported in the literature.[2] Two different models can be used for the nucleation law: continuous nucleation, or instantaneous nucleation. An example of a continuous nucleation rate law is shown in **Eq. 4:**

$$\frac{dN}{dt} = \beta(T_l - T)\frac{dT}{dt}. \quad (4)$$

For an instantaneous nucleation model, the number of grains per unit volume, N, is determined by counting the number of grains in a micrograph of the casting.

An undercooling-dependent equation was used to estimate the growth rate **(Eq. 5):**

$$\frac{dR}{dt} = \mu(T_l - T)^2. \quad (5)$$

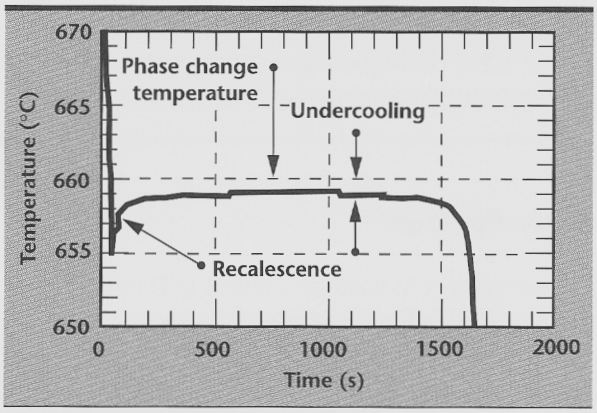

Figure 1. Solidification curve. The curve is the temperature solution of Eqs. 2, 3 and 5, using the variables defined in Table 1. Notice the prediction of recalescence at 50 s.

Table 1. Symbols and values used in the solution of Eqs. 2, 3, and 5.

Symbol	Variable	Values
A	Area	6.0×10^{-4} m^2
c	Heat capacity	920 J/kg °C
h	Convection heat transfer coefficient	2 W/m^2 °C
L	Latent heat	4.44×10^5 J/kg
N	Number of nucleation sites	1.0×10^6 grains/m^3
R	Grain radius	
T	Temperature	
T_∞	Environment temperature	25 °C
T_l	Phase change temperature	660 °C
t	Time	
V	Volume	1.0×10^{-6} m^3
V_s	Solid volume fraction	
β	Nucleation rate law constant	
ρ	Density	2698 kg/m^3
μ	Grain growth law constant	3.0×10^{-6} m/s (°C)^2

Equations 2, **3**, and **5** form a system of ordinary differential equations which can be solved numerically for the temperature, solid fraction, and grain radius, as a function of time. **Figure 1** shows the temperature response for a hypothetical material with properties defined in **Table 1**. Notice the phenomenon of recalescence occurring at a time of 50 s.

Obtaining Rate Constants from Experimental Data

The evaluation of the kinetic laws based on first principles is in the formative stages. An alternate approach is to evaluate the rate constants from experimental results on a simple casting, and then apply the laws to a production casting model. This can be accomplished by recording temperature versus time data from a solidification experiment, and then using an optimization method to calculate the grain growth constant, μ, by minimizing the difference between the experimental data and the temperature response calculated by **Eqs. 2**, **3**, and **5**.

We validated the experimental procedure using aluminum. The recorded temperature data for the top thermocouple in the sample is shown in **Fig. 2**.

A schematic of the experimental apparatus is shown in **Fig. 3**. The size of the crucible and insulation was designed by numerical modeling to produce axial solidification. Notice the horizontal shape of the calculated temperature contours at the bottom of the crucible where we are trying to produce axial solidification **(Fig. 4)**.

The initial condition for all materials in the model was set to 1673 K. Convection and radiation boundary conditions were specified on all exterior surfaces with a convection heat transfer coefficient of 5 W/m^2 °C, an ambient temperature of 298 K, and a surface emissivity of 0.8.

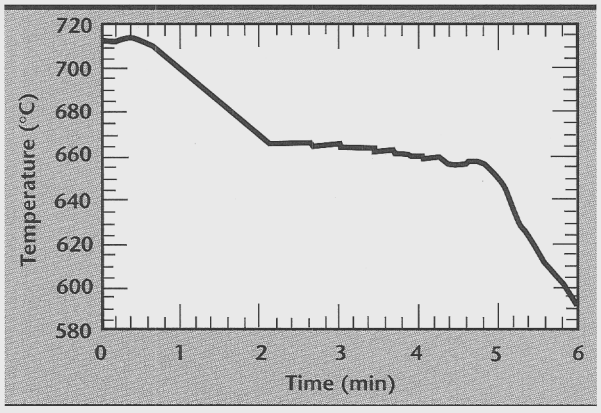

Figure 2. Temperature history recorded by the top thermocouple in Figure 3, for aluminum solidification in the crucible.

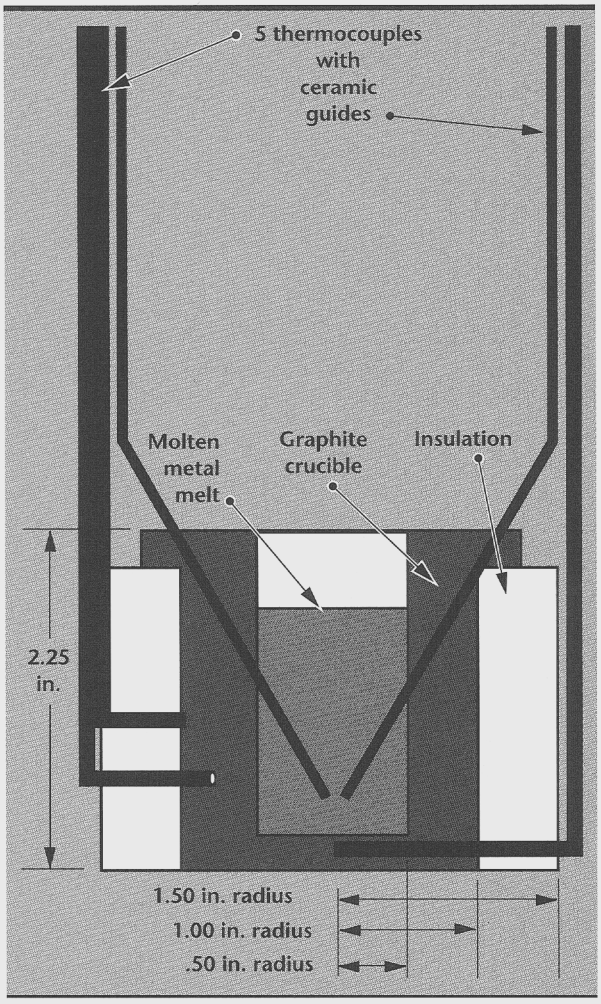

Figure 3. Schematic of the experimental apparatus. The apparatus was designed using numerical modeling to produce 1-D axial solidification, shown in Figure 4.

Future Work

We have developed a methodology to calculate solidification kinetic rate constants and have validated the experimental procedure using aluminum. Future plans are to conduct the experiment using uranium. We plan to calculate the rate constants using the Global Local Optimization code.[3]

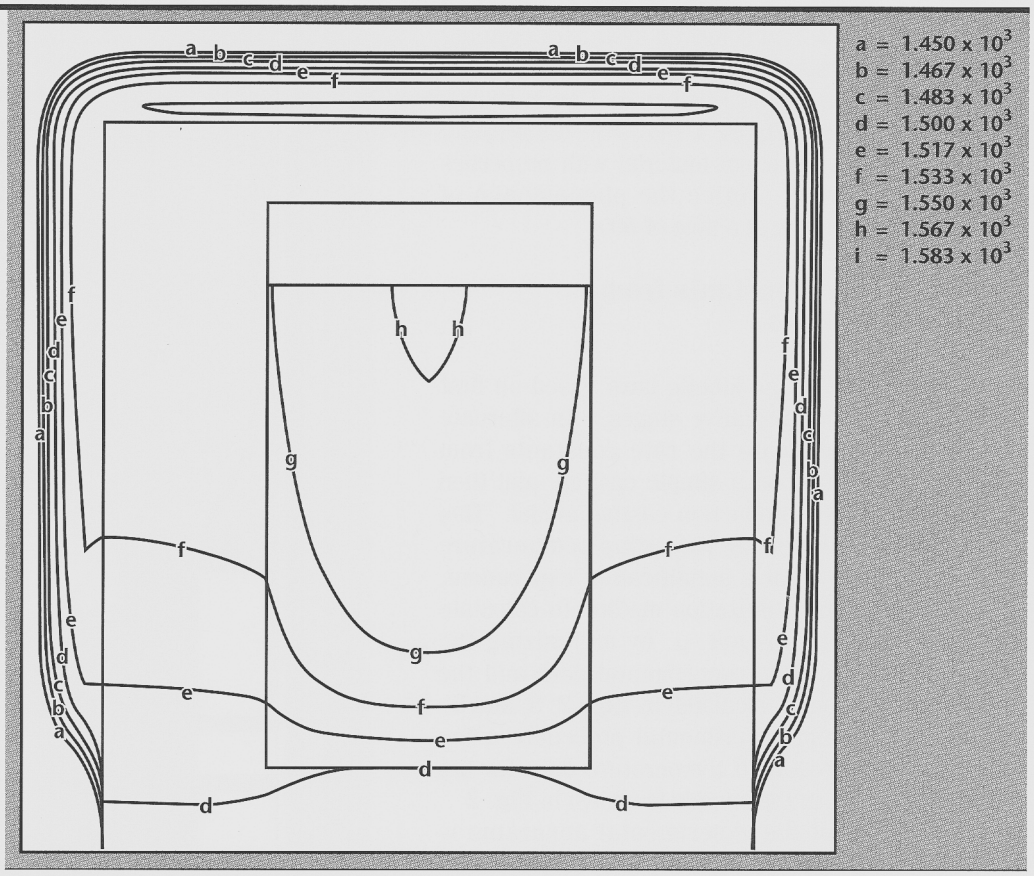

Figure 4. Calculated temperature (K) contours during solidification. Notice the horizontal shape of the contours at the bottom of the crucible where we are trying to produce axial solidification between the two thermocouple positions, as indicated in Figure 3.

References

1. Tu, J. S., and R. K. Foran (1992), "The Application of Defect Maps in the Process Modeling of Single Crystal Investment Casting," *Journal of Metals*, June, pp. 26–28.

2. Stefanescu, D. M., G. Upadhya, D. Bandyopadhyay, and I. G. Chen (1989), "Modeling the Evolution of Equiaxed Microstructure in Castings," *Journal of Metals*, February, pp. 22-25.

3. Murphy, M. J. (1996), *GLO User's Manual*, University of California, Lawrence Livermore National Laboratory, Livermore, CA.

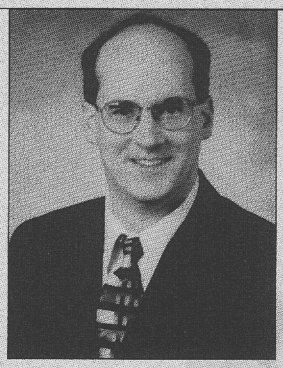

Ronald E. Haigh, Thrust Area Leader

The Power Conversion Technologies thrust area supports initiatives that enhance the core competencies of the Lawrence Livermore National Laboratory (LLNL) Engineering Directorate in the area of solid-state power electronics.

Through partnerships with LLNL programs, projects focus on the development of enabling technologies for existing and emerging programs that have unique power conversion requirements.

This year, a multi-disciplinary effort was supported which demonstrated solid-state, high voltage generation by using a dense, monolithic photovoltaic array. This effort builds upon Engineering's strengths in the core technology areas of power conversion, photonics, and microtechnologies.

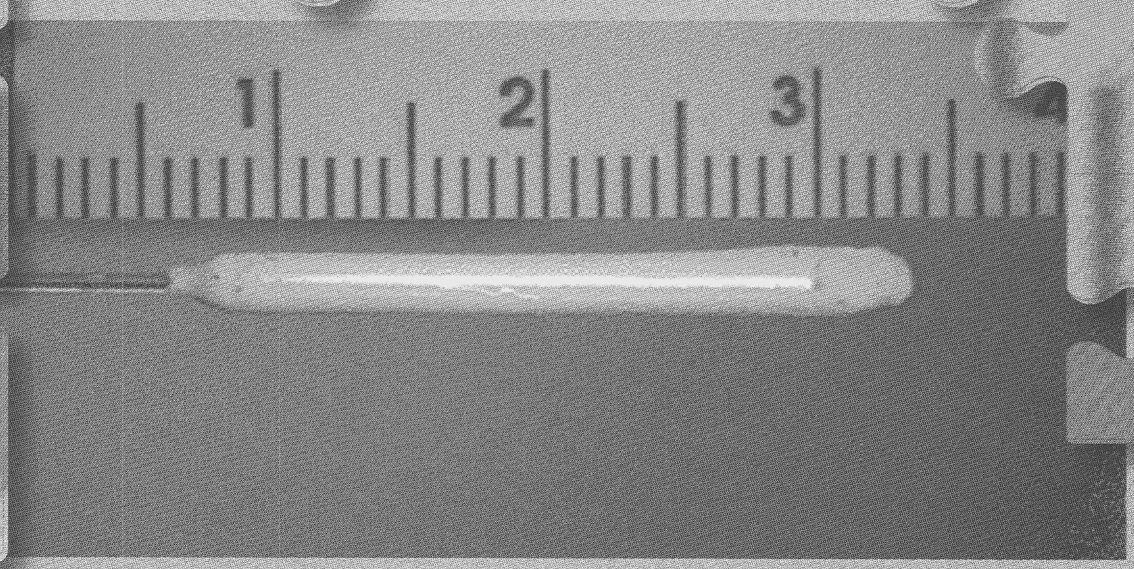

Power Conversion Technologies

6

6. Power Conversion Technologies

Overview
Ronald E. Haigh, Thrust Area Leader

High-Density Photovoltaics
Ronald E. Haigh, Gerard F. Jacobson, and Steve Wojtczuk *6-1*

High-Density Photovoltaics

Ronald E. Haigh and Gerard F. Jacobson
Defense Sciences Engineering Division
Electronics Engineering

Steve Wojtczuk
Spire Corporation
Bedford, Massachusetts

Photovoltaic technology can directly generate high voltages in a solid state material through the series interconnect of many photovoltaic diodes. We are investigating the feasibility of developing an electrically isolated, high-voltage power supply using miniature photovoltaic devices that convert optical energy to electrical energy.

Introduction

Our goals this year were to demonstrate the feasibility of generating high voltages from a monolithic array of solid state photovoltaic diodes that have been connected in series, and to develop a fiber-optic illumination scheme (**Fig. 1**). High voltages developed directly from series interconnected photovoltaic cells are an alternative to transformers and other voltage step-up technologies.

The photovoltaic device is electrically isolated from the laser diode by the silica optical fiber. Electrical isolation is beneficial for applications requiring high-voltage stand-off, lightning and EMI suppression, as well as spark suppression in volatile environments such as mines, fuel tanks, and high explosives. The solid state nature of photovoltaic diode arrays allows them to be incorporated into low profile hybrid circuits for programmatic and commercial applications.

The photovoltaics were designed for maximum efficiency when illuminated with a near infrared laser beam, in contrast to photovoltaics optimized for solar illumination. For a series-connected photovoltaic diode array to function efficiently, each diode in the array must be illuminated uniformly. We have developed a unique scheme based on fiber-optic diffuser technology to address the illumination issue.

Progress

Our efforts focused on developing miniature arrays of photovoltaic diodes in GaAs, due to the high efficiency of this material at the wavelength of our 800 nm laser diode. One hundred photovoltaic diodes arranged in a 2×50 array with a 110-μm pitch were monolithically interconnected in series (**Fig. 2a**). The individual diodes were 220 μm × 50 μm and the array was 0.8 mm × 5.8 mm. Our arrays have achieved more than a 10-fold improvement in voltage per unit area compared to the smallest reported photovoltaic array in this voltage class.[1]

The individual diodes on a semi-insulating substrate are electrically isolated by trenches etched around each device (**Fig. 2b**). Photons entering the trench regions are absorbed in the semi-insulating substrate, the effects of which are discussed later, and do not contribute to useful energy conversion. From **Fig. 2a**, it is apparent that

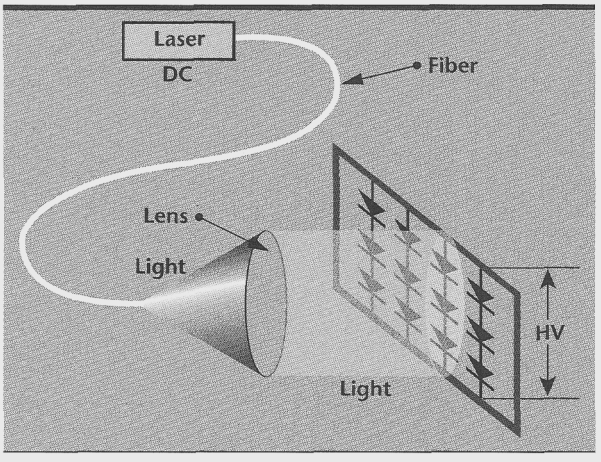

Figure 1. Schematic illustration of fiber-optic illumination system.

the trench regions are a significant fraction of the total active device area. To improve the efficiency of the array, the ratio of trench area to active area should be reduced.

Photovoltaic Device Structure

The series-interconnected array of mesa-isolated photovoltaic devices was developed in a collaboration with Spire Corporation. The metal organic chemical vapor deposition (MOCVD) epitaxial material growth and device processing was performed at Spire.

The basic device structure is an extension of low-voltage multi-junction devices developed earlier by Sandia National Laboratories[2] and those developed commercially by Spire Corporation. The photovoltaic diodes are p-on-n devices, due to higher mobility of the electrons in the n material. The I^2R energy loss due to the sheet resistance of the p material on the upper layer is minimized by incorporating a thin metal finger on the p contact along the length of the device.

The epitaxial structure consists of a heavily p-doped GaAs emitter layer on a thick n-type GaAs base layer with p+ and n+ contact layers on a semi-insulating substrate (**Table 1**). An AlGaAs etch stop layer is incorporated into the epitaxial structure so that the etch depth to the buried n+ contact can be more accurately controlled during processing. The AlGaAs layer also serves as a back-surface field, which improves the efficiency of the cell.[3] Finally a single-layer of quarter-wavelength silicon nitride anti-reflection coating, optimized for 850 nm, is deposited on top of the device. The absorption depth of 800 nm photons is about 1 µm in GaAs so the thickness of the emitter and base layers absorbs 99% of the available photons.

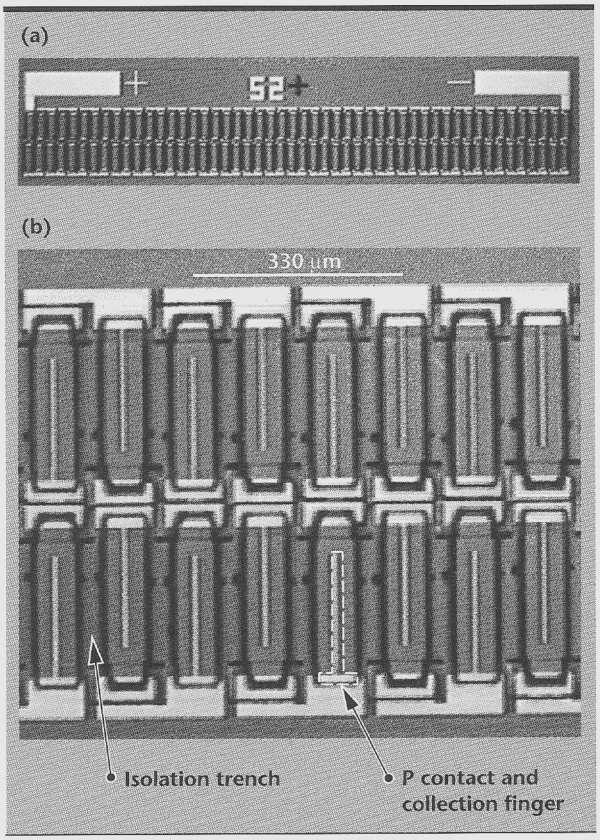

Figure 2. (a) Section of photovoltaic diode array; (b) individual diodes on a semi-insulating substrate.

Results

Individual diode open-circuit voltages as high as 1.1 V and short circuit currents of 0.4 mA, corresponding to a responsivity of 0.4 A/W, were measured at an illumination intensity of 4 W/cm^2. Short circuit currents of 7.75 mA were measured at an illumination intensity of 80 W/cm^2, corresponding to a degraded responsivity of 0.387 A/W.

Individual diode open-circuit voltages as high as 1.1 V and short circuit responsivity of 0.4 A/W were measured at an illumination intensity of 4 W/cm^2. The responsitivity of the device could be improved by incorporating an $Al_xGa_{(1-x)}As$ window layer on top of the emitter to reduce the losses due to surface recombination.[4] Photovoltaics with an $Al_xGa_{(1-x)}As$ window layer have been reported with a responsitivity of 0.6 A/W. The window layer was intentionally omitted from our devices to reduce the complexity of this developmental effort.

Initially the 100-element photovoltaic array produced an output voltage of only 15 V when illuminated with a laser source. It was determined experimentally that photoconductive currents caused by photon absorption in the isolation trenches between the devices shunted the array. An analytical model of the shunting has since been developed to confirm the experimental results. Earlier work on similar devices indicated that the photoconductive shunting effect in the semi-insulating substrate was negligible.[2]

Table 1. Epitaxial layers.

Layer	Material	Thickness
AR coating	Si_3N_4	100 nm
p contact layer	GaAs	0.1 µm
Emitter	GaAs	0.1 µm
Base	GaAs	3.0 µm
Etch Stop/BSF	AlGaAs	0.2 µm
n contact layer	GaAs	3.0 µm
Substrate	GaAs–SI	635 µm

After applying an opaque material in the isolation trenches between the active devices, the output voltage of the array increased to 90 V. The I-V curve for the photovoltaic array after the opaque material was applied is shown in **Fig. 3**. The kink in the curve is due to a non-ideal ohmic contact. This was caused by an inability to sufficiently dope the n contact material at a high enough level, a known limitation at the time the material was grown for these devices.

New material has since been grown that will correct the ohmic contact problem. Furthermore, two approaches to resolve the photoconductive shunting effect are being pursued. In the first approach, metal interconnects are being patterned in the trenches between the devices. The second approach involves incorporating a buried p layer between the diode and the substrate in an attempt to electrically isolate the diode and the substrate via a potential barrier.

The design of the 2 × 50 array was conservative enough to achieve high array yields. A more aggressive design, which doubled the device density, failed to produce any useful devices due to problems in achieving uniform etching during the mesa-isolation process step. Larger arrays of monolithically interconnected devices appear feasible with diodes on the dimension scale of the 2 × 50 array without further investment in process development.

Modeling

A semiconductor modeling tool, PC1D, developed at the Photovoltaics Special Research Centre at the University of New South Wales in Sydney, Australia was used to model performance of the photovoltaic device based on its epitaxial structure and illumination conditions. PC1D is a computer program, written for IBM-compatible personal computers, that solves the fully coupled nonlinear equations for the quasi-one-dimensional transport of electrons and holes in crystalline semiconductor devices, with an emphasis on photovoltaic devices.

The code simulates the performance of the photovoltaic devices, so that the device structures can be optimized. The modeling tool also gives insight into the device performance under different illumination and environmental conditions. For instance we can determine how the illumination wavelength, intensity, or temperature affects the output characteristics of the device.

Shown in **Fig. 4** are the simulated I-V curves at two different ambient temperatures, 300 K and 400 K, for the photovoltaic device under monochromatic 800 nm illumination. The temperature dependence of the open circuit voltage, which may vary as much as 15%, can result in significant voltage changes for large photovoltaic arrays. The simulation agrees well with experimental results of the device temperature dependence of 1.5 mV/C.[2]

Laser Illumination

The output current from a series-connected photovoltaic array is determined by the photovoltaic diode that generates the least amount of current. For arrays with similar diode characteristics, it is necessary to illuminate all the photovoltaic devices uniformly in the linear array, otherwise the output current of the array will be restricted.

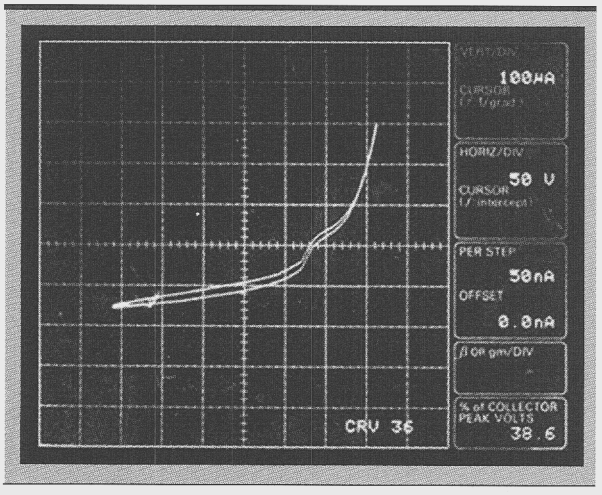

Figure 3. Current vs voltage curve for photovoltaic array after application of opaque material.

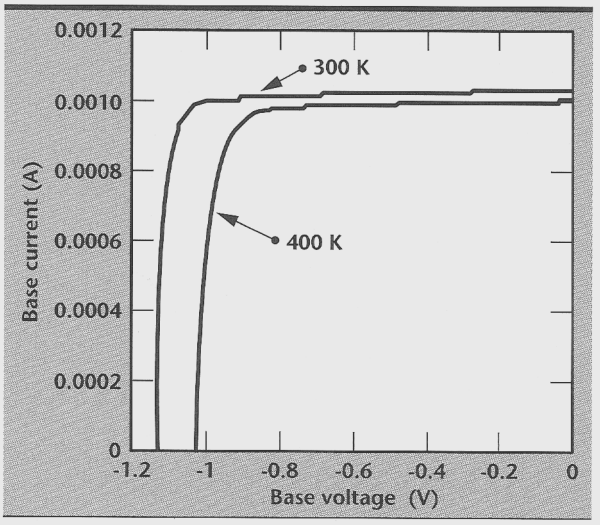

Figure 4. Simulated temperature dependence of a single photovoltaic diode.

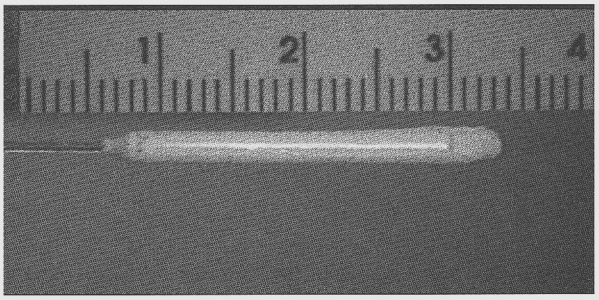

Figure 5. Cylindrical diffuser emitting light from a fiber coupled HeNe laser.

Due to our array geometry, 0.8 mm × 5.8 mm, our illumination system must generate a uniform intensity top hat profile with a high aspect ratio, 10:1. To address this issue, we modified a commercially available fiber-optic diffuser to illuminate the photovoltaic array. The diffuser approach was pursued because it is compact, which substantially decreases the packaging size.

A reflective dielectric coating was applied around the perimeter of the diffuser, leaving only a small slit along the length of the diffuser uncoated for the light to exit (**Fig. 5**). Approximately 50% of the light entering the fiber exits the diffuser within the small output slit. An intensity uniformity along the length of the diffuser of ±%15 was measured with a CCD camera.

Future Work

This year we demonstrated a monolithic photovoltaic array with a 90-V output. We believe higher voltages are obtainable either monolithically or by series connection of multiple devices using hybrid micro-circuit fabrication techniques.

Future research on improving the efficiency of the photovoltaic array and reducing its size even further is possible.

Acknowledgments

The support and encouragement of D. O'Brien, R. Clough, and K. Freytag are greatly appreciated.

References

1. Sakakibara, T., H. Izu, H. Tarat, and S. Kiyama (1997), "Development of High Voltage Photovoltaic Micro-Devices for Driving Micro Actuators," *IEICE Transactions on Electronics,* Feb., Vol. **E80-C**, (2), pp. 309–313.

2. Rose, B. (1992), *Monolithic, Series Connected GaAs Photovoltaic Power Converters for Optoelectronic Component Applications,* Sandia National Laboratory, Livermore, CA, September (SAND-92-1534).

3. MacMillian, H. F., H. C. Hamaker, N. R. Kaminar, and M. S. Kuryla (1988), "28% Efficient GaAs Concentrator Solar Cells," *20th IEEE Photovoltaic Specialists Conf.,* Sept., Vol. **1**, pp. 462–468.

4. Kamath, G. S., J. Ewan, and R. C. Knechtli (1977), "Large-area high-efficiency (AlGa) As-GaAs solar cells," *IEEE Transactions on Electron Devices,* April, Vol. **ED-24**, pp. 473–5.

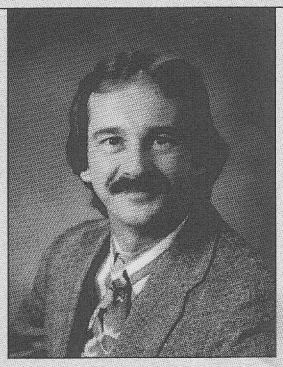

Harry E. Martz, Thrust Area Leader

The Nondestructive Evaluation (NDE) thrust area at Lawrence Livermore National Laboratory (LLNL) supports initiatives that advance inspection science and technology. Our goal is to provide cutting-edge technologies, that show promise for quantitative inspection and characterization tools two to three years into the future.

The NDE thrust area supports a multidisciplinary team, consisting of mechanical and electronics engineers, physicists, materials and computer scientists, chemists, technicians, and radiographers. These team members include personnel that cross departments within LLNL, and some are from academia and industry, within the United States and abroad. This collaboration brings together the necessary and diverse disciplines to provide the key scientific and technological advancements required to meet LLNL programmatic and industrial NDE challenges.

NDE provides materials characterization inspections of finished parts and complex objects, to find flaws and fabrication defects and to determine their physical and chemical characteristics. In addition, applying NDE throughout the life cycle of a part saves time and money and improves quality. For example, NDE is being applied at the beginning of a part to develop new materials and to aid in process design and development.

NDE also encompasses process monitoring and control sensors and the monitoring of in-service damage. NDE also is being applied at the end of a part's life for proper reuse or safe and proper disposal. Therefore, NDE is becoming a front-line and end-of-line technology that strongly impacts issues of certification, life prediction, life extension, reuse, and disposal.

To meet today's programmatic demands, it is important to increase collaboration among LLNL's engineering thrust areas, departments, and programs. This year we collaborated with the Fabrication Technology and Microtechnology thrust areas, Defense Systems, Materials Science and Technology Division, the Life Extension Program, the National Ignition Facility Project, and the Joint Medical Technology Program. Such collaborations enable us to stay at the leading edge of NDE technology, research, and development in support of LLNL programs.

The primary contributions of the NDE thrust area this year are described in the five reports that follow: 1) Image Recovery Techniques for X-Ray Computed Tomography for Limited-Data Environments; 2) Techniques for Enhancing Laser Ultrasonic Nondestructive Evaluation; 3) Optical Inspection of Glass-Epoxy Bonds; 4) Miniature X-Ray Source Development; and 5) Improving Computed Tomography Design and Operation Using Simulation Tools.

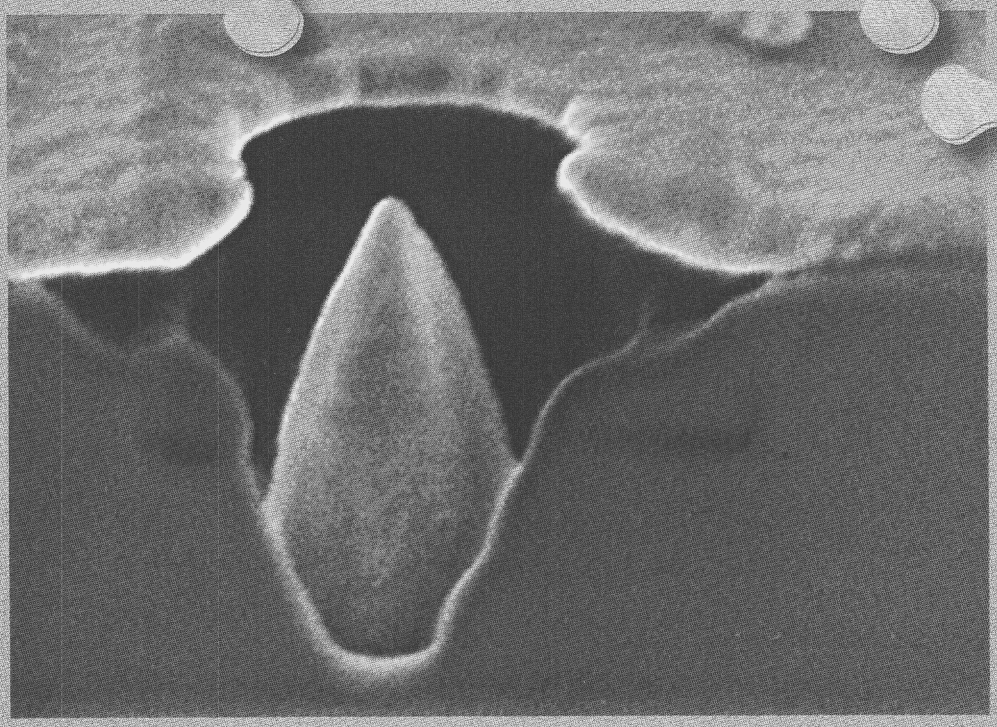

Nondestructive Evaluation

7

7. Nondestructive Evaluation

Overview
Harry E. Martz, Thrust Area Leader

Image Recovery Techniques for X-Ray Computed Tomography in Limited-Data Environments
Dennis M. Goodman, Jessie A. Jackson, and Maurice B. Aufderheide, and Erik M. Johansson *7-1*

Techniques for Enhancing Laser Ultrasonic Nondestructive Evaluation
Graham H. Thomas, Diane J. Chinn, Robert D. Huber, James V. Candy, and James Spicer *7-7*

Optical Inspection of Glass-Epoxy Bonds
Diane J. Chinn, Dwight E. Perkins, and Raymond M. Brusasco *7-11*

Miniature X-Ray Source Development
Jeffrey D. Morse, Robert T. Graff, Alan F. Jankowski, and Jeffrey P. Hayes *7-15*

Improving Computed Tomography Design and Operation Using Simulation Tools
G. Patrick Roberson, Daniel J. Schneberk, Jerry J. Haskins, Clint M. Logan, Harry E. Martz, Dwight E. Perkins, and Derrill R. Rikard *7-19*

Image Recovery Techniques for X-Ray Computed Tomography in Limited-Data Environments

Dennis M. Goodman and Jessie A. Jackson
Laser Engineering Division
Electronics Engineering

Maurice B. Aufderheide
Defense Systems

Erik M. Johansson
Consultant, Tracy, California

The goal of our work is to develop a set of limited-data CT reconstruction tools that may be applied to a wide variety of problems of importance to Lawrence Livermore National Laboratory (LLNL). We are achieving this goal through a balance of algorithm development and application research. In the first year of this two-year project, we have developed a set of reconstruction tools and we have applied them to several practical problems.

Introduction

There is an increasing requirement throughout LLNL for nondestructive evaluation (NDE) using x-ray computed tomography (CT). In many cases, restrictions on data acquisition time, imaging geometry, and budgets make it infeasible to acquire projection data over enough views to achieve desired spatial resolution using conventional CT methods.

In particular, conventional CT methods are noniterative algorithms that have the advantage of low computational effort, but they are not adaptable to incorporating prior information or non-Gaussian statistics. Most currently existing iterative tomography algorithms are based on methods that are time-consuming because they converge very slowly, if at all.

The goal of our work is to develop a set of limited-data CT reconstruction tools that may be applied to a wide variety of problems of importance to Lawrence Livermore National Laboratory (LLNL). We are achieving this goal through a balance of algorithm development and application research. In the first year of this two-year project, we have developed a set of reconstruction tools and we have applied them to several practical problems.

CT Image Reconstruction

CT reconstruction involves solving an inverse problem that yields an image which is in some sense a best match to the observed data. The problem of reconstructing an image from the observed data can be described as follows: given the observed data vector, $\mathbf{y}$, reconstruct an estimate of the object, represented by the vector, $\mathbf{x}$, that produced this data.

The statistical relationship between $\mathbf{x}$ and $\mathbf{y}$ can be written as $L(\mathbf{y},\mathbf{x})$, where $L(\cdot,\cdot)$ is a negative log-likelihood function. The function $L(\cdot,\cdot)$ is determined by the physics of the property being measured, the geometry of the measurement system, and the statistics of the noise corrupting the data.

The maximum likelihood solution for estimating $\mathbf{x}$ from $\mathbf{y}$ is

$$\hat{\mathbf{x}} = \underset{\mathbf{x}}{\text{Argmin}}\left\{L(\mathbf{y},\mathbf{x})\right\}. \qquad (1)$$

The problem with this estimate of $\mathbf{x}$ is that most inverse problems are ill-posed, in the sense that small changes in $\mathbf{y}$ may produce large changes in $\hat{\mathbf{x}}$. This is especially true of limited-data CT reconstructions, where even in the noise-free case, $\mathbf{y}$ may not contain sufficient information to completely define $\mathbf{x}$; that is, the problem is under-determined.

Under these conditions, a good estimate of $\mathbf{x}$ is possible only if prior information or constraints are imposed on the solution to the minimization problem shown in **Eq. 1**. Unfortunately, the usual non-iterative methods (for example, filtered backprojection for the parallel ray problem) generally can not be modified to impose extra constraints. Indeed, it is not even possible to limit the number of variables in $\mathbf{x}$.

This is an important issue because knowledge of the physical extent of the object under test is usually available to the experimenter, and eliminating variables in $\mathbf{x}$ that correspond to regions beyond the known extent of the object reduces unknowns and helps to deal with the under-determined nature of limited-data problems.

Another serious issue with non-iterative methods is that, for such methods, $L(\mathbf{y},\mathbf{x})$ is inherently a squared error function. While the least-squares criterion is appropriate for the usual Gaussian noise assumption, it is not appropriate for low energy levels or emission tomography problems where it is necessary to assume that the data is Poisson-distributed.

For ill-posed problems, $\hat{\mathbf{x}}$ typically is too large and very noisy. A common method for obtaining better estimates is the regularization, or penalized likelihood approach, that adds Euclidean norm and/or absolute value norm terms to $L(\mathbf{y},\mathbf{x})$. These terms penalize large $\hat{\mathbf{x}}$. Frequently, regularization is not sufficient to yield a high-quality image, so any additional prior information about the unknown must be included. Many properties (such as energy, absorption, and reflection) are inherently non-negative, and adding this constraint often greatly enhances image quality.

Furthermore, often there are physical reasons for placing upper bounds on the estimate as well. The result is upper and lower bounds for each component of the image vector $\mathbf{x}$. If we denote the set of $\mathbf{x}$ vectors that obey the bound constraints by $\mathbf{S}$, then our modified maximum likelihood problem is

$$\hat{\mathbf{x}} = \underset{\mathbf{x}\in\mathbf{S}}{\operatorname{Argmin}}\left\{L(\mathbf{y},\mathbf{x}) + \eta\|\mathbf{x}\|_1 + \lambda\|\mathbf{x}\|_2\right\} \qquad (2)$$

where η and λ are parameters that determine the penalty on the size of $\mathbf{x}$ as measured by, respectively, its absolute value norm and its Euclidean norm.

A second problem is the number of variables in **Eq. 1** or **2**. The discretized image usually contains 10^5 to 10^7 pixels (voxels), resulting in an $\mathbf{x}$ vector of the same length. Conventional iterative non-linear minimization algorithms use Newton or quasi-Newton techniques, which require storing an approximation to the inverse of the matrix of second partials of $L(\mathbf{y},\mathbf{x})$ with respect to $\mathbf{x}$. Because even a $10^5 \times 10^5$ matrix is too large to store in memory, these techniques are not appropriate for the problems we are considering.

In the case of an unconstrained problem, such as **Eq. 1**, either the conjugate gradient algorithm, which in effect builds up second derivative information without directly storing it, or limited-memory quasi-Newton algorithms, which store a low rank approximation to the inverse matrix of second partials, are the methods of choice when the number of variables is too large for conventional quasi-Newton methods.

For constrained problems, such as **Eq. 2**, conventional optimization techniques[1,2] usually allow only one variable per iteration to attain a bound, so for very large bounded inverse problems, these techniques are very slow since they spend too much effort finding bounds.

Consequently, standard iterative tomography algorithms are based on the projection onto convex sets (POCS) algorithm, the expectation-maximization (EM) algorithm, or variants of the algebraic reconstruction technique (ART).[3,4] These methods can attain multiple bounds in an iteration, but they essentially use a steepest descent strategy that searches for the next iterate along the negative gradient (with respect to $\mathbf{x}$) of $L(\mathbf{y},\mathbf{x})$. Unfortunately, steepest descent optimization methods exhibit notoriously slow convergence[5] when the matrix of second partials of $L(\mathbf{y},\mathbf{x})$ is ill-conditioned (that is, has widely spread eigenvalues), and ill-posed problems usually make this matrix highly ill-conditioned. Consequently, the standard iterative tomography algorithms converge very slowly, if at all, on limited-data problems.

Progress

We have developed an extension of the conjugate gradient algorithm that incorporates bound constraints on the variables.[6] It is unique in that it incorporates a bending linesearch. Conventional techniques allow only a single variable per iteration to attain a bound, whereas the bending linesearch allows multiple variables per iteration to attain bounds. In addition, like the unconstrained conjugate gradient algorithm, it, in effect, accumulates second-derivative information with each iteration.

Given the large number of variables and the ill-posed nature of our problems of interest, our approach should have major advantages over the conventional image recovery techniques. In previous years, our algorithm was applied with great

success to a variety of practical problems. These included deconvolution,[6] speckle interferometry,[7] 2-D parallel-beam limited view x-ray tomography,[8,9] and crystallography[10] at LLNL, and pulsed photothermal radiometry[11–14] at the Beckman Laser Institute and Medical Clinic of the University of California Irvine Medical School.

This year we developed fast, flexible cone beam projectors and combined them with our constrained conjugate gradient (CCG) code. The resulting algorithm, CCG_Cone, allows reconstructions from cone beam projections with arbitrary magnifications and out-of-plane angles. These improvements are crucial to solving Advanced Hydrodynamic Facility (AHF) imaging problems,[15] because AHF magnifications (3× to 4×) are likely to be larger than the typical NDE magnification (1× to 2×), and views are unlikely to be restricted to a single plane. We have also incorporated the Euclidean and absolute value norm penalty terms described in the Introduction.

We have performed AHF simulations, and have obtained surprisingly good reconstructions from very few projections. Furthermore, even for 10^6 voxels the reconstructions were obtained with few iterations, so computer time was not a serious issue. These simulations have been very useful in understanding AHF design issues.

We present an example using CCG_Cone. Our object consists of seven stacked slabs, as shown in **Fig. 1**. Projection data and reconstruction results are also shown in this figure. The origin of the axes is in the center of the middle slab. Four views are taken in the x-y plane. The angles of these views are equally spaced and are 0°, 45°, 90°, and 135° as measured in the x-y plane from the x axis.

We used only in-plane viewing angles for purposes of comparison with the conventional non-iterative Feldkamp algorithm[16] that is capable of only such angles. Experiments (not shown) with CCG_Cone on this example have demonstrated the advantage of using some out-of-plane viewing angles. The absorption of the slabs is arbitrarily set to 1.0 inside the slabs and 0.0 outside.

The large magnification and resulting large cone angle cause blurring at the extreme angles of the projections. Orthogonal slices through the reconstructions are displayed for both CCG_Cone and Feldkamp. Although a gray-scale scheme is used to display the reconstruction results for both algorithms, note that the scales for the two reconstructions are not the same. In particular, note that Feldkamp exhibits large excursions in both positive and negative directions. Since accurate spatial attenuation values are required in our image recovery, this clearly demonstrates the superiority of CCG_Cone.

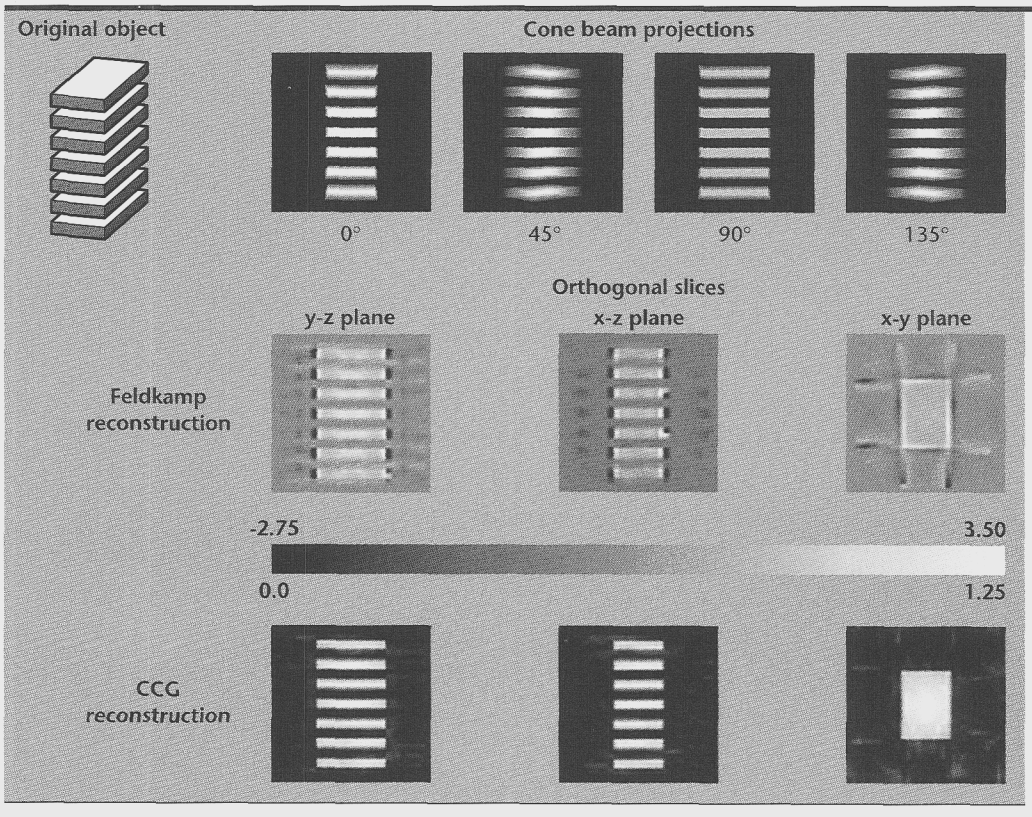

Figure 1. Simulation study of a set of stacked plates (top left). Four equally-spaced cone beam projections are shown in the top row. The resulting reconstructed images are shown for the Feldkamp (middle row) and CCG_Cone (bottom row) algorithms. Note that the gray scale is different for CCG_Cone and Feldkamp.

Another reason for limiting the number of views occurs in medical imaging problems where it is necessary to limit the x-ray dose to the object or patient being imaged. This is an issue for osteoporosis research using the x-ray transmission microscope (XTM) at LLNL.[17] Since the XTM is a parallel-beam geometry scanner, we have applied the parallel beam version of our CCG tomography algorithm to projection data collected with the XTM. The results are shown in **Fig. 2**.

The object under test is an aluminum frame model used to simulate bone structure. The reconstructions on the top row are obtained with filtered back-projection; the reconstructions on the bottom row are obtained with parallel beam CCG. The left-most reconstructions were obtained using the number of projections required to form a complete data set for filtered back-projection. Moving from left to right, the number of projections is reduced from those of the left-most reconstructions by factors of 8, 16, and 32. Visual inspection suggests that the CCG reconstructions degrade much more slowly. We are working to determine the performance by quantitative measures.

Although our conjugate gradient algorithm has performed well, significant improvements to the basic optimization algorithm are necessary to improve performance on the very large and highly ill-conditioned problems that occur in limited-data tomography, and to improve flexibility so that prior knowledge could be more easily imposed on the solution.

Our original proposal suggested implementing a truncated-Newton algorithm because it was not clear how to update limited-memory quasi-Newton matrices when the set of variables at bounds changed during an iteration. However, a recent publication[18] described a limited-memory quasi-Newton algorithm that up-dates the approximate limited memory model in such a way as to permit many variables to attain their bounds during a single iteration, and we decided that this approach was more appropriate. The nature of tomography problems makes bending during the linesearch particularly easy (see the discussion in Reference 19), and we enhanced the algorithm described in Reference 18 by permitting multiple variables to attain bounds during the linesearch, as well as during the approximate model up-date. We accomplished this by using the same bending linesearch subroutine that we used for CCG. Our new algorithm has been debugged, and comparisons with CCG are in progress.

Another contribution was to increase the flexibility of our algorithm to permit its application to problems with non-Gaussian statistics. We are now able to solve problems with other than least-squares fitting criteria. This includes "robust" criteria where, beyond some threshold, a linear, rather than a squared, fitting criterion is used. This makes the recovered image less sensitive to outliers in the projection data.

We added this flexibility in such a way that we maintained the efficiencies we were able to demonstrate for least-squares problems. In particular, although our problems are too large to use the exact inverse of the matrix of second partials in computing the search direction, we were able to use exact

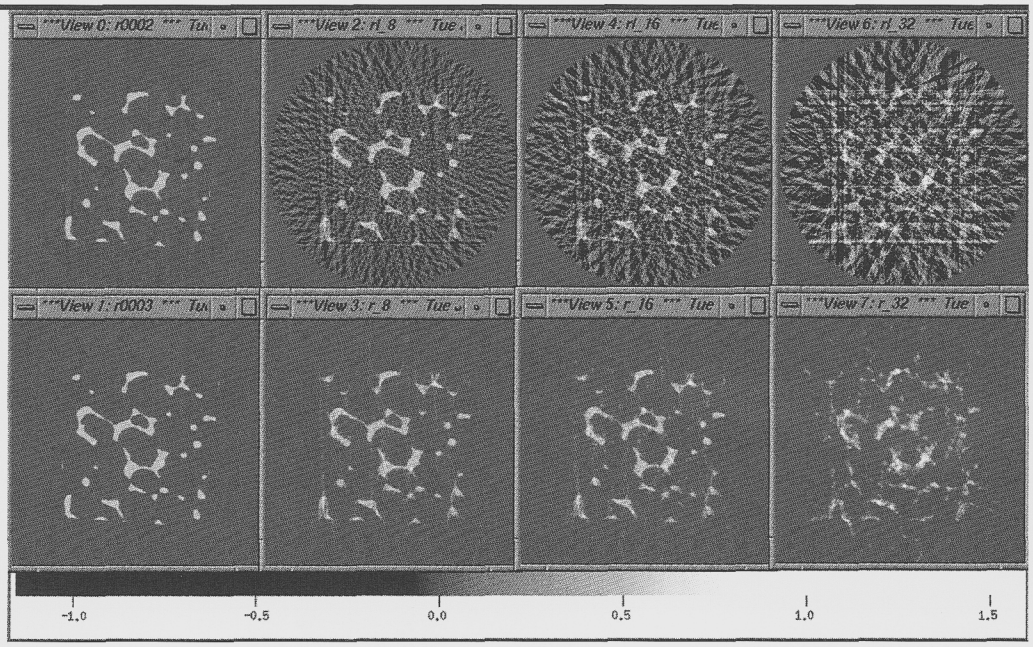

Figure 2. Representative image recovery results for experimental data taken by the XTM of an aluminum structure. Filtered back-projection results are shown along the top row; CCG parallel beam results are shown along the bottom row. From left to right, results are for the complete data set and reduced data sets that use only every 8th, 16th, and 32nd projection. All images use the same gray scale.

second derivative information in computing the initial linesearch estimate; that is, the search length along the search direction vector. We have applied this capability to Poisson statistics for the waste drum scanning problem. Although this problem does not involve limited views, it is a good test of our capabilities.[19]

Another issue in limited-data tomography is system design. Particularly in the case of 3-D cone beam problems, there is not a useful rule for determining the optimum viewing angles, given that the number of views is limited. Monte Carlo simulations could be used, but they are extremely expensive for problems with many voxels. The inverse of the information matrix (derived from the Cramer-Rao bound),[20] gives a lower bound on the error covariance matrix, which provides an estimate of estimation error without resort to Monte Carlo simulations. Although for limited-data problems the information matrix is usually singular, quadratic forms using the information matrix can be used to calculate reconstruction error over regions of the object under test. We have determined the information matrix for tomographic reconstruction problems, and we have determined how to solve for these quadratic forms. This technique should be a useful tool for solving the optimum view problem.

Future Work

In the second and final year of this project, we will continue our applications research on data from AHF simulations and on XTM data. In addition we will try our new algorithms on several other practical tomographic problems. These include projection data obtained from waste drum scanning, reactor fuel pellet scanning, and the Enhanced Surveillance Program.

Our algorithm research will include further work to improve our new quasi-Newton algorithm. We will develop methods to include both soft and hard constraints on the solution as a way to incorporate *a priori* information that is more complex than simple bounds. We will also study preconditioning, and possibly parallelism, with the hope of obtaining faster solutions.

We will continue studying statistical approaches for determining optimum viewing angles, optimum selection of regularization parameters, and estimating the accuracy of reconstructions.

References

1. Gill, P. E., W. Murray, and M. H. Wright (1981), *Practical Optimization*, Academic Press, New York, NY.

2. Fletcher, R. (1987), *Practical Methods of Optimization, 2nd Ed.*, John Wiley, New York, NY.

3. Stark, H., Ed. (1987), *Image Recovery: Theory and Application*, Academic Press, New York, NY.

4. Azevedo, S. G. (1991), *Model-Based Computed Tomography for Nondestructive Evaluation*, Ph.D. thesis, Lawrence Livermore National Laboratory, Livermore, CA, (UCRL-LR-106884).

5. Luenberger, D. G. (1984), *Linear and Nonlinear Programming, 2nd Ed.*, Addison-Wesley, Reading, MA, pp. 214–220.

6. Goodman, D. M., E. M. Johansson, and T. W. Lawrence (1993), "On Applying the Conjugate Gradient Algorithm to Image Processing Problems," *Multivariate Analysis: Future Directions*, C. R. Rao, Ed., Elsevier Science Publishers, Oxford, United Kingdom, (11).

7. Goodman, D. M., T. W. Lawrence, E. M. Johansson, and J. P. Fitch (1993), "Bispectral Speckle Interferometry to Reconstruct Extended Objects from Turbulence-Degraded Telescope Images," *Handbook of Statistics*, N. K. Bose, and C. R. Rao, Eds., North Holland, Vol. **10**, (13).

8. Kolman, J., W. S. Haddad, D. M. Goodman, and K. A. Nugent (1994), "Application of a Constrained Optimization Algorithm to Limited View Tomography," *Proc. SPIE Conf., San Diego, CA*, July.

9. Haddad, W. S., J. E. Trebes, D. M. Goodman, H. R. Lee, I. McNulty, E. H. Anderson, and A. O. Zalensky (1995), "Ultra High Resolution Soft X-Ray Tomography," *Proc. SPIE Conf., San Diego, CA*, July.

10. Somoza, J. R., H. Szöke, D. M. Goodman, P. Béran, D. Truckses, S.-H. Kim, and A. Szöke (1995), "Holographic Methods in X-ray Crystallography IV. A Fast Algorithm and its Application to Macromolecular Crystallography," *Acta Crystallographica*, Vol. **A51**.

11. Milner, T. E., D. M. Goodman, B. S. Tanenbaum, and J. S. Nelson (1995), "Depth Profiling of Laser-Heated Chromophores in Biological Tissues by Pulsed Photothermal Radiometry," *Journal of the Optical Society of America-A*, July, Vol. **12**, (7).

12. Milner, T. E., D. M. Goodman, B. S. Tanenbaum, B. Anvari, L. O. Svasand, and J. S. Nelson (1996), "Imaging of Laser Heated Subsurface Chromophores in Biological Materials: Determination of Lateral Physical Dimensions," *Physics in Medicine and Biology*, Vol. **41**.

13. Milner, T. E., D. J. Smithies, D. M. Goodman, A. Lau, and J. S. Nelson (1996), "Depth Determination of Chromophores in Human Skin by Pulsed Photothermal Radiometry," *Applied Optics*, June.

14. van Gemert, M. J. C., J. S. Nelson, T. E. Milner, D. J. Smithies, W. Verkruysse, J. F. de Boer, G. W. Lucassen, D. M. Goodman, B. S. Tanenbaum, L. T. Norvang, and L. O. Svasand (1997), "Non-Invasive Determination of Port Wine Stain Anatomy and Physiology for Optimal Laser Treatment Strategies," *Physics in Medicine and Biology*, Vol. **42**.

15. US Department of Energy, Defense Programs, Office of Research and Inertial Fusion (1996), *Advanced Hydrodynamic Radiography Technology Development Plan*, Predecisional Draft, February.

16. Feldkamp, L. A., L. C. Davis, and J. W. Kress (1984), "Practical Cone-Beam Algorithm," *Journal of the Optical Society of America*, June, pp. 612–619.

17. Kinney, J. H. (1996), "A Closer Look at Osteoporosis," *LLNL Science and Technology Review*, Lawrence Livermore National Laboratory, Livermore, CA, June.

18. Byrd, R. H., J. Nocedal, and R. B. Schnabel (1994), "Representations of Quasi-Newton Matrices and Their Use in Limited Memory Methods," *Math. Prog.*, January, Vol. **63**, (2).

19. Goodman, D. M. (1997), *Maximum Likelihood Estimation with Poisson (Counting) Statistics for Waste Drum Inspection*, Lawrence Livermore National Laboratory, Livermore, CA, (UCRL-ID-127361).

20. Poor, H. V. (1994), An Introduction to Signal Detection and Estimation 2nd Ed., Springer-Verlag.

Techniques for Enhancing Laser Ultrasonic Nondestructive Evaluation

Graham H. Thomas, Diane J. Chinn, and Robert D. Huber
Manufacturing and Materials Engineering Division
Mechanical Engineering

James V. Candy
Electronics Engineering Technologies Division
Electronics Engineering

James Spicer
Johns Hopkins University
Baltimore, Maryland

Laser-based ultrasonics is an enabling technology that has been implemented in one LLNL program and will benefit many others. This year, we assembled hardware and software tools to conduct research for enhancing laser based ultrasonics; specified and acquired a Fabry-Perot interferometer to significantly improve our laser ultrasonic detection ability; and acquired multi-mode fiber cables to deliver the light from the laser to the specimen, and from the specimen to the Fabry-Perot interferometer. We specified a powerful generation laser to provide uniform ultrasonic signals for our beam-forming effort. The increased repetition rate of this laser will benefit our scanning and imaging research. We developed algorithms for reducing noise and beam forming and wrote software to control data acquisition and specimen scanning.

Introduction

Though ultrasonic nondestructive evaluation is a mature technology, there are still many advances that expand its role in material characterization, manufacturing process control, defect detection, and life cycle management. Ultrasonics is evolving, with improvements such as higher frequencies to sense smaller defects, modern signal processing methods to increase sensitivity, classification algorithms for defect characterization and the most recent imaging techniques to display defects.

A universal limitation however, is the need to transmit the acoustic energy from the transducer into the part, through a fluid, most often water. It is extremely desirable to eliminate this couplant. Laser generation and detection of ultrasonic energy provides a method to perform remote, non-contact ultrasonics.[1] It allows ultrasonic evaluations in high-temperature and radioactive environments, in applications where access is restricted, such as in a vacuum, and on materials that would be damaged by couplant contamination.

For ultrasonic inspections on radioactive materials, the couplant becomes hazardous waste, thus laser ultrasonics reduces hazardous waste.

Laser-based ultrasonics is in its infancy, and there is much to be understood before its full potential can be realized. A significant limitation is that laser-based ultrasonics has reduced sensitivity compared with traditional ultrasonics. To improve the sensitivity, research is being pursued in the areas of increased ultrasonic generation, better detectors, and signal processing to make laser ultrasonics viable.

Progress

We realized improvements in both generation and detection this year. Also, we developed model-based signal processing to improve the signal-to-noise levels of laser acoustics. The following sections contain the results of our research.

This continuing project is exploring the science of generating acoustic energy with a laser pulse and the methodology of detecting ultrasonic signals with

laser interferometers. The goal is not to replace existing piezoelectric-based ultrasonics with laser generation and detection, but to supplement the technology to expand its role in Lawrence Livermore National Laboratory (LLNL) programs. Laser ultrasonics has already been incorporated into a LLNL program: it was selected as a diagnostic for monitoring a laser cutting process.

Another potential application is the characterization of aging effects on special nuclear materials. Ultrasonics is very sensitive to material properties and may be a way to quantify aging damage. When hazardous materials are being characterized, it is desirable to perform the measurements remotely. In this project the material is in a vacuum and the sensing must be accomplished from outside the chamber. Laser ultrasonics is ideally suited for this measurement.

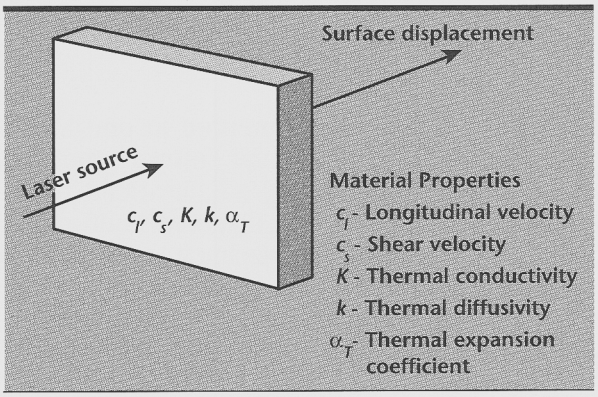

Figure 1. The WAVER code. WAVER calculates the surface displacement resulting from a laser pulse interacting with a material and generating a stress wave.

Model-Based and Beam-Forming Approaches

We have demonstrated the benefits of two signal processing approaches: model-based and beam-forming.

A model-based signal processing technique has been developed and tested.[2,3] Laser-generated acoustic signals are modeled with a code (WAVER) developed at the Johns Hopkins University.[4] The WAVER code calculates the acoustic signal based on the source laser parameters and the material properties (**Fig. 1**). We built signal processing algorithms that minimize the noise and maximize the signal, based on the expected signals calculated by the WAVER model (**Fig. 2a**). **Figure 2b** displays the raw data and the improvement in signal-to-noise produced by our model-based signal processing.

The model-based signal processing was implemented on ultrasonic signals generated with a Nd:YAG laser and detected with a Michelson interferometer. Since the Michelson interferometer can only work with a single speckle (a bright spot on a rough surface that is illuminated with a coherent light field), an aluminum sample with a mirror-like surface was obtained for testing. Ultrasound was generated on one side of the aluminum sample using a pulsed Nd:YAG laser, and it was detected on the polished side of the sample using the Michelson interferometer.

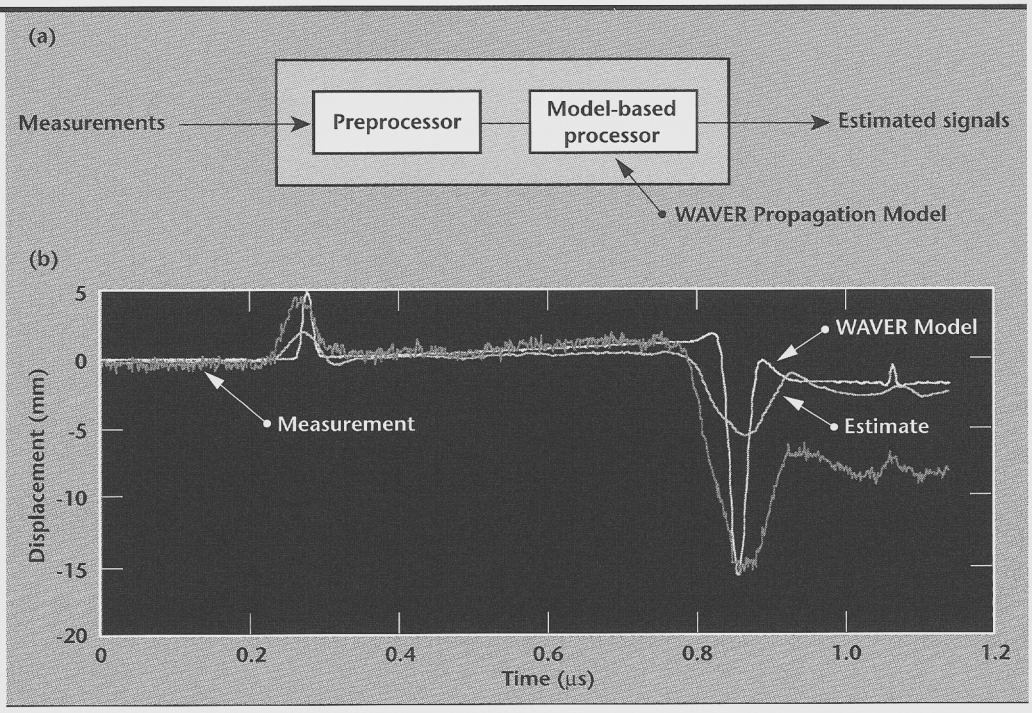

Figure 2. (a) Block diagram of the model-based signal-processing approach to enhance laser ultrasonic signals; (b) typical results of the model-reference processing. Display shows processed input data (measurement), the modeled signal, and the estimated signal.

Another signal processing approach that we have demonstrated is beam-forming. **Figure 3** illustrates the various configurations for the laser ultrasonic arrays that were modeled to improve defect imaging by beam-forming. This method enhances the detection and display of defects by combining the information from an array of sensors.[5] This year we modeled the array and its response to a flaw. Next year, based on these results, we will configure a laser ultrasonic array and confirm the model.

System Up-Grades

We have made significant improvements to our laboratory equipment this year. We added a LISOR (Light In, Signal Out Receiver) interferometer to expand our detection capabilities. This instrument is a Fabry-Perot-based system that complements the earlier path-stabilized Michelson interferometer. The Michelson requires highly-reflective surfaces to sense the ultrasonic signal, whereas the Fabry-Perot works on less reflective surfaces.

This system includes an interferometer and a laser. The laser is a frequency-doubled Nd:YAG which has an output power of 200 mW at a wavelength of 532 nm. Fabry-Perot interferometers can use light scattered from rough surfaces since they can work with multiple speckles. Michelson interferometers work with a single speckle only, which limits their use to polished surfaces.

The LISOR system has been used successfully in the laboratory to detect ultrasound propagating through various materials and specimens. To increase the flexibility of the ultrasonic detection system, an optical fiber cable 20 m long transmits the laser light from the interferometer's laser to the specimen, allowing the testing of items up to that distance away from the laser and interferometer.

Fiber optics has the advantage of allowing large distances between equipment and test location, providing access to hostile or hard-to-reach environments, changing test configuration easily, and eliminating the need for line-of-sight between laser and part.

Figure 4 displays a typical waveform from the LISOR interferometer when the source of ultrasonic energy is a piezoelectric transducer. In this configuration the LISOR has excellent sensitivity. The Michelson has a frequency range of DC to 40 MHz, while the Fabry-Perot has a frequency range of 3 to 100 MHz. Together, these interferometers provide a full range of detection capabilities.

Another addition to the laser ultrasonic facility is a much improved source laser that provides more

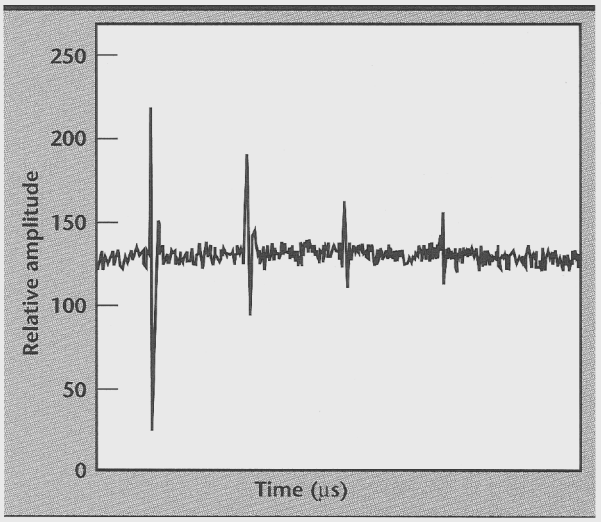

Figure 4. Ultrasonic signals from the LISOR interferometer when the ultrasonic excitation was provided by a laser pulse. The LISOR has excellent sensitivity in this configuration.

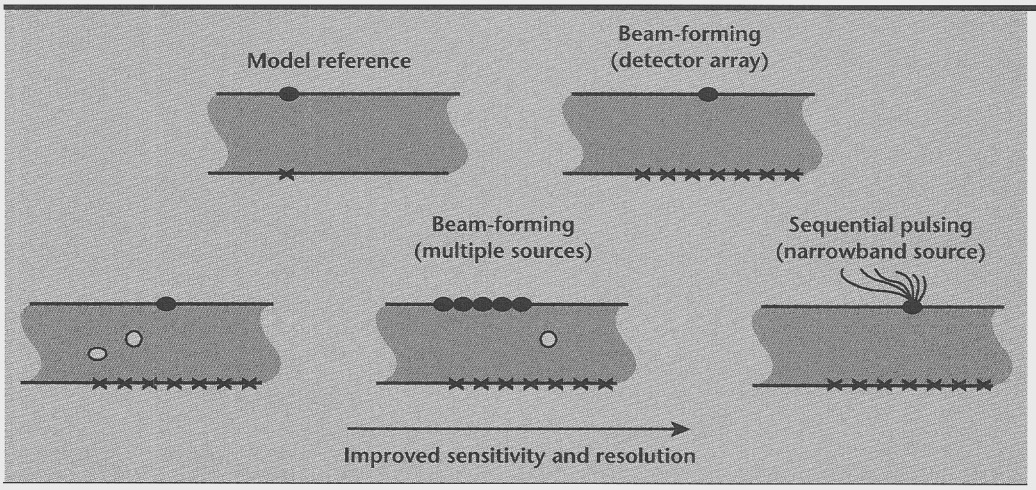

Figure 3. Diagram of laser ultrasonic array configurations for beam-forming research. The upper sequence illustrates the configurations with no defects; the lower sequence includes defects. The solid dots represent laser source generation locations. The ×s represent interferometer detection locations. The open circles represent defects.

light energy, a higher repetition rate and a uniform spot. This source laser is needed to conduct the experiments for signal processing and beam forming.

As part of the data acquisition and imaging effort we acquired computer-controlled motion stages. These stages include two translation stages and one rotation stage that allow the movement of specimens for scanning. Data acquisition and motion control programs have been written to control the stages and capture the ultrasonic signals. The signal-processing and beam-forming algorithms will be combined with this software to render images of defects.

Process Control Demonstration

As a sensor for process control, ultrasonics is extremely valuable. The speed at which ultrasonic testing can acquire measurements facilitates feed back control for machining operations. We selected a process control problem as a vehicle to direct our research. The process was a laser cutting application with a state-of-the-art laser that produces very short duration pulses. The pulses from the cutting laser generate acoustic signals that contain information about the cutting process.

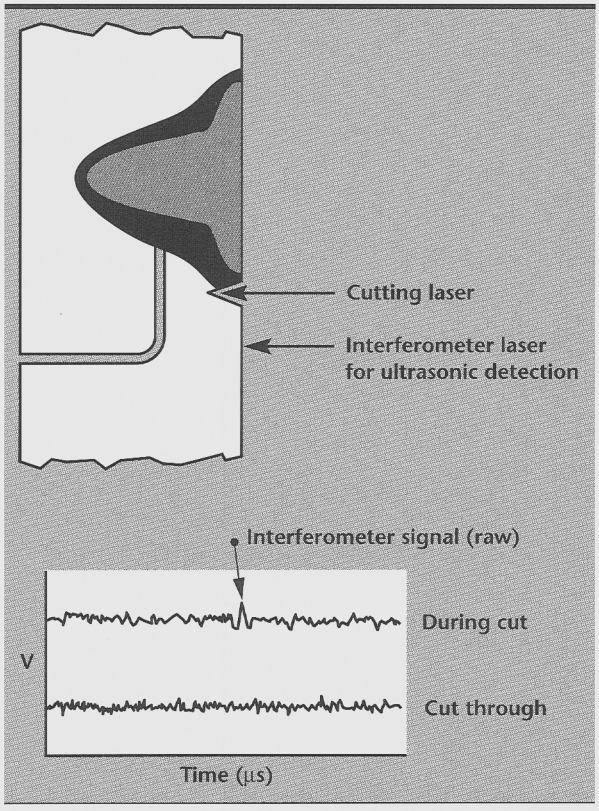

Figure 5. Configuration of cutting laser and interferometer laser for process control. Ultrasonic signals displayed in the upper right corner sense cut-through of the cutting laser and signal the time to stop cutting.

Our first challenge was to understand the phenomenon and the types of ultrasonic waves that are generated. We modeled the system with a computer code that calculates the expected ultrasonic signal, based on laser input parameters and the material properties and geometry. We predicted a dispersive Lamb wave mode which was confirmed by experimentation. The predicted signals were detected in an experiment on flat samples with our Michelson interferometer. The Michelson interferometer then captured ultrasonic signals generated by the cutting laser on a real part.

Figure 5 displays the cut configuration and the ultrasonic signals acquired during the cut of a real part. Once the feasibility was demonstrated, the project purchased a Fabry-Perot interferometer for the cutting station. Presently this laser-based ultrasonic sensor is being integrated into the laser cutting system, a direct result of our research.

References

1. Scruby, C. B., and L. E. Drain (1990), *Laser Ultrasonics, Techniques and Applications,* Adam Hilger, New York, NY.

2. Candy, J. V., G. H. Thomas, D. J. Chinn, and J. B. Spicer (1996), "Laser Ultrasonic Signal Processing: A Model-Reference Approach," *J. Acoustic. Society Am.,* **100**, (1).

3. Huber, R. D., D. J. Chinn, G. H. Thomas, J. V. Candy, and J. Spicer (1996), "Model-Based Signal Processing for Laser Ultrasonic Signal Enhancement," *QNDE Conference,* Brunswick, ME.

4. Spicer, J. (1991), Laser Ultrasonics in Finite Structures: Comprehensive Modeling with Supporting Experiment, Ph.D. thesis. John Hopkins University, Baltimore, MD.

5. Johnson, D., and D. Dudgeon (1993), *Array Signal Processing: Concepts and Techniques,* Prentice-Hall, Princeton, NJ.

Optical Inspection of Glass-Epoxy Bonds

Diane J. Chinn and Dwight E. Perkins
Manufacturing and Materials Engineering Division
Mechanical Engineering

Raymond M. Brusasco
Inertial Confinement Fusion - National Ignition Facility
Laser Programs

We assembled and demonstrated the essential elements for automated inspection of amplifier-slab cladding bonds for the National Ignition Facility (NIF) at Lawrence Livermore National Laboratory (LLNL). From this demonstration, we developed a preliminary design, cost estimate, and completion plan for an automated inspection system that would replace the current manual inspection technique. With this inspection system, NIF will have a reliable, accurate, and recordable tool to evaluate the quality of amplifier-slab cladding bonds.

Introduction

The National Ignition Facility (NIF) at Lawrence Livermore National Laboratory (LLNL) faces new challenges in the inspection of thousands of pieces of precision laser optics. Among these are 3,100 laser amplifier slabs, the 0.8-m x 0.4-m pieces of glass that act as the energy storage medium of the NIF laser. Glass amplifier slabs doped with neodymium absorb energy emitted by flashlamps, and release the energy when a subsequent laser pulse propagates through the glass.

Amplifier slabs have cladding glass bonded to their perimeters to absorb thermal, mechanical, and optical loads. An epoxy bond layer, 5 to 30 µm thick, bonds the cladding glass to the amplifier glass. The bond layer must be index-matched and free of defects so that light can transmit efficiently from the amplifier slab to the cladding glass. A defect in the epoxy, such as a void or bubble larger than 30 µm, provides a scattering mechanism for light to reflect back into the amplifier slab, instead of being transmitted to and absorbed by the cladding. A certain pattern of defects in the epoxy on opposite sides of an amplifier slab will cause light to reflect back and forth in the slab, leading to a build-up in light intensity, reduced laser yield, and resultant damage of the slab.

Optics designers at NIF have developed a complex set of cladding bond specifications that define the allowable relationship between size, shape, and location of defects. Present inspection of the epoxy bond is performed visually by a technician in a dark room, using a flashlight to search for diffracted light spots, and a sketchpad

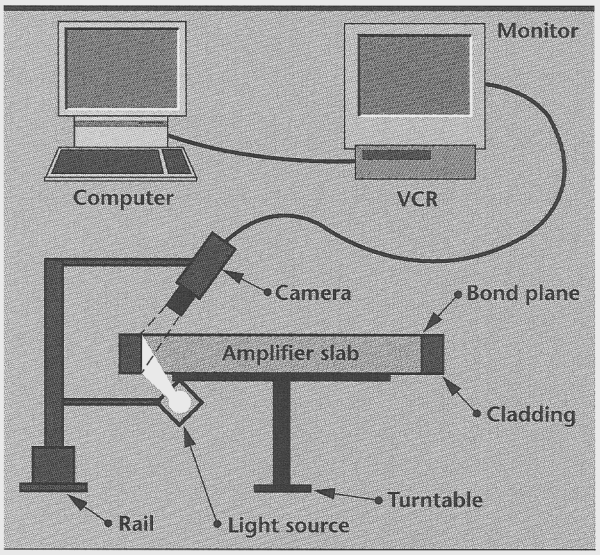

Figure 1. Automated bond inspection system. Features include an angled camera and light source on a translation rail, a turntable slab support, a monitor and VCR, and a computer.

to record defect parameters. The size of the defect is determined by comparing the diffracted light to a sizing chart. The location of the defect is found by measuring distances with a ruler. Amplifier slabs must be lifted and rotated by two people to inspect each of the bond layers on four sides. The technician accepts or rejects the cladding bond, based on subjective interpretation of the complex specifications.

Manual inspection of amplifier slab bond layers is time-consuming and subjective. Sizing defects with a comparator chart leaves considerable room for interpretation. Our project developed a technique to automate optical inspection of the cladding bond line, removing the inspector's subjectivity. If all suppliers use the same standardized and repeatable technique, NIF is assured of a consistent level of bond quality. Archiving the bond data will give NIF a record of the bond condition at fabrication, and will allow unequivocal determination of flaws that occur subsequent to manufacture.

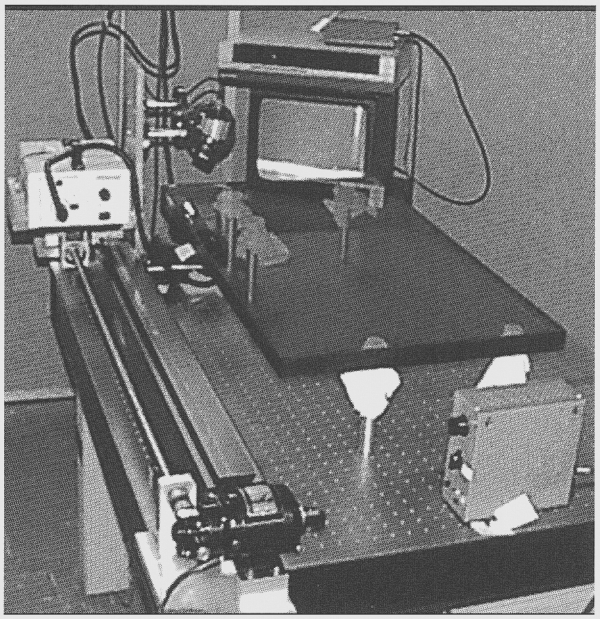

Figure 2. Experimental set-up, allowing the acquisition of digital images from the bond plane of full-size amplifier slabs.

Progress

The conceptual design of an automated optical inspection system for the amplifier cladding bond line is sketched in **Fig. 1**. Several configurations of light source and camera were considered, but the set-up shown, with angled illumination and reflected scattering detection, proved to be the most effective. The optimum camera angle is calculated based on the size and focal length of the camera lens, the thickness of the slab, and the refractive index of the glass. A linear light source illuminates the bond from the same angle as the camera, on the opposite side of the slab.

Both the camera and the light source are mounted to a fixture on a rail. The fixture moves along the cladding bond line on one side of the slab. A turntable holding fixture supports the slab and facilitates rotating the amplifier slab during inspection. For viewing and recording the cladding bond interface, a monitor and videocassette recorder (VCR) are attached to the camera.

Figure 2 shows a photograph of the experimental set-up for the automated inspection system. The slab is supported on posts instead of a turntable in

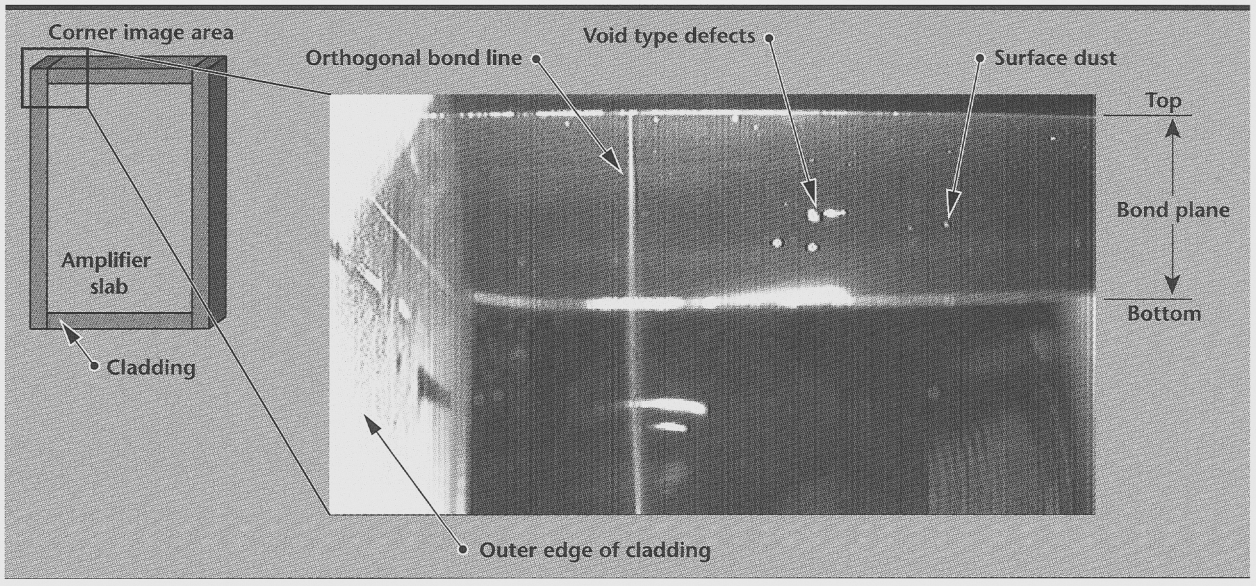

Figure 3. Digital image of the corner of the amplifier slab, showing orthogonal planes, as well as the outer edge of the cladding. The raw image clearly shows three defects, along with scattered surface dust.

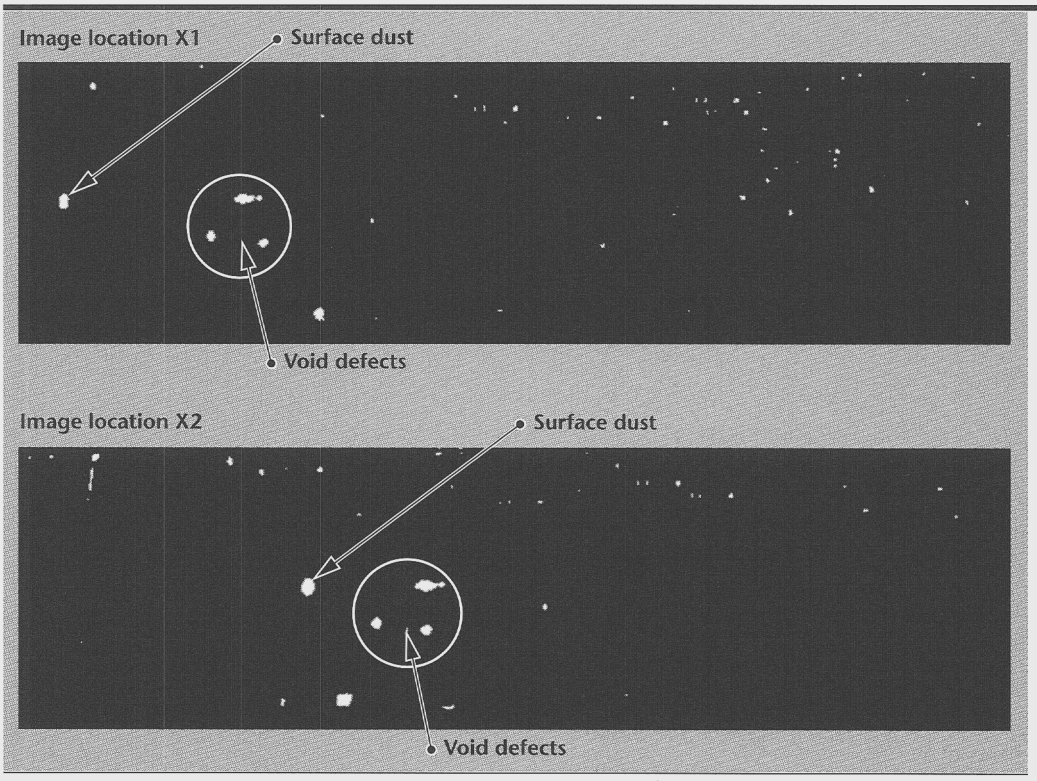

Figure 4. Processed images of the corner bond plane, acquired at locations 40 mm apart, showing how parallax helps distinguish void defects on the bond plane from surface dust. The lateral translation of surface dust indications is greater than the translation of the bond plane defects.

this experimental set-up. A 50-mm fiber optic array light source and a 25-mm focal length lens on a CCD camera gather images of the bond plane that are displayed on the monitor and recorded by the VCR.

A digital image of the bond plane at the corner of the amplifier slab is shown in **Fig. 3**. Both the bond plane and the plane of the orthogonal bond line are indicated in the image. Three void-type defects are clearly shown in the digital image. Surface dust also appears in the image.

Overlapping images taken at different locations help distinguish bond interface defects from surface dust. Two processed images of the corner bond plane area, taken from locations 40 mm apart, are shown in **Fig. 4**. To process these images, adjacent images, 1 mm apart, are differenced and the result is thresholded. Morphological pruning is applied to remove single-pixel noise. Comparing the two images reveals that the voids have translated a distance different from that of the surface dust. As the camera is translated along the cladding bond line, any light scatterer on the bond plane will translate at a rate different from that of light scattered on the surface. Parallax in the image helps distinguish surface dust from defects on the bond plane.

Surface delaminations along the bond plane are very important to detect. An image of a surface delamination is shown in **Fig. 5**. Using visual inspection, this delamination is sized at 100 μm in depth. By scaling the delamination in the image to the height of the bond plane, the delamination is digitally sized more precisely at 120 μm in depth.

Summary

We designed and assembled a proof-of-principle automated bond line inspection instrument. Based on the results of our work, we presented sketches of conceptual designs for an automated bond inspection to the consortium of NIF amplifier-slab finishers. Because of its many advantages, the consortium endorsed pursuing automated cladding inspection.

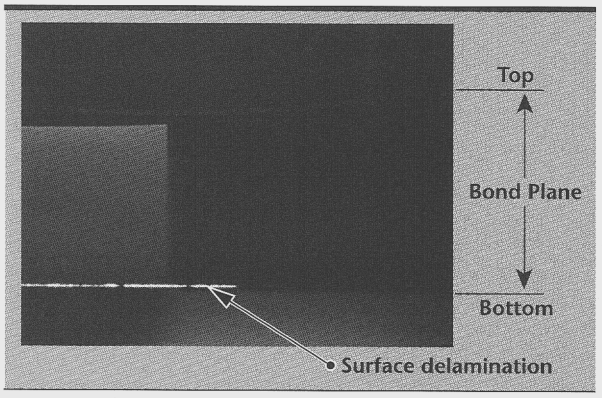

Figure 5. Surface delaminations, clearly visible in the acquired images. This surface delamination is sized at a depth of 120 μm.

The consortium agreed that the quality, reliability, and archiving advantages of an automated system would make it preferable over manual inspection.

Future Work

This year, we demonstrated the feasibility of an optical inspection system for NIF amplifier slab cladding bond interfaces. Further development of prototype systems will require additional work in a few areas, as listed below.

1) Design and fabrication of a test standard with known defects will enable the calibration of images for accurate sizing of defects. Derived from calculated scatter from modeled defects, the comparator chart used for manual sizing can resolve defect sizes to a precision no better than 100 µm. Digital images obtained by the inspection system will afford size precision that is unobtainable through manual sizing. A test standard will be required to calibrate digital sizing algorithms.
2) Drawings for a turntable to rotate the slab are being finalized by NIF mechanical designers. The turntable reduces the amount of labor required to perform the inspection. Without having to lift and rotate the slab to access all four bond planes, inspection of the slab becomes a one-person job, once the slab is placed on the turntable.
3) Additional automation features can be added to the inspection system at any time. Collection of digitized images allows automated classification and sizing of defects through image processing. Preliminary software development has already identified the processing algorithms needed. Several image acquisition and processing packages have been identified that could satisfy the needs of the inspection system. Automated motion control can be added to map the location of defects. Finally, acceptance criteria can be applied to the defect maps to automatically obtain an accept/reject decision for a slab. With automated defect detection and classification, more complicated specifications can be implemented, thus increasing the suppliers' yield when compared to simpler but more restrictive specifications.

Miniature X-Ray Source Development

Jeffrey D. Morse
Electronics Engineering Technologies Division
Electronics Engineering

Robert T. Graff
New Technologies Engineering Division
Mechanical Engineering

Alan F. Jankowski
Materials Science and Technology Division
Chemistry and Materials Science

Jeffrey P. Hayes
Applied Research Engineering Division
Mechanical Engineering

A novel cold cathode electron source is being developed with application to x-ray sources and systems. The implementation of gated field emission cathodes has the potential to realize highly reliable, micro-miniaturized x-ray sources for a variety of applications.

Introduction

Present x-ray tube technology uses a variety of techniques to generate x-ray photons in a specified energy regime. The predominant method is to use cathodes, that are heated by passing current through the filament, and subsequently emit electrons. The electrons are then accelerated in an electric field across a vacuum, gaining energy from the field until they collide with an anode foil. The energy the electrons have gained from the electric field is transferred to the foil through elastic and inelastic collision processes, and depending on the type of material the foil is made of, x-ray photons of a certain spectral range will be emitted.

We have evaluated the design and implementation of miniature x-ray sources and systems to better understand the issues and potential benefits for specific applications. In general, the key components of x-ray tubes used in various applications were evaluated to provide improved performance of the source, or to extend the range of applications for which x-ray sources can be implemented.

The results of this evaluation are that further improvements of tube and electron optics designs are necessary to decrease the spot size for high-resolution imaging. Other conclusions include the need for new cathode designs and performance, and more compact, miniaturized sources for applications in the areas of materials analysis and x-ray spectrometry.

An additional issue is that of anode life-time, which is limited, due to the heat dissipation requirements of the anode foil at the high operating currents that are typical. Imaging-related applications typically require high x-ray energy (>60 keV), and extensive electron optics to efficiently focus the accelerating electrons to a small beam diameter. The electron optics typically involve one or more grids which condition electron flux from the cathode, creating a more uniform velocity distribution. A coil distributes electromagnetic fields in the tube to accelerate and focus the electrons to small spot size dimensions on the anode. The specific electron optics design depends on the electron source and tube design, which tend to vary from one application to the next.

The scope of this effort was 1) to evaluate the impact on overall tube design and performance which could be realized by implementing a new cathode design; and 2) to determine if new applica-

tions could be found for such a source. The scope further included new cathode designs, that were fabricated and evaluated as electron sources, as described in the next section.

While marginal improvements in general x-ray imaging tube technology and performance could be realized through using a new cathode capability, the concept of a microfabricated cathode for a miniature x-ray source now opens up the possibility of an x-ray micro-instrument, which can subsequently be implemented with other microtechnologies to realize a low cost, compact, ruggedized system for a variety of applications.

Progress

Gated field emission, cold cathode electron sources were evaluated as an improved means to generate electrons in x-ray systems. The concept is illustrated in **Fig. 1**. Field emission devices are cathode structures that are formed to atomically sharp tips in proximity to an extraction, or gate electrode. By applying a positive voltage to the gate electrode with respect to the cathode, electrons are emitted into the vacuum above the gate, where they are swept away by the anode electric field.

The efficiency of the field emission process depends on the gate-to-tip spacing, the shape of the tip, and the effective work function of the tip material. The potential advantages of field emission devices as an electron source are improved efficiency, addressability and control, no heating of surrounding areas, and faster turn-on. Furthermore, field emitters are made using standard microfabrication processes, thus are more conducive to implementation into arrays, or specific cathode designs.

The advantages can impact x-ray tube or source performance in several ways. First, the field emission cathode (FEC) is controlled by a gate electrode, therefore is electrically addressable, and uses about one tenth the power of filaments. FECs can be formed in arrays, with different areas of the array being turned on independently, and at different times. This feature has the advantage that the anode can be driven at higher currents with eroding, since its duty cycle is effectively less. This has the potential of providing a higher average power, or flux, of x-ray photons from the source, which may be useful in some imaging applications.

Furthermore, additional focusing electrodes can be monolithically integrated with the FEC to provide electronic focusing and tuning capability for the tube. This relates to a fundamental problem with x-ray tube reliability, in that alignment of electron optics is critical and may vary over time or by impact. Finally, the ability to microfabricate the cathode now enables further miniaturization of the x-ray tube through micromachining processes. This includes additional functionality to an x-ray system, such as integrated micro-channel cooling of the anode, and integrated detection and signal processing for applications such as x-ray fluorescence spectroscopy. These advantages have the potential to enable a novel x-ray micro-instrument capability.

A FEC array was designed having an active emission area ranging from 25 μm × 100 μm (800 emitters) to 100 μm × 200 μm (10,000 emitters). **Figure 2** illustrates the fabrication sequence for

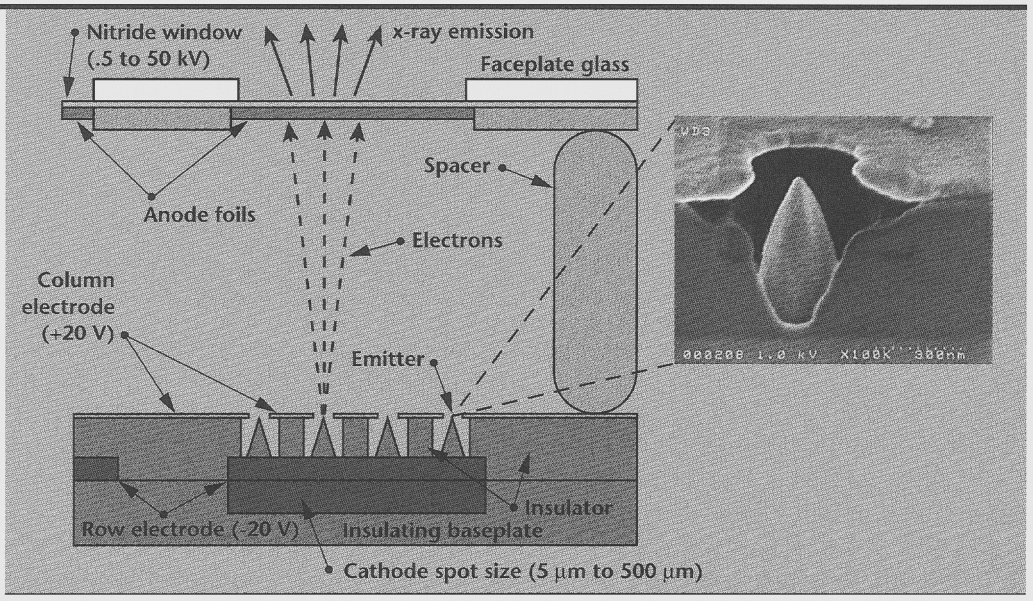

Figure 1. Concept of x-ray source using gated field emission cathode arrays as the electron source.

making a gated field emission cathode device using the Spindt cathode technique.[1–3] Using a proprietary lithographic technique developed at Lawrence Livermore National Laboratory (LLNL), gate-to-tip spacings of <0.1 μm have been achieved, as illustrated in **Fig. 3**. Process development consisted of several iterations of this sequence to optimize problems associated with adhesion of thin films, uniformity of emitters, gate hole diameter, pattern transfer, and gate-to-cathode leakage current. While most of these problems have been addressed and resolved, the issue of gate leakage current remains problematic.

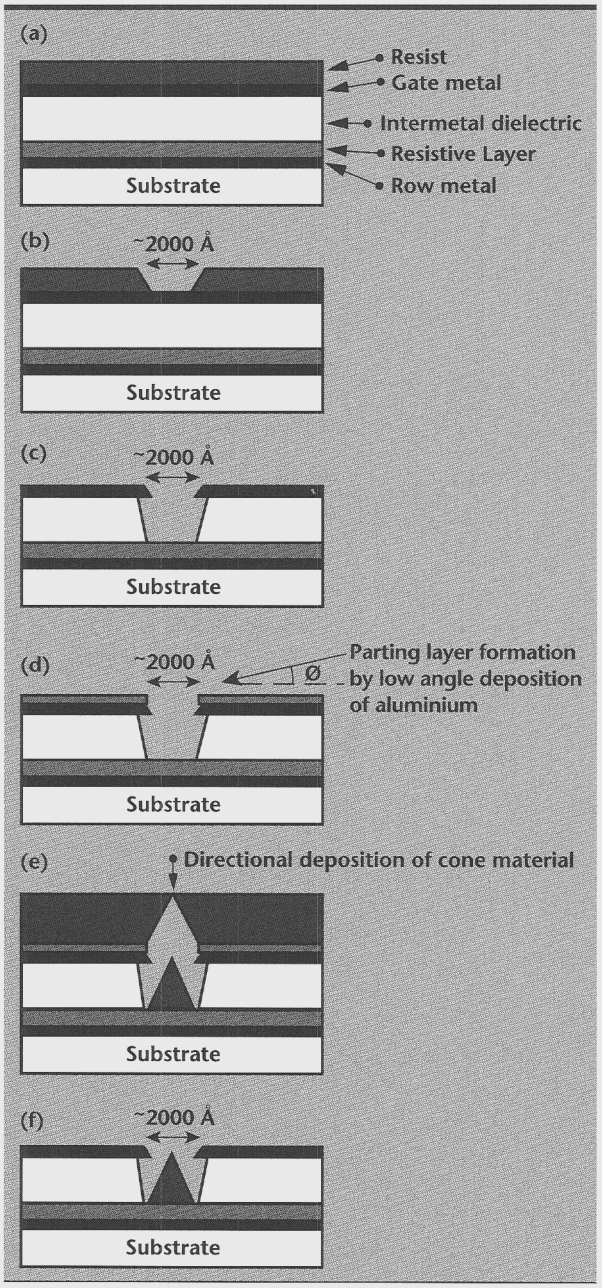

Figure 2. Cross-sectional schematic diagram of field emission cathode fabrication process sequence: (a) initial stack of thin film layer with resist deposited on top; (b) patterning of resist by lithographic techniques to form gate structure; (c) etching of the gate metal through the mask, and of the cavity in the intermetal dielectric; (d) field emitter tips formed by depositing a parting layer; and (e) directional deposition of the tip material. The final emitter structure is formed (f), after lifting the parting layer from the gate metal.

A vacuum test station has been assembled to characterize the FECs at pressures on the order of 10^{-7} Torr, which is typical of x-ray tubes. The test apparatus includes a fixture on which the FEC is mounted. Electrical leads are attached and the anode is then positioned to within 0.5 mm of the cathode array to collect any electrons that are emitted.

Vacuum testing of these devices has demonstrated field emission current turn-on with less than 50 V applied to the gate electrode. As previously mentioned, a limitation of devices fabricated is the excessive gate leakage current which is orders of magnitude greater than the emission current, as illustrated in **Fig. 4**.

This problem, which is being addressed, is likely a result of contamination in the intermetal dielectric, or metal, shorting the tip directly to the gate electrode. The impact on device performance is that the FEC will burn out when the gate current reaches a value, on the order of 100 μA, thus limiting the field emission current to about 50 nA. Other solutions to this problem include an integrated ballast resistor, which in effect will minimize the impact of shorting due to point defects.

Efforts to test the FECs that are being fabricated in an x-ray tube are in progress. The most practical approach is to retro-fit the FEC to an existing x-ray

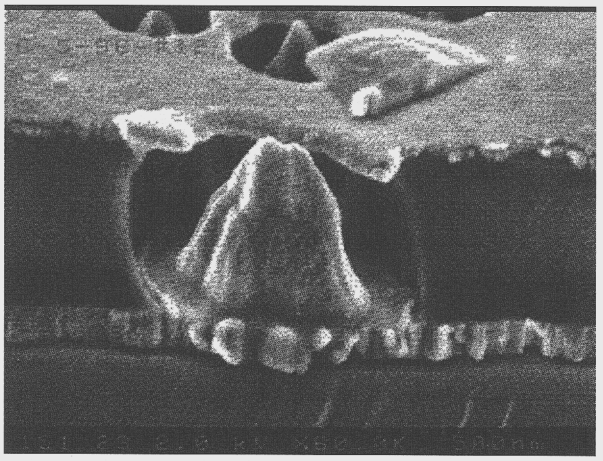

Figure 3. Cross-sectional schematic of gated field emission cathode fabricated using sequence shown in Figure 1. Gate diameter for this device is 2000 Å.

tube with an experimental set-up having adequate voltage sources for the anode, and x-ray windows for diagnostics. To complete this in a feasible manner, Lawrence Livermore National Laboratory (LLNL) has established two collaborations, presently in progress, to provide experiments to evaluate the performance of FEC designs as x-ray sources.

The first collaboration is a formal Cooperative Research and Development Agreement (CRADA) with an industrial partner, and the second is an interaction between LLNL's Y-Program and private industry. The collaborations are for different applications, but each one has the requirement of an efficient, low power, compact electron source, therefore FECs are being investigated. In each case, we are establishing experimental set-ups having approximately 20 kV anode potentials for initial testing.

Other issues being considered are electrode design and packaging to minimize any effects of the high voltage applied to the anode or the cathode.

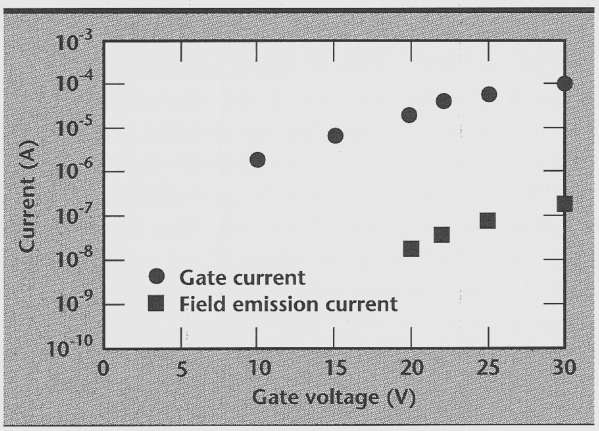

Figure 4. Current/voltage characteristics for field emission cathode array: current measured at anode with 1.5 kV applied, and gate electrode, as a function of gate-to-cathode voltage.

For testing, the system has been modified simply so the cathodes can be retro-fit to replace the filament cathode. This approach essentially minimizes cost and effort involved until the requirements of the system using cold cathodes can be determined.

Future Work

We have identified several applications, both internal to LLNL and for outside agencies and industrial partners, for miniaturized x-ray sources with novel cathode designs. These include an x-ray micro-probe for materials analysis, and imaging, particularly in the region where low energy x-rays are suitable.

Preliminary demonstrations will continue to focus on a reproducible cold cathode technology for generating x rays. Subsequently, the technology will evolve to the development of specific instrumentation designs, depending on the application. Further assessments will also include the use of micromachining technology for applications which could take advantage of micro-miniature systems.

References

1. Spindt, C. A., I. Brodie, L. Humphrey, and E. R. Westerberg (1976), "Physical properties of thin-film field-emission cathodes with molybdenum cones," *J. Appl. Phys.*, **47** (12), p. 5248.

2. Spindt, C. A., C. E. Holland, P. R. Schwoebel, and I. Brodie (1996), "Field-Emitter-Array Development for Microwave Applications," *J. Vac. Sci. Technol. B*, **14** (3), p. 1986.

3. Bozler, C. O., C. T. Harris, S. Rabe, D. D. Rathman, and M. A. Hollis (1994), "Arrays of Gated Field-Emitter Cones Having 0.32-μm Tip-to-Tip Spacing," *J. Vac. Sci. Technol. B*, **12**(2), p. 629.

Improving Computed Tomography Design and Operation Using Simulation Tools

G. Patrick Roberson
Defense Sciences Engineering Division
Electronics Engineering

Daniel J. Schneberk
Computer Applications Sciences and Engineering Division
Computation Organization

Jerry J. Haskins, Clint M. Logan, Harry E. Martz, Dwight E. Perkins, and Derrill R. Rikard
Manufacturing and Materials Engineering Division
Mechanical Engineering

Three-dimensional computed tomography (CT) is a rapidly changing nondestructive characterization technology that is playing an increasingly important role in the manufacturing process. This process consists of all the elements of a component's life, from concept and design, through fabrication, and ending only with retirement from service. This philosophy is equally valid in the industrial and the defense or weapons arenas. Volumetric CT has benefited, and will continue to benefit programs at Lawrence Livermore National Laboratory (LLNL) that require nondestructive evaluation (NDE) of assemblies such as weapons and advanced materials. This year we have focused on improving the quantitative aspects of our CT systems by developing, improving, and documenting alignment procedures. Also, we are trying to better understand the effects of mechanical inaccuracies on the quality of our CT data.

Introduction

Although a variety of commercial industrial CT systems exist, they are typically developed to solve a particular problem, such as a solid rocket motor or turbine blade inspection. At LLNL it has been necessary for us to develop our own CT scanners, due to the large variety of NDE problems that we face, and the fact that we operate at the cutting edge of this technology.[1,2]

Purchasing an optimized CT scanner for each NDE problem that exists at LLNL would be a very expensive endeavor, in part because of the dynamic nature of CT technology. Therefore, our strategy has been to develop a small number of flexible CT scanners that can be configured in a manner that is optimal for the NDE problem at hand. These scanners are modular in design, and changes can be incorporated easily and inexpensively as system components improve.

However, this design philosophy does complicate some important requirements, including the choice of components and alignment procedures. We have a supply of different CT system components that are mixed and matched, depending on the application requirements. It is critical that the effect of the accuracy of these components be well understood, so that the desired results can be obtained. Also, when a system is first developed, or whenever it is reconfigured, a rigorous and time-consuming alignment process must be completed. Good quantitative results depend on accurate components and alignment procedures.

It is not well known how the alignment and accuracy of the mechanical positioning systems affects the outcome of the overall fidelity of the reconstructed image. The propagation of error due to positioning must be well understood if a CT scanner is to perform optimally. The precision of a CT system, like any optical system, is a product of the

quality and the alignment of its component parts.[3] Error sources propagate through the system hardware, as well as through the image pre-processing and reconstruction algorithms composing the system software.

Figure 1 illustrates how error propagates through the major components of a CT system. The four major components are: x-ray generating source, mechanical staging system, detector, and image reconstruction process. Although there are many mechanisms that generate the error that propagates through the CT system components, this year's project is concerned only with geometric factors. These factors include errors due to the mechanical structure of the CT design, such as errors propagated by inaccuracies in the mechanical staging systems, and the misalignment of hardware components.

Progress

We are working to improve the quality of our CT systems by understanding the geometric factors associated with alignment and mechanical precision for all the components.[4,5] This year we have spent considerable time evaluating and documenting procedures related to CT system alignment. We have a large number of diverse CT systems, and each requires a different alignment procedure. Evaluation of these procedures is an on-going effort that will continue until each of our systems, including new ones, is documented.

The entire alignment procedure documentation is too extensive to describe here; therefore, we limit this discussion to a new method being evaluated through simulation that could be used on a variety of CT systems, and has possibilities for use in an automated process. Also, there are many components and sub-assemblies used in a CT system, and they must all be aligned and characterized for accuracy. The discussion here is limited to only one component, the rotational stage.

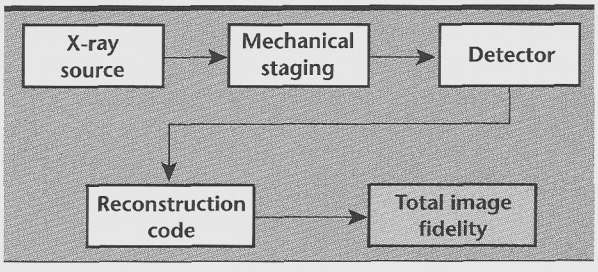

Figure 1. Schematic showing the key CT system components. When error propagates through the CT system, each of the components affects the overall image quality.

The rotational stage is part of the object manipulator and is one of the most important mechanical stages associated with a CT system. We have developed simulation tools to better understand how errors associated with this stage influence the quality of the final reconstructed image. These tools are used for understanding error created by both misalignment and mechanical inaccuracies.

There are further benefits to simulating these errors. If mechanical inaccuracies can be simulated, it should also be possible to correct for these errors if the mechanical stage is well-characterized and repeatable. Correcting for stage inaccuracies using computational methods would allow for less precise staging to be used in a CT system design, yielding a significant cost savings. Also, simulating the alignment procedures and results is providing us with an understanding of how to automate the alignment process.

The following discussion is divided into two sections, the first is related to precision of the rotary stage, and the second involves alignment of the rotary stage to the source and detector.

Mechanical Precision of the Rotary Stage

In a rotary system, there are two main sources of error that can affect the CT data: 1) wobble, which is defined as the angular deviation of the axis of rotation over one revolution, as shown in **Fig. 2**; and 2) eccentricity, which is the deviation of the center of rotation from the mean position. Eccentricity error is sinusoidal in nature, and other errors resulting from imperfections (in the gear

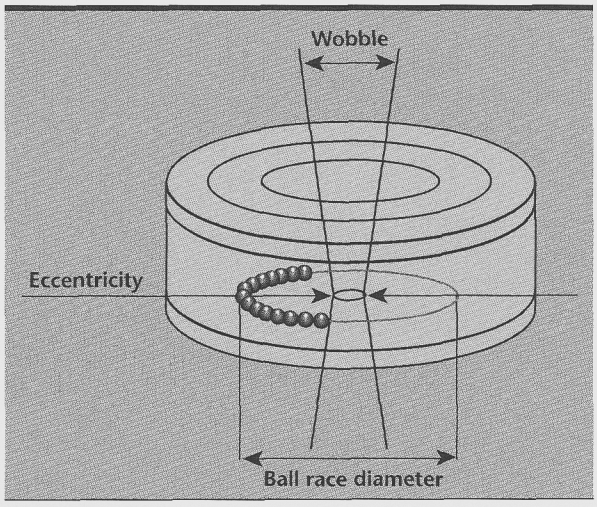

Figure 2. Illustration of the two main sources of error in rotary motion: wobble and eccentricity.

teeth or guides, for example), appear as noise superimposed upon this sinusoid.

Wobble and eccentricity are both important factors if the unwanted movement produced by either is significant enough to produce error in the reconstructed image. The amount of error also depends on how far away from the stage surface the object being examined extends.

During CT data acquisition, radiographs or projections are acquired at different rotational positions as the object is rotated over 180° or 360°. If sufficient wobble and/or eccentricity exists, each of the object radiographs will have a different center axis of rotation, depending on the angular view acquired.

For the reconstruction process, it is important that the center axis of rotation be well known (to better than the spatial resolution of the CT scanner) and not move between projections. If the center axis position changes between projections, error is created and may be visible in the final reconstructed images. If sufficient wobble exists, the amount of eccentricity increases as one travels farther away from the rotational stage top.

Additionally, if wobble exists, portions of the object being examined may be in a detector's planar view (row of detectors) for only a portion of the angular positions and out of view for the others. In parallel-beam CT, if a feature in an object is visible in a particular row of detectors, it should remain visible in that row over all angular positions. If this is not true, the error in positioning the object may generate visible error in the reconstructed image.

We have developed simulation tools to study the effects of both eccentricity and wobble on the final CT reconstructed image. In the simulation process, a 3-D test phantom was generated. A surface rendering is shown in **Fig. 3**.

The test phantom represents an extended cylinder of low-density homogeneous material with a high-density outer wall. The internal material is not visible in the figure because the image threshold has been set above its value. Inside the extended cylinder are solid bars of material similar to the outer cylinder wall. The bars extend out from the center of the object, but do not intersect the outer cylinder wall. The extending bars define four quadrants, and within each quadrant are three solid forms made of the same material as the bars. The solid forms and the bars are fully contained within the cylinder. Each quadrant holds a different solid geometric form.

Figures 3b to **3e** show surface renderings of the four different geometric forms within each quadrant of the phantom. They are: (b) solid ellipsoids; (c) solid spheres; (d) solid cylinders; and (e) solid cubes. The image of the simulated phantom shown in **Fig. 3a** is 256 (x-axis) × 256 (y-axis) × 20 (z-axis) pixels in size.

The z-axis of the phantom image can be divided into 20 planes; three of these are shown in **Figs. 4a** to **c**. The homogeneous cylinder with the dense outer wall appears in all 20 planes. No portion of the bars or the four different geometric forms is contained in the first four planes (0 to 3) or the last four planes (16 to 19) in the simulated 3-D image. The bars and geometric forms are all contained within 12 planes (planes 4 to 15). Planes 3 and 4, and 15 and 16, are transition planes where the bars and geometric forms begin and end, respectively.

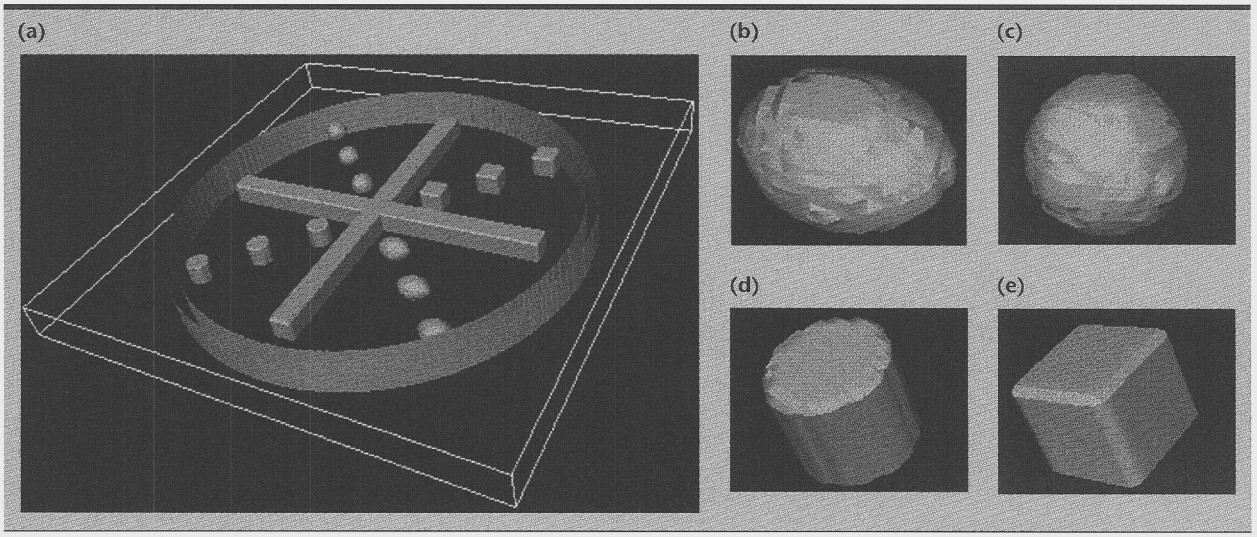

Figure 3. (a) Three-dimensional surface renderings of the phantom used to evaluate stage precision; and magnified views of (b) solid ellipsoids used in the phantom, (c) solid spheres, (d) solid cylinders, and (e) solid cubes.

CT projections were synthesized from the simulated phantom data set. **Figure 5** shows two examples of the projections. There are 402 projections that were generated over 180°. An "ideal" CT system would acquire noiseless projections like these from an object like the one that is described in **Fig. 3**. These simulated projections are used in the reconstruction process to develop 3-D tomograms that are a representation of the phantom or object. Three of the 20 reconstructed tomograms of the

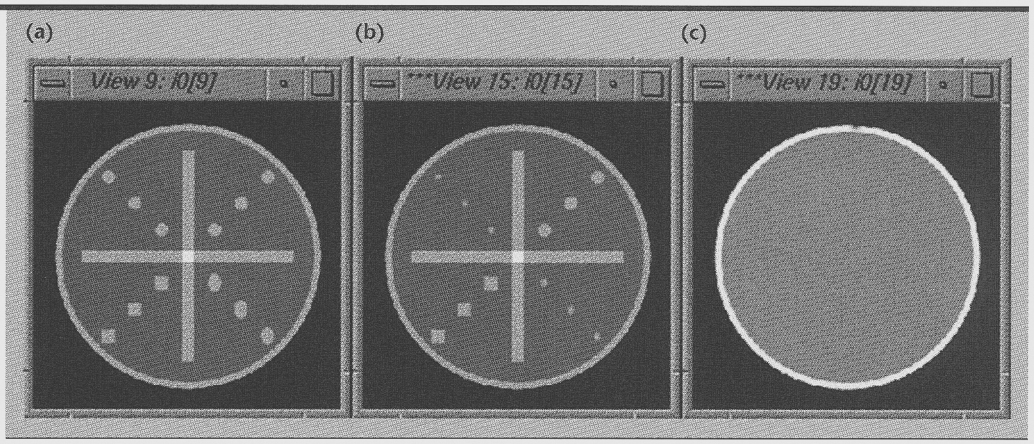

Figure 4. Two-dimensional images for three of the 20 planes that form the simulated phantom showing (a) the center plane; (b) a plane just before the bars and geometric forms end (transition plane); and (c) the last plane, where no geometric forms or bars are visible.

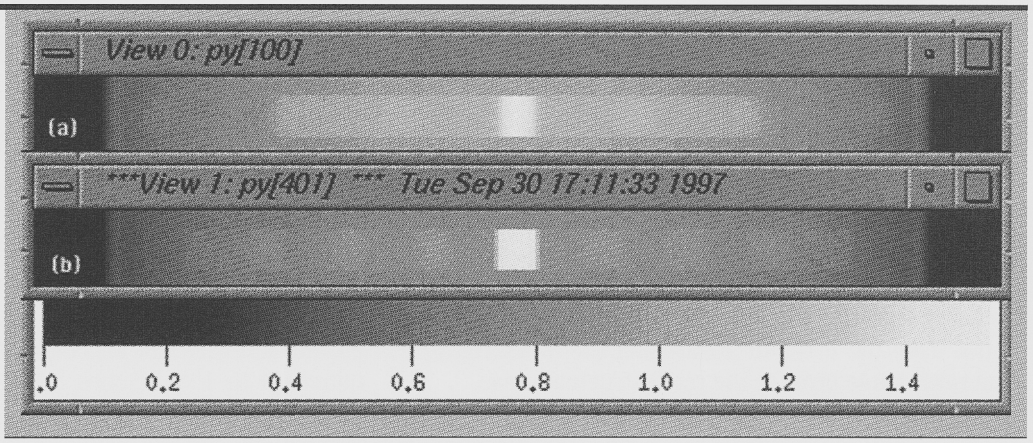

Figure 5. Two examples of synthesized CT projections generated from the phantom in Figure 3: (a) projection 101 out of 402, and (b) projection 402. There were 402 projections, produced over 180°.

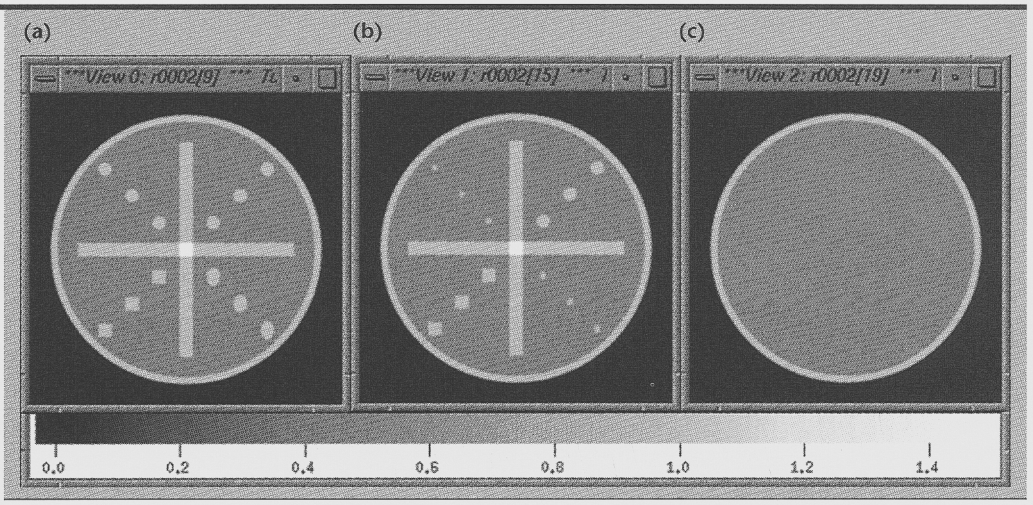

Figure 6. Reconstructed "ideal" tomograms representing the simulated phantom in Figure 3. Twenty slice planes were reconstructed; only three are shown here. Slice planes are located at (a) the center of the object; (b) the transition where the bars and geometric forms end; and (c) the bottom of the object. Note that these are similar to those of the simulated object image slices shown in Figure 4.

phantom are shown in **Fig. 6**. These are basically "ideal" tomograms, where the only error that is contributed comes from the sampling and image reconstruction process. These ideal reconstructed tomograms are used in comparing results to tomograms reconstructed from projections with staging errors introduced.

Wobble and eccentricity were simulated by implementing their effects in the synthesized projection data prior to reconstruction. The effect of eccentricity without wobble is simply a horizontal shift in the projection data with respect to the center axis of rotation. The shift has a sinusoidal weight and is dependent upon the rotary stage position.

When wobble is integrated, a vertical shift must also be implemented, which is again dependent upon the rotary stage position. A simulation tool was developed for this project that implements the shift required in the projection data sets to simulate both wobble and eccentricity. The desired amount of vertical and/or horizontal shift (over all the projections) are input parameters for the tool. The amount of shift is described in pixel, or fraction of pixel length, making the simulation generic to all CT systems.

For example, we have a high spatial resolution CT system that is capable of acquiring radiographs with pixels that are approximately 10 μm × 10 μm in size. A shift of one quarter of a pixel in this case would represent eccentricity of only 2.5 μm over a 180° or 360° movement of the rotational stage.

Four simulations were performed to observe the error produced in a CT reconstructed image as a result of different degrees of wobble and eccentricity.

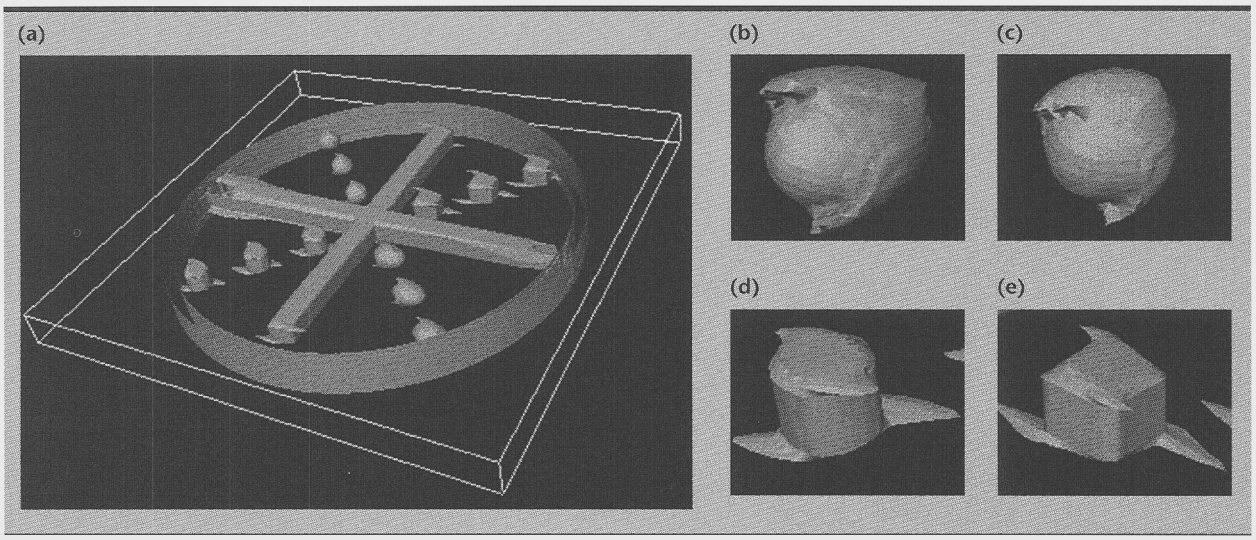

Figure 7. (a) Three-dimensional surface rendering of the reconstructed tomograms of the simulated phantom with 1-pixel wobble and eccentricity error introduced. Magnified views of (b) solid ellipsoids; (c) solid spheres; (d) solid cylinders; and (e) solid cubes are shown with the reconstructed artifacts that are typical to rotary stage inaccuracies.

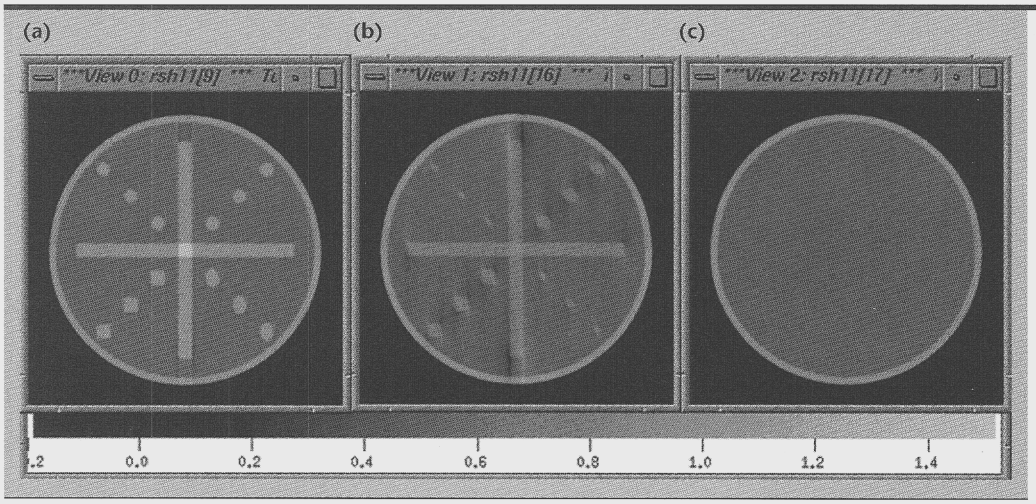

Figure 8. Two-dimensional reconstructed tomograms of the simulated phantom with 1-pixel wobble and eccentricity introduced: (a) tomogram at center of the object; (b) tomogram at a transition slice; and (c) tomogram just below the transition slice.

The first case simulated a horizontal and vertical shift of the object by 1 pixel over 180° of rotational movement. The second simulated a 0.5-pixel movement over 180°, the third a 0.25-pixel movement, and finally, the fourth was a simulation of a 0.1-pixel movement.

Figure 7 shows 3-D surface rendered images of the 1-pixel error simulation after reconstruction. Artifacts are present within the reconstructed image, and they are particularly prevalent at transition boundaries (that is, where the bars end, or the top and bottom of the cubes and cylinders). At the boundaries, or whenever there is a change in attenuation, planar information can be missing or contaminated with other planar information if there is a sufficient amount of wobble. Also, the artifacts appear to be more prevalent where there are sharp edges within the image. The artifacts can also be observed in each slice of the reconstructed tomograms shown in **Fig 8**.

Only three of the 20 slices are shown here, one at the center of the object, one at a transition slice, and one just below the transition slice. The artifacts can be seen here also, and again, they are particularly evident at transition areas. The simulated artifacts that are observed here are caused purely by rotational error in the object handling system. If artifacts are observed in real CT reconstructed images that are similar to these, than rotational stage inaccuracies should be suspect.

A more quantitative measure of error is observed when taking the difference between the "ideal" reconstructed image shown in **Fig. 6** and the reconstructed images that simulate the various degrees of wobble and eccentricity error. **Figures 9a** to **9d** illustrate the amount of error present for the simulated cases of a 1-, 0.5-, 0.25-, and 0.1-pixel vertical and horizontal shift over 180° of rotational movement. It is surprising to see that a shift of merely one quarter of a pixel can cause visible error in the reconstructed image. As mentioned above, eccentricity of only 2.5 μm would produce this type of error in our 10-μm high-spatial resolution CT system.

Alignment of the Rotational Stage

We are developing simulation tools and procedures in an attempt to improve our CT systems alignment, which will improve the quality of our data. It is also possible that the methods and tools being developed will lead to fully automated or semi-automated calibration that would greatly speed up the process. This criterion has influenced the choice of phantoms and operational procedures that are required for alignment. An attempt is made here to fully simulate the interaction between the experimenter and the CT system.

There are two key requirements of an aligned rotational stage. First, the center of rotation should be coincident with the center of the x-ray beam at a specific magnification. It is also advantageous if the center of rotation is located at the center of the detector for the best use of the source and detector. Second, the normal vector projected up from the center of the rotational stage should be parallel with

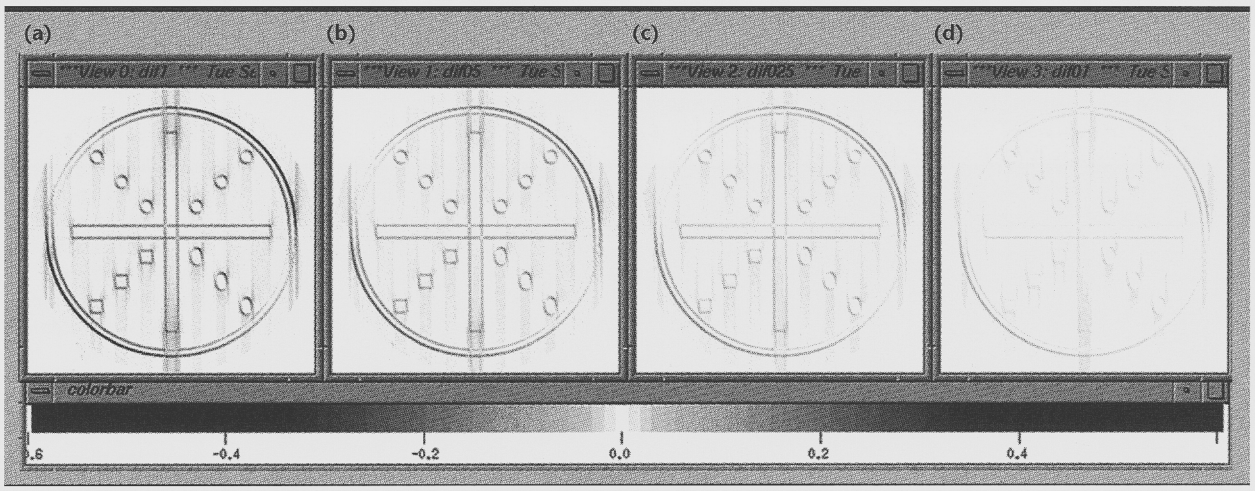

Figure 9. Two-dimensional difference images of the center slice of the simulated phantom. The images are the difference of an "ideal" reconstructed image (shown in Figure 6a) from various degrees of simulated wobble and eccentricity error. The various degrees of error are shown for: (a) 1-pixel vertical and horizontal shift over 180° of rotational movement; (b) 0.5-pixel shift; (c) 0.25-pixel shift; and (d) 0.1-pixel shift.

the plane of the detector face front, and perpendicular to the mid-plane of the x-ray beam.

Figure 10 illustrates an example of misalignment. Alignment is specified by three parameters defined in the detector coordinates: the offsets from midline (τ_t and τ_v), and the rotational tilt (γ).

The task of aligning the rotation stage can be performed using a phantom or test object. The phantom could consist of a cylinder of plastic or some low-Z material with single steel or tungsten balls positioned at different heights along the cylinder. This phantom is called a "ball phantom." A diagram is shown in **Fig. 11a**. Cylinders of different radii should be used to completely fill the field of view of the CT system. CT systems can have different fields of view depending on the systems magnification, which is typically adjustable. The balls should be about 1 to 3 pixels in extent, and positioned at different heights along the cylinder and near the edge of the cylinder (at large radii). All of the operations performed for alignment of the rotational stage use the ball phantom.

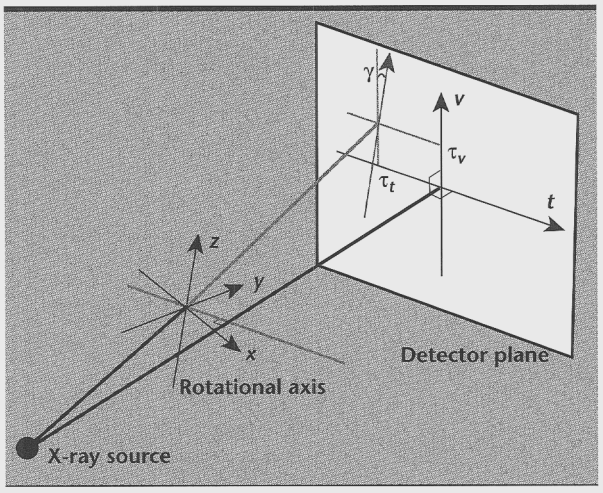

Figure 10. Alignment parameters for a typical 2-D detector CT system.

Figure 11b shows a simulated radiograph (no noise) of a ball phantom. For this simulation, the phantom was positioned at a source-to-object distance of 423.6 mm, and has a diameter of 250 mm to just fill the field of view. To keep the disk space requirements moderate, a 512-×-512 simulated detector was used with 0.685-mm square elements at the detector, yielding 0.525-mm elements at the center of the object (that is 0.525-mm cubic voxels for the canonical reconstruction mesh).

In **Fig. 11b**, the balls are 1.5 mm in extent for this simulated example. The issues about ball size involve a trade-off between contrast sensitivity, the size of a pixel, and the precision that is required to align the system. As the balls get smaller, the contrast requirements can become problematic, a particular problem in real CT data with additional noise content. We want to image the balls clearly, and not guess about their position due to inadequate contrast performance. However, with "perfect" synthetic data, even small differences in attenuation are significant. If it is necessary to see small misalignments, the balls should be small. This may then require higher-Z balls (that is, tungsten) to increase the contrast.

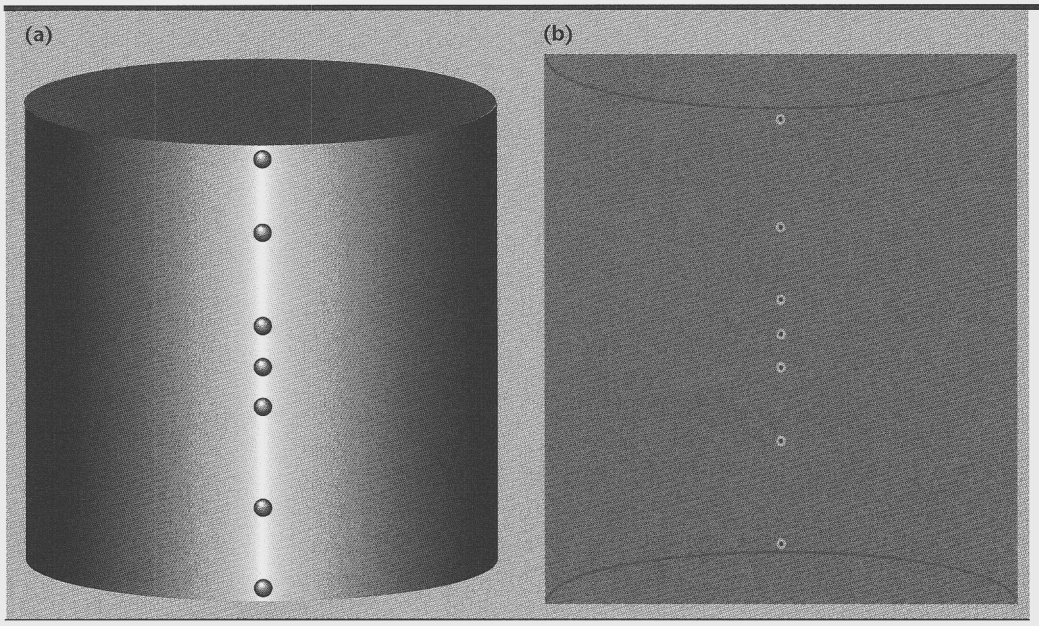

Figure 11. (a) Diagram of the ball phantom containing a low attenuating cylinder with high attenuating balls; (b) simulated radiograph of the ball phantom.

For a CT system with a large field of view, larger balls can be used and regular ball bearing steel will suffice.

During the alignment procedure, the camera acquires a single image while the ball phantom is continuously rotated (typically over 720°). **Figure 12a** shows an approximate image of this type of acquisition for a well-aligned ball phantom. Different torii were used for the balls to simulate the effect of radiographing under constant rotation. Two types of vectors are calculated from this simulation. First, a row-wise projection is calculated from the radiograph, as shown in **Fig. 12b**. Second, the center of mass is calculated for the center ball, as shown in **Fig. 12c**.

To understand the relationship of different types of tilt, different tilts were simulated with the synthetic ball phantom. For example, the phantom was tilted directly to the right 1°. **Figure 13** contains the image of the constantly rotated phantom (**Fig. 13a**) and plots of the two vectors, the row-wise projection vector (**Fig. 13b**) and the center of mass vector (**Fig. 13c**). In the center of mass plot, notice the skew opposite the direction of the tilt.

Figure 14 contains two plots of the vectors showing the differences between the aligned and tilted radiographs. For the projected vector, the effect of tilt results in a decrease in magnitude and widening of the FWHM of the change in attenuation for the middle ball, as shown in **Fig 14a**. The center of mass vector

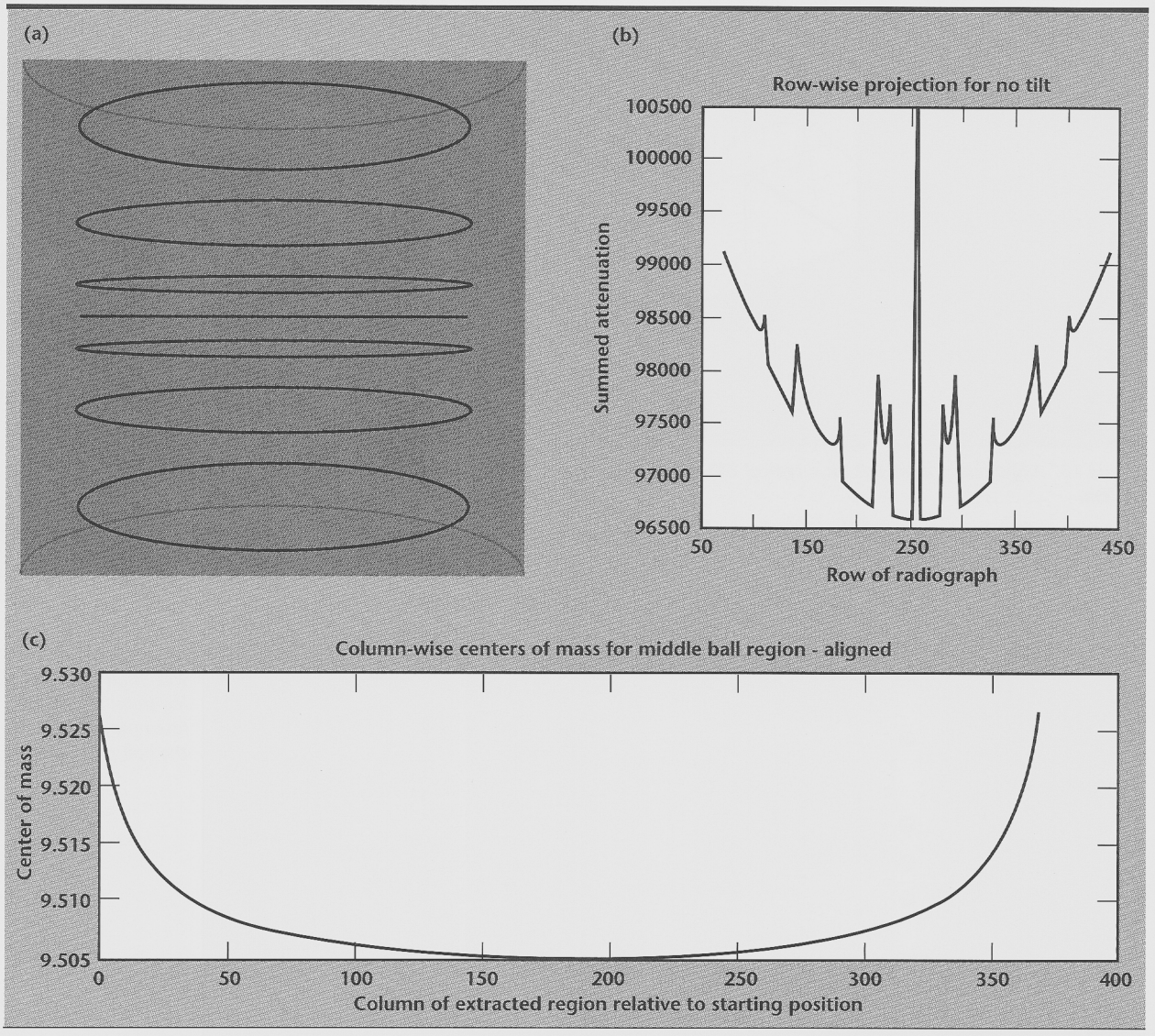

Figure 12. (a) Simulated radiographic image from camera acquiring data while the well-aligned ball phantom is continuously rotated; (b) row-wise projection vector. Note: the summed attenuation of the cylinder (with or without the balls) is higher at the top and bottom, due to the large source cone angle associated with this simulation. X-ray cords are longer through the top and bottom of the cylinder than they are through the center. (c) Center of mass vector for the middle ball.

for the ball at the mid-plane becomes curved at the ends for the tilted case, as shown in **Fig. 14b**.

The basic procedure would be to keep tilting the phantom until the magnitude of the row-wise projection of the center ball is as large as possible, and the width of the projection trace is as small as possible. Any misalignment will cause a spreading of the same mass over more pixels and reduce the intensity of the peak. The direction of tilt for correcting alignment can be determined from the skew of the center of mass plot.

There are a number of possible applications of this technique to automated alignment. The projection vector determines if tilt exists. The width of the row-wise projection will be minimum for the ball on the aligned rotational table (no tilt, and ball on the mid-plane). Also, the curvature of the center of mass plots point to the direction necessary for correcting the tilt. If computer-controlled alignment mechanisms are incorporated in the CT system, the corrective action necessary for the next move of the tilting stages could be calculated from these procedures. However, currently we only use a manual hand-dial driven tilt apparatus to make these corrections. The key is that, once the location of the mid-plane is known, and the system is aligned on the mid-plane, the center of the source cone is known, and the center of rotation can be calculated from the center of mass of the single line of data on the mid-plane.[6]

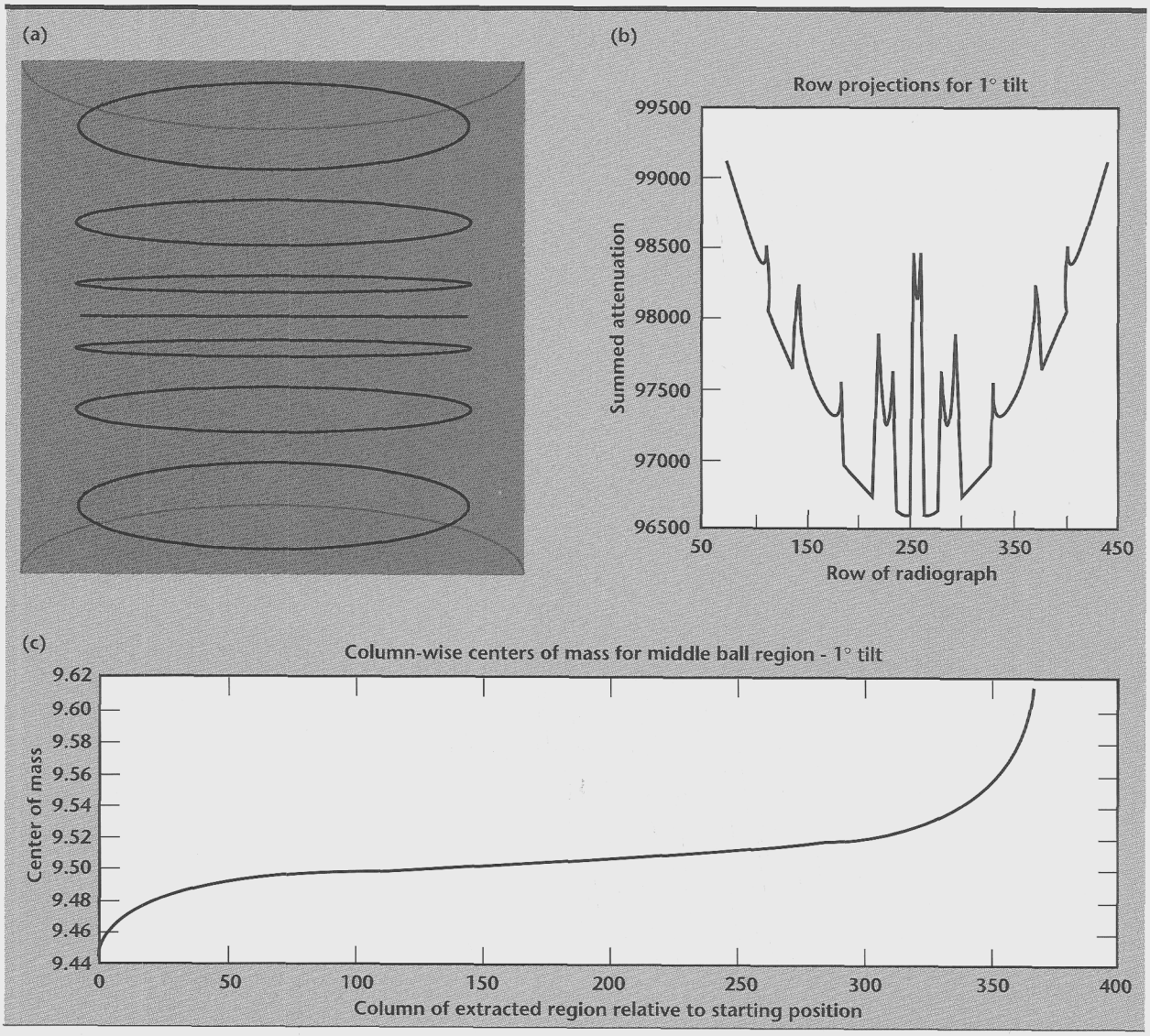

Figure 13. (a) Simulated radiographic image of a tilted ball phantom that is continuously rotated. The phantom is tilted 1° to the right. (b) Row-wise projection vector for this tilted phantom; and (c) center of mass vector for tilted phantom.

The disadvantages of this process are the contrast properties of the ball phantom. If the contrast is low and there is a lot of noise in the images, all of the manipulations of the data will be problematic. This is why it is necessary to carefully choose the size of the balls and the size of the plastic cylinder that is used to develop the phantom. The size of the plastic cylinder should be just slightly less than the field of view (at a specific magnification). If smaller balls are required for more accuracy, then higher attenuating material should be used to increase contrast. Also, the projection vectors help improve the signal-to-noise where the noise is suppressed in the radiographs by summing rows.

Future Work

At LLNL our computed tomography systems are complex and diverse. We use them in a large variety of industrial NDE applications, ranging from high-spatial resolution applications like the micro-scale characterization of soil samples to large-scale lower resolution applications like the characterization of waste drums. To handle these requirements, our CT systems are modular in design and can be adapted to the application. This type of modular design requires that we understand the mechanical accuracy associated with each component and what is required for their alignment. In the development of new CT systems, or when reconfiguring existing systems, this information can be used to mix and match components so that the required results will be obtained.

We are interested in developing a tool to simulate the entire CT system, from the source to the detector. This tool would be used by the CT system designer to choose system components and develop requirements necessary for their alignment. This year we have developed tools to understand one important component of the CT system, the rotary stage. The simulation of other components of the CT system can be based upon what we have learned in simulating the rotary stage.

From simulating the rotary stage, we have discovered that small errors caused by wobble and eccentricity can create visible error in the final CT reconstructed image. Error creating only one quarter of a pixel displacement over one rotation of the rotary stage is sufficient to cause artifacts in the reconstructed image. Reconstructed artifacts that are caused purely by wobble and eccentricity have been simulated so that the effect can be identified in real CT data sets. If we can simulate error caused by wobble and eccentricity, we should also be able to correct for this error if the rotary stage is well-characterized and the error is repeatable.

We have also simulated an alignment procedure for the rotational stage that uses a ball phantom. This procedure generates data that could be used for automated or semi-automated alignment.

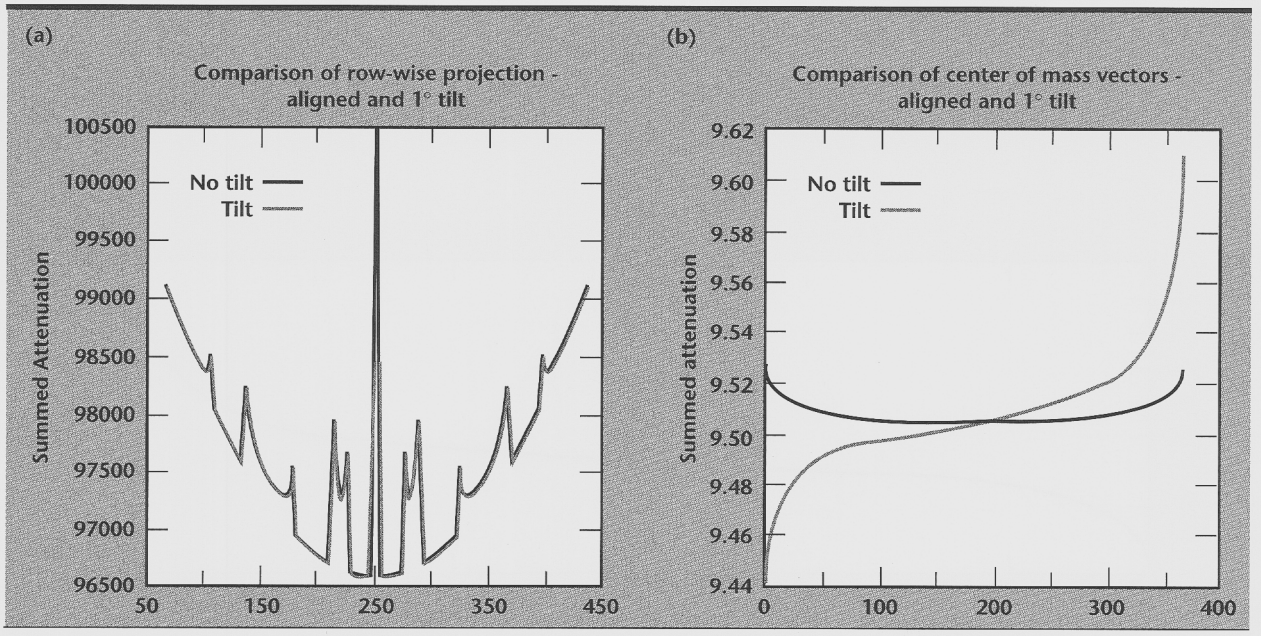

Figure 14. Comparison of the vector sets from the well-aligned phantom and the tilted phantom: (a) comparison of the row-wise projection vectors; and (b) comparison of the center of mass vectors.

References

1. Azevedo, S. G., H. E. Martz, and G. P. Roberson (1990), "Computerized Tomography Reconstruction Technologies," *Energy and Technology Review,* Lawrence Livermore National Laboratory, Livermore, CA, (UCRL-52000-90-11.12).

2. Martz, H. E., G. P. Roberson, and D. J. Schneberk (1990), "Progress in Computerized Tomography Scanners," *Energy and Technology Review,* Lawrence Livermore National Laboratory, Livermore, CA (UCRL-52000-90-11.12).

3. Donaldson, R. R. (1980), "Machine Tool Accuracy - Error Budgets," *Technology of Machine Tools,* Lawrence Livermore National Laboratory, Livermore, CA, (UCRL-52960-5).

4. Barnes, F. L., S. G. Azevedo, H. E. Martz, G. P. Roberson, D. J. Schneberk, and M. F. Skeate (1990), *Geometric Effects in Tomographic Reconstruction,* Lawrence Livermore National Laboratory, Livermore, CA, (UCRL-ID-105130).

5. Schneberk, D. J., S. G. Azevedo, H. E. Martz, and M. F. Skeate (1990), "Sources of Error in Industrial Tomographic Reconstructions," *Materials Evaluation,* Columbus, OH, **48**, p. 609.

6. Azevedo, S. G. (1991), *Model-based Computed Tomography for Nondestructive Evaluation,* Ph.D. thesis, University of California, Davis, CA, (UCRL-LR-106884).

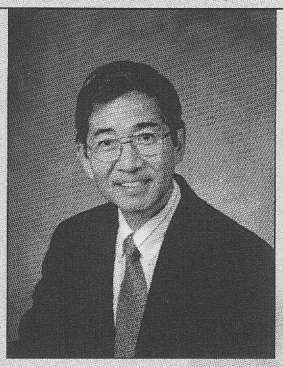

Theodore T. Saito, Thrust Area Leader

The Optical Engineering thrust area at Lawrence Livermore National Laboratory (LLNL) was created in the summer of 1996 with the following main objectives:

1) to foster and stimulate leading edge optical engineering research and efforts key to carrying out LLNL's mission and enabling major new programs;
2) to bring together LLNL's broad spectrum of high level optical engineering expertise to support its programs.

Optical engineering has become a pervasive and key discipline, with applications across an extremely wide range of technologies, spanning the initial conception through the engineering refinements to enhance revolutionary application. It overlaps other technologies and LLNL engineering thrust areas.

The table below is a small sampling of optical engineering's applications. A broader sampling of applications can be appreciated by reviewing the wide range of topics and papers presented by SPIE, the International Optical Engineering Society (http://www.spie.org/home.html).

LLNL's Laser Program is a major customer and supplier of optical engineering with applications that include the development of fast growth methods for KDP, the design and building of the $1.1 B National Ignition Facility (which will be the world's largest optical instrument), advanced microtechnology program, advanced image processing, isotope separation, and the development of diode-pumped solid-state lasers (DPSSLs) which have revolutionary futuristic potential.

The wide range of demanding needs for optical engineering in the Defense Sciences and Non-Proliferation directorates include electro-optics for advanced computing systems, electro-optical applications for advanced weapons systems, and advanced sensors for both above ground nuclear simulation experiments, and for detection of weapons proliferation activities.

Other optical engineering applications at LLNL are in the bioscience, energy, and manufacturing areas.

Optical Engineering Applications

Technology stage	Optical engineering examples
Initial Concept	• Optical design • Materials modeling—optical glass properties; laser media characteristics
Material Development	• Optical glass • Lasing media • Thin films • Deposition parameters • Optical fibers
Fabrication	• Optical polishing and precision machining • Chemical mechanical and ion beam removal and addition
Metrology	• Distance measurement • Shape (figure) and finish (roughness) measurements • Optical and spectroscopic properties • X-ray diagnostics
Special Applications	• Medical • Computational and communications

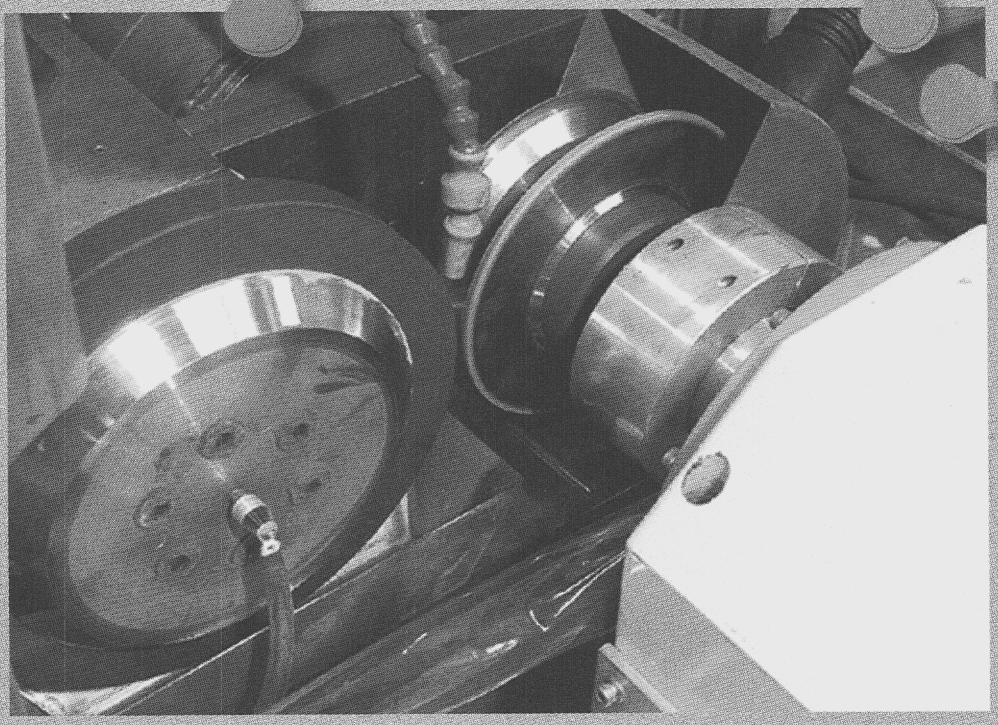

Optical Engineering

8

8. Optical Engineering

Overview
Theodore T. Saito, Thrust Area Leader

Precision Machining of Micro-Features in Structural Ceramics
Mark A. Piscotty, Pete J. Davis, Barry L. Freitas, Jay A. Skidmore, and Theodore T. Saito.....8-1

Precision Machining of Micro-Features in Structural Ceramics

Mark A. Piscotty and Pete J. Davis
Materials and Manufacturing Engineering Division
Mechanical Engineering

Barry L. Freitas
Laser Science Engineering Division
Mechanical Engineering

Jay A. Skidmore
Inertial Confinement Fusion Program
Advanced Lasers and Components

Theodore T. Saito
Advanced Microtechnology Program
Mechanical Engineering

Precision machining has enjoyed an extensive history at Lawrence Livermore National Laboratory (LLNL) with one of its crown jewels being its diamond turning capabilities. In recent years, we have begun a required shift to precision grinding of materials for which diamond turning is not applicable, such as ceramics and other brittle materials. This project focuses on precision grinding of micro-features in structural ceramics such as Al_2O_3 and BeO. The approach uses a combination of experimental and analytical methods to investigate and develop precision grinding of brittle materials. Among the analytical developments are two computer grinding models to predict grinding wheel wear and sub-surface damage depths which result from the grinding operation. An extensive experimental process was developed to provide data in support of the analytical studies and simultaneously produce a method to fabricate BeO heat sink components important to LLNL programs.

Introduction

The objectives of this project are to define and extend our capability to perform precision grinding of brittle materials. Brittle materials are receiving increasing calls for use in high-performance components in a number of LLNL programs. One such material is beryllium oxide (BeO), which has outstanding heat transfer performance characteristics, yet is electrically insulating. BeO is the material of choice for a number of important LLNL and Department of Energy (DOE) programs.

The scope of the project includes modeling development, process analysis, and relevant experiments. The primary tasks for FY-97 included defining the current limits of brittle material precision grinding, establishing a modeling capability, and determining surface and sub-surface quality metrics to extend our precision grinding abilities.

Over the past decades, LLNL has established itself as a leader in precision engineering and lasers. Past engineering research and development have improved important material parameters impacting achievable accuracies and operational characteristics. Process development has included special development of precision fixturing, continuous lap polishing, and precision brittle material removal. Key weapons components and assemblies, as well as optical components (for example, for the Shiva and Nova lasers), have been fabricated.

Precision fabrication has been a key component in the Cooperative Research and Development Agreements (CRADAs) with a number of industrial partners, two of which provide the foundation for this

project. The first was to develop 0.5-µm accuracy for a single-wheel slicing machine for electronic industry ceramic substrates (a factor of 8 in positioning accuracy).[1] The second was to demonstrate cost-effective ceramic removal rates while maintaining precise control of form geometry and the surface conditions that are required in ceramic engine parts.[2]

Progress

Modeling and Analysis

Both the precision and cost of a ground microfeature component are directly affected by the wear characteristics of the grinding wheel. Grinding wheels that appear "soft" in the grinding process wear excessively, resulting in loss of feature geometry control and expensive frequent wheel replacement. On the other hand, grinding wheels that appear too "hard" will maintain form, but due to insufficient breakdown of the bond to expose fresh abrasive, they will not cut freely and will burnish and damage the workpiece.

The need to better understand the wheel wear mechanism has prompted the development of a grinding wheel wear model.[3] This empirically-based model was developed to specifically investigate corner wear of a wheel during a grinding operation. Although this model was originally developed for abrasive wheels with much coarser abrasives than the grinding wheels used for these experiments, we feel this model can be further developed for our application.

Figure 1a shows a close-up schematic of a grinding wheel edge during the grinding of a workpiece. The wear model defines the initial shape of the grinding wheel edge using a specified number of points. The local wear at each point, Δl, may be expressed as

$$\Delta l = f\left(V_{nl}, \rho_l\right) \qquad \text{(Eq. 1)}$$

where V_{nl} is the normal in-feed velocity at each discretized point, and ρ_l is the local curvature at each discrete point.

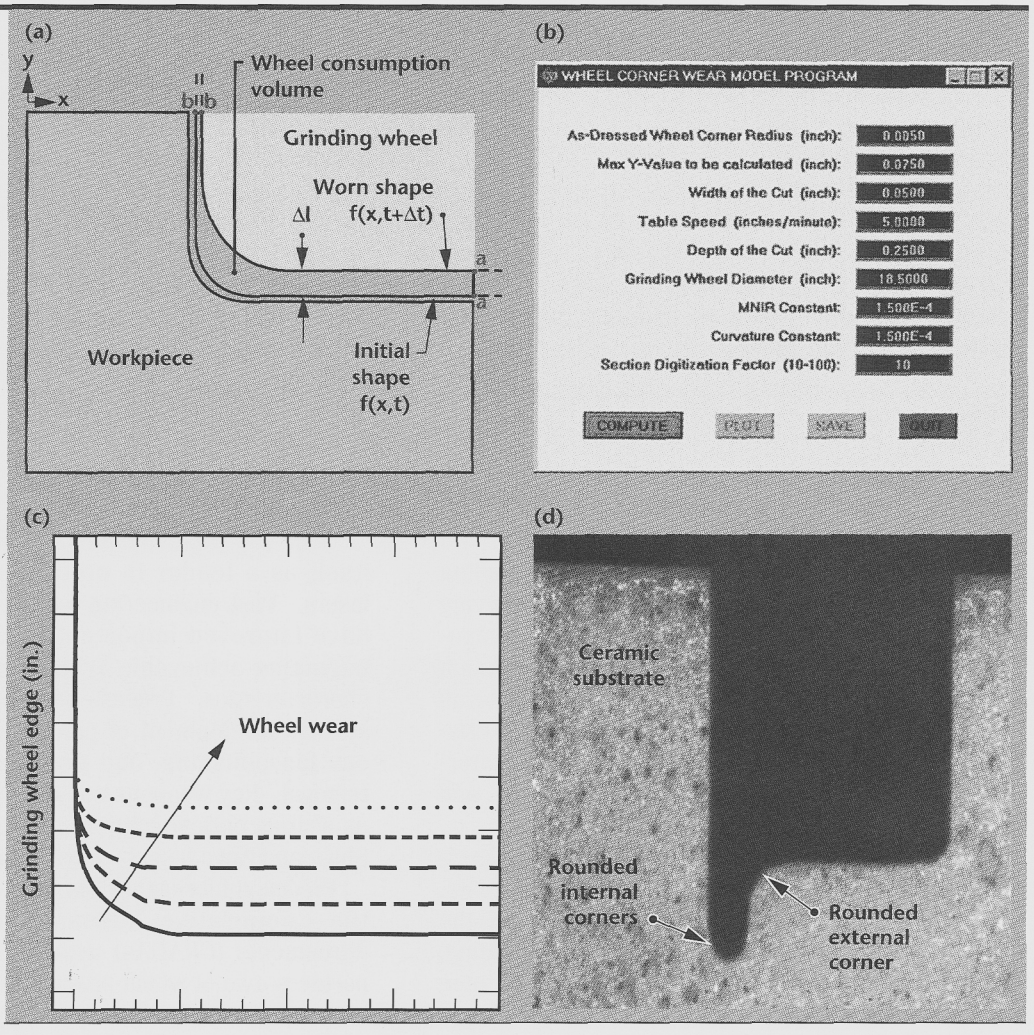

Figure 1. (a) Schematic of grinding wheel edge wear from time t, to time t + Δt; (b) grinding wheel wear model interface screen; (c) calculated wear profiles; and (d) groove image showing rounding of internal and external corners due to wheel wear.

The computer code marches iteratively through time and calculates the next profile, $f(x, t + \Delta t)$ based on V_{nl} and ρ_l. Empirically-based constants are instituted to obtain the local wear at each point along the profile and the local wear is expressed as

$$\Delta l = k_1 V_{nl}\left(1 + k_2 \rho_l\right) \qquad \text{(Eq. 2)}$$

where k_1 is a maximum normal in-feed constant, and k_2 is a curvature constant.

With the grinding wheel corner profile determined as a function of time, the amount of volumetric wheel consumption is calculated by integrating the profiles at t and $t + \Delta t$. This is estimated as

$$\Delta V_{wheel} = \pi D_{nom}\left[\int_a^b f\left(z, t + \Delta t\right)dz - \int_a^b f\left(z, t\right)dz\right] \qquad \text{(Eq. 3)}$$

where ΔV_{wheel} is the volumetric grinding wheel consumption during Δt, and D_{nom} is a nominal grinding wheel diameter for the corner section.

Figure 1b shows the user interface screen of our wear model; **Fig. 1c** shows sample calculated profiles of a grinding wheel corner vs time; and **Fig. 1d** shows a ground groove with non-sharp micro-features due to wheel wear.

Sub-Surface Damage Layer Analysis

Inherent in the vast majority of brittle material grinding processes is a resulting sub-surface damage (SSD) layer made up of a network of intergranular and intragranular cracks. Structural characteristics, such as breaking strength, were found to be a strong function of grinding-induced SSD.[2] Along with structural performance, the heat transfer capability of the ceramic components is often of key interest (particularly with high thermal conductivity materials such as BeO). Dr. B. Zhang (University of Connecticut)[4] has performed extensive experiments to examine the SSD layer (also referred to as the pulverized layer) introduced by a single-point fly cutter, which was used to simulate a single abrasive bound in a grinding wheel. **Figure 2** shows a schematic of a localized SSD layer induced by a single abrasive. The SSD layer consists of bulk material cracks and a pulverized area in which individual grains are crushed, significantly affecting its heat transfer capability.

Our investigation of the SSD includes the use of TEM analysis in which we examine cross-sections of ground specimens to determine the extent of the damaged layer. Using Zhang's grinding model (extrapolated to fine abrasive size grinding wheels), we predicted the SSD layer to be 10 μm thick or less, which, to first order, matches our experimental results. Material properties, wheel type, and grinding conditions all play important roles in creating this SSD layer.

Experimental Design

Precision grinding is a versatile, efficient, and robust process. Based on the methodology developed at LLNL, we use profiled super-abrasive, metal-bond diamond grinding wheels to precision grind ceramic substrates.[2]

Precision grinding, however, is not without its challenges and difficulties. Among these challenges are meeting geometric specifications and maintaining them through the course of a production run. Other issues include workpiece surface quality such as roughness and edge chipping, and the extent of SSD.

The experimental workpiece geometry selected was chosen for two main reasons: 1) it provides several of the most challenging and frequently required geometric features; and 2) it has a direct programmatic application. Among the geometric features to be studied are vertical wall straightness, minimum internal and external radii, surface roughness, and edge chipping.

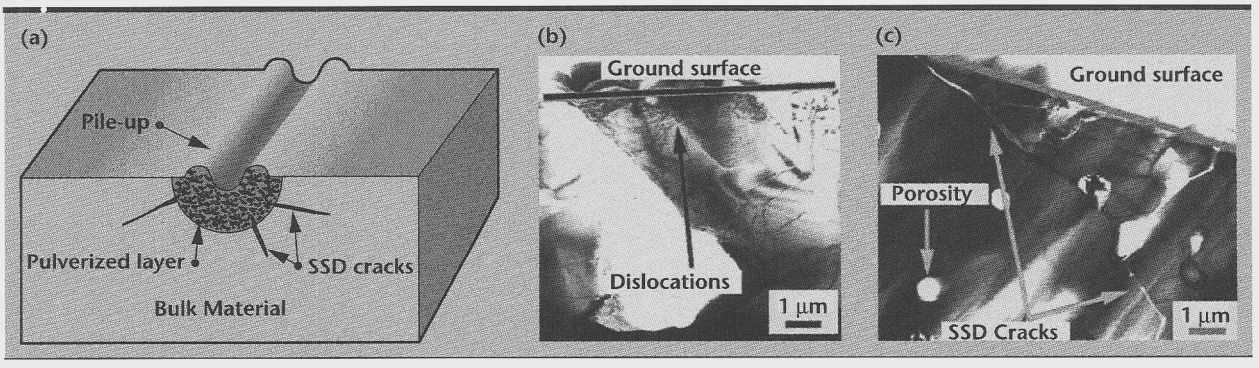

Figure 2. (a) Schematic of sub-surface damage layer as a result of material removal from an individual abrasive; (b) TEM image showing dislocation SSD (0.7 cm/min in-feed rate); and (c) TEM image showing SSD cracks (5.1 cm/min in-feed rate).

Figure 3a shows the experimental workpiece geometry used for this project. The dimensions of each individual groove are shown in the magnified view, and tolerances are nominally ± 1 µm. The pitch spacing between grooves is 1 mm ± 1 µm. Among the most critical features of the groove geometry are the sharpness of the external corner at the top of the 75-µm notch and the straightness of the left vertical wall.

The 75-µm notch (approximate thickness of a sheet of paper) at the bottom of the groove provides an excellent opportunity to investigate limitations of both internal and external corner minimum radii. **Figure 3b** shows a schematic of a double-profiled grinding wheel process and the wheel's progression through the workpiece. The right hand profile removes a majority of the groove, grinds the bottom notch and removes a small amount from the top surface for groove depth control. As the wheel progresses to the next grooves, the left wheel profile removes the remainder of the groove material and generates a sharp corner at the top of the 75-µm notch.

Figure 4a is a schematic showing the layout of the machine tool used for this project. A rotating EDM graphite electrode is profiled using a single-point tool or a grinding wheel. The electrode is used to EDM-true and profile the metal-bonded super-

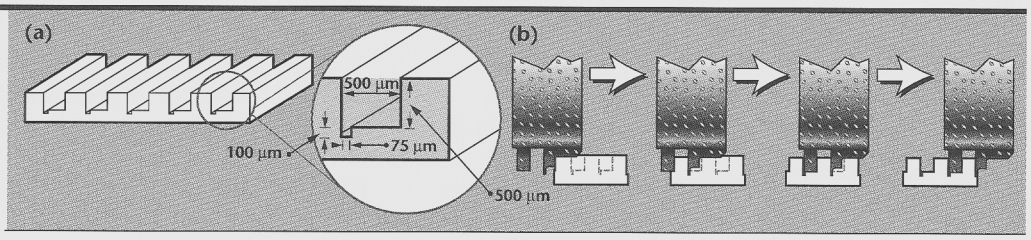

Figure 3.
(a) Experimental workpiece geometry; and (b) progressive grinding wheel procedure using a double-profiled grinding wheel.

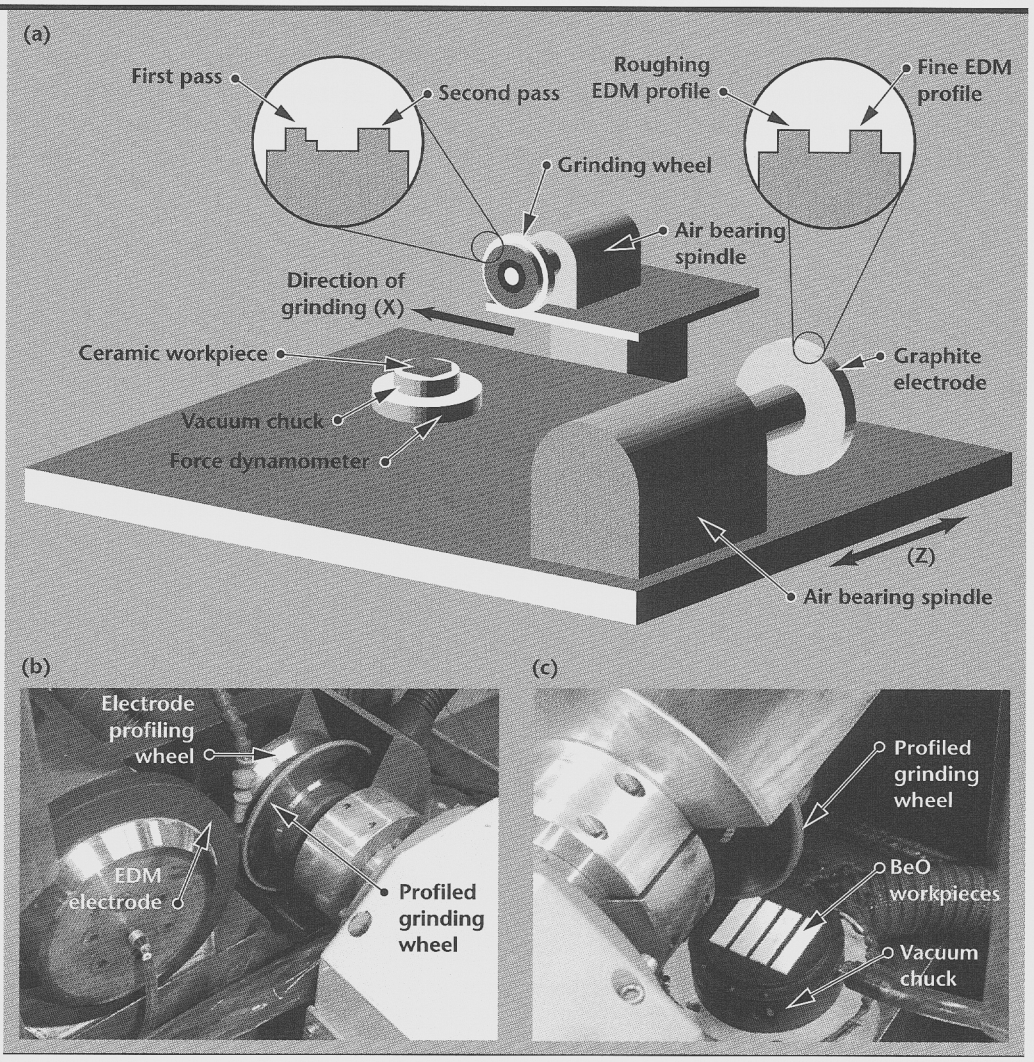

Figure 4.
(a) Grinding machine schematic; (b) EDM profiling and truing a metal-bond grinding wheel; and (c) profiled grinding wheel approaching four BeO workpieces.

abrasive grinding wheel, complete with the two profiles and 75-mm notch feature.

Truing of the grinding wheel is vital to reduce synchronous motion errors, which result in feature degradation and limit the minimum groove width. Once the grinding wheel has been profiled and trued, it is used to creep-feed grind the micro-features in the ceramic workpieces. This method can produce micro-features to small tolerances and, with the appropriate machine design and process, can be a low-cost method for manufacturing micro-features such as grooves.

Figures 4b and **c** are photographs of the grinding work zone of the machine tool used in the project. The machine is a converted T-base diamond turning lathe, with a temperature-controlled oil casing and distance-measuring laser interferometers that provide position resolution of less than 0.1 µm. This machine has been qualified for BeO machining.[5]

Figure 5a shows a completed BeO workpiece (1 cm × 4 cm × 0.2 cm) with 40 precision ground grooves. The table shown in **Fig. 5b** is a list of the typical process parameters and specifications.

Future Work

The future work associated with this project will continue to advance the analytical and experimental aspects of this technology. We will extend our analytical capabilities with continued collaboration with the University of Connecticut to develop applicable grinding models for super-abrasive, precision grinding of ceramics. This will include both grinding wheel wear and SSD modeling and developing experimental methods to corroborate them.

The experimental portion includes reducing the attainable micro-feature size and improving the cost-effectiveness and robustness of the process. Advancing the *in-situ* gaging process to quickly determine the compliance with the required specifications will add flexibility and lead to a more production-oriented process.

This project benefits several core competencies. The precision engineering and manufacturing area will benefit from the extension of achieving 1- to 2-µm feature accuracies in brittle materials. This work is a natural extension of the CRADA work with Cummins Engine Co. and Industrial Tools, Inc. (ITI).

The ITI CRADA demonstrated sub-µm accuracies of less complicated features in a two-phase ceramic, which is easier to cut than BeO. Also the maintenance of the 1- to 2-µm accuracies of period and 2-mrad vertical wall angle for this project is very demanding. We will gain better understanding of the degradation in the slicing process with regard to repeatably maintaining the 1- to 2-µm tolerances. These techniques will have benefit for other microelectronic applications requiring similar demanding tolerances.

(a)

(b)

Parameter	Description
Grinding wheel	SD1000, N100 M, 18 cm Ø
Workpiece	BeO
EDM electrode	Poco Graphite (1 µm grain size)
Wheel speed	105 m/s
Feed rate	7.5 cm/min

Figure 5. (a) BeO slotted component used for the experimental portion of this project; and (b) typical grinding parameters and specifications.

References

1. Deterministic Design of a High-Precision Slicing Machine, Lawrence Livermore National Laboratory, Livermore, CA and Industrial Tools, Inc., Ojai, CA, (CRADA #T-160-91-1-C, March, 1992).

2. Cost-Effective Machining of Ceramic Engine Components, Lawrence Livermore National Laboratory, Livermore, CA and Cummins Engine Co., Columbus, IN, (CRADA #T-178-91-1-C, December, 1992).

3. Mindek, R. B. (1996), *A Study of the Wheel Wear and Thermal Limitations in Creep Feed Grinding with Particular Reference to Coolant Application and the Grinding of Vertical Faces and Slots,* Ph.D. thesis, University of Connecticut, Storrs, CT.

4. Zhang, B., and T. Howes (1995), "Subsurface Evaluation of Ground Ceramics," *Annals of CIRP,* Vol. **44**, (1).

5. Piscotty, M. A. (1997), *Wet Grinding of BeO Ceramic Components,* Lawrence Livermore National Laboratory, Livermore, CA, (OSP 321.83).

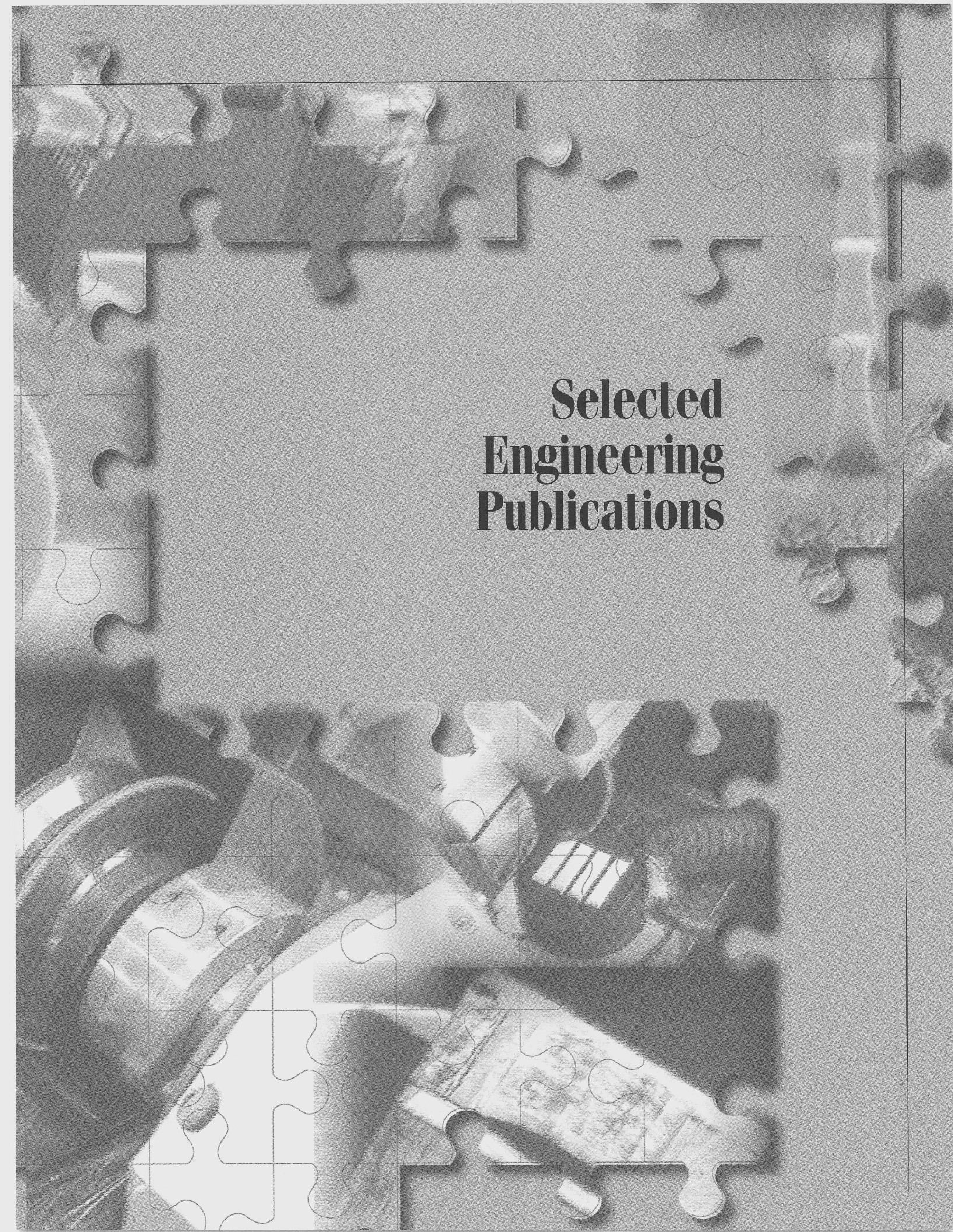

Selected Engineering Publications

Aceves, S., and J. Smith (1996), "A Desiccant Dehumidifier for Electric Vehicle Heating," *Proceedings for 1996 ASME Winter Meeting, Atlanta, GA*, November.

Aceves, S., and J. Smith (1996), "Lean-Burn Hydrogen Spark-Ignited Engines," *Proceedings for ASME Internal Combustion Engine 1996 Fall Conference, Dayton, OH*, October.

Aceves, S., and J. Smith (1997), "Hybrid and Conventional Hydrogen Engine Vehicles that Meet EZEV Emissions, Dec. 10, 96," *SAE International Congress and Exposition, Detroit, MI*, February.

Aceves, S., and J. Smith (1997), "Modeling in Homogeneous Charge Ignition (HCCI) of Methane," *Proceedings for ASME Internal Combustion Engine 1997 Fall Conference, Madison, WI.*

An, J., S. Olivier, K. Avicola, H. Bissinger, J. Brase, D. Gavel, B. Macintosh, C. Max, J. Salmon, and K. Waltjen (1996), "Initial Results from the Lick Observatory Laser Guide Star Adaptive Optics System," *1996 Proceedings for European Southern Observatory Conference, Garching, Germany* (54), p. 75.

Anderson, A., A. Burnham, and M. Tobin (1996), "Modeling and Experiments of X-Ray Ablation of National Ignition Facility First Wall Materials," *ANS 12th Topical Meeting on the Technology of Fusion Energy, Reno, NV*, June.

Anderson, A., and P. Peterson (1997), "Experimental Methods for Measuring X-Ray Ablation Response of Surfaces," *Experimental Heat Transfer*, Vol. **10**, pp. 51–56.

Anderson, A., R. Managan, and M. Tobin (1996), "X-Ray Emission from National Ignition Facility Indirect Drive Targets," *ANS 12th Topical Meeting on the Technology of Fusion Energy, Reno, NV*, June.

Anderson, C., D. Nikkel, P. Goldman, P. Rangaswamy, G. Petrus, L. Ferguson, J. Lathrop, J. Keeney, M. McKenzie, and N. Palle (1996), "Developments of a Carburizing and Quenching Simulation Tool: Numerical Simulations of Rings and Gears," *Second International Conference on Quenching and Control of Distortion, Cleveland, OH*, November.

Azevedo, S., J. Mast, S. Nelson, E. Rosenbury, H. Jones, D. Mullenhoff, T. McEwan, R. Hugenberger, R. Stever, J. Warhus, and M. Wieting (1996), "HERMES: A High-Speed Radar Imaging System for Inspection of Bridge Decks," *SPIE Conference on NDE for Process Control: Nondestructive Evaluation Techniques for Aging Infrastructure and Manufacturing, Scottsdale, AZ*, Vol. **2946**, pp. 195–204.

Baker, J. (1997), "LLNL Acoustic Spectrometer," *SPIE Proceedings, Orlando, FL*, April, Vol. **3081**.

Baker, J., and R. J. Pollins (1997), "Test Beds for Unattended Chemical Sensors," *SPIE Proceedings, Orlando, FL*, April, Vol. **3081**.

Bammann, D., D. Nikkel, V. Prantil, A. Kumar, M. Lusk, J. Lathrop, D. Mosher, G. Krauss, M. Callabresi, H. Jou, W. Elliott, D. Shick, G. Ludtka, W. Dowling, and T. Lowe (1996), "Development of a Carburizing and Quenching Simulation Tool: Material Model for Carburizing Steels Undergoing Phase Transformations," *Second International Conference on Quenching and Control of Distortion, Cleveland, OH*, November.

Bardsley, J., B. Penetrante, B. Merritt, and M. Hsiao (1997), "Kinetic Analysis of Plasmas Used for Pollution Control," *Japanese Journal of Applied Physics*, Vol. **36**, pp. 5007–5017.

Barker, C., J. Auerbach, C. Adams, S. Bumpas, R. Hibbard, C. Lee, D. Roberts, J. Campbell, P. Wegner, B. Van Wonterghem, and J. Caird (1996), "National Ignition Facility Frequency Converter Development," *Proceedings for Second Annual International Conference on Solid-State Lasers for Application to Inertial Confinement Fusion, Paris, France*, October.

Bellow, P., T. Jackson, L. Genova, and D. Shimer (1996), "Progress on PEP-II Magnet Power Conversion System," *European Particle Accelerator Conference (EPCA96), Sitges, Spain*, June.

Belser C., J. Berg, J. Kerns, M. McDaniel, M. Mugge, W. Stoeffl, A. Kulikov, N. Kurita, E. Reuter, and U. Wienands (1996), "High Current RF Shield for PEP-II Vacuum System Expansion Joint," *Proceedings of the Fifth European Particle Accelerator Conference, Barcelona, Spain*, June.

Benapfl, M., K. Kennedy, B. Harteneck, G. Millos, F. King, and R. Kirby (1997), "Titanium Nitride Coating of the PEP-II Low Energy Ring Aluminum Arc Vacuum Chambers," *Proceedings of the 1997 IEEE Particle Accelerator Conference, Vancouver, B.C., Canada*, May.

Berger, D. D. (1996), "Electron Beam Welding of Thick-Cross-Section Copper with Minimal Porosity," *78th Annual American Welding Society Convention, Los Angeles, CA*, April.

Bertolini, L., D. Behne, J. Bowman, D. Hathaway, K. Kishiyama, M. Mugge, and T. Swan (1997), "Design of the Linear Non-Evaporable Getter Pump for the PEP-II B Factory," *Proceedings of the 1997 IEEE Particle Accelerator Conference, Vancouver, B.C., Canada*, May.

Bertolini, L., O. Alford, P. Duffy, R. Holmes, L. Mullins, C. Ng, and M. Sullivan (1997), "Interaction Region Vacuum System Design at the PEP-II B Factory," *Proceedings of the 1997 IEEE Particle Accelerator Conference, Vancouver, B.C., Canada*, May.

Blaedel, K., J. S. Taylor, and J. E. Bibler (1996), "The Effects of Wheel Imbalance and Runout in Fixed-Abrasive Grinding," *ASPE 11th Annual Meeting, Monterey, CA*, November.

Bodemann, A., C. Stolz, N. Kaiser, M. R. Kozlowski, and E. Pierce (1996), "Comparison between 355 nm and 1064 nm Damage of High Grade Dielectric Mirror Coatings," *Laser-Induced Damage to Optical Materials: 1995*, H. E. Bennett, A. H. Guenther, M. R. Kozlowski, B. E. Newnam, and M. J. Soileau, Eds., *SPIE*, Vol. **2714**, pp. 395–404.

Boege, S., R. Zacharias, E. Bliss, C. Chocol, F. Holdener, J. Toeppen, and C. Vann (1996), "NIF Pointing and Centering for Static and Dynamic Alignment Using a 351 μm Laser Source," *Proceedings for Second Annual International Conference for Solid State Lasers for Application to Inertial Confinement Fusion, Paris, France*, October.

Britten, J. A., M. D. Perry, B. W. Shore, R. D. Boyd, G. E. Loomis, and R. Chow (1996), "High Efficiency, Dielectric Multilayer Gratings Optimized for Manufacturability and Laser Damage Threshold, *SPIE*, Vol. **2714**, pp. 511–520.

Candy, J., D. Chinn, G .Thomas, and J. Spicer (1996), "Laser Ultrasonic Signal Processing: A Model-Based Approach," *JASA*, July, Vol. **100** (1), pp. 278–284.

Caird, J., N. Nielson, H. Patton, L. Seppala, C. Thompson, and P. Wegner (1996), "Beamlet Focal Plane Diagnostics," *Proceedings for Second Annual International Conference on Solid-State Lasers for Application to Inertial Confinement Fusion, Paris, France*, October.

Chen, H. L., B. Myers, G. Meyer, and D. Ciarlo (1997), "Materials Processing Using Miniature Low Voltage Electron Beam Guns," *1997 Nuclear Society Annual Meeting, Orlando, FL*, June.

Chinn, D. J., P. F. Durbin, G. H. Thomas, and S. E. Groves (1996), "Tracking Accelerated Aging of Composites with Ultrasonic Attenuation Measurements," *Review of Progress in Quantitative Nondestructive Evaluation*, Plenum Press, NY, Vol. **16**, p. 1893.

Chow, R., and N. Tsujimoto (1996), "Silicon Dioxide and Hafnium Dioxide Evaporation Characteristics from a High-Frequency Sweep E-Beam System," *Applied Optics*, September, Vol. **35** (24), pp. 5095–5101.

Chow, R., G. E. Loomis, C. Bibeau, V. K. Kanz, N. E. Molau, and R. J. Dietch (1996), "Optical Tuning a Dichroic Multilayer for a High Fluence Application," *SPIE*, Vol. **2714**, pp. 560–568.

Clark, G. (1997), "Automatic Event Picking for Velocity Estimation in Seismic Oil Exploration," *Signal Sciences Workshop, Center for Signal and Image Sciences, (CASIS)*, Lawrence Livermore National Laboratory, Livermore, CA, May.

Clark, G., M. Glinsky, K. Devi, J. Robinson, P. Cheng, and G. Ford (1996), "Automatic Event Picking in Pre-Stack Migrated Gathers Using a Probabilistic Neural Network," *Society of Exploration Geophysicists International Exposition and 66th Annual Meeting, Denver, CO*, November.

Couture, S., R. L. Hurd, and K. C. Wilhelmsen (1996), "Robust Telerobotics—An Integrated System for Waste Handling, Characterization and Sorting," *American Nuclear Society Seventh Topical Meeting on Robotics and Remote Systems, Augusta, GA*, April.

Cummings, K., D. Rees, S. Lenci, C. C. Shang, and D. Wilcox (1997), "Experimental Evaluation of 350 MHz RF Accelerator Windows for the Low Energy Demonstration Accelerator Project," *Proceedings of the 1997 IEEE Particle Accelerator Conference, Vancouver, B.C., Canada*, May.

Cutting, J., and D. Spencer (1997), "Aluminum High Efficiency Exploding Foil Initiator Development and Testing," *41st Annual ADPA Fuze Conference, St. Louis, MO*, April.

Davis, D., C. Thompson, C. Knopp, E. Bliss, and P. Pittman (1996), "Multiplexed Systems for NIF Laser Precision Diagnostics and Optics Inspection," *Proceedings for Second Annual International Conference on Solid-State Lasers for Application to Inertial Confinement Fusion, Paris, France*, October.

Dehghani, M., and J. S. Gunasekera (1996), "Residual Stresses in Bi-Metalic Co-Extruded Products," *Proceedings of the ASME Engineering Systems Design and Analysis Conference, Montpelier, France*, July, Vol. **75**, pp. 159–168.

Dehghani, M., and J. S. Gunasekera (1996), "Simulation of Hydraulic Expansion of Thin-Walled Tubes Using the Elasto-Plastic Finite Element Method," *Proceedings of the ASME Engineering Systems Design and Analysis Conference, Montpelier, France*, July, Vol. **75**, pp. 140–158.

Del Grande, N. K. (1996), "Precise Thermal NDE for Quantifying Structural Damage," D. Thompson and D. Chimenti, Eds., Plenum Press, NY, pp. 525–531.

Del Grande, N. K., P. F. Durbin, C. M. Logan, D. E. Perkins, and P. C. Schaich (1996), "Demonstration of Dual-Band Infrared Thermal Imaging at Grass Valley Creek Bridges," *SPIE Conference on NDE for Process Control: Nondestructive Evaluation Techniques for Aging Infrastructure and Manufacturing, Scottsdale, AZ*, December, Vol. **2946**, pp. 166–177.

DeTeresa, S. (1997), "The Kink Band Mechanism for the Compressive Failure of Fiber Composite Materials," *J. Appl. Mechanics*, **64** (1).

Dimolitsas, S. (1997), "Standards Setting Bodies," *The Communications Handbook*, J. D. Gibson, Ed., CRC Press, pp. 155–165.

Dimolitsas, S., F. L. Corcoran, and J. G. Phipps, Jr. (1996), "Impact of Transmission Delay in Audio-Visual Communications," *International Journal of Satellite Communications*, September–October, Vol. **14** (5), pp. 381–387.

Dimolitsas, S., F. L. Corcoran, C. Ravishankar, and B. R. Udaya Bhaskar (1996), "Voice Quality of Digital Wireless Networks Under Fading Channel Conditions," *Proceedings, IEEE Conference on Vehicular Technology (VTC'96), Atlanta, GA*, April–May.

Dolan, K. (1996), "Digital Radiography and Computed Tomography of Cast Light Metals," *Proceedings of American Society for Nondestructive Testing 1996 Fall Conference, Seattle, WA*, October.

Fischer, L. (1996), "International Standard Safe Transport of Radioactive Materials-Leakage Testing on Packages," *ISO* **12807**, September.

Fischer, L. (1997), "International Standard Nuclear Energy-Vocabulary," *ISO* **921**, February.

Franks, M. (1996), "Electron Beam Welding of Thick-Cross-Section Copper with Minimal Porosity," *78th Annual American Welding Society Convention, Los Angeles, CA*, April.

Franks, M. (1997), "Fabrication Processes for the PEP II Cavities," *Proceedings of the 1997 IEEE Particle Accelerator Conference, Vancouver, B.C., Canada*, May.

Franks, M. (1997), "High-Power Testing of the First PEP-II RF Cavity, *Proceedings of the 1997 IEEE Particle Accelerator Conference, Vancouver, B.C., Canada*, May.

Garcia, M. (1997), "Designing Planar Magnetron Cathodes: Analysis and Experiment," *IEEE International Conference on Plasma Science (ICOPS), San Diego, CA*, May.

Glosup, J. (1996), "Cross-Calibration and Data Integration for Neutron NDA Instruments," *Proceedings of the Neutron Users Group Topical Meeting on Combining NDA Techniques, New Orleans, LA.*

Glosup, J. (1996), "Systematic Error Revisited," *Proceedings of the American Statistical Association Section on Physical and Engineering Sciences, Chicago, IL.*

Gogolewski, R. P., D. R. Lesuer, C. K. Syn, R. A. Riddle, and B. J. Cunningham (1996), "On the Importance of Target Material Interfaces During Low Speed Impact," *Proceedings 16th International Symposium on Ballistics, San Francisco, CA.*

Hall, J., F. Dietrich, and C. Logan (1996), "Conceptual Design for a Neutron Imaging System for Thick Target Analysis Operating in the 10-15 MeV Energy Range," *American Society of Nondestructive Testing 1996 Fall Conference, Seattle, WA.*

Hartley, R., R. Zacharias, M. Kartz, A. Hines, W. Behrendt, G. Pollock, E. Bliss, T. Salmon, S. Winters, and B. Van Wonterghem (1996), "Wavefront Correction for Static and Dynamic Aberrations to Within One Second of the System Shot in the NIF Beamlet Demonstration Facility," *Proceedings of the Second Annual International Conference for Solid State Lasers for Application to Inertial Confinement Fusion, Paris, France*, October.

Harvey, A. R., and R. Yamamoto (1996), "Magnet Coil Electrical Gasket of High Compliance and Ampacity," *IEEE Transactions on Magnetics*, IEEE Magnetics Society, July.

Haskins, J. J. (1996), "Nondestructive Evaluation: A Tool for Increased Productivity in Manufacturing," *International Journal of Environmentally Conscious Design and Manufacturing*, Vol. **5**, (3-4).

Hayashi, K., L. N. Mascio, G. Thabit, J. Bogdanske, and M. Markel (1996), "The Effect of Nonablative Laser Energy on the Ultrastructure of Joint Capsular Collagen," *Arthroscopy*, **12**, pp. 474–481.

Henesian, M., P. Renard, J. Auerbach, J. Caird, B. Ehrlich, S. Haney, J. Hunt, J. Lawson, K. Manes, D. Milam, R. Sacks, L. Seppala, I. Smith, R. Speck, C. Thompson, B. Van Wonterghem, P. Wegner, T. Weiland, C. Widmayer, W. Williams, and J. Trenholme (1996), "The Use of Beam Propagation Modeling of Beamlet and Nova to Ensure a Safe National Facility Laser System Design," *Proceedings for Second Annual International Conference on Solid-State Lasers for Application to Inertial Confinement Fusion, Paris, France*, October.

Hernandez, M. (1996), "Design of Ground Water Remediation Control Systems at LLNL," *Spectrum Conference, American Nuclear Society*, September.

Holdener F., E. Abels, E. Bliss, S. Boege, R. Boyd, C. Chocol, D. Davis, R. Demaret, R. English, C. Laumann, J. Miller, and S. Thomas (1996), "Beam Control and Diagnostic Functions in the NIF Transport Spatial Filter, Solid-State Lasers for Applications to Inertial Confinement Fusion," *Proceedings for Second Annual International Conference on Solid-State Lasers for Application to Inertial Confinement Fusion, Paris, France*, October.

Hoover, C. G. (1997), "Temperature Maxima in Stable Two-Dimensional Shock Waves," *Physics Review E*, April.

Hossain, Q. (1996), "National Standards for Natural Hazards," *Proceedings of the Sixth Symposium on Current Issues Related to Nuclear Power Plants, North Carolina State University, Raleigh, NC*, December.

Hossain, Q. (1997), "Seismic and Dynamic Analysis and Design Considerations for High Level Nuclear Repositories," *ASCE*, January.

Hossain, Q., R. Kennedy, R. Murray, K. Mutreja, and B. P. Tripathi (1996), "Structures, Systems and Components Evaluation: Technical Support Document for Accident Analysis for Aircraft Crash in Hazardous Facilities," DOE Standard 3014-96, October.

Houck, T., G. Caporaso, C. C. Shang, and S. Sampayan (1997), "Measured and Theoretical Characterization of the RF Properties of Stacked, High-Gradient Insulator Material," *Proceedings of the 1997 IEEE Particle Accelerator Conference, Vancouver, B.C., Canada*, May.

Hsiao, M., B. Merritt, B. Penetrante, G. Vogtlin, P. Wallman, R. Tonkyn, R. Shah, and T. Orlando (1996), "Plasma Assisted Oxidation of Propene," *Journal of Advanced Oxidation Technologies*, **1**, pp. 79–84.

Hunter, S. (1996), "Tiltmeter Project Extending Fracture Mapping Depth," *Partnership Progress, Natural Gas and Oil Partnership*, DOE, Washington, DC, October, (4), pp. 1–4.

Johnson, G. (1996), "Research of High Heat Flux Heat Transfer in Sub-Millimeter Tubes at Moderate Gin and Pex," *High Heat Flux Engineering III: SPIE Symposium, Denver, CO*, August.

Jorgensen, B. R., and Y. C. Shin (1996), "Dynamics of Machine Tool Spindle/Bearing Systems Under Thermal Growth," *Proceedings for Dynamic Systems and Controls Division, ASME IMECE, Atlanta, GA*, November, pp. 333–340.

Kendall, M., and J. P. Holman (1996), "Spray Cooling Heat Transfer with Subcooled Trichlorotrifluoroethane (Freon-113) for Vertical Constant Heat Flux Surfaces," *International Mechanical Engineering Congress and Exposition, Atlanta, GA*, November.

Knopp, C. (1996), "Multiplexed Systems for NIF Laser Precision Diagnostics and Optics Inspection," *Conference on Solid-State Lasers for Applications to Inertial Confinement Fusion, Paris, France*, October.

Kornblum, B., R. McCallen, and W. Kollmann (1997), "Methods for Analyzing and Comparing Large-Eddy Simulations," *APS Division of Fluid Dynamics Annual Meeting*, Bulletin of the American Physical Society, Vol. **41** (9).

Kornblum, B., R. McCallen, M. Christon, and W. Kollmann (1996), "Large-Eddy Simulation in Complex Domains Using the Finite Element Method," *Proceedings of the ASME Fluids Engineering Summer Meeting, San Diego, CA*, FED-Vol. **238**, pp. 277–284.

Kornblum, B., R. McCallen, M. Christon, and W. Kollmann (1996), "Laminar Backward-Facing Step Flow Using the Finite Element Method," *Proceedings of the ASME Fluids Engineering Summer Meeting, San Diego, CA*, July, FED-Vol. **238**.

Lamont, A. (1996), "Modeling the Impacts of a Market for Emissions Permits" *International Journal of Environmentally Conscious Design and Manufacturing*, Vol. **5**, (3-4).

Lang, D., J. Sinnis, A. Brooks, T. Brown, J. Citrolo, M. Cole, S. Davis, B. Felker, M. Gouge, P. Heitzenroeder, D. Hill, E. Hoffman, C. Kessel, D. Knutson, D. Kungl, D. Lang, D. B. Montgomery, G. H. Neilson, B. Nelson, C. Neumeyer, M. Rennich, J. Schmidt, L. Sevier, D. Slack, J. Spitzer, K. St. Onge, P. Titus, and K. Young (1996), "The Engineering of the 'PCAST' Machine," *ANS Conference, Reno, NV.*

Lawson J., L. Seppala, I. Smith, and C. Thompson (1996), "Beamlet Schlieren Diagnostic and Experiments," *Proceedings for Second Annual International Conference on Solid-State Lasers for Application to Inertial Confinement Fusion, Paris, France*, October.

Lee, C. (1996), "A Higher Order Method of Multiple Scales," *Journal of Sound and Vibration*, Vol. **202** (2).

Lesuer, D. R., C. K. Syn, and O. D. Sherby (1996), "Ultrahigh Carbon Steel for Automotive Applications," *New Steel Products for Automotive Applications, SAE*, (SAE International), SP-1172.

Lesuer, D. R., and C. K. Syn (1996), "Damage Initiation and Propagation in Metal Laminates," *Recent Advances in Solids/Structures and Application of Metallic Materials*, (1996 ASME Winter Annual Meeting), PVP Vol. **342**, MD Vol. **72**, pp. 167–184.

Lesuer, D. R., C. K. Syn, and T. G. Nieh (1996), "Elevated Temperature Tensile and Fatigue Behavior of a 6090-T6/SiC/25p Metal Matrix," *Aluminum and Magnesium for Automotive Applications*, TMS, Warrendale, PA, p. 149.

Lesuer, D. R., C. K. Syn, J. Wadsworth, R. A. Riddle, J. J. Lewandowski, and W. H. Hunt (1996), "Toughening Mechanisms in Al/Al-SiC Laminated Metal Composites," *Layered Materials for Structural Applications Materials Research Society Symposium Proceedings*, (Materials Research Society, Pittsburgh, PA), Vol. **434**, p. 205.

Lesuer, D. R., C. K. Syn, O. D. Sherby, J. Wadsworth, J. J. Lewandowski, and W. H. Hunt (1996), "Mechanical Behavior of Laminated Metal Composites," *International Materials Reviews,*, **41** (5), p. 169.

Lesuer, D. R., C. K. Syn, O. S. Sherby, and D. K. Kim (1996), "Processing and Mechanical Behavior of Hypereutectoid Steel Wires," *Metallurgy, Processing and Applications of Metal Wire: State of the Art Technology and Challenges for the Future*, TMS, Warrendale, PA, p. 109.

Lesuer, D. R., C. K. Syn, R. P. Gogolewski, B. Cunningham, and R. Riddle (1996), "Fracture Toughness and Impact Properties of Laminated Metal Composites," *Proceedings of the Third International Conference on Composites Engineering, New Orleans, LA*, p. 509.

Lesuer, D. R., C. K. Syn, T. G. Nieh, and E. M. Taleff (1997), "Superplastic Deformation in Two Microduplex Stainless Steel," *Superplasticity in Advanced Materials (ICSAM97),* Trans Tech Publications, Zurich, Switzerland, p. 469.

Lesuer, D. R., J. S. Huang, A. J. Schwartz, and T. G. Nieh (1996), "High Temperature Deformation in 2036 Al and 0.2 wt% Zr-2036Al," *Aluminum and Magnesium for Automotive Applications,* TMS, Warrendale, PA.

Lesuer, D. R., T. G. Nieh, and J. Wadsworth (1996), "Forming of Superplastic Ceramics," *Ceramics International,* **22** (5), p. 381.

Loomis, G. (1997), "Design of High-Efficiency Dielectric Reflection Gratings," *JOSA,* Vol. **14** (5), May.

Maltby, J. (1996), "Coupled Monte Carlo/Finite Element Solution of Radiation-Conduction Problems in a Shaded Geometry," *American Institute of Chemical Engineers 1996 National Heat Transfer Conference, Houston, TX,* August.

Mascio, L. N., S. D. Frankel, J. M. Hernandez, and C. Logan (1996), "Building the LLNL/UCSF Digital Mammogram Library with Image Groundtruth," *3rd International Workshop on Digital Mammography, Chicago, IL,* June, K. Doi, M. L. Giger, R. M. Nishikawa, and R. A. Schmidt, Eds., Elsevier Science, New York, NY, International Congress Series **1119**, pp. 427–430.

McCallen, R., J. M. Leone, and W. Kollman (1996), "LES/FEM Method for the Study of Incompressible Flows," *Journal of Computational Physics,* August.

McCallen, R., B. Kornblum, and W. Kollmann, (1996), "Large-Eddy Simulation in Complicated Domains Using the Finite Element Method," *APS Division of Fluid Dynamics Annual Meeting,* Bulletin of the American Physical Society, Vol. **41** (9).

McCue, H. (1996), "Open Architecture Controller Activities in Technology Enabling Agile Manufacturing," *SPIE Proceedings,* November, **#2912**, pp. 46–51.

Merritt, B., B. Penetrante, J. Bardsley, M. Hsiao, A. Kuthi, G. Vogtlin, P. Wallman, J. Bayless, and C. Burkhart (1996), "Electron-Impact and Pulsed Corona Processing of Volatile Organic Compounds in Gas Streams," *Pure and Applied Chemistry,* **68**, pp. 1083–1087.

Meyer, G. (1996), "Performance Measurements of Sealed-Tube Electron Beam Windows," *RadTech Japan Conference Proceedings, Tokyo, Japan,* September, and *RadTech International Proceedings, Tokyo, Japan,* September.

Miller, M. (1996), "Preliminary Results of the LLNL Airborne Experimental Test-Bed SAR System," *Proceedings IEEE 1996 National Radar Conference, Ann Arbor, MI,* May, pp. 60–64.

Minuzzo, K. (1996), "Cooperative, High-Performance Storage in the Accelerated Strategic Computing Initiative (ASCI)," *Fifth NASA Goddard Mass Storage Systems and Technologies Conference Proceedings,* September.

Minuzzo, K. (1997), "Task Force on Network Storage Architecture: Storage for ASCI," *Hawaii International Conference on System Sciences (HICSS) Conference Proceedings,* January.

Murray, R. (1995), "Department of Energy Natural Phenonena Hazards Safety Program," *Fifth DOE Natural Phenomena Hazards Mitigation Conference Proceedings,* November.

Murray, R. (1996), *Independent Review of the Seismic Analyses for the F-Canyon at the Savannah River Site,* August.

Murray, R. (1996), *Independent Review of the Seismic Analyses for the H-Canyon at the Savannah River Site,* September.

Murray, R. (1996), *Seismic Safety Manual,* Lawrence Livermore National Laboratory, Livermore, CA.

Murray, R. (1997), "ASCE Standard 4 Seismic Analyses of Safety-Related Nuclear Structures and Commentary," ASCE, New York, NY, pp. 4-98.

Murray, R. (1997), *Seismic Evaluation Procedure for Equipment in US Department of Energy Facilities.*

Nelson, T. A. (1997), "Recent Trends in Establishing Seismic Design Rules and Standards to Meet Facility Performance Goals, Building to Last," *Proceedings of Structures Congress XV, American Society of Civil Engineers, Portland, OR,* April.

Neto, S., F. L. Corcoran, J. Phipps, Jr., and S. Dimolitsas (1996), "Performance Assessment of 4.8 kbit/s AMBE Coding Under Aeronautical Environmental Conditions," *IEEE International Conference on Acoustics, Speech and Signal Processing (ICASSP'96), Atlanta, GA,* May.

Ng, L. (1997), "Characterization of Ring Laser Gyro Performance Using the Allan Variance Method," *J. Guidance and Control,* January, Vol. **20** (1).

Ng, L., and M. Summers (1996), "Guidance and Control Experiments at the Nevada Test Site," *AIAA/BMDO Technology Readiness Conference, Fort Walton Beach, FL,* September.

Nieh, T. G., D. R. Lesuer, W. Nellis, P. Luo, and D. Benson (1996), "Dynamic Compaction of Aluminum Nanocrystals," *Acta Metallurgica and Materialia,* **44** (9), p. 3781.

Osman, M. T., D. R. Lesuer, and J. J. Lewandowski (1997), "The Fracture Resistance of Layered DRA Laminates: Influence of Laminae Thickness," *Materials Science and Engineering A,* **A229**, p. 1–9.

Penetrante, B., M. Hsiao, B. Merritt, and G. Vogtlin (1997), "Fundamental Limits on NOx Reduction by Plasma," *1997 SAE International Spring Fuels and Lubricants Meeting and Exposition, Dearborn, MI,* May.

Penetrante, B., M. Hsiao, J. Bardsley, B. Merritt, G. Vogtlin, A. Kuthi, C. Burkhart, and J. Bayless (1997), "Decomposition Mechanisms in Non-Thermal Processing of Air Pollutants," *AWMA Specialty Conference on Emerging Solutions to VOC and Air Toxics Control, San Diego, CA,* February.

Penetrante, B., M. Hsiao, J. Bardsley, B. Merritt, G. Vogtlin, A. Kuthi, C. Burkhart, and J. Bayless (1997), "Primary Decomposition Mechanisms in Electron Beam and Electrical Discharge Processing of Volatile Organic Compounds," *Environmental Applications of Ionizng Radiation* (John Wiley and Sons, NY).

Penetrante, B., M. Hsiao, J. Bardsley, A. Kuthi, B. Merritt, G. Vogtlin, C. Burkhart, and J. Bayless (1996), "Basic Energy Efficiency of Plasma Production in Electrical Discharge and Electron Beam Reactors," *NEDO Symposium in Non-Thermal Discharge Plasma Technology for Air Contaminant Control 1996, Tokyo, Japan,* November.

Penetrante, B., M. Hsiao, J. Bardsley, B. Merritt, G. Vogtlin, A. Kuthi C. Burkhart, and J. Bayless (1997), "Decomposition of Methylene Chloride in Non-Thermal Plasmas," *24th IEEE International Conference on Plasma Science, San Diego, CA,* May.

Penetrante, B., M. Hsiao, J. Bardsley, B. Merritt, A. Kuthi, G. Vogtlin, C. Burkhart, and J. Bayless (1996), "Atomic and Molecular Physics of Plasma-Based Environmental Technologies for Abatement of Volatile Organic Compounds," *European Sectional Conference on Atomic and Molecular Physics of Ionized Gases, Poprad, High Tatras, Slovakia,* August.

Penetrante, B., M. Hsiao, J. Bardsley, B. Merritt, G. Vogtlin, A. Kuthi, C. Burkhart, and J. Bayless (1996), "Comparative Assessment of Non-Thermal Plasma Techniques for Control of Dilute, Large-Volume Pollutant Emissions," *International Workshop on Plasma Technologies for Pollution Control and Waste Treatment, Beijing, China,* May.

Penetrante, B., B. Merritt, M. Hsiao, G. Vogtlin, S. Broer, P. Wallman, M. Neiger, O. Wolf, and T. Hammer (1996), "Pulsed Corona and Dielectric-Barrier Discharge Processing of NO in N_2," *Applied Physics Letters,* **68**, pp. 3719–3721.

Penetrante, B., M. Hsiao, J. Bardsley, B. Merritt, A. Kuthi, G. Vogtlin, P. Wallman, J. Bayless, and C. Burkhart (1996), "Comparison of Non-Thermal Plasma Techniques for Abatement of Volatile Organic Compounds and Oxides," *AWMA Specialty Conference on Emerging Solutions to VOC and Air Toxics Control, Clearwater Beach, FL,* February–March.

Penetrante, B., B. Merritt, M. Hsiao, J. Bardsley, A. Kuthi, G. Vogtlin, P. Wallman, J. Bayless, and C. Burkhart (1996), "Power Consumption and Byproducts in Electron Beam and Electrical Discharge Processing of Volatile Organic Compounds," *Second International Symposium on Environmental Applications of Advanced Oxidation Technologies, San Francisco, CA,* February–March.

Penetrante B., B. Merritt, M. Hsiao, J. Bardsley, G. Vogtlin, and P. Wallman (1996), "Electron-Impact Ionization of Air Molecules and Its Application to the Abatement of Volatile Organic Compounds," *Proceedings of NATO Advanced Study Institute on Molecular Physics and Hypersonic Flows, Maratea, Italy,* May 21–June 3.

Perez, M. (1997), "A Cost-Effective Multi-Terrain Autonomous Vehicle for Hostile Environments," *Proceedings ANS 7th Topical Meeting on Remote Systems and Sensors, Augusta, GA,* American Nuclear Society, La Grange Park, IL, April– May, p. 1110.

Perfect, S. (1997), "Changes in Tribial Component Polyethylene Stresses with Joint Position: Effect of Posterior Stabilization," *Transactions of the 43rd Annual Meeting of the Orthopaedic Research Society, San Francisco, CA,* February, Vol. **22**.

Piscotty, M. (1996), "Implementation of an Acoustic Emission Proximity Detector for Use in Generating Glass Optics," *ASPE 1996 Annual Meeting, Annapolis, MD.*

Piscotty, M., J. S. Taylor, and K. L. Blaedel (1996), "Applied Grinding Wheel Performance Evaluation for Optical Fabrication," *Optical Fabrication and Testing Meeting, Optical Society of America, Boston, MA,* May.

Poole, B., W. Ng, C. C., Shang, D. Steich, and G. Caporaso (1996), "Modeling of 3-D Wakefields in Accelerator Structures," *Computational Accelerator Physics Conference, Williamsburg, VA,* September.

Puso, M. A. (1997), "Finite Element Implementation of Anisotropic Quasilinear Viscoelasticity Using a Discrete Spectrum Approximation," *Journal of Bio Engineering,* ASME, January.

Rainer, F., A. Anderson, A. Burnham, D. Milam, and R. Turner (1996), "Lifetime Survivability of Contaminated Target-Chamber Optics," *Laser-Induced Damage in Optical Materials,* SPIE, October, Vol. **2966**, pp. 463–473.

Ravishankar, C., and S. Dimolitsas (1996), "Voice Coding Technology for Digital Aeronautical Communications," *Air Traffic Control Quarterly,* Vol. **4** (3), pp. 196–221.

Roche, T., M. Eli, K. Merz, and S. Sommer (1996), *The January 17, 1994 Northridge Earthquake: Effects on Electric Power and Selected Industrial Facilities,* Electric Power Research Institute, Palo Alto, CA, August, (TR106635).

Rossi, M., G. Baldazzi, E. Querzola, G. Guidi, M. Scannavini, P. Chirco, F. Zanarini, F. Casali and S. Azevedo, (1996), "High Energy Tomography Using Cadmium Zinc Telluride Detectors," *Nuclear Instruments and Methods in Physics Research*, pp. 419–422.

Schaich, P., G. Clark, K. Ziock, and S. Sengupta (1996), "Automatic Image Analysis for Detecting and Quantifying Gamma-Ray Sources in Coded Aperture Images," *IEEE Transactions on Nuclear Science*, August, Vol. **43** (4).

Schauer, D., and S. Perfect (1996), "Lower Extremity Finite Element Model for Crash Simulation," *ASME Advances in Bioengineering, Atlanta, GA*, November, Vol. **33**.

Seidl, P., H. Kirbie, and J. Barnard (1996), "Heavy-Ion Fusion Driver Research at Berkeley and Livermore," *Proceedings of the Sixteenth IAEA Fusion Energy Conference, Montreal, Canada*, October.

Shang, C. C., Y. Chen, G. Caporaso, and T. H. Houck (1997), "BBU Design of Linear Induction Accelerator Cells for Advanced Radiography," *Proceedings of the 1997 IEEE Particle Accelerator Conference, Vancouver, B.C., Canada*, May.

Shang, J. S., and C. C. Shang (1996), "Simulation of Electromagnetic Phenomena on the Intel Paragon XP/S," *Third International Conference on Approximations and Numerical Methods for the Solution of Maxwell Equations, Oxford University, United Kingdom*, June.

Shen, S., K. Kishiyama, J. Parker, N. Wilson, and D. Schrage (1997), "APT/LEDA RFQ Vacuum Pumping System," *Proceedings of the 1997 IEEE Particle Accelerator Conference, Vancouver, B.C., Canada*, May.

Sherby, O. D., D. R. Lesuer, C. K. Syn, and (1996), "Superplastic Behavior of Ultrahigh Carbon Steel Containing Aluminum," *Progress in Advanced Materials and Mechanics*, W. Tzuchiang and T. Chou, Eds., Journal of Mechanics, Chinese Press, Beijing, China, p. 77.

Smith, B., S. Shen, J. Hale, A. Zhukovsky, P. Michael, J. Minervini, M. Olmstead, J. Rosati, R. Camille, C. Gung, F. Silva, and S. Fairfax (1996), "PIF, A New Facility for Pulse Field Testing of Large Scale Superconducting Cables and Joints," *Proceedings of the 1996 IEEE Applied Superconductivity Conference, Pittsburgh, PA*, August.

Sommer, S., and M. Eli (1997), *Standard Review Plan for Dry Cask Storage Systems*, US Nuclear Regulatory Commission, Washington, DC, January, (NUREG-1536).

Stolz, C., F. Y. Genin, M. R. Kozlowski, D. Long, R. Lalezari, Z. L. Wu, and P. Kuo (1996), "Influence of Microstructure on Laser Damage Threshold of IBS Coatings," *Laser-Induced Damage to Optical Materials: 1995*, H. E. Bennett, A. H. Guenther, M. R. Kozlowski, B. E. Newnam, and M. J. Soileau, Eds., SPIE, Vol. **2714**, pp. 351–358.

Stolz, C., R. J. Tench, M. R. Kozlowski, and A. Fornier (1996), "A Comparison of Nodular Defect Seed Geometries from Different Deposition Techniques," *Laser-Induced Damage to Optical Materials: 1995*, H. E. Bennett, A. H. Guenther, M. R. Kozlowski, B. E. Newnam, and M. J. Soileau, Eds. SPIE, Vol. **2714**, pp. 374–382.

Sullivan, M., and M. Kendall (1996), "Interaction Region Design at the PEP-II B Factory," *Proceedings of the Fifth European Particle Accelerator Conference, Sitges, Barcelona, Spain*, June.

Sullivan, M., L. Bertolini, M. Kendall, J. Swan, B. Yamamoto, G. Bowden, S. DeStaebler, S. Ecklund, J. Hodgson, M. Zisman, T. Mattison, M. Nordby, A. Ringwall, J. Seeman, U. Wienands, D. Walz, D. Humphries, and F. Younger (1996), "Interaction Region Design at the PEP-II B Factory," *Proceedings of the Fifth European Particle Accelerator Conference, Sitges, Barcelona, Spain*, June.

Sunwoo, A. (1997), "Effect of Physical Vapor Deposition on Micro-Structure and Properties of Uranium-6% Niobium Alloy," *Journal of Nuclear Materials*, April.

Sunwoo, A. (1997), "Weldability of Cast and Heat Treated Uranium-25% Vanadium Alloy," *Scripta Materials*, May.

Swan, J. M., A. R. Harvey, R. H. Holmes, C. M. Kendall, R. Yamamoto, T. T. Yokota, J. T. Tanabe, and R. D. Schlueter (1996), "The PEP-II B-Factory Septum Quadrupole Magnets," *IEEE Transactions on Magnetics*, IEEE Magnetics Society, July.

Syn, C. K., D. R. Lesuer, and O. D. Sherby (1997), "Tensile Properties of a Thermo Mechanically Processed Ductile Iron," *Metallurgical and Materials Transactions A*, **28A**, p. 1213.

Syn, C. K., D. R. Lesuer, and O. D. Sherby (1996), "Enhancing Tensile Ductility of a Particle Reinforced Aluminum MMC by Lamination with Mg-9% Li," *Materials Science and Engineering*, **A206**, p. 201.

Taleff, E. M., D. R. Lesuer, and J. Wadsworth (1996), "Enhanced Ductility in Non-Superplastic Al-Mg Alloys," *Metallurgical and Materials Transactions*, **27A**, p. 343.

Taleff, E. M., D. R. Lesuer, G. Henshall, T. G. Nieh, and J. Wadsworth (1996), "Enhanced Ductility in Al-Mg Alloys by Solid-Solution Interactions," *Aluminum and Magnesium for Automotive Applications*, TMS, Warrendale, PA.

Taleff, E. M., D. R. Lesuer, C. K. Syn, and G. A. Henshall (1997), "Creep Fracture During Solute-Drag and Superplastic Deformation," *Recent Advances in Fracture,* TMS, Warrendale, PA, p. 295.

Tarver, C. M., S. K. Chidester, and A. L. Nichols (1996), "Critical Conditions for Impact and Shock-Induced Hot Spots in Solid Explosives," *J. Phys. Chem.,* November, Vol. **100**.

Taylor, J. S., M. A. Piscotty, and K. L. Blaedel (1996), "Progress Toward a Performance-Based Specification for Diamond Grinding Wheels," *SuperTech '96 Workshop, Livermore, CA,* November.

Taylor, J. S., M. A. Piscotty, K. L. Blaedel, and F. A. Gray (1996), "Working with the Superabrasives Industry to Optimize Tooling for Grinding Brittle Materials," *ASPE 1996 Spring Topical Meeting, Annapolis, MD,* June.

Toth, D., and W. O'Connell (1996), "Route Assessment Using Comparative Risk Factors Integrated Through a GIS," *1996 International High-Level Radioactive Waste Management Conference, Las Vegas, NV,* April–May.

Van Wonterghem, B., P. J. Wegner, J. Lawson, M. Henesian, J. Auerbach, C. Barker, D. Speck, C. Thompson, and J. Caird (1996), "Recent Performance Results from the National Ignition Facility Beamlet Demonstration Project," *ANS 12th Topical Meeting on the Technology of Fusion Energy, Reno, NV,* June.

Walton, C. C., F.-Y. Genin, R. Chow, M. R. Kozlowski, G. E. Loomis, and E. Pierce (1996), "Effect of Silica Overlayers on Lasers Damage of HfO_2-SiO_2, 56-Degree Incidence High Reflectors," *SPIE,* Vol. **2714**, pp. 550–559.

Wegner P., C. Barker, S. Dixit, M. Henesian, L. Seppala, C. Thompson, and B. Van Wonterghem (1996), "Third-Harmonic Performance of the Beamlet Prototype Laser," *Proceedings for Second Annual International Conference on Solid-State Lasers for Application to Inertial Confinement Fusion, Paris, France,* October.

Wegner, P. J., B. Van Wonterghem, S. Dixit, M. Henesian, C. Barker, C. Thompson, L. Seppala, and J. Caird (1996), "Characterization of Third-Harmonic Target Place Irradiance on National Ignition Facility Beamlet Demonstration Project," *ANS 12th Topical Meeting on the Technology of Fusion Energy, Reno, NV,* June.

Weir, J., H. Kirbie, J. Clark, G. Caporaso, H. Chen, S. Lund, G. Westenskow, and A. Paul (1997), "ETA-II Experiments for Determining Advanced Radiographic Capabilities of Induction Linacs," *Proceedings of the 1997 Particle Accelerator Conference, Vancouver, B.C. Canada,* May.

Weiss, J., D. Schauer, and J. Gardiner (1996), "Modeling Contact in Biological Joints Using Penalty and Augmented Lagrangian Methods," *ASME International Mechanical Engineering Congress and Exposition, Atlanta, GA,* November.

Wilhelmsen, K. C., R. L. Hurd, and S. Couture (1997), "Telerobotic/Autonomous Control Using Control Shell," *American Nuclear Society Seventh Topical Meeting on Robotics and Remote Systems, Augusta, GA,* April.

Woods, B., M. Runkel, M. Yan, M. Staggs, N. Zaitseva, M. Kozlowski, and J. DeYoreo (1996), "Investigations of Laser Damage in KDP Using Light Scattering Techniques," *SPIE,* Vol. **2966**.

Wu, Z. L., C. Stolz, M. Thomsen, P. K. Kuo, Y. S. Lu, and M. R. Kozlowski (1996), "Overview of Photothermal Characterization of Optical Thin Film Coatings," *Laser-Damage to Optical Materials: 1995,* H. E. Bennett, A. H. Guenther, M. Kozlowski, B. E. Newnam, and M. J. Soileau, Eds., SPIE, Vol. **2714**, pp. 395–404.

Wu, Z. L., M. Thomsen, P. K. Kuo, Y. S. Lu, C. Stolz, and M. R. Kozlowski (1997), "Photothermal Characterization of Optical Thin Film Coatings," *Opt. Eng.,* **36**.

Yamamoto, R., J. M. Bowers, A. R. Harvey, R. H. Holmes, G. F. James, M. A. Libkind, R. W. Martin, L. E. Mullins, J. H. Thomas, W. J. Wong, S. H. Aronson, S. A. Kahn, P. J. Kroon, T. K. Shea, R. D. Schlueter, and W. E. Sondheim (1996), "The PHENIX Detector Magnet Subsystem," *IEEE Transactions on Magnetics,* IEEE Magnetics Society, July.

Yan, M., R. Torres, M. Runkel, B. Woods, I. Hutcheon, N. Zaitseva, and J. DeYoreo (1996), "Investigations of Impurities and Laser Induced Damage in Growth Sectors of Rapidly Grown KDP," *SPIE,* Vol. **2966**.

Ze, F., S. Langer, R. Kauffman, J. Kilkenny, O. Landen, D. Ress, M. Rosen, L. Suter, R. Wallace, and J. Wiedwald (1997), "Comparative Study of X-Ray Emission from Laser Spots in Laser-Heated Hohlraums Relative to Spots on Simple Disk Targets," *Phys. Plasmas,* **4** (3), March.

Zywicz, E. (1996), "On the Equivalence of Stress- and Strain-Based Failure Criteria in Elastic Media," *European Journal of Mechanics of Solids,* October.

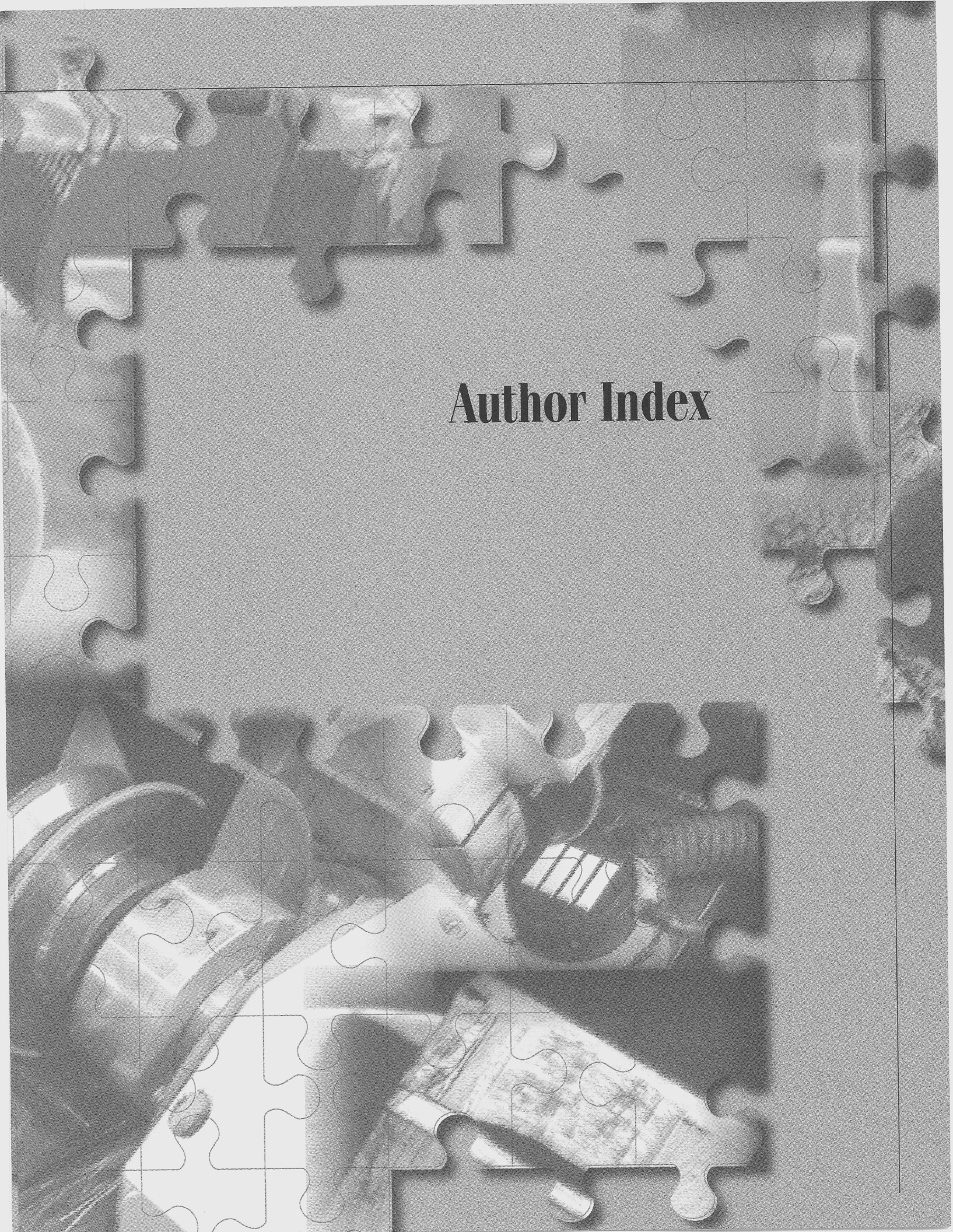

Author Index

Aufderheide, M. B. *7-1*

Badders, D. C. *2-17*
Bernhardt, A. F. *3-11*
Boser, B. E. *3-11*
Brown, A. A. *5-1*
Brusasco, R. M. *7-11*
Burke, G. J. *1-5*

Candy, J. V. *7-7*
Casey, J. *5-1*
Chinn, D. J. *7-7, 7-11*
Ciarlo, D. R. *3-3, 3-5*
Cooper, G. A. *3-25*

Davis, P. J. *8-1*
De Groot, A. J. *2-17*
DenBaars, S. *3-25*
Deri, R. J. *1-11*
DiJaili, S. P. *3-17*

Eckels, J. D. *5-13*

Faux, D. R. *2-11*
Freitas, B. L. *8-1*

Goodman, D. M. *7-1*
Graff, R. T. *3-21, 7-15*

Hagans, K. G. *3-31*
Haigh, R. E. *6-1*
Haskins, J. J. *7-19*
Hayes, J. P. *3-21, 7-15*
Hernandez, M. A. *1-1*
Hollerbach, K. *2-5*
Hoover, C. G. *2-17*
Huber, R. D. *7-7*

Jackson, J. A. *7-1*
Jacobson, G. F. *6-1*
Jankowski, A. F. *3-21, 7-15*
Jensen, S. A. *4-13*
Johansson, E. M. *7-1*
Jorgensen, B. R. *5-7*

Kallman, J. S. *1-5, 1-11*
Koo, J. C. *3-1, 3-21*
Krulewich, D. A. *4-1*

LeBlanc, M. M. *5-7*
Lee, A. P. *3-7*
Lehew, S. L. *3-25*
Lesuer, D. R. *5-7*
Lin, J. I. *2-25*
Logan, C. M. *7-19*

Malba, V. *3-11*
Martz, H. E. *2-5, 7-19*
McConaghy, C. F. *3-7, 3-31*
Meyer, G. A. *3-25*
Morse, J. D. *3-21, 7-15*
Nikkel, Jr., D. J. *5-1*

Ou, J.-J. *3-11*

Perfect, S. A. *2-5*
Perkins, D. E. *7-11, 7-19*
Piscotty, M. A. *8-1*
Pocha, M. D. *1-11*
Puso, M. A. *2-1*

Raley, N. F. *3-1*
Ratowsky, R. P. *1-11*
Riddle, R. A. *5-7*
Rikard, D. R. *7-19*
Roberson, G. P. *7-19*

Saito, T. T. *8-1*
Schneberk, D. J. *7-19*
Shapiro, A. B. *5-13*
Sherwood, R. J. *2-17*
Skidmore, J. A. *8-1*
Spicer, J. *7-7*
Steich, D. J. *1-5*

Thomas, G. H. *7-7*

Walker, J. D. *3-17*
Wojtczuk, S. *6-1*

Young, D. J. *3-11*
Yu, C. N. *3-1*

Zywicz, E. *2-1*
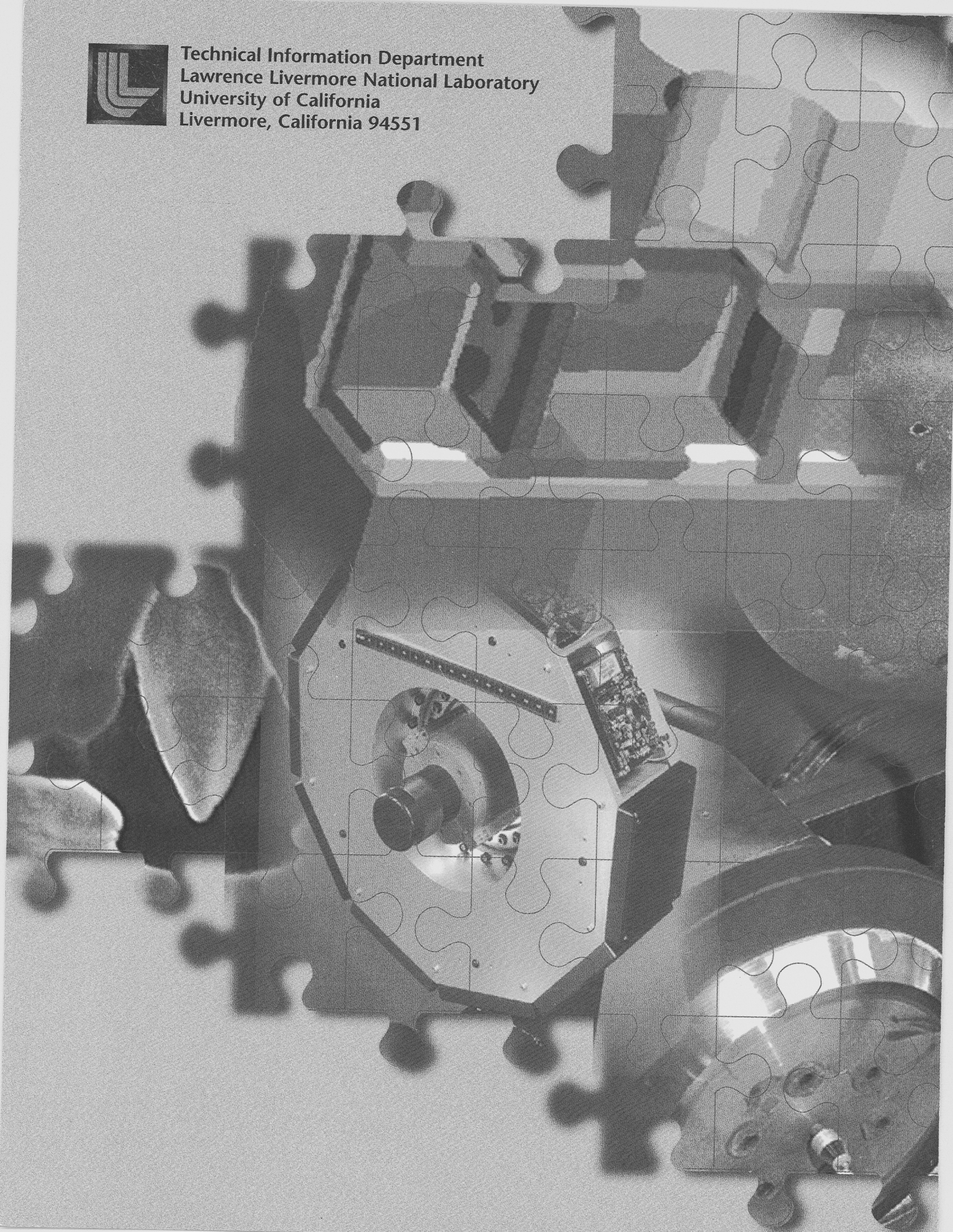
Technical Information Department
Lawrence Livermore National Laboratory
University of California
Livermore, California 94551